

FACULDADE DE ENGENHARIA DA UNIVERSIDADE DO PORTO



3D printing of polycaprolactone/graphene-based materials scaffolds for tissue engineering

João Pedro de Sousa Meneses

MASTER'S THESIS

Mestrado Integrado em Bioengenharia - Engenharia Biomédica

Supervisor: Dr. Artur M. Pinto | FEUP

Co-supervisor: Prof. Dr. Fernão Magalhães | FEUP

Co-supervisor: Prof. Dr. Miguel Castilho | UMC Utrecht

October 29, 2020

3D printing of polycaprolactone/graphene-based materials scaffolds for tissue engineering

João Pedro de Sousa Meneses

Mestrado Integrado em Bioengenharia - Engenharia Biomédica

October 29, 2020

Resumo

A engenharia de tecidos (TE) visa a recriação de substitutos artificiais para melhorar a função de um tecido que havia sido perdida ou danificada. Ao longo dos anos, diferentes biomateriais têm sido explorados nesta área. Entre estes, destaca-se a policaprolactona (PCL), um poliéster alifático sintético, biodegradável e biocompatível, que tem sido amplamente investigado em combinação com técnicas de manufatura aditiva (AM). Não obstante, a PCL apresenta propriedades mecânicas limitadas, sendo assim o seu reforço através da incorporação de cargas uma estratégia comum.

Desde a atribuição do prémio nobel pela realização de procedimentos experimentais inovadores com um material a duas dimensões, o grafeno, o interesse pela área despoletou. O grafeno é o elemento estrutural da grafite e consiste numa monocamada de átomos de carbono com hibridização sp^2 segundo uma estrutura planar semelhante a uma colmeia, composta por diversos anéis benzoicos. A combinação do grafeno com diferentes polímeros tem sido explorada para tirar partido das suas características únicas, como por exemplo as suas propriedades mecânicas e térmicas. Trabalhos prévios demonstraram que os materiais à base de grafeno (GBM) melhoram extensivamente o desempenho mecânico de uma diversidade de polímeros sintéticos, tais como a PCL, mesmo quando incorporados em pequenas quantidades. Assim, cria-se a oportunidade de explorar novos compósitos segundo tecnologias avançadas de processamento.

Recentemente, a capacidade de fabricar implantes com arquiteturas complexas através de técnicas de AM, nomeadamente *melt electrowriting* (MEW), tem-se revelado fundamental no contexto de aplicabilidade biomédica, em particular no que às aplicações em TE diz respeito, sendo dois dos tecidos mais investigados, o muscular esquelético e o cardíaco. A técnica de MEW, resultante da fusão entre *electrospinning* e micro extrusão, apresenta inúmeras vantagens, nomeadamente (i) não requer o uso de solventes, pelo que evita possíveis problemas de citotoxicidade, genericamente associado a outras técnicas; (ii) permite a impressão de fibras à escala micrométrica de forma direta, precisa e sem instabilidades causadas por interferências de campo elétrico.

O objetivo da dissertação foi o desenvolvimento de implantes de PCL de grau médico com GBM segundo a técnica de MEW, com propriedades magnéticas para posterior aplicação em TE. Para tal, foram definidos objetivos específicos: i) preparar GBM magnéticos (@GBM), ii) produzir compósitos PCL/GBM por mistura em fundido; iii) realizar caracterização morfológica, química, térmica, reológica, cristalográfica e magnética das amostras; iv) otimizar a impressão dos compósitos de PCL/GBM; e v) produzir e caracterizar implantes de PCL/GBM com arquiteturas precisas.

Para alcançar o objectivo proposto, dois tipos (M e C) de nanoplaquetas de grafeno (GNP) com diferentes dimensões laterais foram oxidadas através do método de Hummers modificado, e posteriormente magnetizadas segundo o processo de precipitação *in situ* de cloreto de ferro. Através de técnicas de espalhamento dinâmico de luz (DLS) e imagens de microscopia eletrónica de transmissão (TEM), registou-se que a GNP-M, a GNP-C e as nanopartículas de ferro foram obtidas com um tamanho médio de 2 μm , 1 μm e 45 nm respectivamente. Não foram registadas diferenças significativas entre a GNP, a GNP oxidada (GNP-ox) e @GNP quer para o tipo M, quer para o tipo

C. Imagens de TEM revelaram que após o processo de magnetização, as nanopartículas de ferro se encontram a recobrir a superfície da GNP. Por sua vez, os ensaios de potencial zeta revelaram a estabilidade coloidal da GNP, GNP-ox e @GNP para ambos os tipos de GNP produzidos, quando da utilização de água como solvente, sendo que todos valores obtidos foram inferiores a -20 mV.

Seguidamente, filamentos compósitos de PCL/GNP foram obtidos por mistura em fundido. Para este fim, diversas quantidades de @GNP foram testadas, nomeadamente: 2 e 10 wt.% de @GNP-M; 2, 10, 15 e 20 wt.% de @GNP-C. Após a sua produção, imagens de microscopia eletrónica de varrimento (SEM) das secções de corte transversais revelaram que a @GNP não se encontra exposta à superfície dos compósitos, mas homoganeamente distribuída pela matriz polimérica. Assim, técnicas de análise de superfície como espectroscopia no infravermelho por transformada de Fourier (FTIR), e espectroscopia de fotoelétrons excitados por raios-X (XPS) revelaram resultados semelhantes para a PCL e para os compósitos de PCL/GNP. Contrariamente, a técnica de espectroscopia de raios-X por dispersão de energia (EDS) e por consequência de análise em profundidade, revelou um aumento na percentagem atómica de ferro com o aumento da incorporação de @GNP. Ensaio de análise térmica por varredura diferencial de calorimetria (DSC) demonstraram a ação da @GNP como núcleo de cristalização, pois a temperatura de cristalização da PCL aumentou cerca de 94 % com a sua incorporação. Já os ensaios de termogravimetria (TGA) revelaram a @GNP como agente de estabilização térmica, pois a temperatura de degradação máxima da PCL aumentou cerca de 10 e 4 % com a incorporação de @GNP-M e @GNP-C, respetivamente.

Segundo ensaios de difração por raios-X (XRD), a @GNP-M e a @GNP-C apresentaram parâmetros de rede cristalina intermédios entre a Fe_3O_4 e Fe_2O_3 , confirmando assim que os pós obtidos consistem numa mistura entre ambas as estruturas. A presença de Fe-O e PCL nos compósitos de PCL/GNP foi demonstrada através dos seus difractogramas normalizados. Adicionalmente, com a incorporação de quantidades crescentes de @GNP, verificou-se uma intensidade crescente dos picos relativos a Fe-O face aos picos relativos à PCL. Os ensaios de magnetização, realizados por *superconducting quantum interference device* (SQUID), sugerem um comportamento ferromagnético por parte dos materiais testados. A @GNP-M e a @GNP-C apresentaram uma magnetização de saturação (M_S) de 74 e 79 emu g^{-1} , respetivamente. Já a M_S para compósitos de PCL/GNP revelou-se cerca de 70 % do esperado.

Para posteriores estudos de impressão, selecionaram-se os compósitos de PCL/GNP-C em prol dos compósitos de PCL/GNP-M, desde logo pela @GNP-C se ter apresentado com menores dimensões e maior magnetização do que a @GNP-M. Assim, a impressão dos compósitos de PCL/GNP via MEW foi estudada e otimizada de acordo com parâmetros chave, tais como pressão, voltagem e velocidade de coletor. No global, todos os compósitos foram obtidos com diâmetros de fibra a rondar os 20 μm para diversas condições de impressão. Não obstante, a impressão de PCL/GNP-C-20, em função da sua maior viscosidade, revelou-se unicamente precisa para condições de impressão altamente específicas. Por fim, foi apresentado um estudo preliminar acerca da impressão de implantes com poros hexagonais em condições não otimizadas, onde se demonstra que a impressão de PCL e respetivos compósitos segundo estruturas complexas é possível.

Em suma, estes resultados demonstraram, pela primeira vez, a compatibilidade de compósitos de PCL/GNP com tecnologias avançadas de fabricação. A viabilidade de combinar tais compósitos com MEW foi realçada através da impressão de implantes com microarquitecturas complexas. As estruturas 3D obtidas podem ainda ser optimizadas e exploradas para diferentes aplicações biomédicas, incluindo engenharia de tecidos e medicina regenerativa. Estão em curso ensaios de caracterização biológica em implantes de PCL e PCL/GNP com uma linha celular mioblástica imortalizada (C2C12) com o intuito de investigar a sua adesão, proliferação e diferenciação.

Abstract

Tissue engineering (TE) aims to recreate artificial tissue substitutes to improve a lost or damaged tissue function. Over the years, different biomaterials have been explored for the purpose. Among these, polycaprolactone (PCL), a synthetic biodegradable and biocompatible aliphatic polyester, has been widely investigated in combination with additive manufacturing (AM) techniques. Notwithstanding, due to its limited mechanical properties for some of the desired applications, reinforcement with incorporation of fillers is a common procedure.

Since the Nobel Prize "for groundbreaking experiments regarding the two-dimensional material graphene", the interest in graphene has seen a tremendous increase. Graphene, a one carbon atom thick sheet, is the elementary structure of graphite composed of sp^2 carbon atoms arranged in a flat honeycomb structure. Its combination with several polymers has been recently explored mainly due to unique features, such as mechanical and thermal properties. Previous works have demonstrated that graphene-based materials (GBM) are able to extensively improve the mechanical performance of a diversity of synthetic polymers, such as PCL, even when incorporated in small quantities, creating an opportunity to explore such new composite materials using advanced processing technologies.

Recently, the ability to manufacture scaffolds with elaborate architectures by AM techniques, namely melt electrowriting (MEW), has contributed significantly to several studies on biomedical applications, with great potential in the fields of skeletal muscle and cardiovascular TE. MEW is a novel emergent printing technique resulting from merging electrospinning and microextrusion. Main advantages of MEW include (i) a solvent-free processing method, which avoids cytotoxicity concerns commonly associated to other techniques; and (ii) the ability of accurately direct writing microfibers onto a collector without instabilities caused by the electrical field.

Altogether, the primary goal of the thesis was to develop medical-grade PCL/GBM scaffolds with additional magnetic properties via MEW for TE applications. The following specific objectives were set: i) to prepare magnetic GBM (@GBM); ii) to produce PCL/GBM composite filaments by melt-blending; iii) to characterize GBM and PCL/GBM composites in terms of morphological, chemical, thermal, rheological, crystallographic and magnetic properties; iv) to optimize PCL and PCL/GBM printing parameters; and v) to produce and characterize PCL/GBM scaffolds with precise architectures.

To achieve the proposed goal, two grades (M and C) of graphene nanoplatelets (GNP) with different lateral sizes were oxidized through modified Hummers method, and then magnetization was achieved via *in situ* precipitation through the incorporation of iron chloride. Size characterization was performed through dynamic light scattering (DLS) techniques and transmission electron spectroscopy (TEM). GNP-M, GNP-C and iron nanoparticles were obtained with an average size respectively of 2 μm , 1 μm and 45 nm. No significant differences were obtained between GNP, oxidized GNP (GNP-ox) and @GNP for both GNP grade materials. Upon magnetization, iron nanoparticles were found covering GNP surface, as observed by TEM. Zeta potential measurements revealed the colloidal stability of GNP, GNP-ox and @GNP for both GNP grade materials

in aqueous environment, being the obtained values < -20 mV.

Subsequently, composite filaments based on PCL/GNP were produced via melt-blending. For this purpose, different filler ratios were tested: @GNP-M contents were of 2 and 10 wt.%, while for @GNP-C, those were of 2, 10, 15, and 20 wt.%. After production, @GNP were found homogeneously distributed within the polymeric matrix, as observed throughout cross-sections of composite filaments by scanning electron microscopy (SEM). Given that @GNP was not exposed at the surface of composite filaments, surface analysis techniques such as Fourier transform infrared spectroscopy (FTIR), and X-ray photoelectron spectroscopy (XPS) revealed no differences between PCL and PCL/GNP composites. In opposition, energy dispersion X-ray spectroscopy (EDS), which analysis deeper into the samples, revealed an increase in iron at.% with growing @GNP loadings. Furthermore, differential scanning calorimetry (DSC) assays demonstrated that @GNP is behaving as a crystallization nucleus since PCL crystallization temperature increased around 94 % with its incorporation. Thermogravimetric (TGA) analyses revealed @GNP as a thermal stabilizer since PCL maximum degradation rate temperature increased around 10 and 4 % with @GNP-M and @GNP-C incorporation, respectively.

According to X-ray diffraction (XRD) assays, @GNP-M and @GNP-C presented intermediate lattice parameters between Fe_3O_4 and Fe_2O_3 , thus confirming that the powders consisted of a mixture between both structures. PCL/GNP composites normalized diffractograms revealed the presence of Fe-O and PCL. Herein, the higher the @GNP wt.%, the higher the intensity of the peaks of Fe-O material compared to PCL. Magnetic experiments, via superconducting quantum interference device (SQUID), suggested that materials presented a ferromagnetic behaviour. @GNP-M and @GNP-C exhibited a magnetic saturation (M_S) of 74 and 79 emu g^{-1} , respectively, while PCL/GNP composites presented M_S values around 70 % of the theoretical ones, regarding the amounts of filler loaded and its M_S .

These results, namely @GNP-C presenting lower average size, and higher M_S than @GNP-M, enabled the selection of PCL/GNP-C instead of PCL/GNP-M composites for further printing studies. Therefore, PCL/GNP-C composites printability via MEW was investigated and optimized according to key parameters such as feeding pressure, applied voltage and collector speed. Overall, each composite was obtained with fibre diameters around 20 μm for a broad range of printing conditions. Notwithstanding, given PCL/GNP-C-20 higher viscosity, its printability was only accurate to highly specific printing conditions. Finally, through a preliminary study on the printing of hexagonal microstructured scaffolds in non-optimized conditions, it is demonstrated that the printing of PCL and PCL/GNP composites with complex patterns is possible.

Altogether, these results demonstrated, for the first time, the compatibility of PCL/GNP composites with advanced fabrication technologies. The feasibility of combining such composite filaments with MEW was herein proved by printing complex 3D microarchitectures. The obtained 3D structures can be further optimized and explored for different biomedical applications, including tissue engineering and regenerative medicine. Biological characterization experiments are being performed on PCL and PCL/GNP scaffolds with an immortalized myoblastic cell line (C2C12) to investigate their adhesion, proliferation and differentiation.

Agradecimentos

Primeiramente, importa esclarecer que escrevo esta secção ao som do inevitável Pedro Abrunhosa. Assim, desde o “Tudo o que eu te dou”, passando pelo “Se eu fosse um dia o teu olhar”, ao “Para os braços da minha mãe”, tento exprimir o meu apreço e gratidão a todos aqueles que tornaram estes cinco anos tão especiais, tão maravilhosos.

Ao meu orientador, Artur Pinto, um tremendo obrigado pelas críticas, pela paciência, pelos ensinamentos e correções e, sobretudo, pela amizade. Ao Professor Miguel, orientador do meu Erasmus, e co-orientador da minha dissertação, obrigado, sobretudo pela primeira oportunidade de estudar e aprender fora de Portugal. Ao Professor Fernão, obrigado por tornar tudo isto possível. A toda a restante equipa, Diana, Filipa, Joost e Licínia, obrigado. Raquel, para ti, uma palavra especial seja pela tua alegria e boa disposição, seja pela tua humildade e genuinidade, pois são valores que admiro e que não têm preço. À Joana Silva, apesar de não o seres oficialmente, foste como uma co-orientadora para comigo. Sempre disponível, animada e com vontade de aprender mais e mais. Por tudo isso, obrigado!

À Professora e amiga Inês Gonçalves, obrigado! Não só pela simpatia e atenção, como também por rapidamente ter despoletado todo o meu gosto pela área dos Biomateriais. Assim, com orgulho, digo que será a Professora que me irá cartolar.

À Professora Noémia e ao Professor Néry. É impressionante como após tantos anos ainda me recordo dos vossos ensinamentos. Na verdade, a própria quote da presente dissertação reflete uma das frases mais ditas pelo Prof. Néry: “Põe quanto és, no mínimo que fazes”. A verdade é que me receberam de braços abertos. Receberam-me numa turma repleta de meninos bonitos, onde eu seria um dos patinhos feios. Apesar das dificuldades encontradas, nunca desistiram de mim, enquanto pessoa e aluno. Chamaram-me à razão. Deram-me a confiança que precisava. Transformaram-me no aluno ambicioso, com vontade de aprender mais e mais, determinado e trabalhador que sou hoje. Se o 10º ano não foi fácil, o 11º foi estrondosamente bom e o 12º foi o culminar de uma história de amor. Obrigado!

Aos meus pais, aos meus ídolos ... obrigado. Obrigado outra vez. Obrigado outra e outra vez. Sem vocês, este percurso não seria possível. Todos os que me são próximos sabem que se há coisa que me deixa feliz, é sentir que se sentem orgulhosos de mim. Nem sempre vivemos num mar de rosas. Nem sempre jantamos alegres. Mas mantivemo-nos sempre unidos. E hoje ... hoje ... vivemos dias felizes. E isso, não tem preço. Joana ... a ti ... e aos meninos ... refiro-me só no final, pois ainda não me sinto preparado para tal. Nandinho, obrigado. A forma como aparecete e te integraste na família foi incrível. Sempre fizeste extraordinariamente bem à minha irmã. E se lhe fazes bem a ela ... fazes-me bem a mim. Por isso, e por muito mais ... obrigado!

Aos amigos de sempre. Catarina, Francisco, João Soares, Pedro, Mariana, Vítor, Tiago e Zé. O orgulho que tenho em vocês é ridiculamente grande. Já são tantos anos, tantas etapas ultrapassadas em conjunto, tantos cafés, jantaras, festas, gargalhadas, discussões, que é quase impossível dizer algo aqui que nunca vos tenha dito pessoalmente. Ficam as memórias. Desde as festas no moonlight, às idas à praia da rocha, ao azibo, a bitetos, à casa do lago, ao café com

1001 nomes do parque da cidade, às noitadas em minha casa, às tardes de fifa e muito mais. Uma coisa é certa. Já vivemos muito, mas haveremos de viver muito mais. Que todos os outros não me interpretem erradamente, mas a ti, Francisco, tenho de me referir uma vez mais. Lutaste ao máximo por seguir o teu sonho de ser jogador de futebol. “Não conseguiste”. Sofreste. Sofri contigo. Levantaste-te. Não desististe. Entraste na melhor faculdade de desporto de Portugal. Hoje, és quase professor. Por tudo isso, o meu orgulho em ti é ainda maior. Já agora . . . deste-me o presente mais bonito que alguma vez me poderias ter dado. A tua camisola, que desde então me acompanha dia sim, dia sim. Ana Rita e Filipa, sei que no último ano não falamos tanto quanto isso, no entanto, isso não apaga tudo o que fomos vivendo nos anteriores. A vossa simpatia e gentileza, aliadas à perseverança e resiliência, farão de vocês médicas fabulosas, porque a nível pessoal, já o são. Estarei cá para ver e acompanhar. Obrigado por tudo.

Referindo-me agora aos primeiros tempos de faculdade, lembro-me perfeitamente de assumir que encontrar um grupo como o meu de Penafiel não seria possível. Não havia química. Eramos conhecidos. Saímos à noite e tal. Mas não havia uma ligação suficientemente forte entre todos. Talvez por sermos demasiados. Bem, a verdade é que tudo isso mudou assim que ingressámos em biomédica. Não sei se sempre gostamos tanto uns dos outros e não o demonstrávamos, ou se passamos a aprender a gostar uns dos outros em função de termos de o fazer diariamente por três anos. A verdade é que hoje somos unha com carne. Peniche foi a mais recente etapa desta história de amor.

Gu, é tão simples quanto isto, a minha admiração por ti é tremenda. És a minha paixão. Seja na faculdade, no NEB, nas jantaras, nas saídas até às tantas, nas discussões, nos jogos de futebol, nos 1001 desportos onde és o melhor, e em muito mais, é sempre um prazer e orgulho estar ao teu lado. Bruno, Migas e Pedrão. São especiais. Sabem disso. Com o Bruno, formo os gémeos bruneses que de forma fantástica propuseram rápida e eficazmente a melhor viagem de finalistas alguma vez imaginada e planeada . . . a Marrocos. No Pedrão, tenho aquele amigo que me entende, mesmo quando não me expresso tão bem. Por partes: (EU) – Pedrao reconheces esta música? Nnnn, não dá . . . nnnn, não dá. (PEDRAO) – Cafeína. Tenho o companheiro de troca de memes agressivos que ferem suscetibilidades aos mais sensíveis. Migas, em ti tenho o primo “que nunca tive”. És a ratice em pessoa. Estás lá, mesmo quando não estás. É difícil imaginar alguém melhor a anunciar eventos do que tu. Novamente: (TODA A GENTE): Migas, que dizes, para a semana jantarada em tua casa. (MIGAS): não diz nada e a jantarada realiza-se. Em todos vós, tenho os meus abrunhosas.

Raquel e Leonor. As minhas, as nossas gémeas. Sinto sempre muita felicidade quando penso em vocês. Sempre tão especiais e tão estranhamente iguais. Ainda hoje é o dia que aquela mentira me deixa a pensar. Raquel, em ti, tenho a vegetariana que nunca tive na minha vida. Já na Leonor, tenho a pessoa que nunca diz que não a um gin. São incríveis. Adoro-vos por isso e por muito mais. Ana e Pedro Filipe. É difícil tentar lembrar-me de um, sem me lembrar do outro. É como um abrir e piscar de olhos. Abrimos, vocês estão lá. Fechamos. Vocês fugiram. Abrimos, estão vocês na vossa perdição que é a tequila. Mais a mais, já não consigo idealizar ninguém melhor para organizar aniversários de outras pessoas, sem as questionar, do que a minha presidente. Quanto ao Pedrinho, ainda hoje é o dia que te tenho de agradecer por me teres salvo a vida naquela noite muito complicada que vivemos em Milão. Álvaro, Joana e Nataliya. No ÁMS tenho o tronco que nunca conheci, o ser que está sempre preparado para uma boa discussão e que torna sempre os nossos dias um pouco mais cultos. Espero que continues com as tuas leituras para te instruíres para o resto da vida. Joana, tia Jupi. Em ti, tenho sempre a parceira de ir na crocodilagem e sei que se colocas o casaco à cinta, é o fim do game. És um espetáculo. Nataliya, a minha, a nossa slav favorita. Saudades das corridas que ainda não demos. Caso tenha escrito o teu nome errado de novo, não me culpes a mim, culpa o sigarra. Continua com o teu inner- Nataliya que desenvolveste

na quarentena. É a personagem do ano. A todos vós, sem exceção, desejo-vos o triplo do sucesso que desejo para mim.

Os agradecimentos já vão longos, mas ainda tenho inevitavelmente de referir o meu NEB e a minha FOCA. Dois núcleos diferentes, mas ambos especiais. O NEB foi a minha primeira grande atividade extracurricular. Para além de amizades, deu-me alegria, deu-me logística, deu-me rotação, deu-me um grupo de pessoas que admiro e respeito muito. Começou muito bem, terminou ainda melhor. Terminou com a melhor presidência possível e com o simpósio que demonstrou toda a nossa capacidade de adaptação e resiliência para com os obstáculos que a pandemia nos colocou. A FOCA trouxe-me um desafio diferente. Trouxe-me RELEX, uma equipa sempre animada e motivada. Ana Rita, para ti uma palavra especial, ou ... devo dizer ... um beijinho, dada a tua aptidão para tal.

Aos meus 4 percalços, Alfa, Chave, Facada e Madena. Ainda hoje é o dia que não percebo como me pediram para padrinho unicamente após três ou quatro meses de nos “conhecermos”. Tenho feito tudo por vós, pois merecem isso e muito mais. Sorrio e sofro convosco. Sorrio mais porque estão sempre todas animadas. Acompanhar-vos-ei em todo o vosso percurso. E de uma coisa podem ter a certeza. Em mim, têm um amigo para a vida.

Chegamos assim ao momento de me referir a ti, minha Joana. Agradeço-te pelo que fizeste por mim desde sempre. Desde a me ires buscar aos “bailes de finalistas” de 7º ao 9º e respetivas “noitadas” de agrival para os pais não acordarem. Engraçado que diziam sempre que não dormiam enquanto não chegasse a casa, no entanto, sempre que chegávamos, estavam a dormir. Acompanhaste-me em todas as etapas. Chegaste inclusive a ir a reuniões do meu secundário por a mãe sentir que eu me portava mal. Deste tudo por mim. Dás tudo por mim. A pessoa que eu sou hoje, deve-se sobretudo a ti. Tive o 1º momento mais feliz da minha vida no teu casamento. O 2º e o 3º nos nascimentos do Tomás e da Inês. Sinto que por ti, pouco ou nada posso fazer. Assim, resta-me te garantir que farei o que fizeste por mim, pelo Tomás e pela Inês, pois melhor será difícil, para não dizer impossível. Dizer “tenho a melhor irmã do mundo” é o que todos dizem, eu digo: TENHO A MELHOR IRMÃ QUE ALGUMA VEZ PODERIA TER SONHADO.

João Meneses

*“Para ser grande, sê inteiro: nada
Teu exagera ou exclui.
Sê todo em cada coisa. Põe quanto és
No mínimo que fazes.
Assim em cada lago a lua toda
Brilha, porque alta vive.”*

Fernando Pessoa, Odes de Ricardo Reis

Contents

1	Introduction	1
1.1	Context	1
1.2	Motivation	3
1.3	Goals	5
1.4	Structure	5
2	Polycaprolactone	7
2.1	Scope	7
2.2	State-of-the-art	8
2.2.1	Synthesis and physicochemical properties	8
2.2.2	Biodegradation	10
2.2.3	Biocompatibility	10
2.2.4	Biomedical applications	11
3	Graphene-based materials	13
3.1	Scope	13
3.2	State-of-the-art	15
3.2.1	Synthesis and physicochemical properties	15
3.2.2	GBM composites	16
3.2.3	Biodegradation	17
3.2.4	Biocompatibility	19
3.2.5	Biomedical applications	20
4	Additive manufacturing	23
4.1	Scope	23
4.2	AM techniques	24
4.2.1	Laser-based technologies	24
4.2.2	Fused deposition modelling	24
4.2.3	Pressure-assisted microsyringe deposition	25
4.2.4	3D bioplotting and ink-jet bioprinting	25
4.2.5	Electrospinning	26
4.2.6	Melt electrowriting	27
4.3	3D printed scaffolds for biomedical applications	31
4.3.1	Polycaprolactone/graphene-based materials	31
4.3.2	Other polymers/graphene-based materials	33

5	Materials and Methods	35
5.1	Materials Production	35
5.1.1	GBM oxidation and magnetization	35
5.1.2	Melt blending of PCL/graphene-based materials composites	36
5.2	Materials characterization	37
5.2.1	Morphological characterization	37
5.2.2	Chemical characterization	37
5.2.3	Thermal characterization	39
5.2.4	Rheological characterization	40
5.2.5	Crystallographic characterization	40
5.2.6	Magnetic characterization	40
5.3	Materials printing	41
5.3.1	Melt electrowriting	41
5.3.2	MEW experimental parameters	42
5.3.3	Fabrication process	42
5.4	Statistical analysis	44
6	Results	45
6.1	GBM morphological properties, particle size, and stability	45
6.2	Chemical characterization of GBM	51
6.3	Thermal analysis	59
6.4	Rheological properties	65
6.5	Crystallographic and magnetic characterization	67
6.6	Fibre diameter and morphology	72
6.7	Preliminary study on scaffolds printability	76
7	Discussion	77
8	Conclusions and Future work	85
8.1	Conclusions	85
8.2	Ongoing and Future work	87
	Bibliography	89
A	Supplementary material for Chapter 4	107
B	Supplementary material for Chapter 6	111
C	List of publications	133
D	List of presentations	135

List of Figures

2.1	Number of publications on tissue engineering, in which polycaprolactone was used.	8
2.2	Ring-opening polymerization of ϵ -caprolactone to polycaprolactone.	8
2.3	List of reported materials to blend with polycaprolactone.	9
3.1	Graphene as the 2D building block of hexagonally bonded carbon materials.	14
3.2	Graphene-based materials family and its production methods.	14
3.3	Number of publications on graphene in the context of biomedical applications.	15
3.4	Graphene-based materials biodegradation categorization.	18
4.1	Number of publications on additive manufacturing in the context of biomedical applications.	24
4.2	List of 3D bioplotting printable materials.	26
4.3	List of MEW polycaprolactone scaffolds designs.	29
5.1	Magnetic graphene nanoplatelets (@GNP) production method.	36
5.2	Schematic of the custom-built MEW device and its principal components.	41
5.3	Critical translational speed (CTS) evaluation pattern.	43
5.4	Theoretical relationship between CTS, collector speed (C_S), fibre morphology and fibre diameter (F_d).	44
6.1	Transmission electron microscopy (TEM) images of GNP-M, GNP-C, GNP-M-ox, GNP-C-ox, @GNP-M, and @GNP-C.	46
6.2	Scanning electron microscopy (SEM) images of @GNP-M and @GNP-C powders.	46
6.3	Average particle size of iron nanoparticles, GNP-M and GNP-C grade materials, determined from TEM images.	47
6.4	Particle size distribution in volume and number for GNP-M and GNP-C grade materials, determined by dynamic light scattering (DLS), using a Beckman Coulter equipment.	48
6.5	Particle size distribution in volume and number for iron nanoparticles, GNP-M and GNP-C grade materials, determined from TEM images and DLS, using a Beckman Coulter and a Litesizer equipment.	49
6.6	Surface charge of iron nanoparticles, GNP-M, GNP-M-ox, @GNP-M, GNP-C, GNP-C-ox and @GNP-C aqueous dispersions determined with a Zetasizer equipment.	50
6.7	Average particle or particle agglomerates size of @GNP-M and @GNP-C in PCL/GNP-M and PCL/GNP-C filaments cross-sections, determined from SEM images.	50
6.8	SEM images of PCL/GNP filaments.	51
6.9	Fourier transform infrared (FTIR) spectra of GNP-M, GNP-C, GNP-M-ox, GNP-C-ox, @GNP-M and @GNP-C.	52

6.10	FTIR spectra of PCL.	53
6.11	FTIR spectra of PCL, PCL/GNP-M and PCL/GNP-C scaffolds.	53
6.12	SEM images and energy dispersive x-ray spectroscopy (EDS) analysis maps of GNP, GNP-ox and @GNP, for GNP-M and GNP-C grade materials.	55
6.13	X-ray photoelectron spectroscopy (XPS) analysis of @GNP-M and @GNP-C. Deconvolution of high-resolution C 1s, O 1s and Fe 2p XPS spectra. Content of C 1s, O 1s and Fe 2p chemical groups resulting from spectra fitting.	56
6.14	XPS analysis of PCL. Deconvolution of high-resolution C 1s and O 1s XPS spectra. Content of C 1s and O 1s chemical groups resulting from spectra fitting.	58
6.15	Sessile drop water contact angle for PCL, PCL/GNP-M and PCL/GNP-C filaments.	58
6.16	Differential scanning calorimetry (DSC) thermograms for PCL, PCL/GNP-M and PCL/GNP-C filaments and scaffolds.	59
6.17	Thermogravimetric (TGA) curves for GNP-M, GNP-C, GNP-M-ox, GNP-C-ox, @GNP-C and @GNP-M powders and iron nanoparticles, under nitrogen atmosphere.	61
6.18	TGA curves for PCL, PCL/GNP-M and PCL/GNP-C scaffolds, under nitrogen atmosphere.	63
6.19	Isothermal curves for PCL, PCL/GNP-M and PCL/GNP-C filaments 90 and 130 °C, during 8 hours.	64
6.20	Loss factor (loss (G'') / storage (G') moduli) for PCL at 90, 130 and 180 °C.	66
6.21	Loss factor for PCL, PCL/GNP-M and PCL/GNP-C filaments contents at 90 and 130 °C.	66
6.22	Crystallographic patterns of GNP-M, GNP-C, GNP-M-ox and GNP-C-ox through X-ray diffraction (XRD).	67
6.23	Magnetic-hysteresis (M-H) curves of GNP-M, GNP-C, GNP-M-ox and GNP-C-ox determined from superconducting quantum interference device (SQUID) magnetometry, at room temperature.	68
6.24	Crystallographic patterns and M-H curves of @GNP-M and @GNP-C, at room temperature.	69
6.25	Magnetic behaviour of @GNP-C. Zero-field-cooled/field-cooled (ZFC/FC) measurement at a fixed magnetic field of $H=100$ Oe; isothermal M-H measurement at 100, 200 and 300 K	70
6.26	Crystallographic patterns and M-H curves for PCL, at room temperature.	71
6.27	Crystallographic patterns and M-H curves of PCL/GNP-M and PCL/GNP-C filaments through XRD and SQUID, respectively, at room temperature.	72
6.28	CTS of PCL and PCL/GNP-C composites.	73
6.29	Influence of feeding pressure (P), applied voltage (V) and C_S on F_D for PCL and PCL/GNP-C composites.	74
6.30	PCL and PCL/GNP-C composites extrusion jet for 2 bar and 6 KV at several C_S	75
6.31	SEM images of PCL and PCL/GNP hexagonal microstructured scaffolds composed of multiple stacked microfibers.	76
A.1	Summary of additive manufacturing techniques.	108
B.1	SEM images of GNP-M, GNP-M-ox, @GNP-M, GNP-C, GNP-C-ox and @GNP-C powders.	112
B.2	Average particle size of iron nanoparticles and both grades of GNP from TEM images.	113

B.3	Box-plot of particle size distribution in number of iron nanoparticles and both grades of GNP from TEM images.	114
B.4	Particle size distribution for both GNP-M and GNP-C grade materials in volume and number, determined by DLS, using a Litesizer equipment.	115
B.5	Surface charge of iron nanoparticles, GNP-M, GNP-M-ox, @GNP-M, GNP-C, GNP-C-ox and @GNP-C aqueous dispersions determined with a Zetasizer.	116
B.6	SEM images of PCL/GNP-C 15 wt.% cross-section.	116
B.7	FTIR spectra of PCL, PCL/GNP-M and PCL/GNP-C filaments.	117
B.8	XPS survey spectra @GNP-M and @GNP-C.	118
B.9	XPS survey spectra for PCL/GNP-M and PCL/GNP-C filaments.	118
B.10	XPS survey spectra for PCL, PCL/GNP-M and PCL/GNP-C scaffolds.	119
B.11	XPS analysis of PCL/GNP-M and PCL/GNP-C filaments. Deconvolution of high-resolution C 1s XPS spectra. Content of C 1s chemical groups resulting from spectra fitting.	120
B.12	XPS analysis of PCL/GNP-M and PCL/GNP-C filaments. Deconvolution of high-resolution O 1s XPS spectra. Content of O 1s chemical groups resulting from spectra fitting.	121
B.13	XPS analysis of PCL/GNP-M and PCL/GNP-C scaffolds. Deconvolution of high-resolution C 1s XPS spectra. Content of C 1s chemical groups resulting from spectra fitting.	122
B.14	XPS analysis of PCL/GNP-M and PCL/GNP-C scaffolds. Deconvolution of high-resolution O 1s XPS spectra. Content of O 1s chemical groups resulting from spectra fitting.	123
B.15	Sessile drop water contact angle for PCL, PCL/GNP-M and PCL/GNP-C filaments.	123
B.16	-dTG curves for PCL, PCL/GNP-M and PCL/GNP-C filament and scaffolds, under nitrogen atmosphere.	124
B.17	Dependence of the saturation and remanent magnetization (M_s and M_r , respectively) on the concentration of @GNP-M and @GNP-C.	127
B.18	Crystallographic patterns and M-H curves of PCL/GNP-M and PCL/GNP-C scaffolds through XRD and SQUID, respectively, at room temperature.	127
B.19	Fibre morphology of PCL and PCL/GNP-C grade materials at 0.5 CTS, 0.75 CTS, 0.9 CTS and CTS.	129

List of Tables

2.1	Summary of polycaprolactone physicochemical properties	9
3.1	Essential material properties on biological response influence.	19
4.1	Summary of MEW designs and its printing parameters.	30
4.2	List of studies on PCL/GBM scaffolds, its printing techniques and aims.	32
5.1	Main features of GNP-M and GNP-C grade materials.	35
5.2	Range of stable printing conditions namely feeding pressure (P) and applied voltage (V) at critical translational speed (CTS) for PCL and PCL/GNP composites.	42
6.1	EDS and XPS analysis of GNP, GNP-ox and @GNP powders, PCL, PCL/GNP filaments and scaffolds. EDS outlines the content of C, O and Fe, while XPS presents the content of C 1s, O 1s and Fe 2p. C/O ratio for each sample is present by both methods.	54
6.2	Crystallization temperatures (T_{c1} and T_{c2}), melting temperatures (T_{m1} and T_{m2}) and degree of crystallization (χ_{c1} and χ_{c2}) for PCL, PCL/GNP-M and PCL/GNP-C filaments and scaffolds containing different filler contents.	60
6.3	Weight loss (%) values for GNP-M, GNP-C, GNP-M-ox, GNP-C-ox, @GNP-M, @GNP-C powders and iron nanoparticles, under nitrogen atmosphere.	62
6.4	Thermogravimetric parameters of PCL, PCL/GNP-M and PCL/GNP-C filament and scaffolds, namely 5% degradation temperature, $T_{5\%}$, the temperature of maximum degradation rate, T_d , and measured weight at 545 °C and 1000 °C.	63
6.5	Total weight loss (%) values at 90 and 130 °C for PCL, PCL/GNP-M and PCL/GNP-C filaments, under nitrogen atmosphere.	65
A.1	List of studies on AM of polymer/GBM 3D printed scaffolds, and its main goals.	109
B.1	Relationship between the zeta potential values and the solution stability behaviour.	115
B.2	Crystallization temperatures (T_{c1} and T_{c2}), melting temperatures (T_{m1} and T_{m2}), crystallization enthalpy (ΔH_{c1} , ΔH_{c2}), melting enthalpy (ΔH_{m1} , ΔH_{m2}) and degree of crystallization (χ_{c1} and χ_{c2}) for PCL, PCL/GNP-M and PCL/GNP-C filaments and scaffolds containing different filler contents.	125
B.3	Loss factor values for PCL, PCL/GNP-M and PCL/GNP-C filaments at 90 °C, 130 °C and 180 °C.	126
B.4	Saturation magnetization (M_s), coercivity (H_c) and remanent magnetization M_r values of GNP, GNP-ox and @GNP powders, as well as PCL/GNP filaments and scaffolds.	128

B.5	CTS for PCL and PCL/GNP-C composites. Ratio between the real fibre diameter (F_D) and the relative peak to peak fibre diameter (F_D').	130
B.6	Influence of feeding pressure on F_D for PCL and PCL/GNP-C composites.	130
B.7	Influence of applied voltage on F_D for PCL and PCL/GNP-C composites.	131
B.8	Influence of C_S on F_D for PCL and PCL/GNP-C composites.	131

List of Abbreviations

@	magnetic
2D	Two dimensional
3D	Three dimensional
4D	Four dimensional
AM	Additive manufacturing
at.%	Atomic percentage
CBM	Carbon-based materials
C_s	Collector speed
CTS	Critical translational speed
DLS	Dynamic light scattering
DSC	Differential scanning calorimetry
ECM	Extracellular matrix
EDS	Energy Dispersive X-ray spectroscopy
ELS	Electrophoretic light scattering
F_D	Fibre diameter
FDA	Food and Drug Administration
FDM	Fused deposition modelling
FLG	Few-layer graphene
FTIR	Fourier-transform infrared spectroscopy
G	Graphene
GBM	Graphene-based materials
GNP	Graphene nanoplatelets
GO	Graphene oxide
Gt	Graphite
GtO	Graphite oxide
MEW	Melt electrowriting
MHM	Modified Hummers method
PCL	Polycaprolactone
PLA	Poly lactic acid
rGO	Reduced graphene oxide
SEM	Scanning electron microscopy
SLA	Stereolithography
SLS	Selective laser sintering
SQUID	Superconducting quantum interference devices
TE	Tissue engineering
TEM	Transmission electronic microscopy
TGA	Thermogravimetric analysis
TR	Tissue regeneration
wt.%	Weight percentage
XPS	X-ray photoelectron spectroscopy
XRD	X-ray diffraction

Chapter 1

Introduction

1.1 Context

Globally, around 230 million major surgical procedures are performed [1]. Most of these involve repair, replacement or regeneration of one or more damaged tissues or organs through disease or injury [2]. The current gold standard treatment for these issues is the autograft, that is the tissue transplant from one site to another in the same patient. It is also possible to transplant from one patient to another (allograft). However, both approaches have major problems [3]. On one hand, the amount of available donor tissue, as well as the need for a second injury site, which results either in additional trauma to the patient either in new possible consequences such as pain, infection, and donor-site morbidity, limits the autograft approach. On the other hand, the hurdle to the allografts approach is based not only on the restrict amount of tissue available for all of the patients who require them but also on the rejection risk by the patient immune system and the subsequent possibility of infection or disease introduced on the patient, from the donor [2].

As an alternative, come out the concept of Tissue Engineering (TE), which was first pointed out in 1998 in a National Science Foundation workshop being defined as "the application of principles and methods of engineering and life sciences toward the fundamental understanding of structure-function relationships in normal and pathological mammalian tissues and the development of biological substitutes to restore, maintain or improve tissue function" [4]. Thereby, TE field involves a multidisciplinary knowledge, passed from experts on mechanical engineering, clinical medicine, genetics, materials science to related disciplines from both engineering and life sciences [4]. The acceptance process of tissue-engineered constructs has been changing over the last few years. In the beginning, the constructs were prepared outside the body and only then incorporated into the living being. Currently, the use of the constructs on a clinical environment implies the successful implantation and evaluation of the prepared tissue/organ [5].

TE attention from the scientific community has increased terrifically over the last 25 years, not only in the proper scientific point of view, according to the 1.2 million results on Google Scholar [6], but also in the economic point of view. Kim *et al.* [6] reported that currently, there are a total of 49 publicly listed TE companies in the US, employing nearly 146 millions of people. Another

study pointed out that TE market is expected to grow from \$10.8 billion in 2016 to over \$22 billion in 2025 worldwide [7].

Regardless of the tissue type, several key considerations are important when designing a scaffold for use in TE, namely its mean pore size and architecture, which accuracy is highly dependent on the manufacturing technique. These factors will directly influence both mechanical and biological properties, namely scaffolds biocompatibility and biodegradability [4]. Highlighting the biological behaviour, the clinical environment for TE constructs is getting closer. The biggest hurdle has been the regulatory issues, being that 86 % of all clinical trials in 2018 to get Food and Drug Administration (FDA) approval failed, which originated a huge economic burden [8].

All the criteria mentioned above are dependent on the selected biomaterial, which is the basis for scaffold production. In 1976, in the first Consensus Conference of the European Society for Biomaterials, a biomaterial definition was given: "a nonviable material used in a medical device, intended to interact with biological systems" [4]. Nowadays, the concept of biomaterial is different since its understanding moved from only interacting with the body to influencing biological processes toward the goal of tissue regeneration (TR). The current definition of biomaterial is a "any substance or combination of substances, other than drugs, synthetic or natural in origin, which can be used for any period of time, which augments or replaces partially or totally any tissue, organ or function of the body, in order to maintain or improve the quality of life of the individual" [9].

Typically, three groups of biomaterials - ceramics, natural and synthetic polymers - are used in the fabrication of scaffolds for TE. Each of these biomaterial groups has specific advantages and disadvantages, therefore the use of composite scaffolds comprised of different phases is becoming increasingly common [4]. Ceramic scaffolds, although not generally used for soft TE, there has been widespread use of it, such as hydroxyapatite and tri-calcium phosphate, for bone TR applications [4]. Natural polymers like hyaluronic acid, fibrin, chitosan, and collagen have good biological compatibility, low immunogenicity, and osteoconductivity. However, natural polymers suffer from high degradation rates and low mechanical stability. Opposingly, synthetic polymers, like polycaprolactone (PCL) and polylactic acid (PLA) exhibit controlled degradation rates. Moreover, they possess the ability to be fabricated into complex shapes and have improved cell attachment. Synthetic polymers can also be produced at low cost, in large quantities and have a longer shelf life [10]. An emerging class of materials, smart (bio)polymers, besides being biodegradable, biocompatible, renewal as well as inexpensive, exhibit a characteristic feature of undergoing fast and reversible changes due to being sensitive to some factors such as temperature, humidity, pH, the intensity of light, solvent or ionic composition, the introduction of specific ions and electrical or magnetic fields [11].

1.2 Motivation

The growing need for organs and tissues continuously stimulates the development of TE. Initially, TE appeared with two dimensional (2D) scaffolds, which allows the growth of cells as a monolayer culture flask, involving a single type of cells on a planar surface. Thus 2D scaffolds are not a perfect representation of the normal environment in an organism, due to the limited cell-cell interaction and lack of cellular organization [12, 13]. Therefore, the future of TE depends on three-dimensional (3D) scaffolds [14, 15].

In 3D cell culture, aiming to mimic the real-life scenario, a cellular microenvironment is created in the cell-cell or cell-extracellular matrix (ECM) interactions. There is also the possibility of co-culture several types of cells [16, 17]. Moreover, 3D scaffolds which consist of nanofibres, nanotubes or nanoparticles, are often made of polymers such as PCL and PLA, which were found to be effective in influencing the fate of stem cells. Besides polymers, carbon-based materials (CBM) offer an alternative of nanomaterials for TE due to their biocompatibility and mechanical strength [18].

Regarding CBM and its compatibility with the natural ECM, scaffold based on them can enhance both cell-cell interaction and normal cellular functions in TE. CBM of different dimensions such as fullerenes, carbon nanotubes, and graphite were successfully employed in many TE investigations due to their mechanical stability [19, 20]. These carbon nanomaterials are considered as a physical analogue of ECM components such as collagen fibres due to their similar dimensions [20, 21].

Graphene (G), being a one carbon atom thick sheet, is the elementary structure of graphite and is composed of sp^2 carbon atoms arranged in a flat honeycomb structure. Graphene-based materials (GBM) can present different structure and properties such as graphene oxide (GO), reduced graphene oxide (rGO), graphene quantum dots (GQD), graphene nanosheets and graphene nanoplatelets (GNP), also known as few-layer graphene (FLG).

Previous studies suggest that integration of G components have excitingly enhanced the cytocompatibility of biomaterials by osteointegration, stem cell differentiation into a variety of cells, improved neuronal growth and branching, which boost the production of vascular endothelial growth factor/pro-angiogenic gene for cardiac repair [22, 23, 24]. There are already several scaffold fabrication techniques available including solvent casting [25], particulate leaching [26], gas foaming, solution electrospinning [27], phase separation [28] and freeze-drying [28].

The main disadvantages of the previous scaffold manufacturing techniques are mainly based on the use of organic solvents which is often related to cytotoxicity issues [29, 30]. Currently, the challenge is the development of new scaffold designs and manufacturing approaches that allow the printing of a dynamic and accurately defined 3D pore architecture. Regarding this need, appears additive manufacturing (AM) techniques [31, 32]. AM is a broad term that concerns several methods that by using a computer-aided design can fabricate scaffolds via layer-by-layer fibre deposition.

An alternative processing technique for the fabrication of scaffolds for TE applications is solution electrospinning [30], which is generally not considered as an AM technique due to the dynamic and chaotic nature of fibre deposition. Generally, the limitations of AM include lower resolution fabrication limits, while electrospinning is unable to accurately reproduce structured 3D scaffolds accurately [33].

Therefore, it appears a technique designated as melt electrowriting (MEW). It can produce sub-micron diameter fibres - as low as 270 nm [34] - but these are exceptions rather than the rule. This means that MEW does not normally result in the production of "nanofibres", which is one of the original goals of electrospinning. However, MEW can readily produce fibres with "low micron diameters" that allow the design of scaffolds for TE applications [35]. While MEW is not considered useful for nanofibre production, there are compelling arguments for its use in TE scaffold production, namely being a reproducible, robust and flexible process in manufacturing biomedical materials [35].

Explained the current scenario on 3D cell culture, GBM and AM techniques is now essential to enhance the onset of GBM scaffolds as a way to surpass the concerns on cell adhesion, proliferation and differentiation in the biomedical context. Currently, 3D printed GBM scaffolds, due to its unique mechanical and electrical properties, are used for TE of heart, bone, cartilage, nerve, skin, liver, etc [36, 37]. Additionally, several studies reported GBM biocompatibility and antibacterial properties [38, 39].

The primary concern among the use of 3D printed GBM scaffolds is its toxicity. Despite this worry, many investigations have been successful in proving its biocompatible nature [40]. Another concern is related to both mass transfer and oxygenation of the cells. These factors can be improved by the manufacturer of a scaffold with a suitable pore size range and distribution.

Recently another key topic has started to be explored in the TE field, namely the achievement of the fourth dimension (4D). To accomplish this goal, the scientific community has begun to fabricate scaffolds with suitable smart materials to closely mimic the dynamic nature of tissues against natural stimuli [41]. Therefore, a 4D printed scaffold is one that can be spatiotemporally controlled over its physicochemical properties and structure. Physical stimuli include temperature, light, and magnetic field, whereas humidity and pH are examples of chemical stimuli being the most relevant for the present study the magnetic-responsive ones [41].

In summary, to the best of our knowledge, there is no reported work on the development of magnetic PCL/GBM composites via MEW. So, here it is proposed an insightful approach to achieve such materials.

1.3 Goals

The main goal of the present work was to develop PCL/GBM scaffolds with additional magnetic properties via MEW for TE.

To achieve this goal, the research pipeline was to:

1. Prepare magnetic GBM (@GBM) powders, namely GNP of grades M and C, via *in situ* precipitation and produce PCL/GNP composite filaments by melt-blending.
2. Assess the morphological, chemical, thermal, rheological, crystallographic and magnetic characterization of GNP powders and PCL/GNP composites.
3. Optimize PCL/GNP printability according to key MEW parameters.
4. Produce PCL/GNP scaffolds with linear and non-linear architectures via MEW.
5. Perform the characterization stated in 2) for the MEW printed scaffolds.
6. Evaluate scaffolds biocompatibility and tissue regeneration performance.

1.4 Structure

The remainder of this work has the following structure: Chapters 2, 3 and 4 present an overview on PCL, GBM, and AM, respectively. Each chapter contains a brief scope, a detailed state-of-the-art and a set of biomedical applications. Chapter 5 reports the used materials and the adopted experimental methodologies to prepare @GNP powders, to produce, print and characterize PCL/GNP composites. Chapter 6 covers the obtained experimental results. It is divided into several sections that include GBM morphological properties, particle size, and stability; materials characterization and printability. Chapter 7 comprises a general discussion of the most relevant results, in light of the most recently available literature reports. Finally, chapter 8 presents the major conclusions that can be drawn from the work presented in this thesis. Ongoing and future work is also presented and proposed.

Chapter 2

Polycaprolactone

2.1 Scope

Over the last years, biomaterials such as biodegradable polymers have attracted massive attention in medical, pharmaceutical and biomedical engineering applications. Due to their biocompatibility, biodegradability and higher hydrolysability in the human body, aliphatic polyesters embrace one of the most powerful classes of synthetic biodegradable polymers [42].

Polycaprolactone (PCL) was one of the earliest polymers synthesized by the Carothers group in the early 1930s [43]. It is a family member of synthetic biodegradable aliphatic polyesters which have found relevant use as a biomaterial in sutures, prosthetics and drug delivery systems.

Commercially, PCL is approved by the Food and Drug Administration (FDA) for use in humans. The main features of PCL that made this approval possible are biodegradability, biocompatibility, compatibility with a broad range of other polymers and good processibility due to its high thermal stability and relatively low cost, which enables the fabrication of a variety of structures and shapes [44].

Currently, PCL is widely used mainly due to the birth of TE. However, after attracting tremendous attention from the scientific community, the popularity of other resorbable polymers such as polylactides and polyglycolides overcame PCL. These allow the polymer matrix to release encapsulated drugs within days or weeks with complete resorption 2-4 months after implantation [45]. Another crucial factor to its loss of popularity was related to the unsuitable mechanical properties to be applied in high load-bearing applications such as the replacement of metal devices - screws, plates, nails, among others - by using biodegradable implants.

In summary, for most of two decades, PCL as a long-term degradation polymer was passed over due to the scientific community preference on faster resorbable polymers. The trend of interest in PCL in the biomaterials field, namely in TE applications, is outlined in Figure 2.1, which represents its recent resurgence.

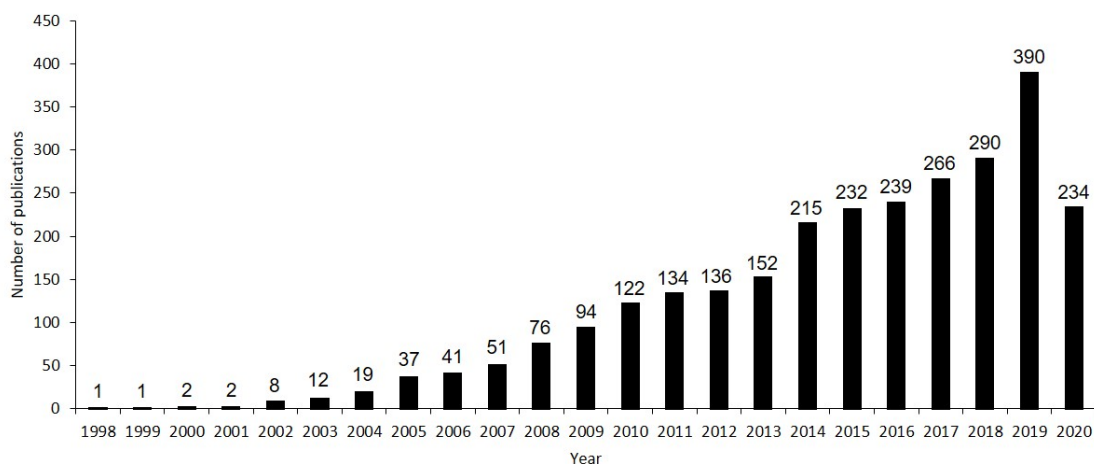


Figure 2.1: Number of publications on tissue engineering, in which PCL was used from 1998 until 2020. [Source: Web of Science]

2.2 State-of-the-art

2.2.1 Synthesis and physicochemical properties

Ring-opening polymerisation (ROP) of ϵ -caprolactone is the main synthesis process of PCL - the chemical reaction is described in Figure 2.2. However, over the last years, many efficient catalysts have been used for that purpose [46, 47]. The polymerisation of PCL can be explained by several mechanisms, namely anionic, cationic, coordination and radical one. Each method affects PCL final molecular weight, end group composition and chemical structure of the possible copolymers [48]. Several catalysts can be used to do this polymerisation, namely tin- and aluminium-based ones. Stannous(II) 2-ethylhexanoate is a representative example of tin-based compounds. Generally, these catalysts are referred to as stannous octoate molecules. To have control over the molecular weight of the PCL samples, it is necessary to use low molecular weight alcohols.

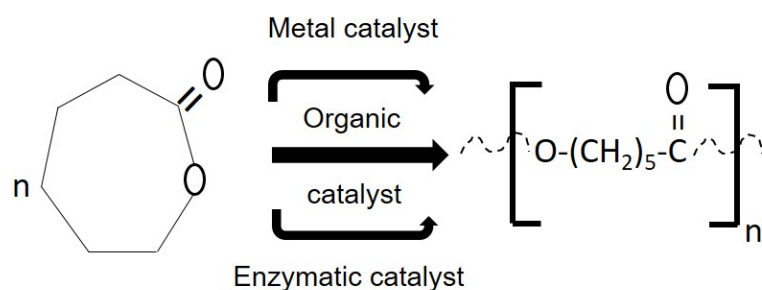


Figure 2.2: Ring-opening polymerization (ROP) of ϵ -caprolactone to polycaprolactone. Reprinted from [49]. Copyright © 2020 Informa UK Limited.

According to PCL physicochemical properties (Table 2.1), it is a semi-crystalline polymer with a melting temperature between 56 and 65 °C, and a glass transition temperature around -60 °C. Its average molecular weight usually varies from 530 to 630 000 g mol⁻¹. PCL is soluble in benzene, carbon tetrachloride, chloroform, cyclohexanone, dichloromethane, 2-nitropropane and toluene, at room temperature. On the other hand, it has low solubility in 2-butanone, acetone, dimethylformamide, ethyl acetate and acetonitrile. It is a versatile polymer since its chemical and mechanical properties can be modified by copolymerization or, blending. Figure 2.3 represents possible combinations of PCL with other materials [50].

Regarding the long-term degradation of PCL, it can take from months to two years. The exact amount of time is dependent on the degree of crystallization, molecular weight and degradation conditions [51].

Table 2.1: Summary of PCL physicochemical properties. Adapted from [49].

Property	Range
Approximate degradation time (months)	< 24
Average molecular weight (g mol ⁻¹)	530 to 630 000
Crystallinity (%)	< 69
Decomposition temperature (°C)	350
Density (g cm ⁻³)	1.07 to 1.20
Elongation at break (%)	20 - 1000
Glass transition temperature (°C)	-65 to -61
Melting temperature (°C)	56 to 65
Surface tension (mM m ⁻¹)	51
Tensile stress at break or max (MPa)	14
Water permeability at 25 °C (g m ⁻²)	177
Young modulus (GPa)	0.21 to 0.44

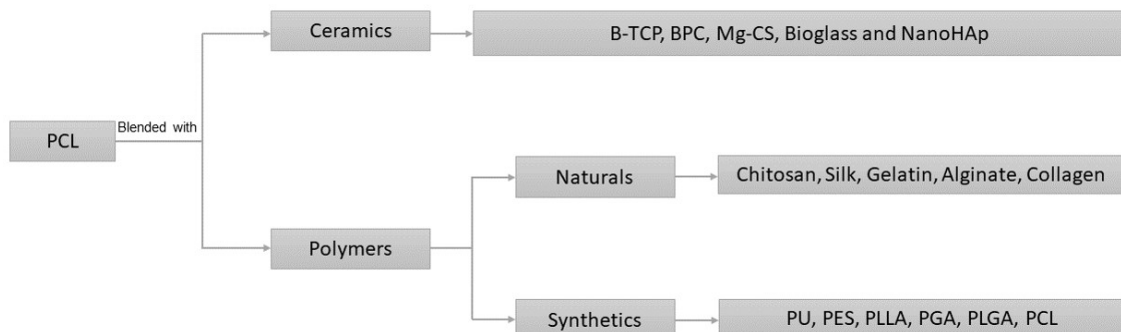


Figure 2.3: List of reported materials to blend with polycaprolactone, namely ceramics, natural or synthetic polymers. Adapted from [50].

2.2.2 Biodegradation

PCL has received considerable attention as a long term implantable biomaterial being that its degradation rate is even slower than polylactic acid's. In physiological conditions, such as in the human body, it is degraded by the hydrolysis of its ester linkages [44].

The degradation of a semicrystalline polyester such as PCL in aqueous media occurs in a two-stage process. The first step starts with the non-enzymatic hydrolytic cleavage of ester groups leading to mass loss, while the second step is related to intracellular degradation of PCL. According to Azimi *et al.* [44] this was observed during experiments of PCL fragments uptake in phagosomes of macrophages and giant cells. Additionally, it can be said that the first stage of the degradation rate of PCL is virtually identical to the *in vitro* hydrolysis at 40 °C and obeyed first-order kinetics. Therefore, the condition to guarantee that PCL is going to be fully resorbed and degraded via an intracellular mechanism is having a molecular weight equal or less than 3.000 g mol⁻¹.

Generally, at high temperatures, PCL degrades by end-chain scission, while at low temperatures, it degrades by random chain scission [52]. During hydrolysis, carboxylic acids are formed, which allow the auto catalyzation of the degradation. Notwithstanding, to achieve a faster decomposition, the catalyzation can be performed by enzymes [53, 54].

In summary, regarding PCL molecular weight, distribution and possible copolymerization with other glycolides, lactides or lactones, it can have a total degradation from months to two years.

2.2.3 Biocompatibility

In 1987, the following definition was suggested by Williams D.F "biocompatibility is the ability of a material to be used with an appropriate and suitable reaction of the host for a specific application". Recently a new definition of biocompatibility was set as "a set of the different interrelations between a biomaterial and its environment, and their biological local or general consequences, immediate or delayed, reversible or definitive" [55].

Indeed, biocompatibility takes into consideration the interactions between the biomaterial and its biological environment. Additionally, the effect of one in the other and vice versa is also considered. The interactions that exist in the interface differ in duration and intensity. Both factors depend on the biomaterial and the desired tissue [55].

Inflammation can be triggered due to several factors namely the leaching of low molecular mass compounds, which can happen via degradation or due to the presence of leachable impurities. Additionally, secondary inflammatory reactions can be activated due to the release of acidic degradation products from implants and bioresorbable polymers. A key factor is the capacity of the surrounding tissues in eliminate the by-products. Local temporary disturbances can be generated if this capacity is low, mainly due to low metabolic activity or poor vascularization [45]. Lofti *et al.* [55] reported a work in which the local fluid accumulation and the transient sinus formation led to an increase in osmotic pressure. So, both bioresorbability and biodegradability are significant factors when concerning biocompatibility problems on aliphatic polyesters.

In this context, Manoukian *et al.* [56] outlined that PCL, after both short and long-term studies performed did not exhibit any adverse reactions from the host tissue. Therefore, it was determined to be biocompatible. In another work, Sell *et al.* [57] reported that besides PCL composites being able to support and promote the growth of human coronary artery endothelial cells and adipose-derived stem cells, the fibrous electrospun scaffolds when blended to gelatin, exhibited exceptional biocompatibility with bone marrow stromal cells.

Another example of the biocompatibility and versatility of PCL is described by Samavedi *et al.* [58] where the fabricated scaffolds of poly(ester urethane) with nHAPPCL via electrospinning provided an alternative method for the regeneration of the damaged anterior cruciate ligament. Its biocompatibility was assessed through the use of an MC3T3-E1 osteoprogenitor cell line. The results indicated an active metabolic behaviour of the cells on the meshes.

Hence, regarding the use of polymers in scaffolds, medical devices or even drug-delivery systems, biocompatibility is a factor that must be considered.

2.2.4 Biomedical applications

To conclude the chapter, this subsection concerns PCL biomedical applications, namely the TE ones, which are viable due to its intrinsic physicochemical, mechanical and biological properties. So far, PCL has been used in bone, cardiac, cartilage and skeletal muscle TE, among others.

Currently, the major worldwide cause of death is cardiovascular disease [59]. Therefore, improvement of the current and new designs on heart valves, vascular grafts and heart stent components, are needed. Nonetheless, the current most crucial challenge is the creation of cardiac engineered-tissue [49]. Kai *et al.* [60] outlined the manufacturing of randomly and aligned PCL/gelatin-based scaffolds via electrospinning aiming the study of the fibres alignment influence on cell attachment and alignment. The results showed that both scaffolds presented anisotropic wetting features such as the ones demonstrated by the native cardiac tissue. Additionally, when seeded in rabbit cardiomyocytes, the aligned PCL/gelatin scaffolds were able of trigger an increase in cell attachment and alignment.

Concerning the skeletal muscle, Mondal *et al.* [49] stated that it constitutes around 48 % of the body mass. Its main functions are the maintenance of the structural shape and the control of Human body voluntary movement. Currently, the research on skeletal muscle TE mainly focuses on PCL scaffolds with natural polymers such as collagen [61] and gelatin [62].

Summing up, besides over the last few years a considerable amount of work focused on PCL and its composites for TE has been developed, there are still many challenges to address. Therefore, alternatives are needed, such as combining PCL with GBM.

Chapter 3

Graphene-based materials

3.1 Scope

Since the Nobel Prize in Physics in 2010, Graphene (G), as a carbon allotrope, in a "gold rush" has triggered tremendous attention within the scientific community. A standard definition for G is a two-dimensional (2D) crystalline material with sp^2 hybridized atoms. It is the fundamental building block of hexagonally bonded carbon materials and consists of a 6-ring honeycomb lattice structure where each carbon atom is bonded to three neighbouring atoms. When wrapped up, G forms fullerene, rolled up generates carbon nanotubes (CNT) and stacked creates 3D graphite (Gt) [63], as it is represented in Figure 3.1. Other graphene-based materials (GBM) described in the literature comprise graphene oxide (GO), reduced graphene oxide (rGO) and graphene nanoplatelets (GNP). GO is usually produced by the modified Hummers method (MHM), which consists of carrying out a reaction of Gt powder with $KMnO_4$ and $NaNO_3$ in concentrated H_2SO_4 . Both $KMnO_4$ and $NaNO_3$ represents oxidant agents, while H_2SO_4 is used to promote the formation of epoxy groups and surface defects on the honeycomb structure. During this reaction, the temperature must be kept at a maximum of 45 °C. To stop the reaction, H_2O_2 must be added. GO possesses several oxygen-containing functional groups, namely hydroxyl and epoxy in the basal plane, while at the edges carbonyl and carboxyl are present [64]. Due to its strong oxygenation, GO is considered hydrophilic and can be easily dispersed in water and further functionalized [65]. GNP or few-layer graphene (FLG) are constituted by stacked graphene sheets with a thickness of 2 to 10 layers [66]. Figure 3.2 presents the chemical structures of different GBM, namely Gt, graphite oxide (GtO), G, GO and rGO [67].

Currently, GBM are applied in diverse research areas, mainly due to its electrical, magnetic, mechanical and optical properties. Furthermore, G and GBM have been described as having bactericidal action, a property which made them an attractive choice for designing antimicrobial materials. Figure 3.3 shows the growing interest of GBM in the biomedical field.

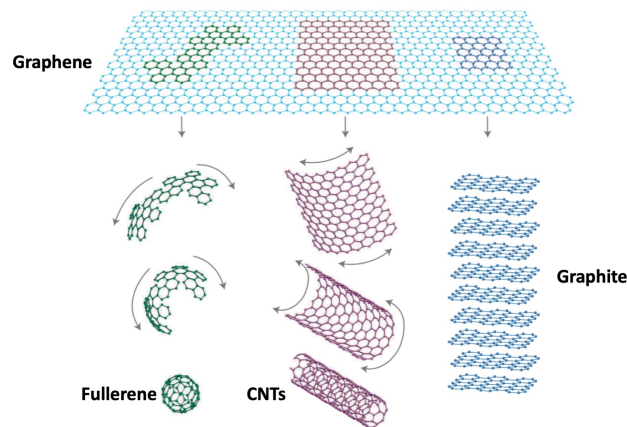


Figure 3.1: Graphene (G) as the 2D building block of hexagonally bonded carbon materials. Adapted from [63].

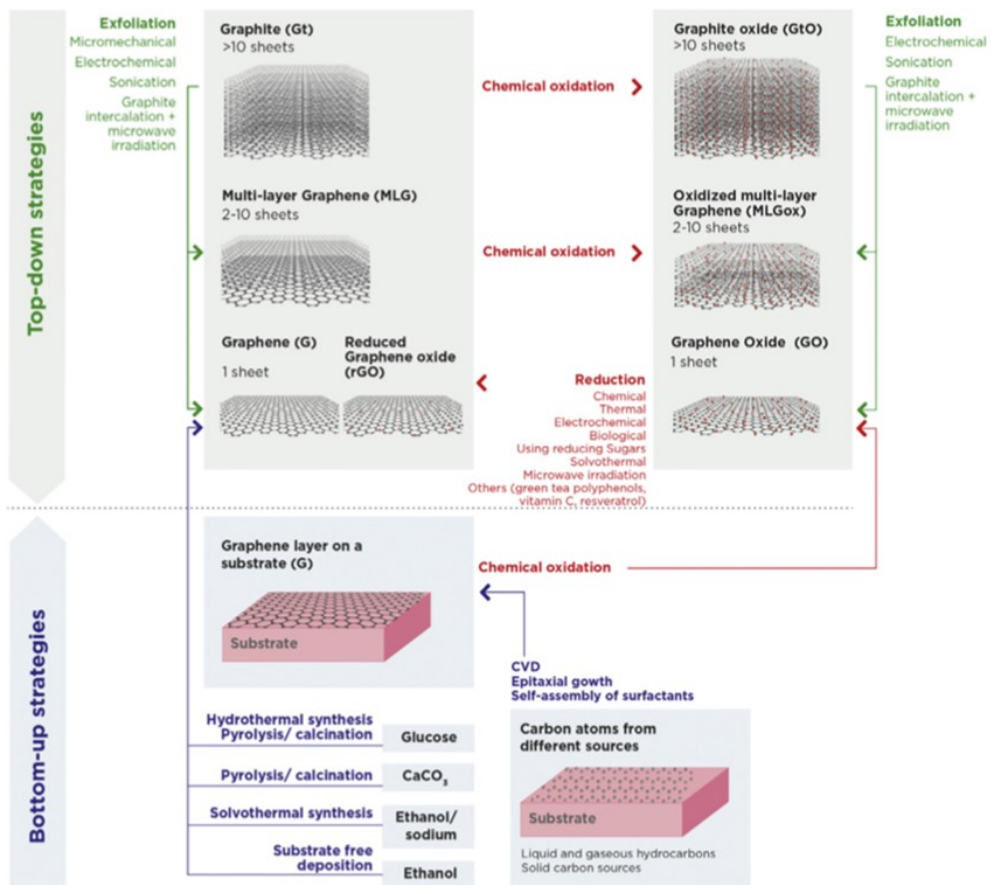


Figure 3.2: Graphene-based materials family and its production methods. Reprinted from [67]. Copyright © 2020 Elsevier B.V.

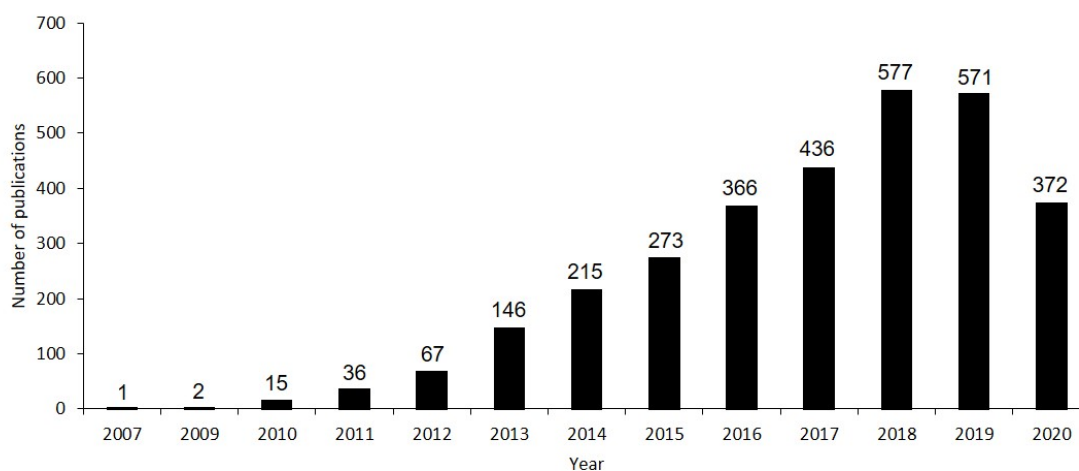


Figure 3.3: Number of publications on graphene in the context of biomedical applications from 2007 to 2020. [Source- Web of Science]

3.2 State-of-the-art

3.2.1 Synthesis and physicochemical properties

In 1999, G was exfoliated into thin lamellae comprising multiple G layers by Ruoff and co-workers via a micromechanical approach [68]. In 2004, Geim, Novoselov *et al.* [69] achieved single-layer G through the use of a similar approach but followed by the use of scotch tape to repetitively peel off flakes from Gt. Since then, several studies have been focused on their production and scale-up. To be applied in the most diverse research areas, particular criteria need to be met, therefore methods to achieve controlled morphology, thickness and size are paramount.

Concerning G synthesis methods, it can be produced from top-down or bottom-up approaches. Top-down approaches such as micromechanical, electrochemical and sonochemical exfoliation-based methods can be complex and result in low yields [70]. Additionally, Gt intercalation followed by microwave irradiation is also performed [67]. As bottom-up approaches, there is the chemical vapour deposition, from liquid and gaseous hydrocarbons solid carbon sources, pyrolysis/calcination, from glucose and CaCO_3 , solvothermal synthesis, from ethanol/sodium and substrate-free deposition, from ethanol [67]. Figure 3.2 assembles some of the GBM types mentioned in the text, together with a succinct description of the corresponding synthesis methods.

GBM oxidation disrupts the aromatic system, introducing oxygen in the form of hydroxyl and ether groups at the bulk surface and carboxyl and carbonyl at the edges of the sheets, leading to a decrease of conductivity, which can be partially reestablished by reduction, resulting in rGO when GO is used. There are several kinds of reduction processes namely chemical, thermal, electrochemical, biological by the use of reducing sugars, solvothermal, microwave irradiation and even though green tea polyphenols, vitamin C and resveratrol [67]. The most used are the chemical and the thermal ones.

1. Chemical Reduction: GO samples are immersed in a chosen chemical reduction agent for a certain temperature range and time. At the end of the process, materials have less oxygen-containing functional groups. It allows processing of large batches [71].
2. Thermal reduction: Very efficient method in terms of the production of rGO powders with high performance. The method, itself, consists of removing both water and oxygen functional groups via its evaporation [72].

Concerning the physicochemical properties, G stands out as a significant reference since it owns plenty of unique properties, such as remarkably lightweight, high elasticity, unique specific strength (G has a value of $48\,000\text{ KN m Kg}^{-1}$ while steel has 154 KN m Kg^{-1}), high thermal conductivity (G has a value nearby 3000 W m K^{-1} while copper is around 400 W m K^{-1}) and high electrical conductivity. G has the tremendous ability to support high densities of electric current (higher than copper in a factor of 1000). As G is easily chemically functionalised, it can be combined with several materials and devices according to the final application.

3.2.2 GBM composites

Since the discovery of G remarkable physicochemical properties and ability to be dispersed in several polymer matrices, a new class of polymer composites with GBM as fillers has been created. The production methods, characterization techniques, properties and applications of these polymer/GBM composites have been extensively reviewed in the literature since GBM incorporation can significantly improve the properties of host polymers, even at minimal amounts [73, 74].

Polymer/GBM composites can be produced by solvent blending, melt blending, *in situ* polymerization and covalent bonds. Solvent blending consists of blending the polymer with organic solvents followed by solvent removal. Melt blending involves mixing polymer melt and filler (in a dried powder form) under high shear conditions. *In situ* polymerization comprises the mixing of GBM in a solution of monomers followed by polymerization. Covalent bonds between the polymer matrix and GBM can also be done [74].

Solvent blending being the method that allows better GBM dispersion, has the disadvantage of using organic solvents. Melt blending allows a large scale and more economical production of polymer/GBM composites by using melt extrusion. However, its use has been hindered due to the thermal instability of most chemically modified G [73]. Thereby, some challenges need to be overcome to produce polymer/GBM composites, namely the homogeneous dispersion of GBM with minimal restacking, and the effective blending of GBM with the polymer matrix.

The incorporation of GBM into polymeric chains has been used to improve their mechanical, thermal or electrical properties. Sayyar *et al.* [75] produced a composite of PCL with well dispersed and chemically modified rGO via solvent blending. The Young modulus and tensile strength increased to more than double when compared to PCL while the electrical conductivity increased around 14-fold. Wang *et al.* [76] prepared a nanocomposite of PCL with poly(sodium 4-styrene sulfonate) modified graphene via solution blending. Young's modulus and yield strength

of PCL were improved by around 12 % with 0.5 wt.% incorporation of modified graphene. PCL crystallization rate increased approximately 6-fold by the addition of merely 0.05 wt.%.

Yu *et al.* [77] prepared PCL/GO composites via *in situ* polymerization by focusing on the crystallization behaviour, namely on GO influence as a nucleation agent. Via wide-angle x-ray scattering patterns, the authors identified that PCL crystalline structure was not affected. Differential scanning calorimetry measurements indicated that crystallization temperature of PCL increased around 1.2-fold with the incorporation of 1.5 wt.% of GO. Wang *et al.* [78] developed nanocomposites based on PCL and GO nanosheets via *in situ* polymerization. Thermal and mechanical properties of PCL remarkably increased, namely its degree of crystallization that increased around 1.4-fold. In comparison, tensile strength and Young modulus increased 2.5 and 1.5-fold, respectively, without a significant loss of elongation at break.

Composites with PCL and carbon-based materials have also been explored via melt blending. Chin *et al.* [79] reported the preparation of PCL/multi-walled carbon nanotubes (PCL/MWCNT) via this process in a twin-screw extruder with low rheological and electrical percolation thresholds. MWCNT addition to PCL increased its crystallization temperature in 17 °C and degree of crystallization in 65 %. Potschke *et al.* [80] also prepared PCL/MWCNT composites with only 0.5 wt.% of MWCNT at different rotation speeds via melt blending by using a micro-compounder. The lowest resistivity (104 Ω m), as well as the better dispersion, were achieved at 250 rotations per minute (rpm). At this rotation, the crystallization temperature of PCL increased from 26 to 42 °C, while crystallinity values from 39 to 53 %.

3.2.3 Biodegradation

Fadeel *et al.* [81] defined biodegradation as a process where a microorganism transforms the structure of an organic material via enzymatic or metabolic reactions.

Previously to describe the current state-of-art on the biodegradation of GBM, it is necessary to highlight the urgent need on developing and optimize eco-friendly methods for GBM oxidation and degradation. For the record, the heavy use of strong oxidants and concentrated acids such as KMnO_4 and H_2SO_4 threatens the environment. Additionally, vast amounts of graphitized materials are discharged into it. Thus, they tend to be toxic to both fauna and flora [82].

Initially, GBM were considered as structurally persistent, however, subsequent *in vitro* and *in vivo* studies evidenced that the degradation of both CNT and GO could be catalysed through the use of oxidative enzymes, namely peroxidases [83, 84]. In another study, Jiménez *et al.* [85] reported that several material properties influence the ability of each GBM in being biodegraded, namely the lateral dimension, the number of layers, the nanomaterial dispersibility, the synthetic energy, the C/O ratio [81] and the role played by surface functionalisation [86]. Figure 3.4 categorizes several GBM tested in biodegradation studies, namely GO, rGO, GNP, graphene oxide nanoribbons (GONR) and rGONR.

In terms of biological behaviour, between GBM, the most studied 2D material is GO mainly due to its easy surface modification and aqueous dispersibility. Kuraphati *et al.* [86] demonstrated that myeloperoxidase could catalyze the degradation of GO in the presence of H_2O_2 . Moreover, the

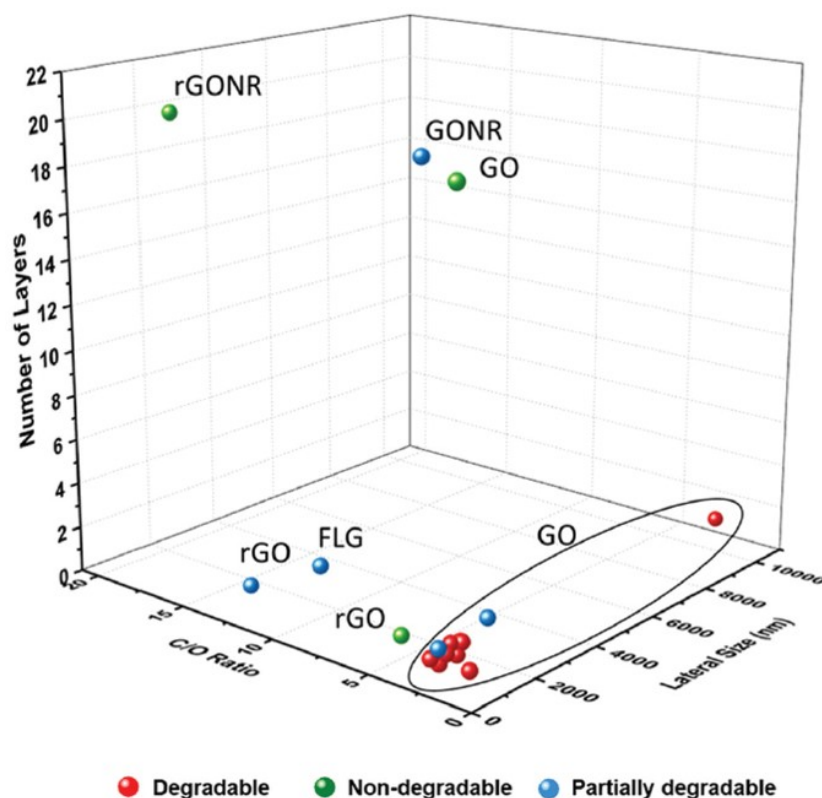


Figure 3.4: GBM biodegradation categorization in terms of number of layers, C/O ratio and lateral size. Reprinted from [85]. Copyright 2018 American Chemical Society.

authors were able to show that GO biodegradation could be enhanced through its functionalization with catechol and coumarin, which are natural ligands of horseradish peroxidase. Overall, the higher the degree of dispersibility, the higher the biodegradation extent. The different degrees of dispersibility were proportional to the percentage of GO carboxylic groups.

Newly, it was outlined that isolated human neutrophils could promptly degrade single-layer GO sheets with different lateral dimensions if, and only if, stimulated to produce neutrophil extracellular traps or activated to undergo degranulation with the release of myeloperoxidase [87]. Despite recent progress, much work remains to be done, namely in the biodegradation and clearance of the GO.

Finally, three primary guidelines concerning the development, optimization and application of GBM in the biomedical context were set. According to Bussy *et al.* [88], by using such guidelines, the overall safety from exposure of the material is increased while the risk of adverse responses happening is decreased.

1. Individual nano-G sheets should be used. It is related to the non-use of large, long and wide structures. Indeed, research groups should use these sheets since they will be efficiently internalized and fully removed from the deposition sites by macrophages.

2. Adequate surface hydrophilicity should be present. Essentially, the use of stable colloidal dispersions as well as hydrophilic individual nano-G sheets will minimize the *in vivo* aggregation.
3. Tissues accumulation should be avoided. Fundamentally, the research groups should use a material that can be directly excreted or one that when chemically modified could be efficiently degraded as well.

3.2.4 Biocompatibility

Firstly, it must be enhanced that all the fundamental definitions and concepts behind biocompatibility are present in subsection 2.2.3. Indeed, the linkage of the final application with the biological response contrasts toxicity and biocompatibility. Therefore, a material can be intrinsically biocompatible but toxic if not used in agreement with its final application.

Two factors must be considered in biocompatibility studies, namely the material intrinsic physicochemical properties and the material derived properties from the interaction with biological environment. Table 3.1 describes those properties [89]. Such considerations became even more fundamental when studying new materials, *i.e.*, materials without clinical history and limited knowledge about its toxic profile as is the case of GBM. Additionally, GBM differ in chemical composition (*e.g.*, G, GO, rGO, among others), which makes understanding even more complex.

The current incapacity of design and develop soft devices that besides being safe are also sufficiently flexible to match the mechanical needs of the host tissue, has revealed itself as a significant hindrance to the formulation of fully integrated biomaterials. Notwithstanding is of common scientific sense that differences between the elastic moduli of the host tissue and the biomaterial may trigger diverse unwanted biological responses [90]. Therefore, there is a high expectation from the scientific community on GBM becoming the materials that can satisfy the tissue integration needs mainly due to their tremendous flexibility [91]. As materials with planar atom-thin structure, they can not only create flexible materials and maintain their mechanical properties but also increase their weaker aspects, such as improve its stability and decrease its brittleness [90].

Table 3.1: Essential material properties on biological response influence. Adapted from [89].

Material intrinsic physicochemical properties	Material derived properties from interactions with the biological environment
Elastic constants	Ability to produce free radicals
Dimensions and shape	Byproducts size and chemical properties
Porosity	Degradation, corrosion, or wear profile
Surface chemistry, roughness and morphology	Protein adsorption and desorption

Recently, there have been several research groups reporting implanted GBM as having non or minimal cytotoxicity [92], while others reported intense tissue fibrosis [81]. Thus, the current conflicting information enhances the lack of knowledge in terms of GBM implants biological responses.

GBM biocompatibility at the macroscale level is mainly influenced by surface chemistry and surface reactivity along with its possible coating, either with biomolecules, either with chemical contaminants. Nonetheless, for medical devices applications, GBM surface is the most desired point of modification and subsequently of interest [93].

Concerning the chemical contamination, Bullock *et al.* [89] reported that it must be avoided and that sterilization and depyrogenation are not minor issues. Additionally, it is worth mentioning that several chemical compounds that are regularly used in the production of GBM are/can be highly toxic and subsequently impact negatively in the body response to GBM implantation. Having in mind the planarity and high surface area of GBM, these chemical compounds will be bioavailable since they are directly present in their surface.

Therefore, identifying these potentially dangerous chemicals in GBM synthesis process and proceed to its substitution for more green alternatives is an urgent need [94]. As an example, hydrazine which is a chemical compound used to (partially) reduced oxidized GBM is extremely cytotoxic and carcinogenic. Currently, hydrazine substitution is not possible, so it is mandatory to ensure the elimination of possible toxic residues via a full cleaning/purification process [95].

Overall, further studies in this research field are mandatory since GBM biological behaviour remains unknown or, at least, not fully understood.

3.2.5 Biomedical applications

Over the last few years, the unique physicochemical properties along with biocompatibility have made GBM highly attractive in several applications, namely in biological biosensing through the development of electrochemical, fluorescent and field-effect transistor biosensors, in TE, namely in bone, cardiac, cartilage, neural and skeletal muscle, in drug/gene delivery, in bioimaging and photoacoustic imaging, in photothermal and photodynamic therapy, in the development of bio-compatible scaffolds for cell culture, stem cell differentiation, among others [96]. According to Banerjee *et al.* [97], GBM biomedical applications (67 %) have surpassed the non-biomedical ones.

As described in subsection 2.2.4, myocardial infarction and coronary artery diseases are the primary worldwide causes of death [59]. Regarding the limited capacity of regeneration from cardiac tissue, any injury or damage may become a permanent one. Due to its anisotropy and presence of properly aligned collagen nanofibers with a diameter in between 10 and 100 nm [98] the cardiac tissue possesses outstanding mechanical properties and systematic contractile rhythm. Additionally, it has high electrical conductivity (0.005 and 0.1 S m^{-1} in the transverse and longitudinal direction, respectively).

So far, some research groups reported the regulation of the differentiation of a stem cell lineage *in vivo* by using GBM, namely a G structure conjugated with a ring of pyrene. The advantage

of using G was related to its high electrical conductivity [39]. Another study outlined cardiomyogenic differentiation using G, without signs of cytotoxicity [99]. Recently, it was reported the improvement of efficacy in myocardial repair by rGO [100]. Overall, due to its unique properties, namely mechanical, electrical conductivity and easy surface functionalization, GBM holds a magnificent promise for cardiac TE applications. To date, the most used materials in this field are hydrogels. However, they have weaker mechanical properties than the desired ones as well as low values of electrical conductivity.

Concerning cartilage TE, firstly is necessary to highlight that trauma, ageing, sports injury or even degenerative diseases can lead to cartilage defects. Cartilage is an elastic and resilient tissue, mainly due to the highly ordered arrangement of chondrocytes in the ECM. Nevertheless, since it is an aneural avascular tissue, it has a limited ability to regenerate [101].

Newly, GBM has started to be tested as a scaffold material to promote cell adhesion, proliferation and differentiation mainly through its stimulation [102]. Qian *et al.* [103] reported the full repair of a rabbit knee defect after just 18 weeks via the use of a 3D porous scaffold reinforced with GO, in contrast to the one without GO. In another work, Kim *et al.* [104] outlined the use of GO either as a substrate to promote cell adhesion, either as a protein, *i.e.*, growth factor with the finality of promoting the differentiation of chondrogenic adult stem cells. Besides the preliminary work with GBM in this field, especially with GO, further work must be developed.

Regarding skeletal muscle TE, recently, Palmieri *et al.* [105] reviewed the use of GBM composites on it as well as its futures perspectives. According to it, Chaudhuri *et al.* [106] described a PCL/GNP composite capable of promoting the formation of myotubes in human skeletal muscle cells derived from umbilical cord blood-derived mesenchymal stem cells. Later, Chaudhuri *et al.* [107] developed a PCL/GO composite with $\approx 85\%$ of porosity to ensure mouse myoblast cells (C2C12) growth. Probably due to enhanced conductivity of the composites, the authors were able to guarantee a higher myogenic differentiation and ensure the expression of two myogenic proteins, namely Desmin and MyoD. In a different perspective, Patel *et al.* [108] developed an electrospun PCL/G composite to promote C2C12 cells adhesion, proliferation and differentiation into myoblasts. Remarkably, PCL/G with 1 and 2 wt.% of G demonstrated higher myoblast activity, thus showing that the tuning of G concentration allowed the control over the biological activity of the developed scaffolds. In summary, polymer/GBM composites appeared as a promising class of composites capable of promoting and drive skeletal muscle tissue regeneration.

Chapter 4

Additive manufacturing

4.1 Scope

Additive manufacturing (AM) is currently defined as "a very promising group of technologies for scaffold developments with rigorously controlled internal architectures and mechanical properties for tissue and organ regeneration" [109]. Indeed, as a novel approach, AM is a broad term that concerns several methods that by using a computer-aided design can fabricate scaffolds via layer-by-layer fibre deposition. AM trend in terms of published papers in biomedical applications over the last few years is retreated by Fig. 4.1. Nevertheless, there are still some challenges that must be surpassed [110]:

- Create advanced, closed and modular platforms that allow the automatization of the manufacturing process.
- Define versatile, reliable and consistent starting materials.
- Develop standard and easy regulatory pathways to produce new biomedical devices.
- Design and implement novel systems to allow control of the printing accuracy of the fabricated products.

Another primary concern is the absence of an agreed and accepted terminology. To date, the lack of consensus within the scientific community is generating uncertainty and misunderstandings in the description of possible new approaches. In this chapter, AM techniques such as laser-based technologies, namely stereolithography (SLA) and two-photon polymerization (2PP); fused deposition modelling (FDM), pressure-assisted microsyringe (PAM) deposition, 3D biplotting, ink-jet bioprinting, electrospinning and melt electrowriting (MEW) are reviewed. Afterwards, the focus is on the biomedical applications, namely in tissue engineering (TE).

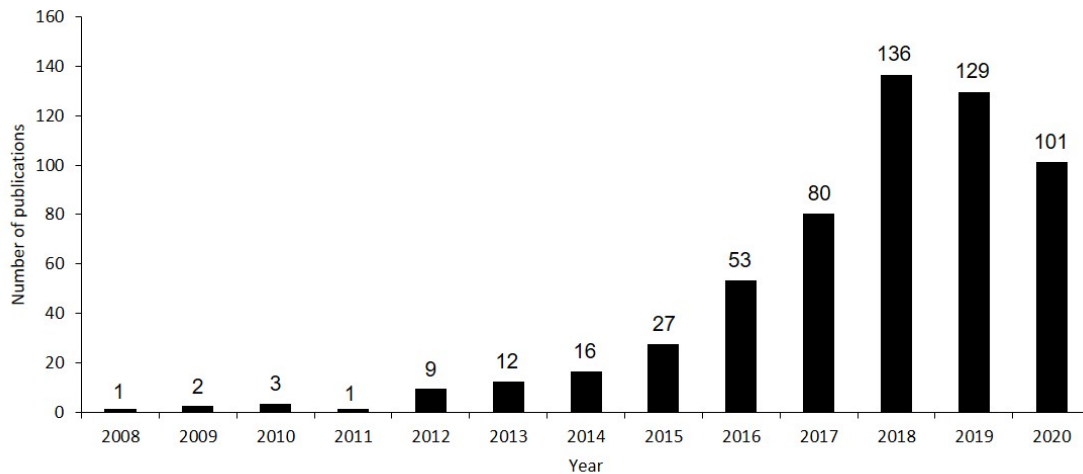


Figure 4.1: Number of publications on additive manufacturing in the context of biomedical applications from 2008 to 2020. [Source: Web of Science]

4.2 AM techniques

4.2.1 Laser-based technologies

SLA technique is based on the scanning of an ultraviolet (UV) laser over the upper part of a liquid bath associated with a photopolymerizable material. The polymerization of the bath occurs only in the places where the UV laser beam hits the bath surface. As a result, the first solid plastic layer is created. Then, the layer is lowered into the bath. Afterwards, the polymerization process is repeated until a precise architecture, and a specific number of layers is achieved [45].

Overall, SLA technique is not much used in the design and fabrication of scaffolds for TE applications, mainly due to the limited number of available photopolymerizable biomaterials. Currently, the materials used by SLA equipment are epoxy-based or acrylate-based resins. Despite the available materials offer durable, robust, and accurate models, they lack in both biodegradability and biocompatibility aspects [45].

To achieve the sub-micron scale appears the 2PP technique, in which a photosensitive resin is polymerized via laser beam control in both time and spatial domain [111]. Nevertheless, this method takes a long time to manufacture large structures.

4.2.2 Fused deposition modelling

FDM technique was invented and patented by Scott Crump in 1989. The first FDM 3D printer was produced and commercialized by Scott's Stratasys company. To develop scaffolds for TE applications, FDM uses a computer-aided design (CAD) system to control the fibre extrusion of a molten thermoplastic polymer. This principle makes possible the scaffolds mechanical properties modulation [112].

Over the last two decades, FDM has proved itself as a reliable technique. Notwithstanding, it possesses limitations such as being able only to extrude thermoplastic polymers at high temperatures as well as not allow the incorporation of living cells or growth factors. Additionally, the higher the number of layers, the higher the surface roughness.

FDM has also inspired several other extrusion-based techniques to fabricate 3D printed scaffolds such as 3D-fiber deposition (3DF) and bioextrusion. These techniques are multi-dispensing systems, *i.e.*, systems that can simultaneously dispense more than one material allowing the manufacturing of scaffolds with different local physicochemical properties [112, 113]. In opposition to FDM, in both 3DF and bioextrusion printing techniques, materials are filled in a cartridge as pellets. Due to the longer time at high temperatures that materials are submitted to, both 3DF and bioextrusion printing techniques are even more susceptible to thermal degradation. In summary, FDM is a flexible technology platform that is highly used for processing thermoplastics polymers such as polylactic acid (PLA), polycaprolactone (PCL) and elastomers.

4.2.3 Pressure-assisted microsyringe deposition

To solve the high processing temperature concerns of FDM, other techniques such as PAM and wet-spun automated extrusion systems appeared, being able to manufacture scaffolds with a fibre diameter of 20 μm [114].

It is worth mentioning that in PAM, several working modules can be installed in parallel on a robotic micro-positioner. Thus, allowing the processability of polymer solutions and living cell suspensions [114]. The primary shortcoming of these techniques is the low vertical dimension resolution. Despite the improvements from FDM to PAM, hydrogels based in natural polymers are still difficult to process.

Nevertheless, Tan *et al.* [115] reported the development of porous PLA/gelatin scaffolds via an indirect fabrication approach based on rapid prototyping technology. For instance, the scaffolds presented a 3D network of interconnected channels through which the nutrient supply to the culture media was facilitated. Overall, the scaffolds showed no cytotoxicity. However, studies about cell proliferation and differentiation throughout the pores were not assessed.

4.2.4 3D bioplotting and ink-jet bioprinting

So far, none of the described techniques can print scaffolds and seed cells simultaneously, and subsequently are not capable of mimicking the cell distribution in native tissues. Therefore, new AM techniques appeared, such as 3D bioplotting, ink-jet and valve-jet bioprinting.

Regarding 3D bioplotting, Figure 4.2 describes all the possible printable materials. The most common printing paradigm is the encapsulation of cells into the hydrogel carrier. Afterwards, by the application of pressure, the material is extruded. Although allowing the deposition of different types of cells into the hydrogel, 3D bioplotting is limited about the fabrication of scaffolds with complex shape, mostly due to the lack of optimal hydrogel carriers [116]. Another shortcoming of 3D bioplotting concerns scaffolds post-processing stability. Indeed, it is necessary to prevent the

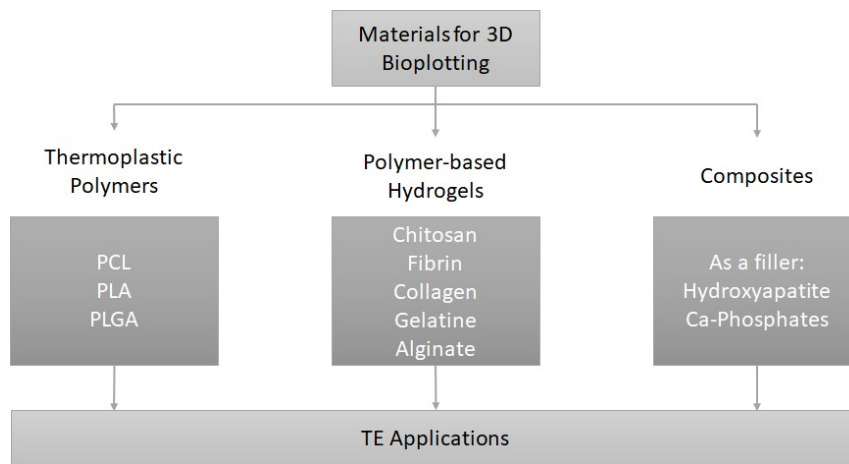


Figure 4.2: List of 3D bioplotting printable materials. Adapted from [119].

deformation of the construct by matching the density and viscosity properties of the used hydrogel carrier. Highley *et al.* [117] described the use of self-healing hydrogels, being such printing possible due to guest-host hydrogels noncovalent and reversible bonds which could be disrupted by the application of a physical stimulus such as shear stress. Therefore, the used guest-host hydrogels deformed to accommodate the extruded materials and self-healed to maintain material consistency.

In opposition to 3D bioplotting, ink-jet bioprinting uses droplets to dispense cells. It is worth mentioning that droplets are dispensed by the generation of an electromagnetic, piezoelectric, or thermal stimulus. As the used droplets are in the picolitre range, the available resolution to print live cells is high. Nevertheless, due to nozzle clogging, high-stress shears are generated and cell viability is limited. Valve-jet bioprinting dispenses droplets containing bio-inks by using solenoid microvalves driven by pneumatic pressure. It can generate an average of 1000 droplets per second, contains high spatial precision, and uses volumes in the nanolitre range. Notwithstanding, and similarly to ink-jet, valve-jet bioprinting is still a nozzle-based printing technology. Therefore, cell viability is limited by the possibility of nozzle blockage [118].

4.2.5 Electrospinning

Electrospinning is a technique that uses a strong electrical field to obtain a network of polymeric fibres, with a diameter range from micro to nanoscale, being the nano the most commonly achieved scale. Via electrospinning is possible to print a wide variety of materials since volatile solutions of natural to synthetic polymers. Regarding its extrusion process, the fibres are spun from an electrodynamic Taylor cone that is formed as soon as the applied electric field overcomes the surface tension of the polymer solution. The cost-effectiveness, rapid fabrication, simplicity and versatility are some of the reasons for its increasing popularity in TE [120]. Overall, electrospinning promotes fibres random deposition to resemble its arrangement in ECM. Thus, it is expected that cells migrate, proliferate and differentiate as it happens in the biologic tissues.

In opposition to achieve randomly oriented nanofibres, appears a technique designated as MEW, which allows complete control over fibre deposition at the microscale. Therefore, compared to electrospinning, MEW is able to accurately mimic the native structural organization of ECM [121, 122].

4.2.6 Melt electrowriting

Historically, the first MEW approach was in 2011 [121]. Since that, MEW has been described with different terminologies, namely direct-writing melt electrospinning (MES), melt electrodynamic 3D printing and near-field MES. Currently, the general definition is melt electrowriting, MEW, and derives from "melt electrostatic writing", which is distinct from "melt electrostatic spinning" as it was firstly described by Daryl *et al.* [123].

MEW allows an accurate fibre deposition through a direct-write jet without electrical instabilities. Nevertheless, it must be enhanced the newly discovered facts about MEW [124]:

1. capacity to control the inherent jet/processing conditions instabilities, *i.e.*, "fibre pulsing".
2. ability to overcome charges issues when manufacturing constructs with large volume via the exploration of the present dynamic electric fields.
3. capacity to digitize the electrified jet and subsequently provide in-process quality control and a reproducible outcome.
4. potential to process a wider range of polymers besides the gold standard (PCL).
5. aptitude to enhance scaffolds mechanical properties through the use of different MEW fibre designs constructs with soft networks.

Notwithstanding, Taylor cone, as well as the ability of direct writing the molten jet with control into a grounded collector plate, are the two critical factors to understand MEW. Additionally, to achieve an accurately-printed MEW pattern having a stable jet is fundamental. Therefore, processing parameters must be optimized.

In the next paragraphs, some key concepts, such as fibre pulsing, critical translational speed (CTS), MEW processing parameters, MEW electrical field and MEW workflow, will be covered. Further, the current printed MEW designs, MEW polymers, as well as the biomedical applications and future perspectives, will be detailed.

MEW, besides requiring a heating source and a feeding pressure to continuously extrude the polymer from the spinneret to the translating collector, needs an applied voltage to stabilize the jet. It is worth mentioning that fibre pulsing is highly dependent on the applied voltage and mass flow. Therefore, its combination can promote or avoid this phenomenon, being that if equilibrium between the applied voltage and the mass flow is not verified, the jet becomes unstable, causing an unpredictable and undesired fibre deposition [125].

CTS must be achieved to print stable and straight fibres. It is defined as the collector speed that matches the speed of the electrified jet. Below this speed, the direct-written fibre presents sinusoidal, side-loops or even circular morphology, due to jet buckling phenomenon [122].

MEW is affected by several processing parameters, namely the feeding pressure, the applied voltage and the collector speed. Additionally, the distance to the collector, the syringe spinneret diameter, the downstream pulling and the upstream resistive forces also influence MEW printability. Nevertheless, to obtain a steady-state, a balance between CTS and the combination of downstream and upstream forces must be achieved [126].

Concerning the influence of feeding pressure, applied voltage and collector speed on fibre diameter, the higher the pressure, the lower the voltage, the higher the collector speed, the lower the resultant fibre diameter [127, 128]. Recently, Ko *et al.* [129] described that fibre diameter would increase with a lower melt viscosity.

Newly, Ding *et al.* [130] reported a charge distributed model to define the charge transport pathway during the printing process. Additionally, z-axis adjustments and voltage increment during the MEW process were implemented to produce high-volume scaffolds with linear patterns and uniform fibre diameters. Overall, it was determined from simulations and experiments that the creation of defects in the upper layers are mainly due to the accumulation of charge, therefore preventing a linear stackability.

To manufacture the next generation of MEW scaffolds, a standard workflow is mandatory. According to Robinson *et al.* [124], it will involve three main steps:

1. parameter screening.
2. dimension-based design.
3. application.

Concerning the first step, MEW key parameters, such as the ones previously mentioned, are systematically investigated. Typically a well-known polymer, such as the gold standard (PCL), should be used. By the end of this step, the researchers should be able to eliminate the possibility of occurrence of fibre pulsing, accurately identify the CTS, the minimum fibre spacing, and the ideal height for the scaffold. Overall, the generated data guides the researches into the second step. Here, to achieve a precise architecture, a fine-tuning/adjusting of the previously defined parameters should be done. Such parameters are mainly related to fibre spacing, fibre diameter and scaffolds height. If needed, the out-of-plane fibre arrangement should be adjusted as well. The final step is intrinsically related to the fibre alignment of the desired tissue/organ.

4.2.6.1 MEW Designs

To accurately describe the current published MEW designs as well as its printing conditions, both Figure 4.3 and Table 4.1 are used.

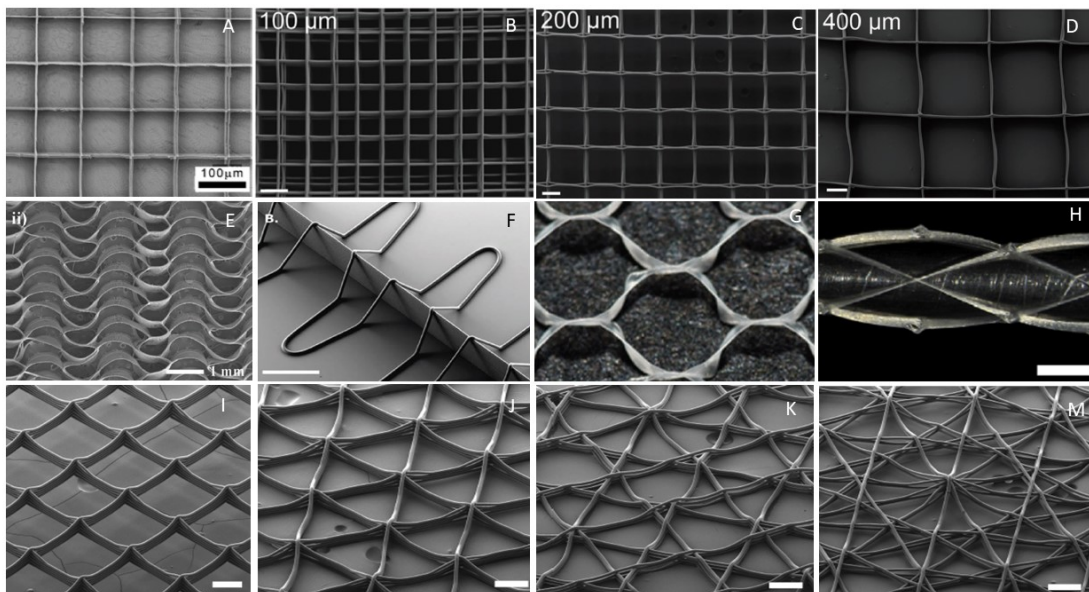


Figure 4.3: List of MEW PCL scaffolds designs through the representation of SEM images. A) square box [131], B-D) layers with different porosities [132], E) sinusoidal/serpentine [133], F) out of plane [134], G) hexagonal shape [135], H) precision tubes [136], I-M) square, hexagonal, octagonal and dodecagonal shape, respectively.[137] The copyrights are the following: A) © Copyright 2020 IOP Publishing, B-G) Copyright © 1999-2019 John Wiley & Sons, Inc. H-M) Copyright 2020 Elsevier B.V.,

Before describing each manufactured construct, it is worth mentioning a few general notes about MEW stackability principles, compositions and designs. For instance, MEW constructs are obtained via a repetitive fibre-by-fibre stacking. Moreover, by controlling the fibre diameter during the printing, through the change of feeding pressure, applied voltage or even collector speed, it is possible to produce multiphasic MEW compositions. Notwithstanding, by controlling the placement of MEW fibres is possible to mimic a particular tissue shape. Overall, MEW can manufacture constructs with linear (square or rectangle) and non-linear patterns (floral, hexagons, which mimics the honeycomb structure, among others) with a high surface to volume ratio.

MEW resolution limits were explored by Hochleitner *et al.* [131], who reported the manufacturing of a high volume multimodal box-structured scaffold with a fibre diameter around 820 nm (Fig. 4.3A) for TE.

In another study, it was reported the development of multiphasic scaffolds within a fibre-reinforced matrix to develop a 2D electrophysiologic system. The design principle was based on stacking fibres with different porosities. Overall, three box-shaped scaffolds were manufactured. The first presented a 125 μm spacing (Fig. 4.3B), the second represented a membrane mesh (Fig. 4.3C), and the third was manufactured with a fibre spacing of 250 μm (Fig. 4.3D) [132].

Table 4.1: Summary of MEW designs and its printing parameters, namely feeding pressure (P), applied voltage (V) and processing temperature (T). Fibre diameter (F_d) and final application of each design is also presented. Adapted from [124]. Copyright 1999-2019 John Wiley & Sons, Inc.

Design	F_d (μm)	P (bar)	V (kV)	T ($^{\circ}\text{C}$)	Application/Aim	Ref
square	0.82 ± 0.16	2.8	2.9	84	high volume structures	[131]
layers with porosities	11.18 ± 0.40	0.5	8.5	73	electrophysiologic system	[132]
	30.51 ± 2.42	2.0				
	49.93 ± 2.62	4.0				
sinusoidal/serpentine	19.76 ± 1.54	2.0	6.5	85	heart valve TE	[133]
out of plane	13.30 ± 0.30	2.0	6.0	90	shear properties	[134]
hexagon	-	1.0	4.5	85	cardiac TE	[135]
cylindric	18.20 ± 2.10	1.0	7.0	90	charge effects on fibre alignment	[136]
square, hexagon, octagon, dodecagon	11.23 ± 0.53	0.4	4.5	73	cell infiltration	[137]

Saidy *et al.* [133] outlined the development of a mechanically enhanced scaffold for heart valve TE. MEW was used to create collagen-based scaffolds with a controlled fibre deposition, to mimic its natural wavy appearance. Thus, it was designed a scaffold with a sinusoidal/serpentine architecture with an arc diameter of 1 mm and a circular fibre spacing of 0.5 mm (Fig. 4.3D).

De Ruijter *et al.* [134] designed a set of out-of-plane stabilizing fibres to improve the shear modulus of hydrogel composites (Fig. 4.3E). To achieve such a complex structure, the electrified molten jet was written in a back and forth way across a reproducible and consistent structure similar to a wall.

Castilho *et al.* [135] reported the design of a novel hexagonal shape (Fig. 4.3G) to obtain stretchable and mechanically enhanced scaffolds for myocardial regeneration. *In vivo* experiments were performed with human induced pluripotent stem cell-derived cardiomyocytes. Through its stimulation, the cells differentiated into human adult-like engineered myocardium.

McColl *et al.* [136] outlined a novel tubular design (Fig. 4.3H). Basically, controlled direct writing of medical-grade PCL into a cylinder was performed. Overall, the paper provided insightful knowledge on how the residual charge compromises the control over fibre alignment.

Finally, Youssef *et al.* [137] described the design of four different structures, namely a box (Fig. 4.3I), a hexagon (Fig. 4.3J), a octagon (Fig. 4.3K) and a dodecagon (Fig. 4.3M). Due to its high porosity, the generated scaffolds presented high infiltration capacity. In detail, a tomography-based X-Ray submicrometer was used to generate local thickness maps comprising all the possibilities between the different diameter, fibre-spacing and laydown patterns.

4.2.6.2 MEW Polymers

In this subsection, polymers that were processed by MEW for TE applications are highlighted, being that PCL remains as the gold standard printable material due to its intrinsic properties such

as low melting temperature, high thermal stability and long-time degradation. Notably, over the last few years, several polymers have been printed for the first time, such as the commercially available polypropylene, polyvinylidene fluoride, PCL-based composites [138], (AB)_n-type segmented copolymers [139] and photo-cross linkable polymers [122]. Additionally, Robinson *et al.* [124] described poly(ureasiloxane) as a future viable MEW processable polymer.

Thermoplastic polymers are always an interesting starting point for a technique such as MEW since besides being flexible are easily deformed above a specific temperature [125]. It is worth mentioning that deformation is possible since the intermolecular forces that allow the polymer chains to interact with each other are easily weakened. Hochleitner *et al.* [122] removed the lactide component of poly-L-lactide-co-caprolactone-acryloyl carbonate (poly(LLA-CL-AC)) through the use of UV radiation, and obtained PCL-co-AC, *i.e.*, a copolymer with higher thermal stability and subsequently a better printability.

In a different perspective, Castilho *et al.* [138] outlined the creation of polyhydroxy - methyl - glycoside - co - caprolactone by the conjugation of PCL with a hydroxyl group. The authors described the influence of scaffold architecture on cell alignment. The square-shaped scaffolds promoted random cell arrangement. In comparison, the rectangular-shaped scaffolds induced cell alignment according to fibre orientation. In another work, Hochleitner *et al.* [125] reported a novel strategy to induce the formation of new bone tissue, through the junction of a triblock copolymer, based on PLA-PEG-PLA and bioglass.

4.3 3D printed scaffolds for biomedical applications

To conclude the present chapter, this section highlights MEW manufactured structures for biomedical applications, namely TE. It is worth mentioning the existence of two subsections, being the first related to PCL/GBM scaffolds, and the second to a broader range of polymer/GBM scaffolds, which are summarized in Tables 4.2 and A.1, respectively.

4.3.1 Polycaprolactone/graphene-based materials

Song *et al.* [140] outlined the manufacturing of a thermally and mechanically enhanced PCL/GO scaffold via electrospinning aiming the estimation of its biocompatibility. The authors have used low-differentiated mouse pheochromocytoma (PC12-L) and mouse marrow mesenchymal stem cells (mMSCs). The results suggested that the incorporation of GO (0.3 - 0.5 wt.%) enhanced the ability of PC12-L and mMSCs to adhere, proliferate and differentiate into osteo- and neuro-like cells, respectively.

In another work, Melo *et al.* [141] reported the manufacturing of PCL/GBM composite fibres via a combination of wet-spinning and AM techniques aiming the development of medical devices with no bacterial infection signs. The best design definition was obtained when using an ethanol bath due to better dispersion of GBM and dissolution of PCL. Fibres were obtained in the microscale, having diameters of 100 μm .

Table 4.2: List of studies on PCL/GBM scaffolds, its printing techniques and aims.

Scaffold	Technique	Aim	Ref
PCL/GO	electrospinning	stimulate cell adhesion, proliferation and differentiation on low-differentiated mouse pheochromocytoma (PC12-L) and mouse mesenchymal stem cells (mMSC).	[140]
PCL/GBM	wet-spinning combined with AM	develop medical devices with no bacterial infection signs.	[141]
PCL/GO	extrusion AM	scaffolds mean pore size and wt. % of GO influence on murine pre-osteoblasts differentiation capacity.	[142]
PCL/pristine graphene	extrusion AM	surface chemical modification (with NaOH) effects on scaffolds biological behaviour.	[143]
P1-Latex coated PCL/GO	screw-assisted extrusion AM	induce osteogenic cell proliferation and differentiation with no signs of cytotoxicity.	[144]
PCL/GO	electrospinning	investigation of mechanical properties and bioactivity during scaffolds biomineralization process.	[145]

Concerning bone TE, Unagolla *et al.* [142] developed a PCL/GO scaffold via an extrusion-based AM technique. The authors reported the study of the influence of scaffolds mean pore size (400 and 800 μm) and GO incorporated content (0.1 and 0.5 wt. %) on murine pre-osteoblasts. Overall, scaffolds showed no signs of cytotoxicity, as the pre-osteoblasts attached, proliferated and differentiated well. Wang *et al.* [143] developed a PCL/pristine graphene scaffold via an extrusion-based AM technique, aiming the investigation of surface chemical modifications influence on scaffolds biological behaviour. The results showed that the incorporation of 5 M NaOH, increased the hydrophilicity of the scaffolds ($\approx 13\%$ and $\approx 36\%$ for 0.5 wt.% and 0.75 wt.% of pristine G) and consequently made them more suitable to promote cell behaviour. Once more, no sign of cytotoxicity. Caetano *et al.* [144] reported the manufacturing of a PCL scaffold reinforced by the presence of graphene via a simple extrusion AM. After guaranteeing the homogeneous dispersibility of graphene on the polymeric matrix, the scaffolds were coated with a specific protein (P1-latex). Besides presenting no signs of cytotoxicity, the protein-coated scaffolds enhanced osteogenic cell proliferation and differentiation.

Focusing on the general concept of biomedical applications, Wan *et al.* [145] reported the study of mechanical properties and bioactivity of electrospun PCL/GO scaffolds. The results showed that tensile strength, Young modulus and energy at break increased significantly (95 %, 66 % and 416 %, respectively) just by the incorporation of 0.3 wt.% GO. Additionally, its incorporation induced the improvement of bioactivity during the biomineralization process. Thus, it was concluded that the developed highly porous electrospun PCL/GO scaffolds presented great potential for biomedical applications.

4.3.2 Other polymers/graphene-based materials

As previously stated, this subsection highlights the current published works on other polymers than PCL and GBM composite scaffolds for biomedical applications.

Starting by the non-TE ones, Bao *et al.* [146] showed the manufacturing of polyvinyl acetate/GO nanocomposites via electrospinning in the field of photonics aiming the obtention of efficient materials with ultrashort and fast pulses.

Aiming the creation of a novel strategy for lung cancer treatment, Ardeshirzadeh *et al.* [147] developed a polyethene oxide/chitosan/GO (PEO/CS/GO) scaffold by electrospinning, with a fibre diameter of 85 nm for 0.5 wt.% of GO. Overall, the developed scaffold had a maximum drug loading of 85 % and an efficient controlled doxorubicin release at a pH of 5.3.

In a different perspective, Zhu *et al.* [148] reported the fabrication of a periodic lightweight scaffold based on GO via direct ink writing to form a micro lattice aerogel. Overall, the developed scaffold revealed itself as being highly conductive and having a compressive strain above 90 %. Thus, highlighting its potential to play a crucial role as catalysts.

Concerning the fields of energy storage and electronics, Li *et al.* [149] reported the manufacturing of a flexible circuit based on rGO homogeneously dispersed in a PLA matrix. For instance, PLA electrical conductivity increased as soon as rGO was incorporated. Nevertheless, the maximum achieved value was 4.76 S cm^{-1} , with 6 % of rGO.

Aiming the investigation of biocompatibility and antibacterial properties of GO, An *et al.* [150] reported the development of an electrospun PLA/PU/GO scaffold. After its characterization via scanning electron microscopy, transmission electron microscopy and x-ray diffraction, it was verified that both attachment and proliferation of microbes were prevented through the addition of 3 and 5 wt.% of GO to the PLA/PU composite. It is worth mentioning that two types of microbes were used, namely the gram-negative *Escherichia Coli* and the gram-positive *staphylococcus aureus*. Indeed this study opened the possible application on antibacterial components and enhanced the biocompatibility of GO in particular concentrations.

To explore the tremendous potential of graphene-based scaffolds in TE applications, Zhang *et al.* [151] reported the fabrication of a nanofibrous PLA/GO scaffold by electrospinning. Additionally, to improve the adhesion between PLA and GO, the GO surface was coated with polyethylene glycol. Overall, the authors proclaimed that surface-functionalized GO addition did not comprise the scaffolds cytocompatibility.

Regarding bone TE, Qi *et al.* [152] outlined an electrospun nanofibrous scaffold based on polyvinyl alcohol and GO. Macro and microstructure of the developed scaffolds were evaluated in terms of morphology, crystallinity, mechanical and biological properties by using mouse osteoblastic cells (MC3T3-E1). Overall, cellular viability was not affected by the addition of GO. Nevertheless, the MC3T3-E1 cells could attach, grow and spread on the surface of the scaffolds.

Concerning skeletal muscle TE, Shin *et al.* [153] reported the development of a hybrid porous poly-lactic-co-glycolic acid (PLGA) and collagen (Col) scaffold based on GO (PLGA-Col-GO) via electrospinning and subsequently with continuous but randomly oriented fibres. In the study,

an immortalized myoblastic cell line (C2C12) was used, and its attachment, proliferation and differentiation were investigated.

Overall, electrospinning has been the most used printing technique while GO revealed itself as the most used GBM. To conclude, so far, no PCL/GBM scaffold either with linear either with non-linear patterns has been manufactured by MEW. Moreover, in these conditions, to the best of our knowledge, no work has been published in PCL/GBM electric or magnetic stimuable scaffolds.

Chapter 5

Materials and Methods

5.1 Materials Production

Granular medical-grade polycaprolactone (PCL) (Purasorb PC 12) was purchased from Purac Biomaterials, The Netherlands. Graphene nanoplatelets (GNP) grades M and C, were acquired from XG Sciences, USA. According to the supplier, GNP were prepared through exfoliation of sulfuric acid-based intercalated graphite by rapid heating in a microwave environment, followed by ultrasonic processing [154]. Its main features are present in Table 5.1. Additionally, the typical sizes of a GNP-C sample can vary from diameter below to 100 nm, small flakes, to about 1-2 μm , larger flakes. In contrast, the diameter of GNP-M is around 5 μm and its thickness between 5-8 nm [155].

Sulphuric acid (H_2SO_4 , 95-98 %) and hydrogen peroxide (H_2O_2) were acquired from VWR, Germany; Phosphoric acid (H_3PO_4 , 85 %) and potassium permanganate (KMnO_4) were purchased from Chem-lab, Belgium and JMGS, Portugal, respectively. Iron (II) chloride tetrahydrate ($\text{FeCl}_2 \cdot 4\text{H}_2\text{O}$, 99.0 %, Acros Organics) and ammonium hydroxide (NH_4OH , 28.0-30.0 % NH_3 basis) were purchased from ThermoFisher Scientific, USA. Filters with 5-8 and 17-30 μm of pore size were purchased from Filtres Fioroni, France.

Table 5.1: Main features of GNP-M and GNP-C grade materials. Adapted from [155].

Grade	Average thickness (nm)	Maximum length (μm)	Surface area ($\text{m}^2 \text{g}^{-1}$)
M	[5-8]	5	120-150
C	2	<2	750

5.1.1 GBM oxidation and magnetization

Figure 5.1 describes magnetic graphene nanoplatelets (@GNP) production method. Firstly, GNP is oxidized into GNP-ox via the modified Hummers method (MHM) as described by Pinto *et al.* [156] Briefly, a mixture of 320 mL of H_2SO_4 and 80 mL of H_3PO_4 were added to 8 g of GNP while stirring, and the solution was cooled using an ice bath. Then 48 g of KMnO_4 were added

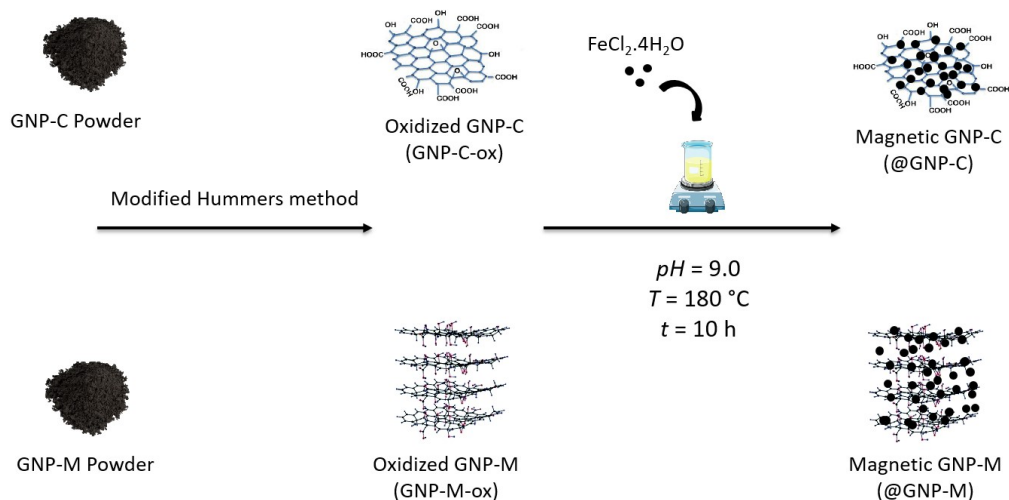


Figure 5.1: Magnetic graphene nanoplatelets (@GNP) production method.

gradually and the solution was heated to $35\text{ }^\circ\text{C}$ and stirred for 2 hours, followed by the slow addition of 1200 mL of distilled water, under stirring with temperature being controlled using an ice bath. Finally, 52 mL of H_2O_2 were added to stop the reaction. After overnight resting, the solution was decanted to separate the solid phase from the acidic solution, centrifuged at 4000 rpm during 15 minutes, re-dispersed in distilled water and the process repeated until water pH was achieved in the supernatant.

To obtain @GNP, a solution of iron chloride, namely $\text{FeCl}_2 \cdot 4\text{H}_2\text{O}$, is added in a proportion of 1:20 (GNP-ox:iron chloride). Briefly, GNP-ox (2 mg mL^{-1}) and $\text{FeCl}_2 \cdot 4\text{H}_2\text{O}$ (40 mg mL^{-1}) dispersions were mixed and sonicated for 10 minutes (Bandelin Sonorex R K512 H, Germany), pH was adjusted to 9 with ammonium hydroxide and the dispersion kept under stirring at $180\text{ }^\circ\text{C}$ overnight. Then, excess iron was removed by centrifuging five times at 4000 rpm for 15 minutes and filtration using 5 L of distilled water to wash the material. In detail, two different filters were used, one with $5\text{--}8\text{ }\mu\text{m}$, and another one with $17\text{--}30\text{ }\mu\text{m}$. The larger one was used to prevent the loss of @GNP in case the smaller filter tears. @GNP retained in the filter was further washed by centrifugation, as described above.

5.1.2 Melt blending of PCL/graphene-based materials composites

PCL/GNP composites were prepared by melt blending in a Thermo Haake PolyLab (Thermo Fisher Scientific, The Netherlands) with an internal mixing volume of 60 cm^3 at a temperature of $90\text{ }^\circ\text{C}$. Firstly, PCL granules were, directly and gradually, added into the melt compounder under a rotor speed of 100 rpm, and when all the sample was added, the rotor speed was increased to 250 rpm and left to operate for 3 minutes. Then, the rotor speed was decreased to 100 rpm to add the @GNP powder. As all the sample was added, the rotor speed was increased to 250 rpm and left to operate for 3 minutes. After the blending process, the composites were extruded as filaments with

a maximum diameter of 3 mm to allow printing. GNP-M contents tested were of 2 and 10 wt.%, while for GNP-C, those were of 2, 10, 15, and 20 wt.% in a total of 5 g per sample (PCL+@GNP).

5.2 Materials characterization

5.2.1 Morphological characterization

5.2.1.1 Transmission electron microscopy (TEM)

Aqueous dispersions of GNP, GNP-ox, and @GNP were prepared at a concentration of $50 \mu\text{g mL}^{-1}$ and sonicated for 1 hour using an ultrasound bath (Bandelin Sonorex R K512H, Germany). Just before sample testing, sonication was performed for 10 minutes to re-disperse agglomerates. Afterwards, $10 \mu\text{L}$ of each sample was deposited on a carbon-coated TEM grid and allowed to deposit for 1 minute, followed by excess material removal by capillarity using filter paper.

Visualization was performed at 80 kV in a JEM 1400 microscope (JEOL, Japan), and digital images were acquired using a CCD digital camera Orious 1100 W (Hamamatsu Photonics, Japan). Sample's lateral dimensions were measured from several TEM images using ImageJ software.

5.2.1.2 Scanning electron microscopy (SEM)

GNP, GNP-ox and @GNP powders, extruded filaments (cross-sections performed by cutting with a sharp blade) and 3D printed scaffolds were applied on conductive carbon strips for visualization. There was no need to submit the samples to any sputtering technique.

SEM imaging of @GNP powders, extruded filaments and 3D printed scaffolds, except the ones with 15 wt.% of @GNP-C, was performed using an FEI QUANTA 400 FEG SEM (FEI company, Hillsboro, OR, USA) with an acceleration voltage of 3 kV, at Centro de Materiais da Universidade do Porto (CEMUP).

SEM imaging of GNP, GNP-ox and @GNP powders as well as PCL/GNP-C 15 wt.% extruded filament was performed using a Phenom XL Desktop SEM (Thermo Fisher Scientific, USA) at Associação Rede de Competência em Polímeros (ARCP).

5.2.2 Chemical characterization

5.2.2.1 Particle size distribution

Particle size distributions of GNP, GNP-ox and @GNP were determined by dynamic light scattering (DLS) through two types of equipment namely LS230 (Beckman Coulter, USA) and Litesizer 500 (Anton Paar, Austria).

Independently of the used equipment, before the measurements, the materials were dispersed in distilled water at a concentration of $50 \mu\text{g mL}^{-1}$ and sonicated for 1 hour. Just before sample testing, sonication was performed for 10 minutes to re-disperse agglomerates.

Data from LS230 Beckman Coulter was collected performing three scans of 60 seconds, including polarization intensity differential scattering and using Fraunhofer's model. This model

assumes a spherical shape for particles in suspension. This evaluation of size distributions does not correspond to precise estimations of particle size and must be considered as relative evaluations of deagglomeration of the different materials in water. Data from Litesizer 500 was collected performing five scans of 60 seconds. The main difference to the other equipment is the conjugation of the dynamic light scattering (DLS), electrophoretic light scattering (ELS), and static light scattering (SLS) phenomena.

5.2.2.2 Zeta potential

Before any zeta potential measurement, aqueous dispersions of GNP, GNP-ox, and @GNP were prepared at a concentration of $50 \mu\text{g mL}^{-1}$ and sonicated for 1 hour. Just before sample testing, sonication was performed for 10 minutes to re-disperse agglomerates.

Zeta potential of the aqueous dispersions was determined using a Zetasizer Nano ZS (Malvern Instruments, UK). Each measurement was performed in triplicate at 37°C in a disposable Zetasizer cuvette. Results are reported as mean and standard deviation. Generally, Zetasizer Nano ZS is equipped with a 4 mW HeNe laser beam with a wavelength of 633 nm and a scattering angle of 13° .

5.2.2.3 Fourier transform infrared spectroscopy (FTIR)

GNP, GNP-ox and @GNP powders, extruded filaments, and 3D printed scaffolds FTIR spectra were recorded using a VERTEX 70 FTIR spectrometer (BRUKER, Germany) in transmittance mode at room temperature. Samples were measured in attenuated total reflection (ATR) with an A225/Q PLATINUM ATR Diamond crystal with a single reflection accessory. The spectra were recorded from 4000 to 400 cm^{-1} with 60 scans and a resolution of 4 cm^{-1} .

5.2.2.4 Energy-Dispersive Spectroscopy (EDS)

EDS data of @GNP, extruded filaments and 3D printed scaffolds, except the ones with 15 wt.% of @GNP-C, were obtained with EDAX Genesis X4M software (Oxford Instruments, Oxfordshire, UK) according to the use of an FEI QUANTA 400 FEG SEM (FEI company, Hillsboro, OR, USA) with an acceleration voltage of 3 kV, at Centro de Materiais da Universidade do Porto (CEMUP).

EDS data of GNP, GNP-ox, @GNP and PCL/GNP-C 15 wt.% extruded filament were obtained with Element Identification (EID) package fully integrated on the Phenom XL Desktop SEM (Thermo Fisher Scientific, USA) at Associação Rede de Competência em Polímeros (ARCP).

5.2.2.5 X-ray photoelectron spectroscopy (XPS)

@GNP films, extruded filaments, and 3D printed scaffolds surface were analyzed using a Kratos Axis Ultra HSA equipment (Kratos Analytical, Manchester, UK) with VISION software for data acquisition and CASAXPS software (Casa Software Ltd, UK) for data analysis. The analysis was carried out with a monochromatic Al K X-ray source (1486.7 eV), operating at 15 kV (90 W),

in fixed analyzer transmission (FAT) mode, with a pass energy of 40 eV and a step of 0.1 eV for regions (C, O, and Fe) and 160 eV of pass energy and 1.0 eV of step for the survey. The peaks were fitted using a Gaussian-Lorentzian shape and a Shirley background.

Before the measurements, @GNP solutions were submitted to sonication for 10 minutes to re-disperse agglomerates. Then, one drop of each solution was added to a silicon substrate, which was subsequently dried in an oven for 10 minutes at 45 °C. This procedure was repeated between 3 to 4 times per solution to cover the silicon substrate uniformly, leading to the formation of @GNP films. Three samples of each extruded filament (cross-sections performed by cutting with a sharp blade) and 3D printed scaffolds, except the ones with 15 wt.% of @GNP-C, were applied on conductive carbon strips.

5.2.2.6 Water contact angle (WCA)

Contact angle measurements were conducted with an ASTM C813 Optical contact angle (OCA) and contour analysis equipment (Dataphysics instruments, Germany), and recorded with a Service-component architecture (SCA) 20 under room temperature. Characterization was performed via the Sessile drop technique. A distilled water droplet of 4 μL , with a dosing rate of 4 $\mu\text{L s}^{-1}$ was deposited on three different points of the PCL, PCL/GNP-M and PCL/GNP-C extruded filaments over 120 s. A 700 series microliter syringe (Hamilton, USA) was used. Each measurement was performed two times.

Before the measurements, the extruded filaments were cut with a sharp blade and placed under an aluminum foil. Then, they were placed in an oven for 3 minutes at 90 °C and subsequently uniformly spread with a spatula. This method guarantees that one of the surfaces of each produced sample is flat, to allow measurements not affected by surface topography.

5.2.3 Thermal characterization

5.2.3.1 Differential scanning calorimetry (DSC)

Melting temperatures (T_m), crystallization temperatures (T_c), and degree of crystallization (X_c) of GNP, GNP-ox and @GNP powders, extruded filaments, and 3D printed scaffolds were determined with a DSC 214 Polyma (Netzsch, Selb, Germany). Sample amounts ranged from 6 to 10 mg.

The materials were heated to 150 °C at a heating rate of 10 °C min^{-1} , then cooled down to -20 °C at a cooling rate of 10 °C min^{-1} . Heating and cooling steps were repeated twice. Nitrogen gas (30 mL min^{-1}) was used to maintain the inert atmosphere, and small sample size was preferred to avoid the temperature gradient inside the sample.

The degree of crystallization (X_c) was calculated using Eq. 5.1:

$$X_C = \frac{\Delta H_m}{\Delta H_m^0 \times (1 - wt_{filler})} \quad (5.1)$$

Where ΔH_m is the melting enthalpy, ΔH_m^0 is the melting enthalpy of 100 % crystalline PCL and $(1 - wt_{filler})$ stands for the actual weight of polymer whose crystallinity is being evaluated.

The specific heat of fusion of 100 % crystalline PCL is 139.5 J g⁻¹ [157].

5.2.3.2 Thermogravimetric analysis (TGA)

The thermal stability of GNP, GNP-ox and @GNP powders, extruded filaments, and 3D printed scaffolds were determined with an STA 449 F3 Jupiter (Netzsch, Selb, Germany). Sample amounts ranged from 6 to 10 mg.

The thermograms were carried out from 30 to 1000 °C at a heating rate of 10 °C min⁻¹ in alumina crucibles under a 30 mL min⁻¹ nitrogen flow.

Isothermal curves of extruded filaments were carried out at 90 and 130 °C in aluminum crucibles for 8 hours under a 30 mL min⁻¹ nitrogen flow.

5.2.4 Rheological characterization

Amplitude sweep tests were performed with an MCR 72/92 Modular Compact Rheometer (Anton Paar, Austria). Extruded filaments were cut in pieces with a sharp blade and then placed over a stainless-steel plate system with 40 mm diameter. PCL samples temperature was equilibrated for 5 minutes at 90, 130 and 180 °C, while for PCL/GNP-M and PCL/GNP-C 90 and 130 °C were used. Subsequently, samples were subjected to an oscillatory stress sweep ranging from 10 to 1000 Pa, at a frequency of 1 Hz. Storage (G') and loss modulus (G'') were recorded.

5.2.5 Crystallographic characterization

The crystallographic patterns of GNP, GNP-ox, @GNP, extruded filaments, and 3D printed scaffolds were obtained by X-ray diffraction analysis (XRD), using a Smartlab diffractometer (Rigaku, USA) in the Bragg-Brentano geometry over a $2\theta = 15^\circ - 70^\circ$ range, at room temperature. The beam consisted of Cu K α radiation with $\lambda = 1.540593 \text{ \AA}$.

5.2.6 Magnetic characterization

GNP, GNP-ox and @GNP powders, extruded filaments, and 3D printed scaffolds magnetic measurements were performed using a commercial Superconducting quantum interference device (SQUID) magnetometer (Quantum design, Germany). The magnetization (M) as a function of the applied magnetic field (H) at 310 K was obtained by applying a magnetic field up to 50 kOe. The temperature-dependent zero-field-cooled/field-cooled (ZFC/FC) measurements were performed over the temperature range of 5 K to ≈ 370 K with $H = 100$ Oe.

5.3 Materials printing

5.3.1 Melt electrowriting

Melt electrowriting of the developed materials was performed in a custom-built device, as schematically represented in Figure 5.2. The system was developed at the University Medical Center Utrecht (UMC) as described elsewhere [135]. It is composed of four main modules namely, a dispensing unit, a heating system, an electric field circuit and a computer-controlled collector plate.

The dispensing module contains a disposable glass syringe (3 mL Fortuna Optima Luer Lock Tip, Poulten & Graf GmbH, Wertheim, Germany) where the raw polymers are inserted, coupled to one end to a thin metallic nozzle (27 G, Unimed, Switzerland), and to the other end to a proportional pressure regulator (Festo, Germany), which operates with air. The heating module is composed of an electrical heating coil element wrapped around the glass syringe and directly connected to a proportional–integral–derivative controller (TR 400, HKEtec, Germany) to control the polymer melting temperature.

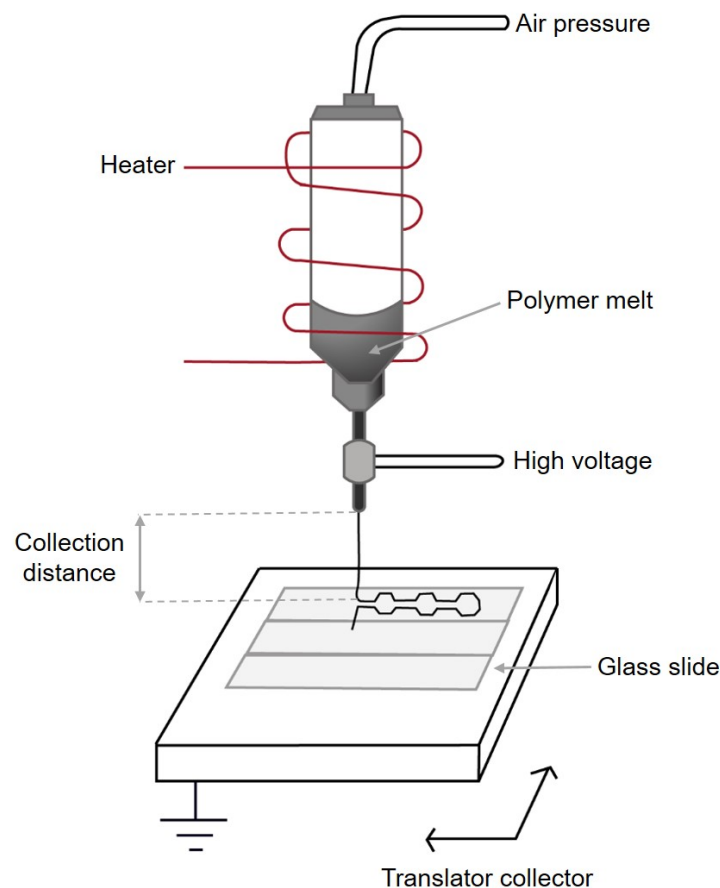


Figure 5.2: Schematic of the custom-built MEW device and its principal components, namely a dispensing unit assisted by air-pressure; a heating system; a high voltage source electrode; and a computer-assisted collector plate.

The electric field is generated by a high voltage (HV) source (LNC 30000, Heinzinger Power supplies, Rosenheim, Germany) between a positive output applied to the syringe nozzle and the grounded planar aluminum collector plate. The plate is driven by an advanced 3-axis motor controller by two servomotors and one stepper-motor (Trio Motion Technology Ltd., UK). Fibre collection was performed through the use of uncoated microscope glass slides (VWR International GmbH, Germany).

5.3.2 MEW experimental parameters

PCL and PCL/GNP composites printability was systematically investigated according to key MEW parameters namely the feeding pressure (P), the applied voltage (V) and the collector speed (C_S). Distance to the collector (D_tC) and syringe spinneret diameter (S_d) were kept constant during the investigation at 4.0 mm and 0.4 mm, respectively [135, 138].

The applied temperature (T) was set at 90 °C for PCL and PCL/GNP-C-2, at 105 °C for PCL/GNP-C-10 and PCL/GNP-C-15 and at 120 °C for PCL/GNP-C-20, and kept constant through the printing process.

The range of stable printing conditions namely feeding pressure (P) and applied voltage (V) at critical translational speed (CTS) for PCL and PCL/GNP composites containing different filler contents is shown in Table 5.2.

Table 5.2: Range of stable printing conditions namely feeding pressure (P) and applied voltage (V) at critical translational speed (CTS) for PCL and PCL/GNP composites containing different filler contents. Printing temperatures (T), distance to the collector (D_tC) and syringe spinneret diameter (S_d) variables are also present.

Material / Variable	T (°C)	D_tC (mm)	S_d (mm)	P (bar)	voltage (kV)
PCL	90	4.0	0.4	1 - 3	5 - 7
PCL/GNP-C-2	90	4.0	0.4	1 - 3	5 - 7
PCL/GNP-C-10	105	4.0	0.4	1.5 - 3	5 - 6
PCL/GNP-C-15	105	4.0	0.4	1.5 - 3	5 - 7
PCL/GNP-C-20	120	4.0	0.4	1.5 - 3	5 - 7

5.3.3 Fabrication process

Processing compatibility of the developed PCL and PCL/GNP composites was systematically investigated through the following methodology:

1. Find the Critical translational speed (CTS).

In detail, a combination of P and V was adjusted until a stable and continuous extrusion jet was obtained. Then, a CTS selection basic tool path (Figure 5.3), with the following properties, was prepared:

- Rectangular pattern, with long lines to allow jet stabilization after C_S variation.

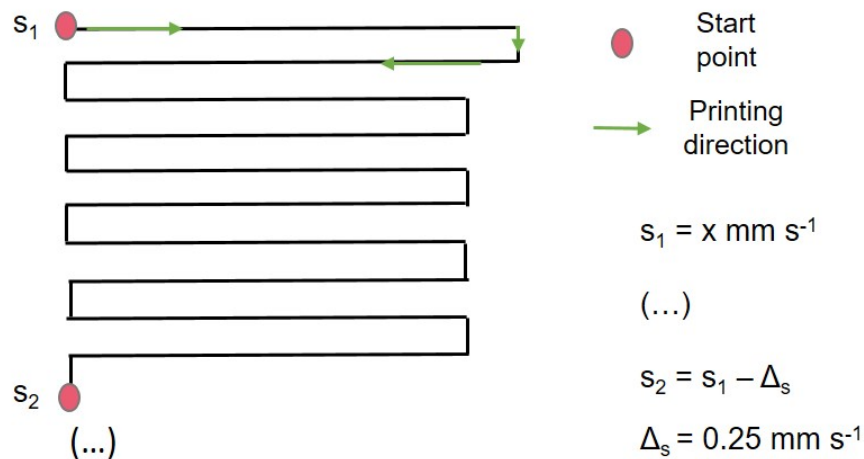


Figure 5.3: Critical translational speed (CTS) evaluation pattern.

- Single-layer pattern.
- Between the beginning and the end of the entire pattern, C_S was constant.
- After each pattern, C_S was changed.

The C_S gradient was chosen such that the minimum C_S is below the anticipated CTS and the maximum C_S is above it. Typical values were between 10 and 2 mm s^{-1} [135, 127].

Afterwards, a pattern was written using a large range of different C_S (*i.e.* $s = 2 \dots 10 \text{ mm s}^{-1}$ in $\Delta s = 0.25 \text{ mm s}^{-1}$ steps).

Finally, the pattern was assessed with an Olympus BX43 microscope (Olympus Corporation, The Netherlands) to find the threshold where the CTS was exceeded (*e.g.* CTS was found to be 5 mm s^{-1}). For the record, CTS was exceeded as no apparent coiling or wiggling in the fibre path was visualized (Figure 5.4). Thus, the CTS was obtained with a precision of 0.25 mm s^{-1} .

2. Study the influence of feeding pressure (P), applied voltage (V) and collector speed (C_S) on fibre diameter (F_D) and morphology.

Concerning the feeding pressure, PCL and PCL/GNP-C-2 were printed in a range of 1-3 bar, while PCL/GNP-C-10, PCL/GNP-C-15 and PCL/GNP-C-20 range from 1.5 to 3 bar. Regarding the applied voltage, all materials were printed from 5 to 7 kV, except PCL/GNP-C-10 which was printed from 5 to 6 kV. All printings were performed at CTS.

To study the influence of C_S , firstly a combination of P and V was chosen, namely 2 bar and 6 kV (intermediate values regarding the ones presented in Table tab:SingleFibresPrintingConditions). Afterwards, a set of straight fibres was made at CTS, 1.2 CTS, 1.4 CTS, 1.6 CTS and 1.8

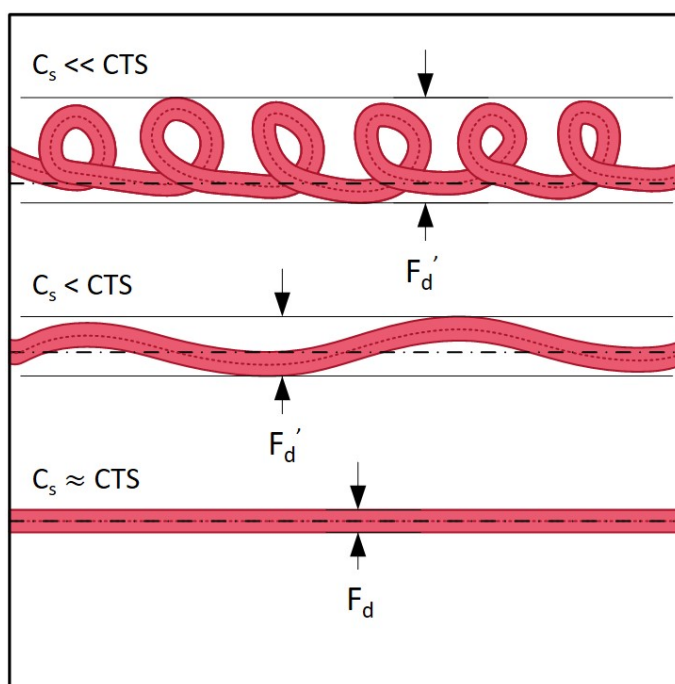


Figure 5.4: Theoretical relationship between the critical translational speed (CTS), collector speed (C_s), fibre morphology and fibre diameter (F_d).

CTS. Subsequently, fibre visualization was performed through an Olympus BX43 microscope (Olympus Corporation, The Netherlands), and its diameter was measured using ImageJ software ($n=20$).

A Dino-Lite digital microscope (AnMo Electronics Corporation, Taiwan) was used to monitor jet during printing.

5.4 Statistical analysis

Statistical analyses were performed using GraphPad Prism software (version 8.4.2, San Diego, CA, USA). One-way analysis of variance (ANOVA) with Tukey tests for multiple comparisons were performed. Differences between experimental groups were considered significant with a confidence interval of 95 %, whenever $p < 0.05$.

Chapter 6

Results

6.1 GBM morphological properties, particle size, and stability

TEM imaging of the powders (Figure 6.1) shows that GNP-M is constituted by individual platelets with a length around $2\ \mu\text{m}$ while GNP-C length is $< 1\ \mu\text{m}$. GNP-M platelets have planar conformation, smooth surface with irregular and sharp edges. GNP-C platelets are more wrinkled, presenting usually less sharp edges.

After oxidation, platelets planar form, as well as the sharp edges, are lost. GNP-M-ox and GNP-C-ox have a wrinkled appearance and folded edges, which are indicated by yellow arrows in Figure 6.1. It probably occurs because, during oxidation, oxygen-containing functional groups are attached to the basal plane of GNP sheets, resulting in lattice distortion [64]. Additionally, the platelets short dimensions allowing the oxygen-containing functional groups at the edges to form hydrogen bonds, distorting the sheets [158].

@GNP-M and @GNP-C images confirm the successful incorporation and distribution of the iron nanoparticles across GNP surface, which are indicated by green arrows and green dotted lines in Figure 6.1, respectively. Besides, loose iron nanoparticles were not found.

SEM imaging gives another perspective of the powders. According to Figure 6.2, iron nanoparticles, represented by green lines, cover @GNP-C surface and are well dispersed, while they are not so visible at @GNP-M surface. This is possibly explained by GNP-M higher number of graphene single layers and higher lateral dimensions, which seems to affect iron nanoparticles morphology and drive them preferentially between graphene layers instead of being exposed at the surface, as in @GNP-C. It is worth mentioning that SEM images of all powders with lower resolution and magnification are present in the appendix, in Figure B.1, and were used to analytically quantify the atomic elements (carbon, oxygen and iron) present in the samples via Energy-dispersive X-ray spectroscopy (EDS).

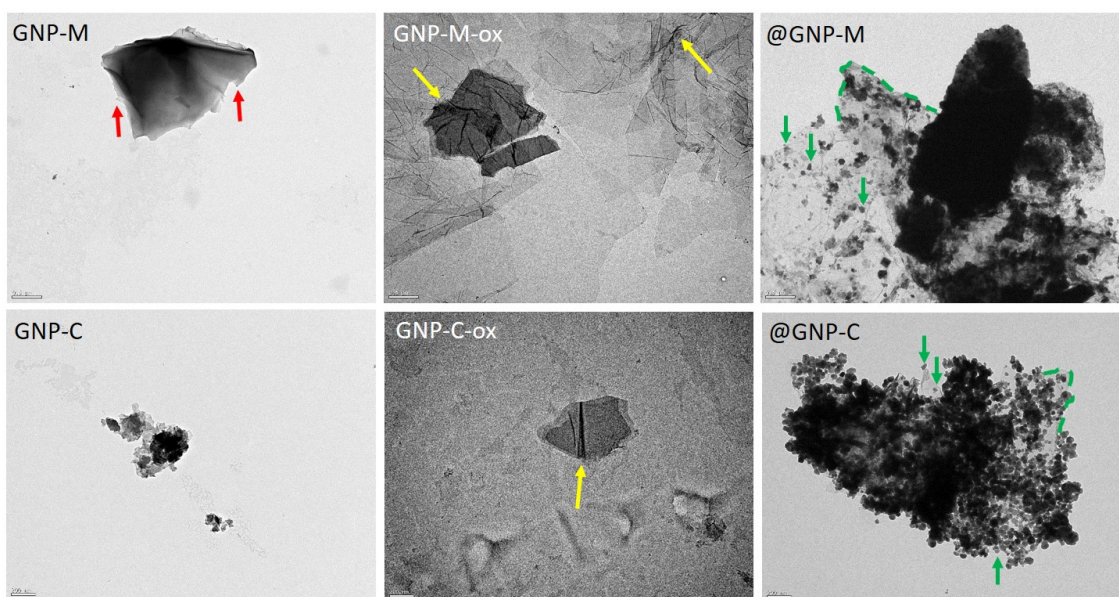


Figure 6.1: Transmission electron microscopy (TEM) images of GNP-M, GNP-C, GNP-M-ox, GNP-C-ox, @GNP-M, and @GNP-C. Sharp and folded edges are indicated by red and yellow arrows, respectively. Green arrows point out iron nanoparticles, while green dotted lines indicate GNP edges. Scale bars represent 0.5 μm for GNP-M, GNP-M-ox and @GNP-M and 200 nm for GNP-C, GNP-C-ox and @GNP-C.

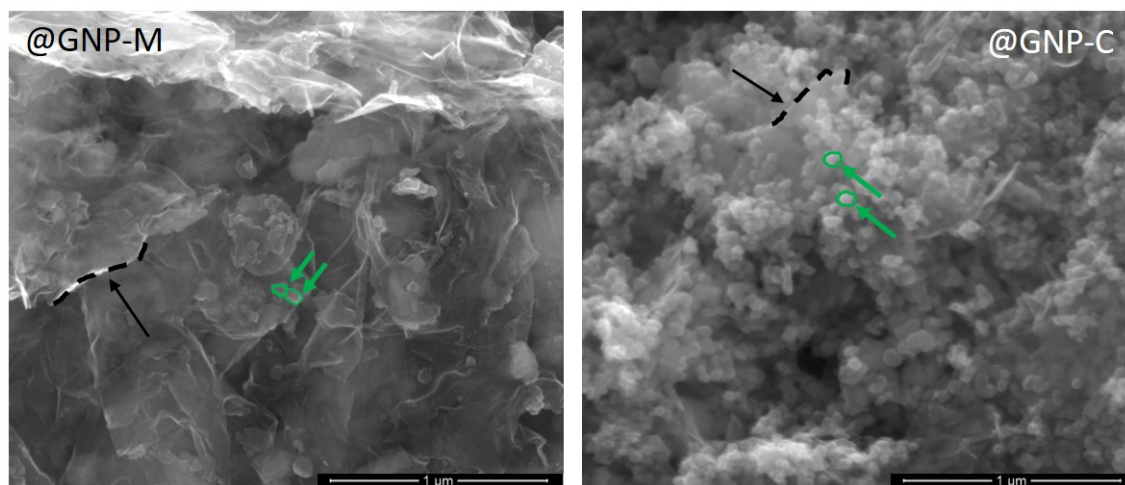


Figure 6.2: Scanning electron microscopy (SEM) images of @GNP-M and @GNP-C powders. Black arrows indicate GNP edges, which are represented by a black dotted line, while green arrows point out iron nanoparticles circled by a green line. Scale bars represent 1 μm .

Lateral dimensions of iron nanoparticles and GNP powders were firstly determined from TEM image analysis. Average particle size with and without statistical analysis are shown in Figures 6.3 and B.2. Additionally, box-plot of its particle size distribution is shown in Figure B.3.

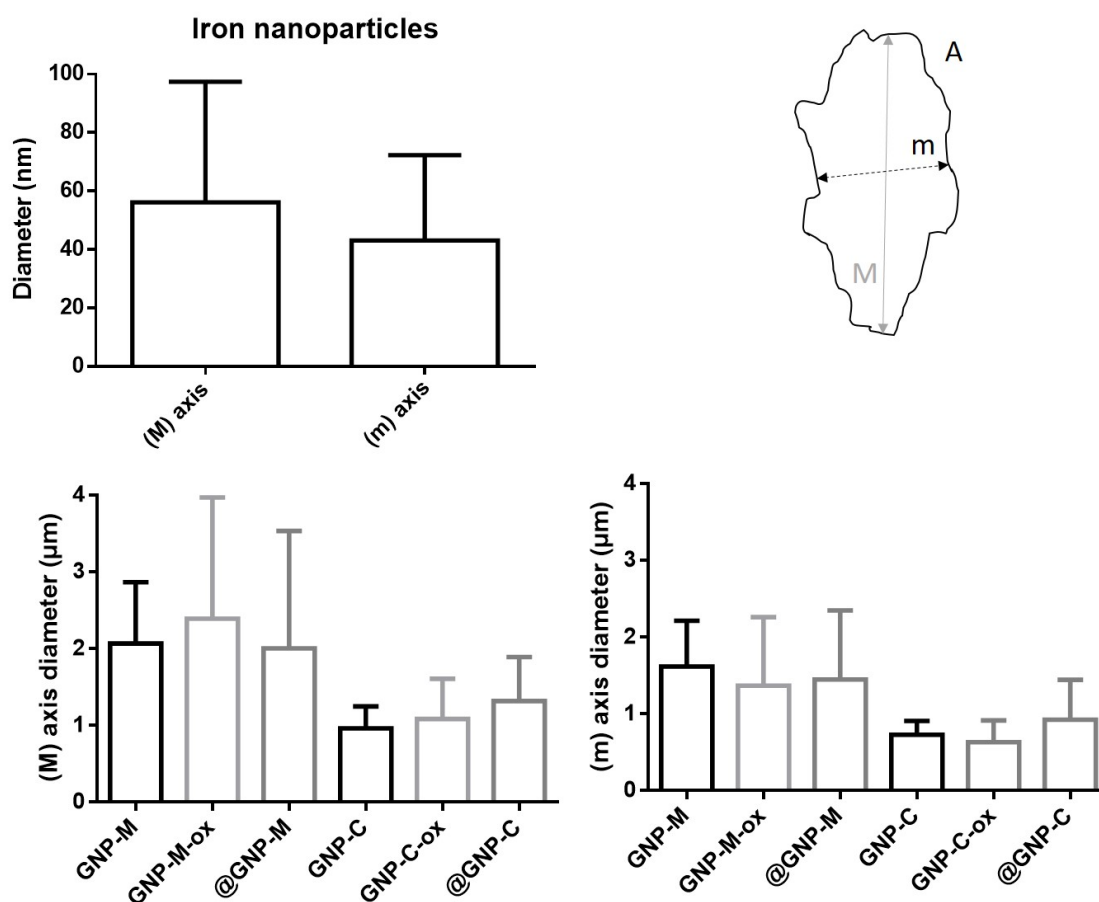


Figure 6.3: Average particle size of iron nanoparticles, GNP-M and GNP-C grade materials, for its major (M) and minor (m) axis, determined from TEM images. A) represents a graphene nanoplatelet as well as its (M) and (m) axis.

As GNP particles length is irregular, whenever any measurement was carried out, the major (M) and minor (m) axis were taken into account. Iron nanoparticles were obtained with an average size respectively of 56.1 ± 31.28 and 43.1 ± 21.67 nm for its (M) and (m) axis. The average particle sizes for GNP-M, GNP-M-ox and @GNP-M were respectively of 2.1 ± 0.60 , 2.4 ± 1.17 and 2.0 ± 1.14 μm ; 1.6 ± 0.45 , 1.4 ± 0.68 and 1.4 ± 0.72 μm for its (M) and (m) axis. In comparison, GNP-C, GNP-C-ox and @GNP-C presented average particle sizes respectively of 0.9 ± 0.22 , 1.1 ± 0.39 and 1.3 ± 0.43 μm ; 0.7 ± 0.14 , 0.6 ± 0.23 and 0.9 ± 0.40 μm for its (M) and (m) axis. According to the statistical analysis, GNP-M, GNP-M-ox, and @GNP-M are not significantly different from each other. The same is observed within GNP-C grade materials. However, the differences between GNP-M and GNP-C grade materials are statistically significant ($p < 0.001$), as expected since according to manufacturer's data, the maximum length of GNP-M is around 5 μm , while for GNP-C it is usually < 2 μm (Table 5.1).

Particle size distribution was also determined by dynamic light scattering (DLS) via Coulter and Litesizer equipment (Figures 6.4 and B.4). GNP-M was obtained with an average size re-

spectively of 5.3 ± 2.08 (Coulter) and 6.1 ± 2.47 (Litesizer) μm in volume; 1.9 ± 0.98 (Coulter) and 2.1 ± 1.45 (Litesizer) μm in number. Results obtained for the same sample were very similar for the two types of equipment, which shows the reliability of the presented data. The difference between particle size distribution in volume and number is mainly due to the existence of larger size agglomerates, which take a relatively high volume of the sample. Figure 6.4 demonstrates this phenomenon since there are two sharp peaks for the distribution in volume and only one for the distribution in number. GNP-M-ox was obtained with an average size respectively of 5.5 ± 2.14 (Coulter) and 5.5 ± 2.35 (Litesizer) μm in volume; 1.9 ± 0.98 (Coulter) and 2.1 ± 1.45 (Litesizer) μm in number; @GNP-M presented an average size respectively of 5.2 ± 2.06 (Coulter) and 5.0 ± 2.24 (Litesizer) μm in volume; 1.9 ± 0.98 (Coulter) and 1.5 ± 1.24 (Litesizer) μm in number. Indeed, these values show the similarity between the particle size distribution of GNP-M, GNP-M-ox and @GNP-M.

Similarly, GNP-C presented an average size respectively of 2.3 ± 1.54 (Coulter) and 1.1 ± 1.06 (Litesizer) μm in volume; 1.3 ± 1.17 (Coulter) and 1.0 ± 1.00 (Litesizer) μm in number. In comparison, GNP-C-ox was obtained with an average size respectively of 1.2 ± 0.54 (Coulter) and 1.0 ± 1.02 (Litesizer) μm in volume; 0.8 ± 0.94 (Coulter) and 0.9 ± 0.96 (Litesizer) μm in number, while @GNP-C presented an average size respectively of 1.6 ± 0.81 (Coulter) and 1.1 ± 1.07 (Litesizer) μm in volume; 0.9 ± 0.92 (Coulter) and 1.0 ± 1.05 (Litesizer) μm in number. A summary of all methods taken into account is shown in Figure 6.5.

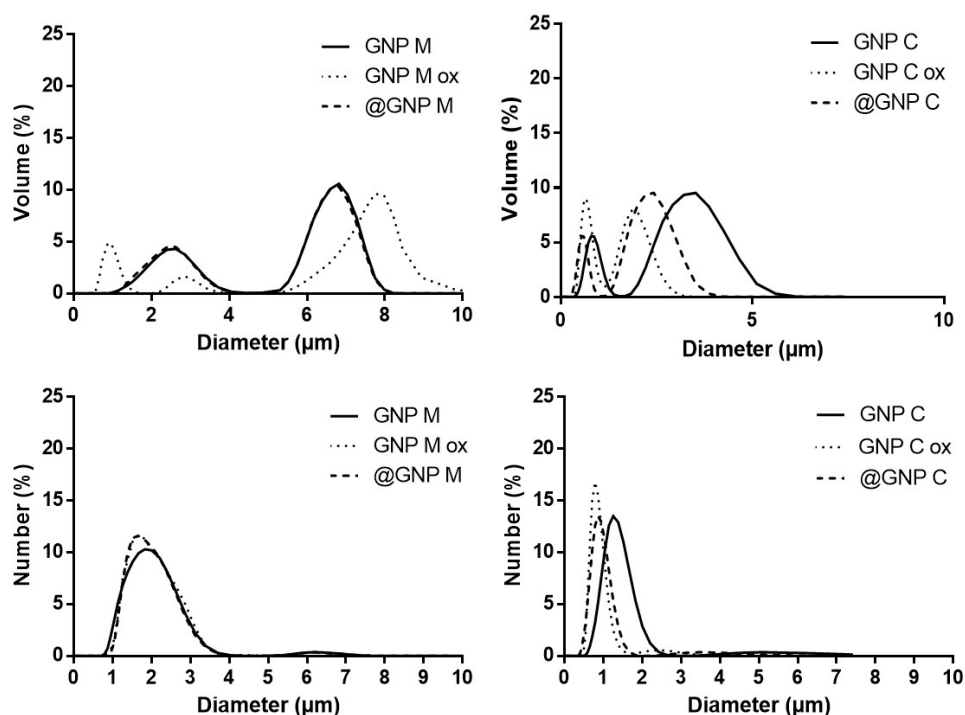


Figure 6.4: Particle size distribution in volume (%) and number (%) for GNP-M and GNP-C grade materials, determined by dynamic light scattering (DLS), using a Beckman Coulter equipment.

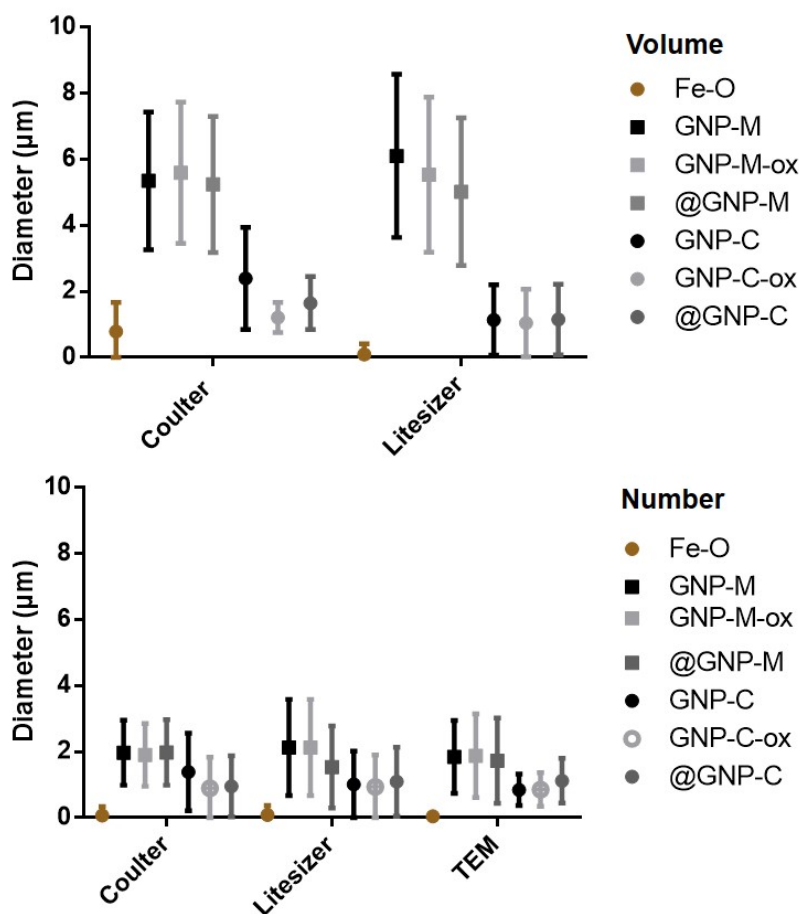


Figure 6.5: Particle size distribution in volume and number for iron nanoparticles (Fe-O), GNP-M and GNP-C grade materials, determined from TEM images and DLS, using a Beckman Coulter and a Litesizer equipment.

Both grades of GNP exhibited comparable colloidal stability in aqueous dispersions, according to zeta (ζ)-potential measurements (Figures 6.6, B.5 and Table B.1). GNP-M and GNP-C presented a surface charge of -27.6 ± 0.6 mV and -28.3 ± 0.6 mV. In comparison, GNP-M-ox and GNP-C-ox displayed a higher surface charge (-29.1 ± 0.7 mV and -29.6 ± 0.3 mV), and therefore higher colloidal stability. In opposition, @GNP-M and @GNP-C presented a surface charge of -18.4 ± 4.75 mV and -21.0 ± 2.6 mV, respectively. The decrease in magnetized powders surface charge in comparison to GNP and GNP-ox is due to the incorporation of iron nanoparticles, which presented a charge of just -16.1 ± 3.1 mV [159].

GNP were incorporated in PCL by melt-blending and resulting PCL/GNP filaments morphology investigated using SEM. Figure 6.7 presents the average size of @GNP-M and @GNP-C particles or particle agglomerates within the polymeric matrix, while Figure 6.8 shows PCL/GNP filaments cross-sections where the embedded particles can be observed.

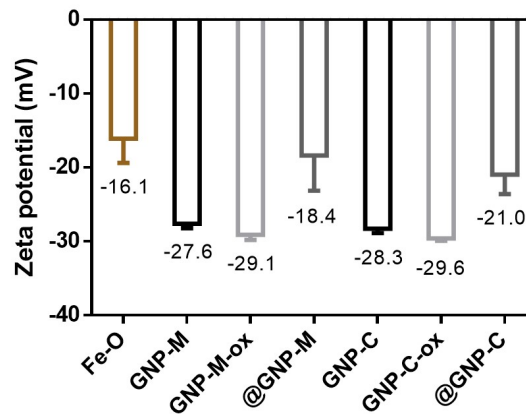


Figure 6.6: Surface charge of iron nanoparticles (Fe-O), GNP-M, GNP-M-ox, @GNP-M, GNP-C, GNP-C-ox and @GNP-C aqueous dispersions at an initial concentration of $50 \mu\text{g mL}^{-1}$ and pH 7.4 ($n = 3$) determined with a Zetasizer equipment.

In PCL/GNP-M-2 and PCL/GNP-M-10 samples, @GNP-M presented an average size respectively of 2.1 ± 0.53 and $2.4 \pm 0.81 \mu\text{m}$. In comparison, in PCL/GNP-C-2, PCL/GNP-C-10 and PCL/GNP-C-20 samples, @GNP-C presented an average size respectively of 1.0 ± 0.45 , 1.1 ± 0.33 and $1.5 \pm 0.48 \mu\text{m}$. These data is in agreement with @GNP-M and @GNP-C average particle size determined via TEM and DLS (Coulter and Litesizer equipment) (Figure 6.5), since, according to these techniques, the average particle size of @GNP-M and @GNP-C was around 2 and 1 μm , respectively. Additionally, it can be concluded that the higher the @GNP loading, the higher the average particle size due to increased degree of agglomeration.

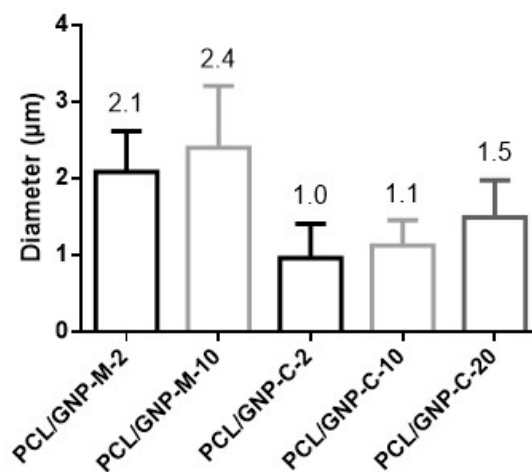


Figure 6.7: Average particle or particle agglomerates size of @GNP-M and @GNP-C in PCL/GNP-M and PCL/GNP-C filaments cross-sections, determined from SEM images. ($n = 50$).

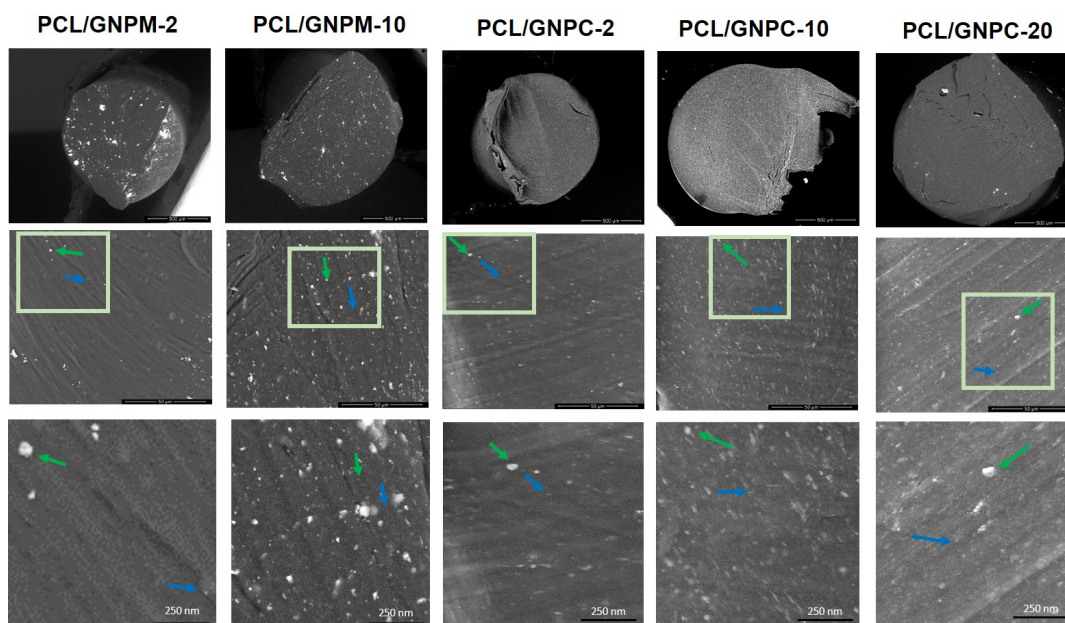


Figure 6.8: SEM images of PCL/GNP filaments cross-sections. The green arrows indicate the GNP agglomerates, while the blue arrows point to individual GNP. Scale bars represent 500 μm , 50 μm and 250 nm for top, middle and bottom line images, respectively. Bottom line images are a zoom in from the light green square.

6.2 Chemical characterization of GBM

GNP powders Fourier transform infrared (FTIR) spectra were obtained to confirm the presence of oxygen functionalities at the surface of GNP-M-ox and GNP-C-ox, as well as its partial reduction into @GNP-M and @GNP-C.

FTIR spectra (Figure 6.9) revealed that a peak around 1995 cm^{-1} was identifiable for all samples (more visible on GNP-M, GNP-C, @GNP-M and @GNP-C) which is assigned to the aromatic C-H bending vibrations. A sharp peak at around 1725 cm^{-1} is present in GNP-M-ox and GNP-C-ox spectra, being assigned to C=O stretching vibrations, which demonstrates the presence of carbonyl and carboxyl groups [95].

Although not visible in GNP-M and GNP-C spectra, the peak around 1608 cm^{-1} in GNP-M-ox and GNP-C-ox and around 1565 cm^{-1} in @GNP-M and @GNP-C is present due to the stretching of cyclical alkene (C=C) from the unoxidized graphitic domain [160].

The presence of ethers is evidenced by the appearance of strong absorption bands around 1275 and 1224 cm^{-1} for GNP-M-ox, GNP-C-ox, @GNP-M and @GNP-C and around 1041 cm^{-1} for GNP-M-ox and GNP-C-ox, which are assigned to C-O stretching vibrations. Additionally, there is a broad peak around 965 cm^{-1} to GNP-M-ox and GNP-C-ox, which is assigned to C=C (alkene) bending vibrations [95].

In summary, successful oxidation is confirmed by the identification of several oxygen functionalities at the surface of GNP-M-ox and GNP-C-ox, in opposition to original GNP-M and GNP-C.

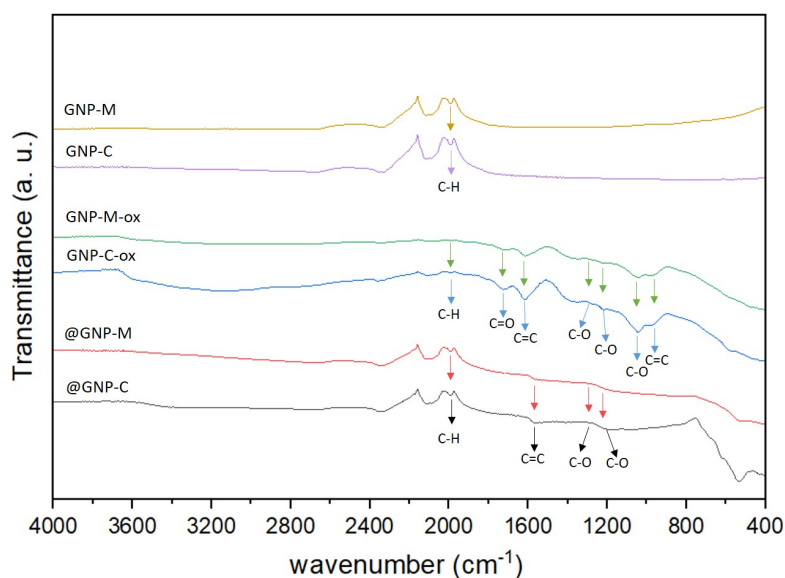


Figure 6.9: FTIR spectra of GNP-M, GNP-C, GNP-M-ox, GNP-C-ox, @GNP-M and @GNP-C. The arrows indicate the contribution of several surface functionalities.

The partial reduction step is also demonstrated due to a decrease in the intensity of bands assigned to oxygen-containing functional groups in @GNP-M and @GNP-C, comparing with GNP-M-ox and GNP-C-ox.

PCL FTIR spectra (Figure 6.10) presents two sharp peaks around 2943 and 2854 cm^{-1} , which can be assigned to asymmetric and symmetric CH_2 stretching vibrations. A clear peak around 1725 cm^{-1} is also present, being attributed to $\text{C}=\text{O}$ stretching vibrations, which demonstrates the presence of ester groups. The peak nearby 1470 cm^{-1} corresponds to CH_2 bending vibrations.

According to Elzein *et al.* [161], the peak around 1293 cm^{-1} (ν^{cr}) is attributed to the backbone $\text{C}-\text{C}$ and $\text{C}-\text{O}$ stretching modes in the crystalline PCL. Additionally, two other peaks are present around 1237 cm^{-1} and 1163 cm^{-1} and are assigned to asymmetric and symmetric $\text{C}-\text{O}-\text{C}$ stretching, respectively.

FTIR spectra from PCL/GNP filaments and scaffolds (Figures B.7 and 6.11, respectively) are similar to the ones from PCL polymer without GNP incorporation. The absence of changes in PCL/GNP filaments, when compared to PCL polymer, was expected since @GNP is not exposed at the surface of PCL/GNP composites but homogeneously distributed within its polymeric matrix (Figure 6.8). Regarding the scaffolds, the absence of changes demonstrates that the used printing technique does not interfere with samples in the chemical point of view, neither regarding GNP exposure at the surface.

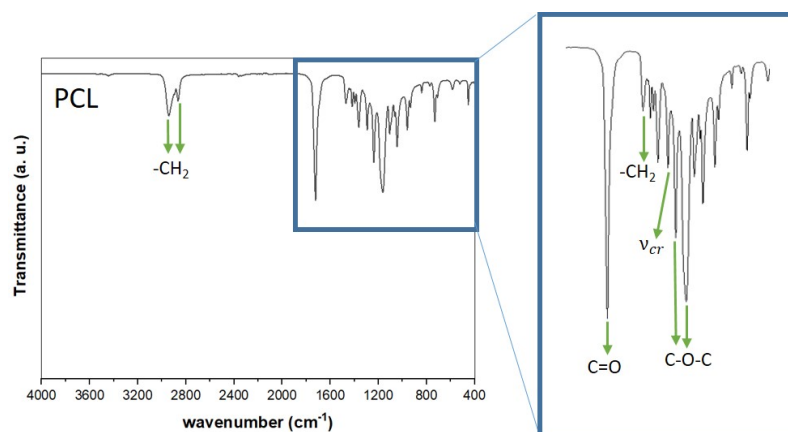


Figure 6.10: FTIR spectra of PCL. The arrows indicate the contribution of several surface functionalities.

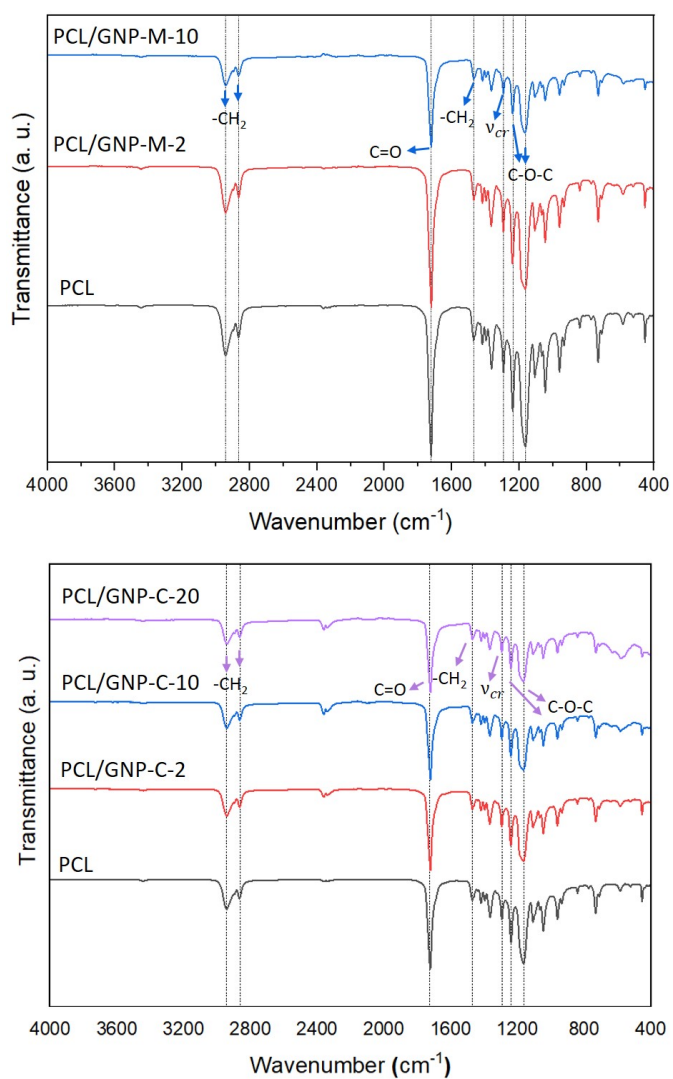


Figure 6.11: FTIR spectra of PCL, PCL/GNP-M and PCL/GNP-C scaffolds. The arrows indicate the contribution of several surface functionalities, while the dotted lines point out similar peaks.

Energy-dispersive x-ray spectroscopy (EDS) analyses were performed to characterize GNP powders before and after chemical oxidation and magnetization steps (Table 6.1). The distribution of C, O and Fe atomic elements was determined for all powders and is presented in Figure 6.12 and Table 6.1.

GNP-M and GNP-C presented a O at.% respectively of 12.4 and 10.9 %. In comparison, GNP-M-ox and GNP-C-ox presented a O at.% respectively of 47.1 and 52.9 %. Such increase in O at.% from GNP to GNP-ox, demonstrates the successful introduction of oxygen functionalities at both GNP grade materials surface. This quantitative contrast between C at.% and O at.% is visible in Figure 6.12 through the greater blue colour intensity (oxygen) shown by both GNP when compared to GNP-ox. Moreover, the EDS maps revealed that C and O atomic elements are homogeneously distributed through GNP samples. At the same time, some heterogeneity is verified for GNP-ox, which probably occurs due to the higher degree of folding of GNP-ox when compared to GNP (Figure 6.1).

Table 6.1: EDS and XPS analysis of GNP, GNP-ox and @GNP powders, PCL, PCL/GNP filaments and scaffolds. EDS outlines the content of C, O and Fe, while XPS presents the content of C 1s, O 1s and Fe 2p. C/O ratio for each sample is present by both methods.

At. %		EDS				XPS			
Type	Sample/Element	C	O	Fe	C/O	C 1s	O 1s	Fe 2p	C/O
Powders	GNP-M	87.6	12.4	-	7.1	-	-	-	-
	GNP-C	89.1	10.9	-	8.2	-	-	-	-
	GNP-M-ox	52.2	47.8	-	1.1	-	-	-	-
	GNP-C-ox	47.1	52.9	-	0.9	-	-	-	-
	@GNP-M	25.5	40.1	34.4	0.6	82.7	12.9	4.4	6.40
	@GNP-C	20.7	42.3	37.0	0.5	49.2	28.1	22.7	1.8
Filaments	PCL/GNP-M-2	78.2	19.8	2.0	4.0	76.4	23.6	-	3.2
	PCL/GNP-M-10	67.3	26.0	6.7	2.6	76.4	23.6	-	3.2
	PCL/GNP-C-2	77.1	21.5	1.4	3.6	85.8	14.2	-	6.1
	PCL/GNP-C-10	73.2	20.3	6.5	3.6	78.2	21.8	-	3.6
	PCL/GNP-C-20	67.7	22.3	10.0	3.0	78.8	21.2	-	3.7
Scaffolds	PCL	75.2	24.8	-	2.6	75.6	24.4	-	3.1
	PCL/GNP-M-2	73.8	25.6	0.6	2.9	76.2	23.8	-	3.2
	PCL/GNP-M-10	74.2	24.3	1.5	3.1	76.5	23.5	-	3.3
	PCL/GNP-C-2	74.3	24.7	1.0	3.0	76.7	23.3	-	3.3
	PCL/GNP-C-10	65.7	32.9	1.4	2.0	75.7	24.3	-	3.1
	PCL/GNP-C-20	68.4	24.3	7.3	2.8	75.3	24.7	-	3.1

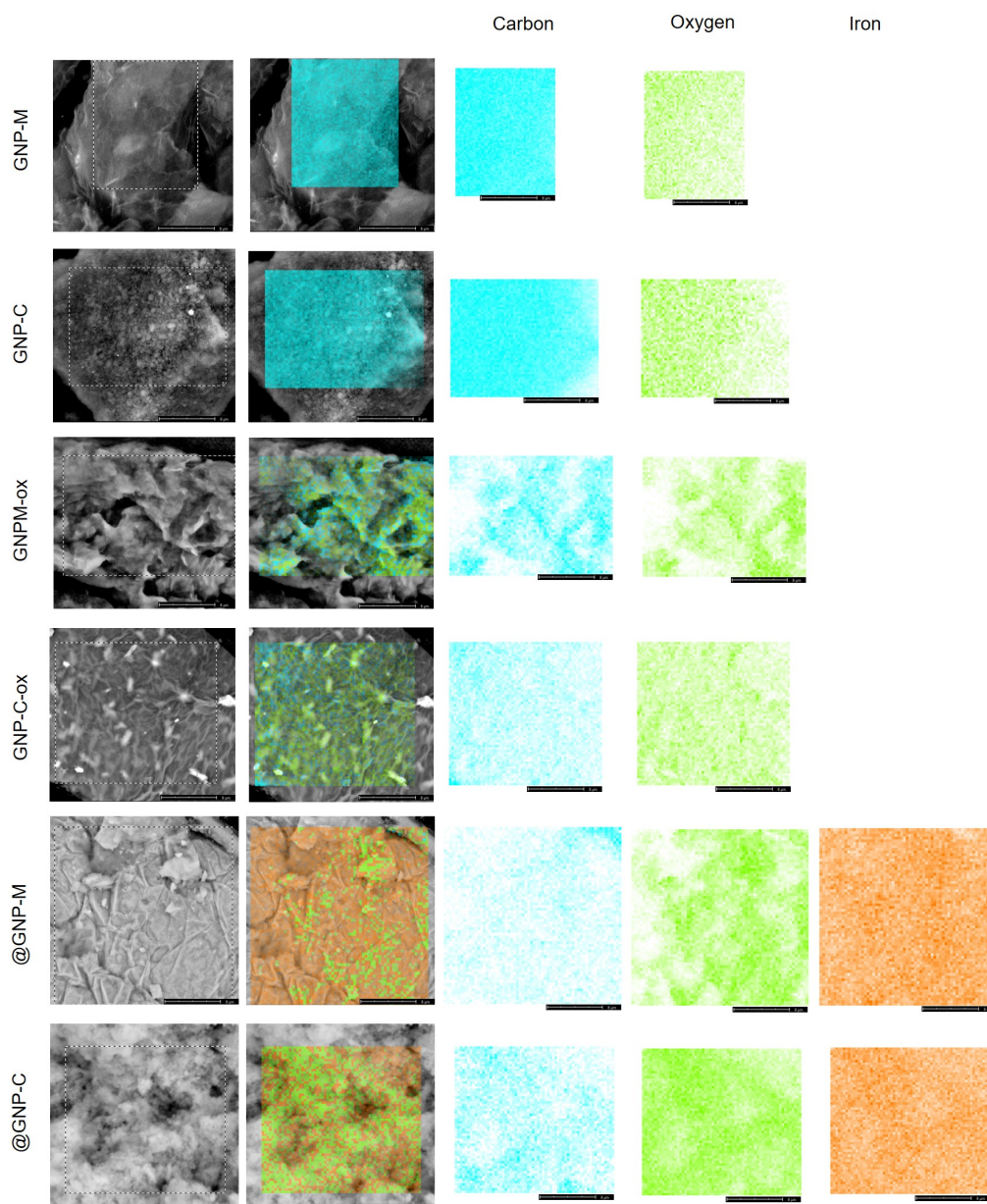


Figure 6.12: SEM images and EDS analysis maps of GNP, GNP-ox and @GNP, for GNP-M and GNP-C grade materials. Scale bar represents 8 μm .

The partial reduction step is verified by the decrease of O at.% from 47.8 % and 52.9 % to 40.1 % and 42.3 % for @GNP-M and @GNP-C, respectively. On one hand, oxygen-containing functional groups were removed due to the reduction process. On the other hand, through the magnetization process, oxygen atoms were introduced due to the use of (Fe_3O_4) . @GNP-M and @GNP-C Fe at.% were of 34.4 and 37.0, respectively. EDS maps revealed that C and O are arranged with some heterogeneity in @GNP-M; @GNP-C also presented some heterogeneity on C distribution. Generally, Fe is homogeneously distributed through the samples.

EDS analysis were also performed to characterize the incorporation of the magnetized powders into PCL matrix in both filament and scaffold structure (Table 6.1). Concerning the filaments, PCL presented C and O at.% of 75 and 25 %, respectively, which is in agreement with the values found in literature [162]. PCL/GNP-M-2 presented C, O and Fe at.% of 78.2, 19.8 and 2.0 %, respectively. In comparison, PCL/GNP-C-2 presented values of 77.1, 21.5 and 1.4 %. By loading PCL with 10 wt.% of @GNP-M, its C, O and Fe at.% changed to 67.3, 26.0 and 6.7 %, respectively, while PCL/GNP-C-10 presented 73.2, 20.3 and 6.5 %. Thus, as the amount of filler increases, there is a decrease in C at.% and an increase in O and Fe at.%. PCL/GNP-C-20 revealed even higher Fe at.% (10 %). For PCL/GNP scaffolds a similar trend was observed.

X-ray photoelectron spectroscopy (XPS) analyses were performed to characterize the magnetization degree of @GNP-M and @GNP-C as well as the effect of its incorporation into PCL matrix, both in filaments and scaffolds (Table 6.1, Figures 6.13, 6.14, B.8, B.9, B.10, B.11, B.12, B.13 and B.14). @GNP-M and @GNP-C presented a Fe 2p at.% of 4.3 and 22.7, respectively.

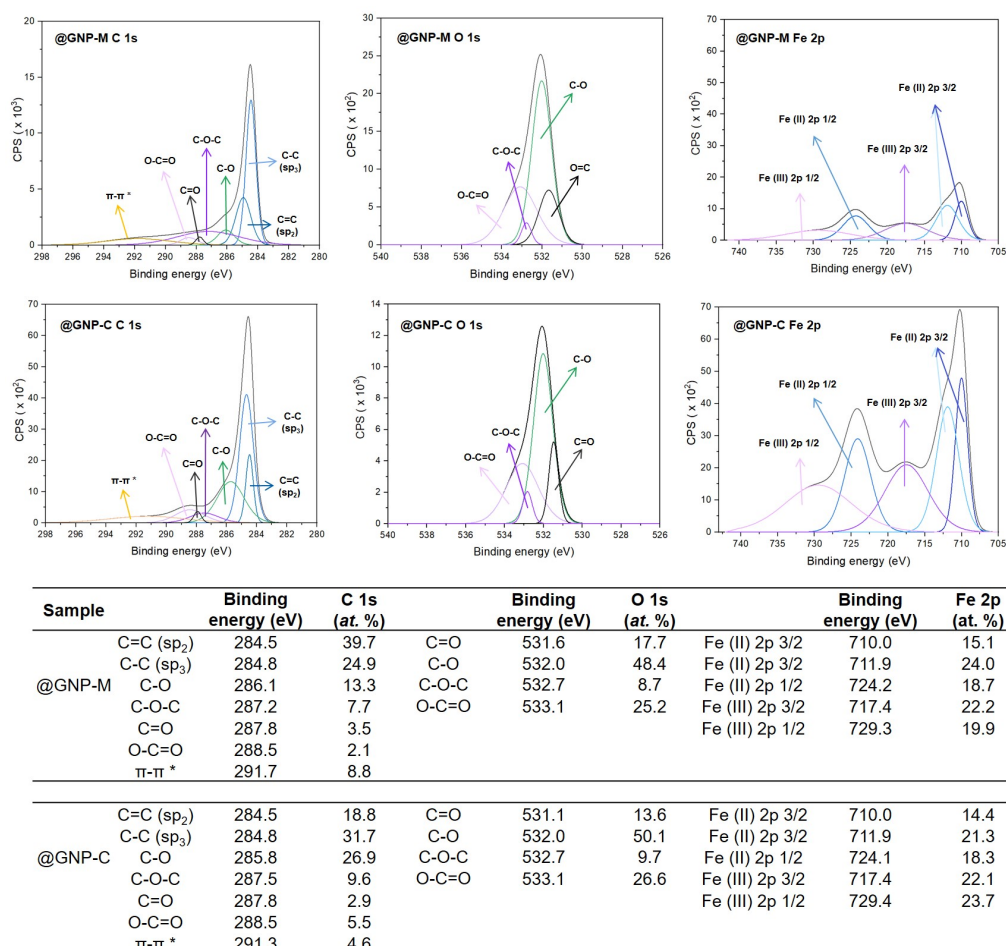


Figure 6.13: XPS analysis of @GNP-M and @GNP-C. Deconvolution of high-resolution C 1s, O 1s and Fe 2p XPS spectra. Content of C 1s, O 1s and Fe 2p chemical groups resulting from spectra fitting.

Such numerical difference is possibly explained by GNP-M higher number of graphene single layers and higher lateral dimensions, which seems to drive the iron nanoparticles preferentially between graphene layers instead of being exposed at the surface, as in @GNP-C (Figure 6.2).

Analysis of C 1s spectra of @GNP-M and @GNP-C revealed one broad peak, which could be further deconvoluted in seven peaks (Figure 6.13). The first and second binding energies were attributed to C=C (284.5 eV) and C-C (284.8 eV), for @GNP-M (C 1s at.% of 39.7 and 22.9, respectively) and @GNP-C (C 1s at.% of 13.8 and 29.7, respectively) due to the formation of sp^2 and sp^3 hybridizations of carbon in the graphitic backbone. The third binding energy values, 286.1 and 285.8 eV, were associated with single bonds of C-O for @GNP-M and @GNP-C, being C 1s at.% of 13.3 and 26.9, respectively. The fourth binding energy evidenced the presence of ethers (287.2 and 287.5 eV) for @GNP-M and @GNP-C, being C 1s at.% of 7.7 and 9.6, respectively. Carbonyl (287.8 eV) and carboxyl groups (288.5 eV) are also present in @GNP-M and @GNP-C, being C 1s at.% of 3.5 and 2.1; 3.9 and 13.5, respectively. Finally, π - π^* bonds (291.7 and 291.3 eV) were observed due to the presence of delocalized π electrons in the graphene lattice of @GNP-M and @GNP-C, being C 1s at.% of 10.8 and 2.6, respectively [95].

Regarding @GNP-M and @GNP-C O 1s spectra analysis, one broad peak was observed, which could be deconvoluted in four peaks (Figure 6.13). The first binding energy value was attributed to C=O due to the presence of carbonyl groups (531.6 and 531.1 eV) for @GNP-M and @GNP-C, being O 1s at.% of 17.7 and 13.6, respectively. The second binding energy value, 532 eV, was associated with single bonds of C-O for @GNP-M and @GNP-C, being O 1s at.% of 48.4 and 50.1, respectively. Ethers (532.7 eV) and carboxyl groups (533.1 eV) are also present in @GNP-M and @GNP-C, being O 1s at.% of 8.7 and 25.2; 9.7 and 26.6, respectively [95, 163].

Fe 2p spectra for magnetic powders exhibited two main peaks, which could be further deconvoluted in five peaks (Figure 6.13). The first (710.0 eV) and second (711.9 eV) binding energies were attributed to Fe (II) 2p $3/2$ for @GNP-M and @GNP-C, being Fe 2p at.% of 15.1 and 24.0; 14.4 and 21.3, respectively. In comparison, the fourth energy value was attributed to Fe (II) 2p $1/2$ (724.1 and 724.2 eV) for @GNP-M and @GNP-C, being Fe 2p at.% of 18.7 and 18.3, respectively. The third and fifth binding energies were attributed to Fe (III) 2p $3/2$ (717.4 eV) and Fe (III) 2p $1/2$ (729.4 eV) for @GNP-M and @GNP-C, being Fe 2p at.% of 22.2 and 19.9; 22.1 and 23.7, respectively. The presence of Fe (II) and Fe (III) suggests that the magnetic powders consist of a mixture between Fe_2O_3 and Fe_3O_4 .

XPS analysis were also performed to characterize the incorporation of @GNP into PCL matrix in both filament and scaffolds (Table 6.1). Similarly to EDS, PCL filament and scaffolds presented a C at.% of 75 and a O at.% of 25. For PCL/GNP composites similar values were obtained, except for PCL/GNP-C-2 filament which presented 85.8 % of C 1s and 14.1 % of O 1s. Besides, no iron is detected at the surface of any sample.

PCL C 1s high-resolution spectra can be fitted with the sum of three components (Figure 6.14), namely hydrocarbons (284.5 eV), ether (286.0 eV) and ester (288.5 eV) groups, being C 1s at.% of 69.5, 19.3 and 11.2, respectively. Analysis of O 1s spectra of PCL revealed one broad peak, which could be further deconvoluted in two peaks (Figure 6.14). The first (532.2 eV) and second

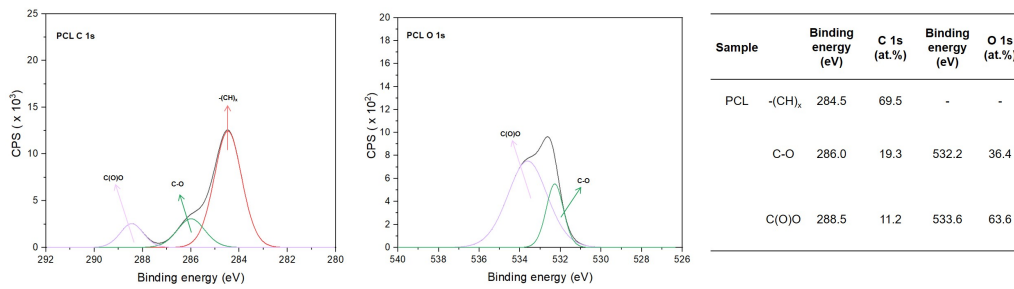


Figure 6.14: XPS analysis of PCL. Deconvolution of high-resolution C 1s and O 1s XPS spectra. Content of C 1s and O 1s chemical groups resulting from spectra fitting.

(533.6 eV) binding energies were attributed to the presence of ether and ester groups, being O 1s at.% of 36.4 and 63.6, respectively [164, 165].

Binding energies, C 1s and O 1s at.% presented a similar trend to PCL/GNP-M and PCL/GNP-C filaments (Figures B.11 and B.12) and scaffolds (Figures B.13 and B.14), when compared with PCL. The only exception to this tendency was PCL/GNP-C-2 filament which presented about 87.8 % of C at.% and 12.2 % of O at.%. Overall, the absence of changes from PCL to PCL/GNP filaments and scaffolds was expected since @GNP is not exposed at the surface of PCL/GNP composites but homogeneously distributed within its polymeric matrix (Figure 6.8). This result is in agreement with FTIR data which revealed a similar spectra for every composite (Figures B.7 and 6.11).

The water contact angles at the surface of PCL, PCL/GNP-M and PCL/GNP-C filaments were determined and results presented in Figures 6.15 and B.15.

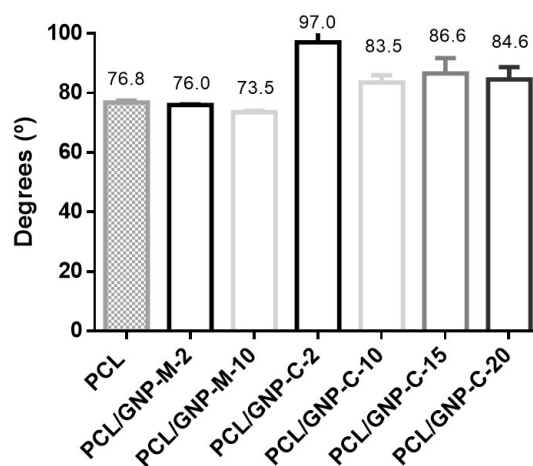


Figure 6.15: Sessile drop water contact angle for PCL, PCL/GNP-M and PCL/GNP-C filaments containing different filler contents.

PCL presented a water contact angle of 76.8° , which demonstrates its near hydrophobicity since a sample is considered hydrophobic when presenting a water contact angle higher than 90° [166]. PCL/GNP-M-2 and PCL/GNP-M-10 presented a water contact angle of 76.0° and 73.5° , respectively, therefore being similar to PCL. In opposition, PCL/GNP-C-2 presented a water contact angle of 97.0° , which is significantly higher than the one observed for PCL. Regarding that the lower the O 1s at.%, the higher the hydrophobicity and subsequently the higher the water contact angle, this result is in agreement with XPS data since PCL/GNP-C-2 presented an O 1s at.% of 14.13 % while PCL presented 24.0 % (Table 6.1) All the other PCL/GNP-C samples, although having a higher contact angle than PCL, and so being slightly more hydrophobic, are similar between them, and its contact angles were around 85° .

6.3 Thermal analysis

Differential scanning calorimetry (DSC) was performed for PCL, PCL/GNP-M and PCL/GNP-C composites. The results are shown in Figure 6.16 and in Tables 6.2 and B.2.

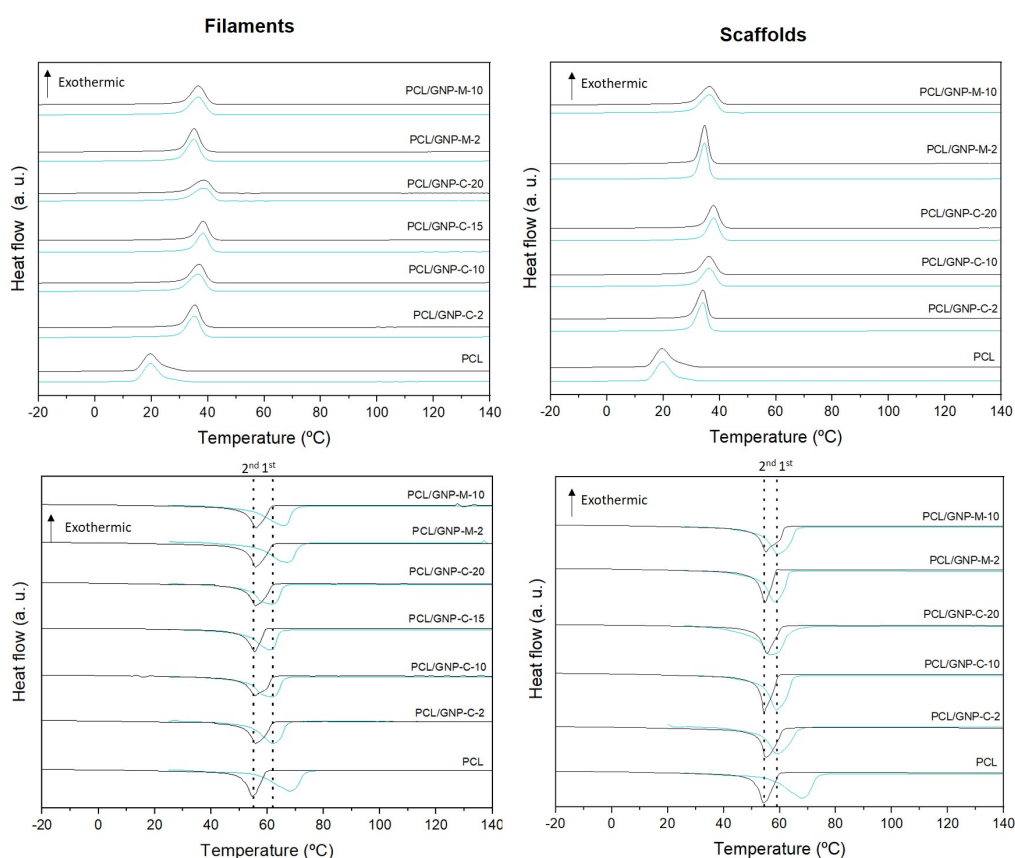


Figure 6.16: DSC thermograms for PCL, PCL/GNP-M and PCL/GNP-C filaments and scaffolds containing different filler contents. First and second (heating and cooling) scans are represented by green and black lines, respectively.

Table 6.2: Crystallization temperatures (T_{c1} and T_{c2}), melting temperatures (T_{m1} and T_{m2}) and degree of crystallization (χ_{c1} and χ_{c2}) for PCL, PCL/GNP-M and PCL/GNP-C filaments and scaffolds containing different filler contents.

Type	Sample	T_{c1} (°C)	T_{c2} (°C)	T_{m1} (°C)	T_{m2} (°C)	χ_{c1} (%)	χ_{c2} (%)
Filaments	PCL	19.8	19.4	66.9	54.2	52.6	47.0
	PCL/GNP-M-2	36.2	36.3	65.5	55.5	47.3	48.7
	PCL/GNP-M-10	37.3	37.6	64.6	55.8	51.2	44.3
	PCL/GNP-C-2	36.2	36.3	61.6	55.7	45.6	48.2
	PCL/GNP-C-10	37.5	37.7	60.9	55.3	47.8	48.5
	PCL/GNP-C-15	38.6	38.6	60.8	55.5	42.8	45.0
	PCL/GNP-C-20	38.7	38.7	56.7	55.4	49.1	49.7
Scaffolds	PCL	19.8	19.4	66.9	54.2	45.6	39.1
	PCL/GNP-M-2	35.5	35.6	58.6	54.6	53.6	47.8
	PCL/GNP-M-10	37.4	37.3	58.7	55.2	48.3	48.7
	PCL/GNP-C-2	35.1	35.1	55.2	55.2	42.3	39.1
	PCL/GNP-C-10	37.1	37.0	56.3	55.7	52.1	42.0
	PCL/GNP-C-15	38.6	38.6	60.8	55.5	42.8	45.0
	PCL/GNP-C-20	38.3	38.3	58.5	55.1	57.1	42.6

The experiment consists of two series of heating and cooling scans, however, the first heating scan is performed to erase the thermal history of the polymer. This phenomenon is quite evident in PCL since it presented similar crystallization temperatures (T_c) ($T_{c1} = 19.8$ °C and $T_{c2} = 19.4$ °C) but different melting temperatures (T_m) ($T_{m1} = 66.9$ °C and $T_{m2} = 54.2$ °C).

Regarding the filaments, PCL/GNP-M-2 and PCL/GNP-C-2 presented a T_{c2} of 36.3 °C. Thus, the incorporation of just 2 wt.% of @GNP into PCL matrix, lead to an increase of its T_c , indicating that the @GNP is behaving as crystallization nucleus, as proposed by Castilla-Cortázar *et al.* [167] for PCL/GO, and similarly observed by Manafi *et al.* [168] for PLA/GNP composites.

By loading PCL with 10, 15 and 20 wt.% of @GNP, T_{c2} still slightly increases. In detail, PCL/GNP-M-10, PCL/GNP-C-10, PCL/GNP-C-15 and PCL/GNP-C-20 exhibited a value of 37.6, 37.7, 38.6 and 38.7 °C, respectively. As PCL is loaded with @GNP, its T_m do not change significantly comparing with pristine PCL. Overall, PCL/GNP composites presented T_{m2} values around 55 °C.

The degree of crystallization (χ_c) was determined and is presented in Tables 6.2 and B.2. PCL filament exhibited a χ_{c2} of 47.0 %, which is in agreement with its semicrystalline structure [167]. @GNP incorporation into the polymer matrix seems to have no effect on crystallinity since χ_{c2} values varied only between 44.3 % (PCL/GNP-M-10) and 49.7 % (PCL/GNP-C-20). For PCL/GNP scaffolds, a similar trend was observed when compared to PCL/GNP filaments. By calculating the mean and standard deviation of all χ_{c2} values, filaments exhibited a value of 47.3 ± 1.6 % while the scaffolds displayed a value of 43.3 ± 3.3 %. Such similarity between mean values of χ_{c2} for PCL/GNP filaments and scaffolds shows that the printing process does not affect samples crystallographic properties.

Thermogravimetric analysis (TGA) was used to evaluate the thermal stability of GNP, GNP-ox, @GNP and iron nanoparticles as well as PCL, PCL/GNP filaments and scaffolds.

Thermograms (under a nitrogen atmosphere) for GNP, GNP-ox, @GNP and iron nanoparticles are shown in Figure 6.17. The data revealed three main weight loss steps at temperatures above 100 °C, mainly for GNP-ox and iron nanoparticles.

The first weight loss occurred between 100 and 225 °C. Thermal decomposition during this first step was quantified and is presented in Table 6.3. GNP-M-ox, GNP-C-ox and iron nanoparticles presented weight losses of 34.7, 32.8 and 17.0 %, respectively, which corresponds to the loss of oxygen-containing functional groups, namely carboxyl and epoxy [95]. @GNP powders exhibited no weight loss between 100 and 225 °C, which suggests fewer oxygen-containing groups are present following partial reduction and magnetization process.

The second weight loss occurred between 225 and 600 °C. In the case of GNP-M-ox and GNP-C-ox, the weight loss (15.5 and 16.7 %, respectively) corresponds to the partial combustion of carbon skeleton and more stable functionalities such as carbonyls [169]. According to Ebrahimezhad *et al.* [170], the iron nanoparticle substantial weight loss (36.5 %) mainly around 300 °C is attributed to the presence of carbonyls and hydroxyls.

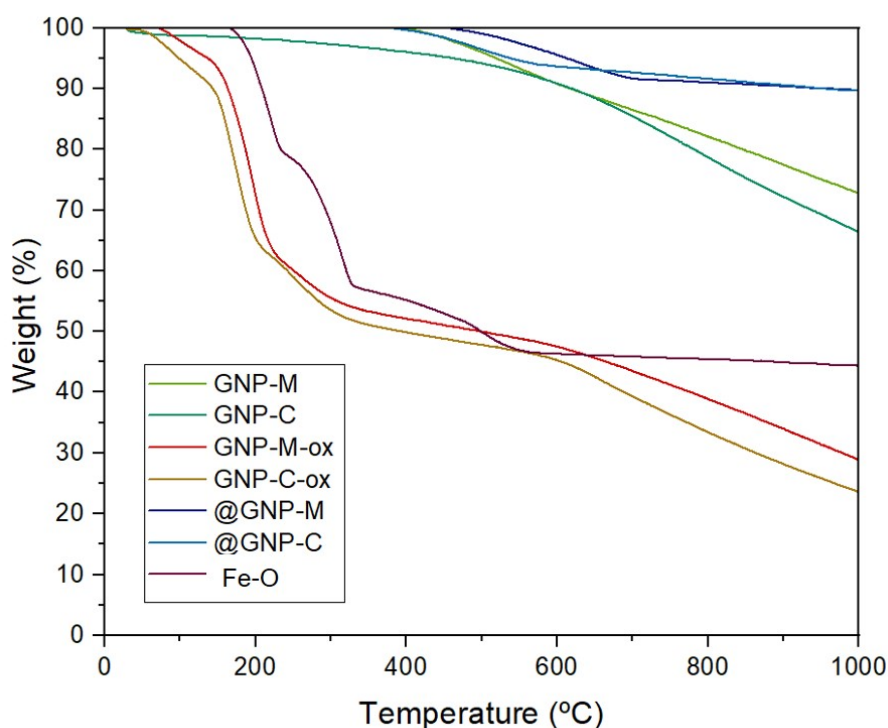


Figure 6.17: TGA curves for GNP-M, GNP-C, GNP-M-ox, GNP-C-ox, @GNP-C and @GNP-M powders and iron nanoparticles, under nitrogen atmosphere.

Table 6.3: Weight loss (%) values for GNP-M, GNP-C, GNP-M-ox, GNP-C-ox, @GNP-M, @GNP-C powders and iron nanoparticles according to three temperature intervals, under nitrogen atmosphere.

Sample	Weight loss (%) between		
	100 - 225 °C	225 - 600 °C	600 - 1000 °C
GNP-M	0	9.2	17.9
GNP-C	0.6	7.1	24.3
GNP-M-ox	34.7	15.5	18.5
GNP-C-ox	32.8	16.7	21.6
@GNP-M	0	4.4	5.8
@GNP-C	0	6.2	2.6
Fe-O	17.0	36.5	1.9

The third weight loss step happened between 600 and 1000 °C. Here, both GNP and GNP-ox have significant weight losses (17.9, 24.3 % for GNP-M and GNP-C; 18.5 and 21.6 % for GNP-M-ox and GNP-C-ox, respectively), which corresponds to the continuous combustion of the carbon skeleton, already initiated in the previous step for GNP-ox samples. After all oxygen-containing functional groups being lost in the previous two temperature steps, in this one iron nanoparticles presented a weight loss of just 1.9 %; while @GNP-M and @GNP-C presented values respectively of 5.8 and 2.6 %.

In summary, GNP-M and GNP-C presented total weight losses respectively of 27.1 and 32.2 %, while GNP-M-ox and GNP-C-ox exhibited total weight losses respectively of 68.9 and 71.2 %. Nevertheless, GNP weight loss is mainly due to carbon skeleton combustion, while GNP-ox is mainly due to the loss of oxygen-containing functional groups for both GNP grade materials. In comparison, @GNP-M and @GNP-C presented total weight losses respectively of 10.2 and 8.9 %.

To understand the previous result, it is worth mentioning that @GNP possesses more oxygen-containing functional groups than GNP. However, less than GNP-ox, so it was expected that its total percentage weight loss was an intermediate value between the GNP and GNP-ox. Nevertheless, @GNP-M and @GNP-C presented the lower total percentage weight loss, which is probably due to the presence of iron nanoparticles (total percentage weight loss of 55.4 %), since others [171, 172] reported the same behaviour.

Figure 6.18 shows the TGA curves obtained for PCL, PCL/GNP-M and PCL/GNP-C composites. Thermal degradation is similar for all samples: a single step degradation mainly between 250 and 400 °C is observed. Table 6.4 presents the initial decomposition (5% weight loss, $T_{5\%}$) and maximum degradation rate temperatures (T_d), as well as the weight measured at 545 °C and 1000 °C. Regarding the filaments, PCL presented a $T_{5\%}$ of 288.9 °C. In comparison, when @GNP is loaded, PCL $T_{5\%}$ increased to around 350 °C for all samples, except for PCL/GNP-C-2, whose value is around 330 °C.

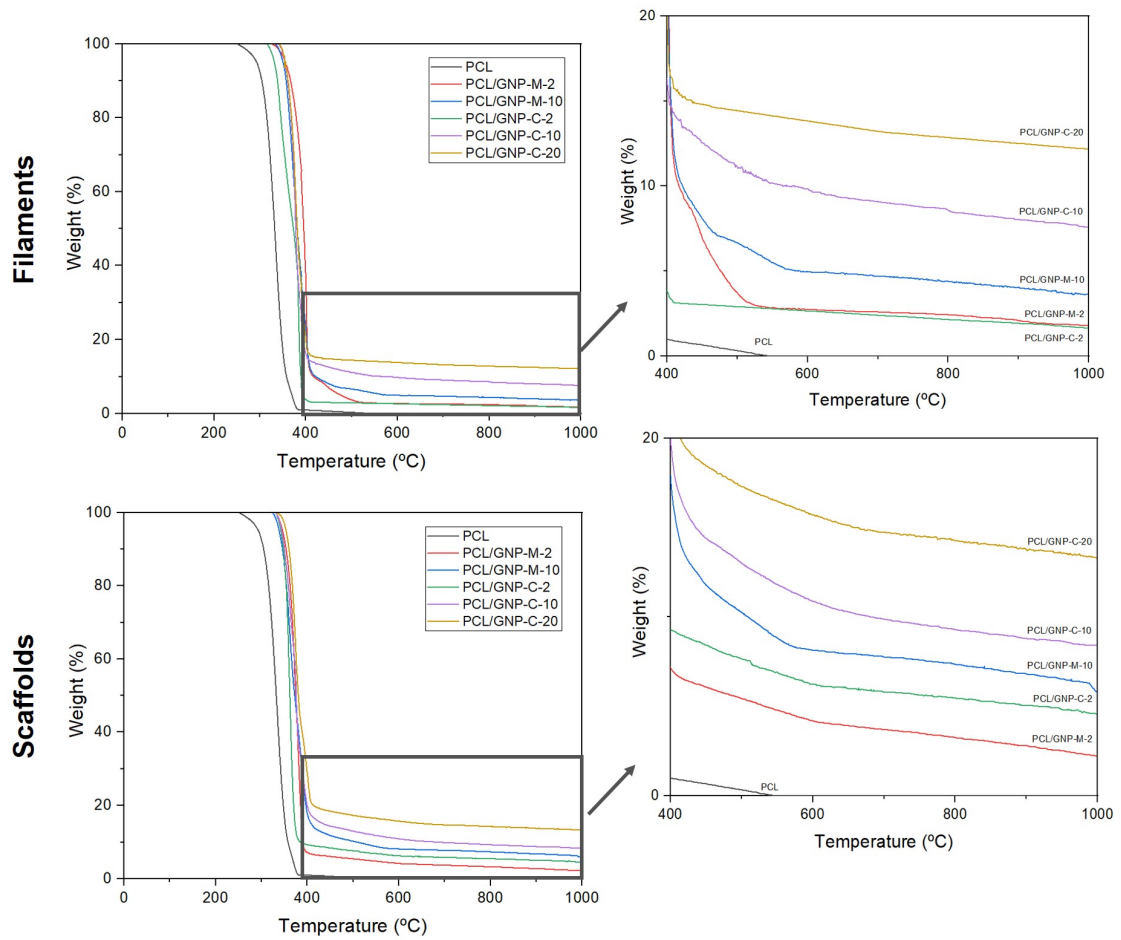


Figure 6.18: TGA curves for PCL, PCL/GNP-M and PCL/GNP-C scaffolds containing different filler contents, under nitrogen atmosphere.

Table 6.4: Thermogravimetric parameters of PCL, PCL/GNP-M and PCL/GNP-C filament and scaffolds, namely 5% degradation temperature, $T_{5\%}$, the temperature of maximum degradation rate, T_d , and measured weight at 545 °C and 1000 °C.

Type	Sample	$T_{5\%}$ (°C)	T_d (°C)	Weight (%) at	
				545 °C	1000 °C
Filaments	PCL	288.9	355.8	0	0
	PCL/GNP-M-2	352.3	396.0	2.8	1.8
	PCL/GNP-M-10	350.4	390.5	5.6	3.6
	PCL/GNP-C-2	329.4	349.9	2.7	1.6
	PCL/GNP-C-10	353.0	377.0	10.2	7.5
	PCL/GNP-C-20	353.9	378.5	14.1	12.1
Scaffolds	PCL	289.0	352.0	0	0
	PCL/GNP-M-2	344.2	372.5	4.8	2.0
	PCL/GNP-M-10	336.9	361.7	8.9	5.8
	PCL/GNP-C-2	340.8	361.2	6.9	4.5
	PCL/GNP-C-10	342.7	375.8	11.9	8.4
	PCL/GNP-C-20	352.0	372.9	16.5	13.3

The weight loss derivative (dTG) curves (Figure B.16) allow better differentiation between the results. For instance, PCL presented a T_d of 355.8 °C, while PCL/GNP-M-2 and PCL/GNP-M-10 presented 396.0 and 390.5 °C. By loading PCL with 2, 10 and 20 wt.% of @GNP-C, its T_d changed to 349.9, 377.0 and 378.5 °C, respectively. Thus, T_d increase with graphene loading, which possibly indicates that @GNP is acting as a thermal stabilizer [173]. For PCL/GNP scaffolds, a similar trend for both $T_{5\%}$ and T_d was observed.

PCL fully degraded around 545 °C. Therefore, the weight measured at 545 °C for PCL/GNP composites represents the actual amount of incorporated graphene. PCL/GNP-M-2 and PCL/GNP-C-2 filaments presented 2.8 and 2.7 %, while PCL/GNP-M-10, PCL/GNP-C-10 and PCL/GNP-C-20 presented 5.6, 10.2 and 14.1 %, respectively. A similar trend was observed for PCL/GNP scaffolds, except for PCL/GNP-M-2 and PCL/GNP-C-2, which presented 4.8 and 6.9 % of the initial samples, respectively. It is worth mentioning that from the moment where PCL fully degraded until the end of the experiment, samples continued its degradation although at a slower rate.

Isothermal curves, under nitrogen atmosphere, were performed to characterize the thermal stability of PCL, PCL/GNP-M and PCL/GNP-C filaments during eight hours at 90 and 130 °C (Figure 6.19). Thus, these curves serve as a simulation of how the materials behave during a day of printing. It is worth mentioning that 90 and 130 °C are the minima and maximum temperatures at which the materials were processed, respectively.

After 8 hours, PCL presented a weight loss of 6.8 and 8.5 % at 90 and 130 °C, respectively (Table 6.5). Taking into account the thermal stability demonstrated by the polymer at these temperatures in a short period in the previous TGA experiments (Figure 6.18), as well as the temperature values itself (around 100 °C), the small weight loss is probably due to the loss of water.

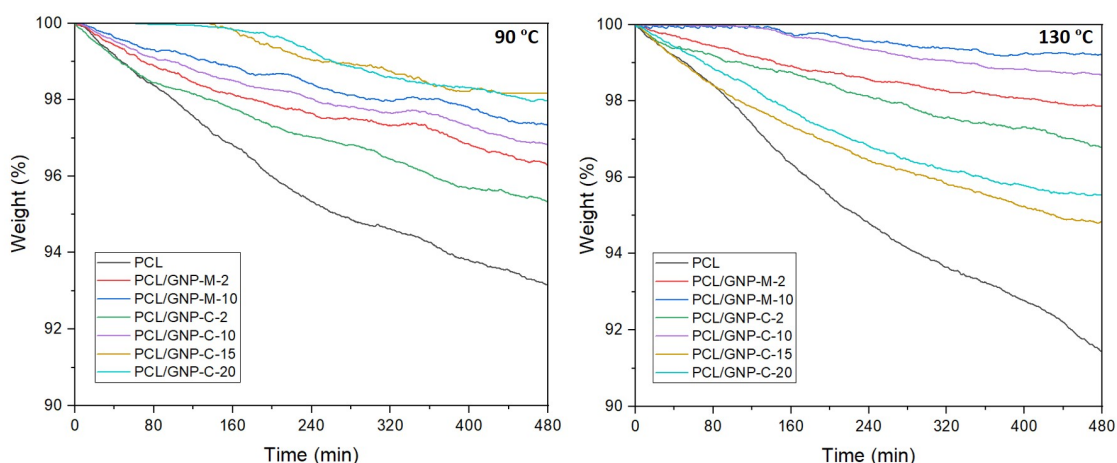


Figure 6.19: Isothermal curves for PCL, PCL/GNP-M and PCL/GNP-C filaments containing different filler contents at 90 and 130 °C, during 8 hours.

Table 6.5: Total weight loss (%) values at 90 and 130 °C for PCL, PCL/GNP-M and PCL/GNP-C filaments containing different filler contents, under nitrogen atmosphere.

Sample	Total weight loss (%) at	
	90 °C	130 °C
PCL	6.8	8.5
PCL/GNP-M-2	3.7	2.1
PCL/GNP-M-10	2.6	0.7
PCL/GNP-C-2	4.6	3.2
PCL/GNP-C-10	3.1	1.3
PCL/GNP-C-15	1.8	5.1
PCL/GNP-C-20	2.0	4.4

At 90 °C, PCL/GNP-M-2 and PCL/GNP-C-2 presented weight losses respectively of 3.7 and 4.6 %. In comparison, PCL/GNP-M-10 and PCL/GNP-C-10 exhibited weight losses respectively of 2.6 and 3.1 %, while PCL/GNP-C-15 and PCL/GNP-C-20 displayed weight losses around 2.0 %. Thus, at this temperature, the higher the @GNP loading, the lower the weight loss. However, at 130 °C, PLC/GNP-15 and PCL/GNP-20 presented higher weight losses than all other composites. Therefore, no conclusion can be taken about the relation between the loading of @GNP and samples weight loss.

6.4 Rheological properties

To infer about filaments viscous behaviour during the printing, their rheological properties were evaluated at 90, 130 and 180 °C (Figures 6.20 and 6.21). As previously referred, 90 and 130 °C are the minima and maximum printing temperatures, respectively. However, this experiment was also performed at an extreme temperature for PCL polymer, 180 °C.

PCL presented a loss factor (loss (G'') / storage (G') moduli) of 7.6 ± 0.6 , 18.0 ± 1.6 and 47.9 ± 4.3 at 90, 130 and 180 °C, respectively. Thus, the higher the temperature, the higher the loss factor. As PCL behaves like a viscoelastic liquid [174, 175], the presented values are mainly associated with category B of the image shown in Figure 6.20 which is in agreement with PCL being considered the gold standard polymer for 3D printing.

PCL/GNP-M-2, PCL/GNP-C-2 and PCL/GNP-C-10 presented a loss factor of 6.6 ± 0.1 , 7.0 ± 0.2 and 6.4 ± 0.4 for 90 °C. Although from a statistical point of view, the loss factor differences are already significant when compared to PCL, both materials should still be viewed as part of B category. However, a shift from category B to category C and so a hampering to the printing of the materials can be seen in PCL/GNP-M-10, PCL/GNP-C-15 and PCL/GNP-C-20 which presented a loss factor of 3.5 ± 0.1 , 4.0 ± 0.5 and 2.2 ± 0.3 , respectively.

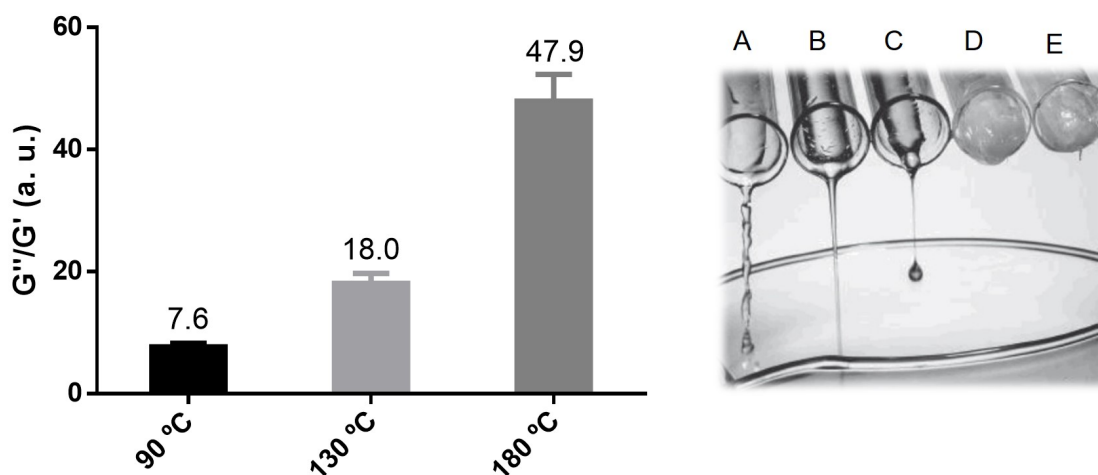


Figure 6.20: Loss factor (loss (G'') / storage (G') moduli) for PCL at 90, 130 and 180 °C. A) to E) represent several kinds of behaviour of water samples with increasing amounts of thickener. A) ideally viscous ($G'' \gg G'$), B) viscoelastic liquid ($G'' > G'$), C) sol/gel transition ($G'' = G'$), D) viscoelastic solid or gel-like ($G'' < G'$), and E) ideally elastic ($G'' \ll G'$).

By increasing the temperature from 90 to 130 °C, PCL/GNP-M-2 and PCL/GNP-C-2 loss factor slightly increased to 18.0 ± 1.6 and 18.4 ± 1.4 (still similar to PCL), while for PCL/GNP-M-10 and PCL/GNP-C-10 it raised to 9.1 ± 1.0 and 9.0 ± 0.6 , thus overtaking the viscosity problem with PCL/GNP-M-10. In comparison, PCL/GNP-C-15 and PCL/GNP-C-20 still presented a low loss factor, namely 2.8 ± 0.6 and 1.6 ± 0.4 , respectively. Loss factor values can be seen in detail in Table B.3.

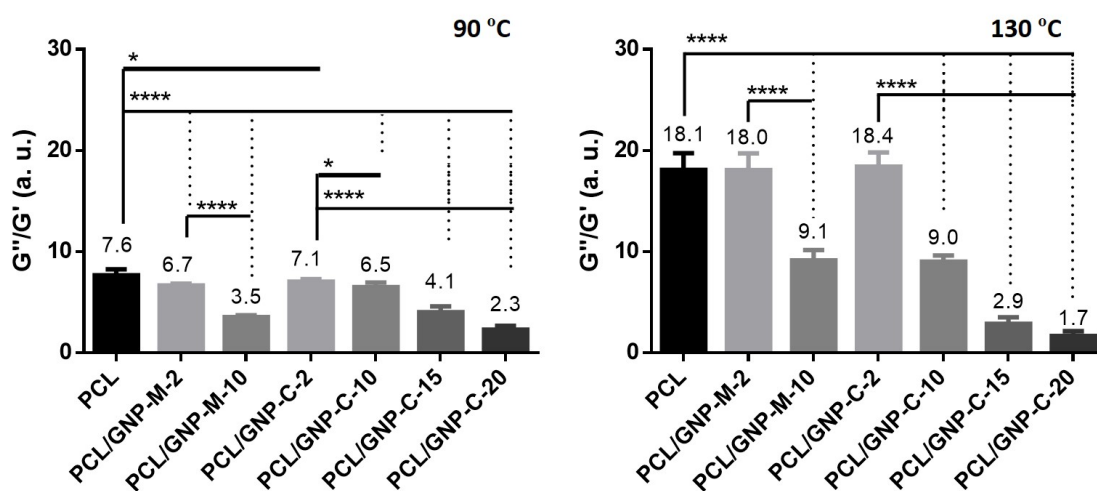


Figure 6.21: Loss factor (G''/G') for PCL, PCL/GNP-M and PCL/GNP-C filaments containing different filler contents at 90 and 130 °C.

6.5 Crystallographic and magnetic characterization

The crystallographic patterns and magnetic behaviour of GNP and GNP-ox for both GNP grade materials were evaluated through X-ray diffraction (XRD) (Figure 6.22) and Superconducting quantum interference device (SQUID) magnetometry (Figure 6.23).

GNP-M and GNP-C presented a sharp diffraction peak around $2\theta = 26.5^\circ$ corresponding to the reflection of graphite (002) [176]. In comparison, GNP-M-ox and GNP-C-ox displayed a peak around $2\theta = 10^\circ$ which corresponds to the typical reflection of GO (001). The presence of a peak corresponding to the (001) plane indicates the presence of oxygen-containing functional groups, thus confirming, the oxidation of GNP into GNP-ox [176].

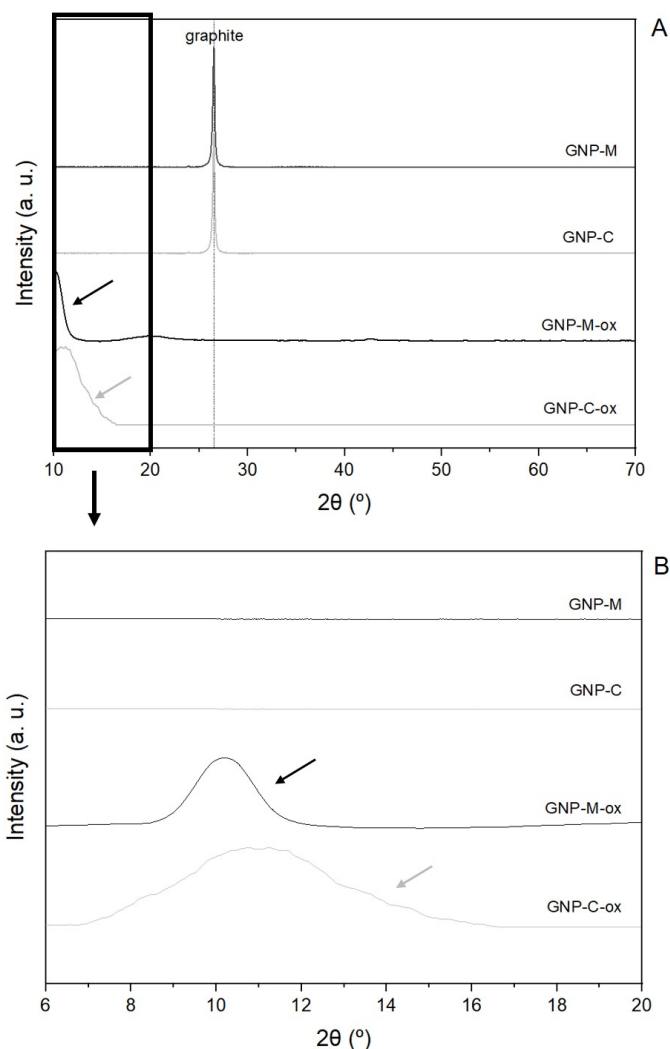


Figure 6.22: Crystallographic patterns of GNP-M, GNP-C, GNP-M-ox and GNP-C-ox through X-ray diffraction (XRD). B) represents a zoom-in of A) in the x-axis, from 6 to 20° . The arrows indicate the presence of oxygen-containing functional groups.

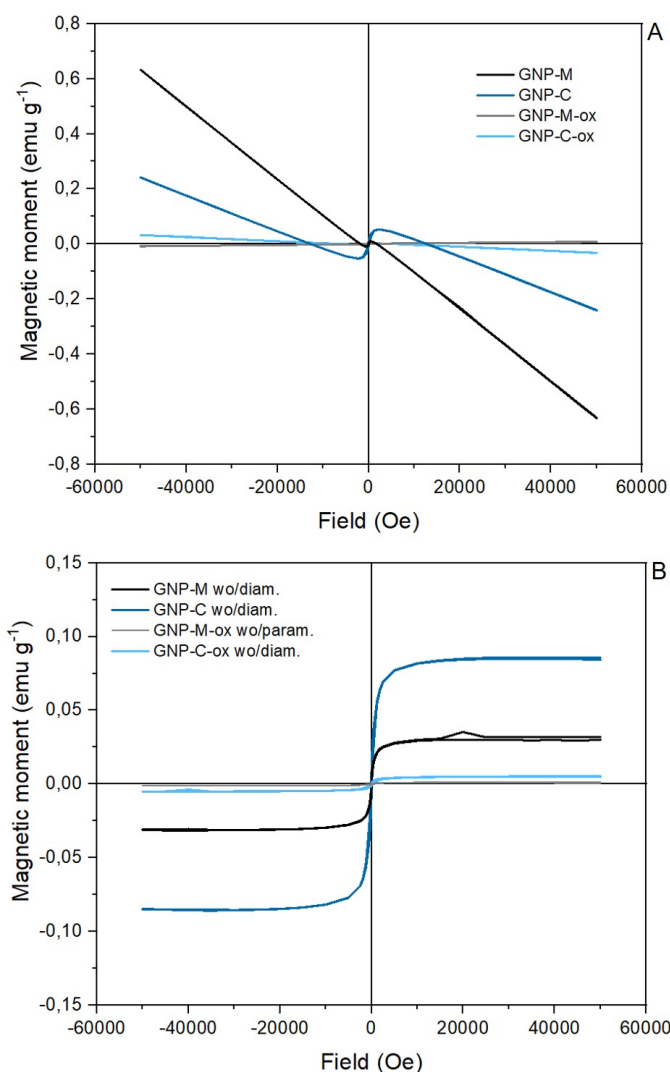


Figure 6.23: Magnetic-hysteresis (M-H) curves of GNP-M, GNP-C, GNP-M-ox and GNP-C-ox before and after subtraction of the diamagnetic and paramagnetic components, determined from superconducting quantum interference device (SQUID) magnetometry, at room temperature.

Regarding the magnetic behaviour of the samples, the isothermal magnetic measurements revealed that GNP and GNP-ox presented remanent magnetization in the order of 10^{-3} to 10^{-4} emu g⁻¹ for both GNP-M and GNP-C grade materials, which indicates a ferromagnetic state. Nonetheless, GNP-M, GNP-C and GNP-C-ox also presented a diamagnetic dependence, as can be determined from the negative slope of the linear component. In comparison, GNP-M-ox presented a paramagnetic behaviour denoted by the positive slope of the linear component. The remanent magnetization and coercivity of the samples are summarized in Table B.4.

@GNP-M and @GNP-C diffractograms are shown in Figure 6.24A. Neither @GNP-M, neither @GNP-C presented the peak around $2\theta = 10^\circ$. Thus, indicating the (partial) reduction of GNP-ox into @GNP, for both GNP grade materials, which is in agreement with FTIR (Figure

6.9) and EDS data (Table 6.1) Moreover, @GNP-C presented a diffraction peak around $2\theta = 26.6^\circ$ corresponding to the reflection of maghemite (Fe_2O_3) (211) [177]. Overall, the Miller indices indicated the characteristic reflection peaks related to the crystallographic structure of cubic spinel structures presenting an $Fd\bar{3}m$ symmetry, which is characteristic of iron oxides materials, namely magnetite (Fe_3O_4) and maghemite (Fe_2O_3) structures [178, 179],

Regarding the lattice parameters, @GNP-M presented $a = 8.382 \text{ \AA}$, while @GNP-C presented $a = 8.364 \text{ \AA}$, which are intermediate lattice parameters between Fe_3O_4 ($a = 8.396 \text{ \AA}$, JCPDS no. 19-0629) and Fe_2O_3 ($a = 8.346 \text{ \AA}$, JCPDS no. 39-1346). Thus, showing that the powders consist of a mixture between both oxides.

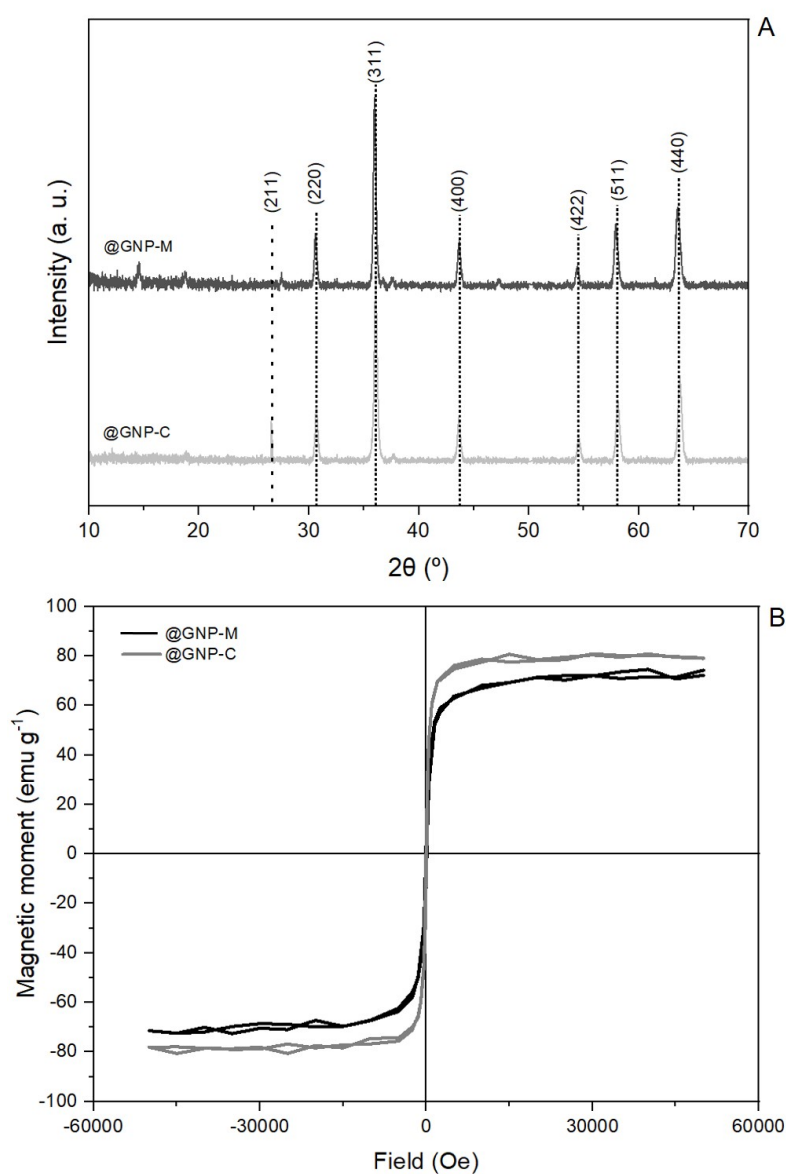


Figure 6.24: Crystallographic patterns (A) and M-H curves (B) of @GNP-M and @GNP-C, at room temperature.

The isothermal magnetic cycles were obtained for both samples and are presented in Figure 6.24B. The saturation magnetization (M_s) of @GNP-M, $M_s = 74 \text{ emu g}^{-1}$, is lower than that of @GNP-C, $M_s = 79 \text{ emu g}^{-1}$. According to the analysis of the lattice parameters of both magnetic samples, @GNP-M is composed of more (Fe_3O_4) phase than @GNP-C, and since this phase has a higher magnetic moment than (Fe_2O_3) phase, the magnetic moment of the @GNP-M should be larger. To better understand this disagreement, EDS and XPS data (Table 6.1 and Figure 6.13) should be highlighted. For instance, according to EDS data, @GNP-M and @GNP-C presented an at.% of 34.39 % and 36.99%. In comparison, according to XPS data, @GNP-M and @GNP-C presented a Fe 2p at.% of 4.37 and 22.74 %. Additionally, through the XPS high-resolution spectra, @GNP-M and @GNP-C presented a Fe 2p (II) at.% of 57.9 % and 54.2 %, respectively. Overall, @GNP-C presenting the higher M_s is explained not by @GNP-C being the material that presented the highest Fe_3O_4 phase, but rather, by being the material that presented the highest amount of Fe-O nanoparticles.

The temperature-dependent zero-field-cooled/field-cooled (ZFC/FC) measurement of @GNP-C was performed and is shown in Figure 6.25A. @GNP-C presented a ferromagnetic behaviour throughout the temperature range of 5 K to 370 K. Figure 6.25B depicts the magnetic-hysteresis (M-H) cycles of @GNP-C at the temperatures of 100, 200 and 300 K. @GNP-C presented a M_s at 100 K of 91 emu g^{-1} . In comparison, by increasing the temperature to 300 K, the M_s decreased to 81 emu g^{-1} . Therefore, the higher the temperature, the lower the M_s . Additionally, the coercive field also decreased with increasing temperature, from 124 Oe (100 K) to 54 Oe (300 K).

PCL crystallization pattern and M-H curve were assessed and are shown in Figure 6.26. PCL presented two strong diffraction peaks at $2\theta = 21.88^\circ$ and 24.21° corresponding to (110) and (200) lattice planes of the orthorhombic crystalline form [180]. These data corroborate the PCL's degree of crystallization obtained through DSC, which was around 40 % (Table 6.2).

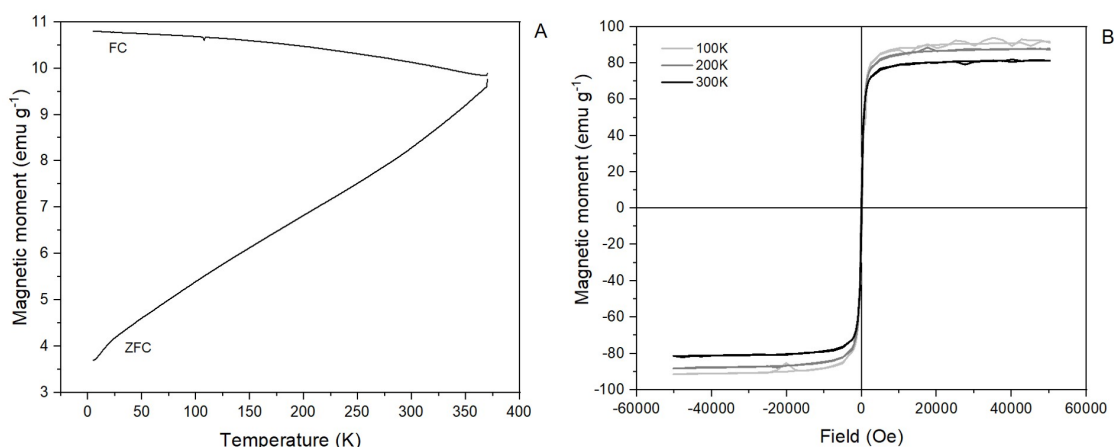


Figure 6.25: Magnetic behaviour of @GNP-C. A) Zero-field-cooled/field-cooled (ZFC/FC) measurement at a fixed magnetic field of $H=100 \text{ Oe}$; B) isothermal magnetic-hysteresis (M-H) measurement at 100, 200 and 300K

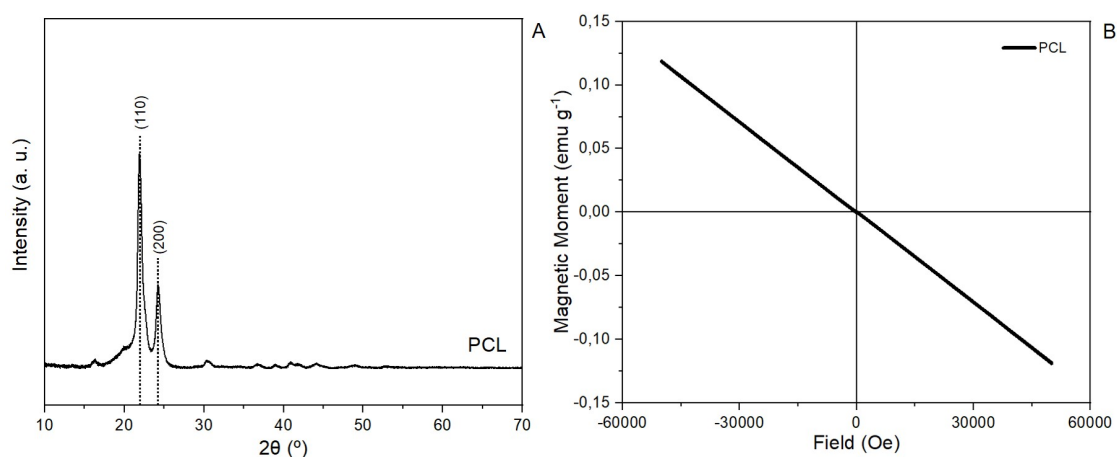


Figure 6.26: Crystallographic patterns (A) and M-H curves (B) for PCL, at room temperature.

Normalized diffractograms of PCL/GNP filaments based on @GNP-M (Figure 6.27A) and @GNP-C (Figure 6.27B) confirmed the presence of both iron oxide (Fe-O) and PCL on the filaments. The diffractograms were sorted from highest to lowest ratio of @GNP to PCL. A noticeable decrease in the intensity of the peaks of Fe-O material compared to the PCL peaks was observed, for both PCL/GNP-M and PCL/GNP-C composites. It is worth mentioning the presence of PCL/GNP-C-30 and PCL/GNP-C-40 filaments in these experiments as part of an initial optimization process aiming the comprehension of which materials could simultaneously present the best possible magnetization properties and be accurately printed.

PCL/GNP filaments M-H curves were assessed and are shown in Figure 6.27. Having @GNP-M and @GNP-C as references, which as previously stated, presented a M_s of 74 emu g^{-1} and 79 emu g^{-1} , the expected M_s for each composition was determined and the measured values are consistently smaller than the expected values (Table B.4).

PCL/GNP-C-2 presented a M_s of 1.4 emu g^{-1} , while PCL/GNP-C-10 presented a M_s of 4.6 emu g^{-1} . In comparison, its expected values were 1.6 emu g^{-1} and 7.9 emu g^{-1} , respectively.

For the other PCL/GNP composites a similar trend was observed, except for PCL/GNP-M-2 which presented a M_s of just 0.05 emu g^{-1} . Overall, the experimental values are about 70 % of the expected ones. It is worth mentioning that these results are more reliable for PCL/GNP-C filaments due to the higher number of samples comparing with PCL/GNP-M. Overall, the materials behave as soft magnetic materials due to their low coercivity [181].

Normalized diffractograms of PCL/GNP scaffolds based on @GNP-M (Figure B.18A) and @GNP-C (Figure B.18B) confirmed the presence of both iron oxide (Fe-O) and PCL. A reduction in the intensity of the peaks of Fe-O compared to the PCL peaks was noticeable, for both PCL/GNP-M and PCL/GNP-C scaffolds. It is worth mentioning that the same result was verified for PCL/GNP filaments, as detailed above.

Regarding the M-H curves, PCL/GNP-C-2 scaffolds presented a M_s of 1.4 emu g^{-1} . By loading the PCL with 10 and 20 wt.% of @GNP-C, its M_s increased to 4.6 and 10.6 emu g^{-1} , for 2, 10

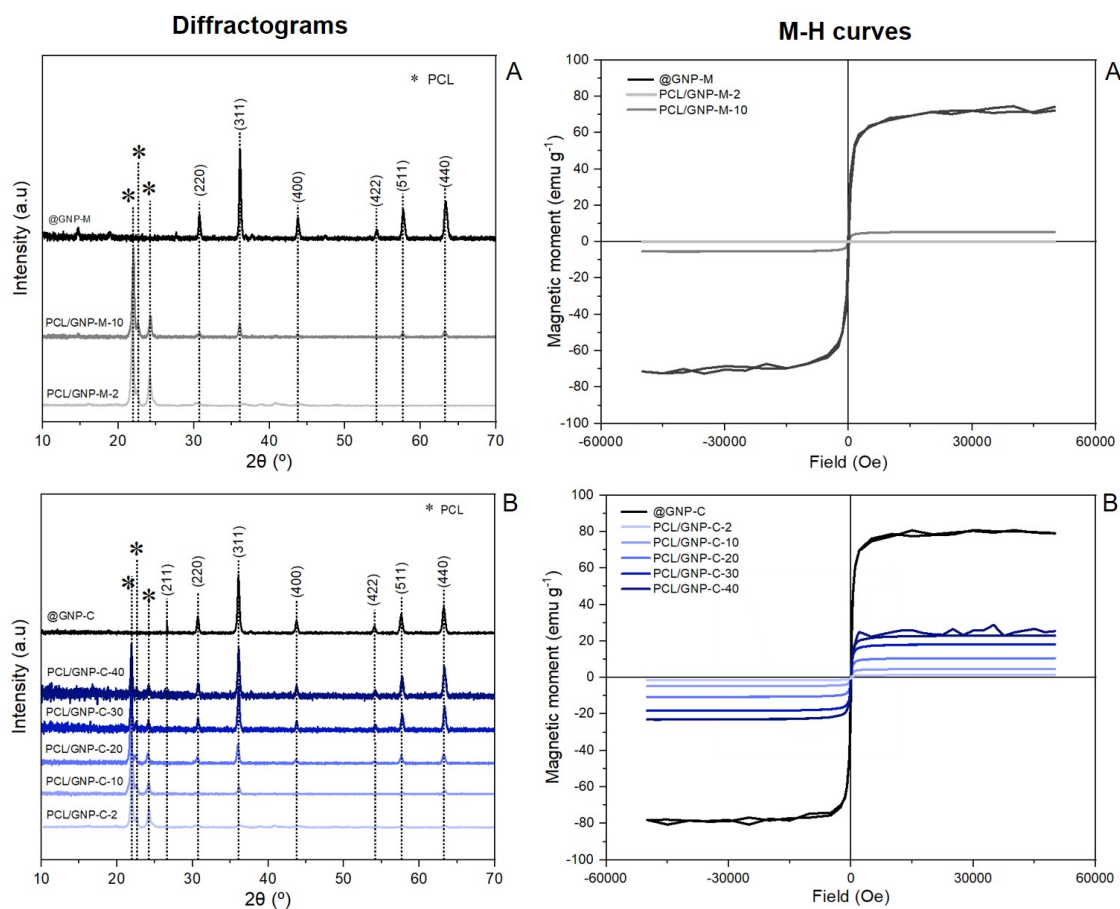


Figure 6.27: Crystallographic patterns and M-H curves of A) PCL/GNP-M and B) PCL/GNP-C filaments containing different filler contents through XRD and SQUID, respectively, at room temperature.

and 20 wt.%. In comparison, their expected values were 1.6, 7.9 and 15.8 $emu\ g^{-1}$, respectively. PCL/GNP-M-2 was the exception since shown no M_S , while PCL/GNP-M-10 presented a M_S of 5.4 $emu\ g^{-1}$. In comparison, its expected value was 7.4 $emu\ g^{-1}$.

In summary, these results indicate that the processing of PCL/GNP filaments into scaffolds does not affect the magnetization state of the composites.

6.6 Fibre diameter and morphology

The fabrication process was split into two steps, as previously stated in methods subsection 5.3.3. The first step consisted on assessment of the printing parameters that allowed deposition of straight fibres for PCL and PCL/GNP composites. Critical translational speed (CTS) was determined from the ratio between the real fibre diameter (F_D) and the relative peak to peak fibre diameter (F'_D) and was obtained whereas $F_D/F'_D = 1$, as illustrated in Figure 5.4.

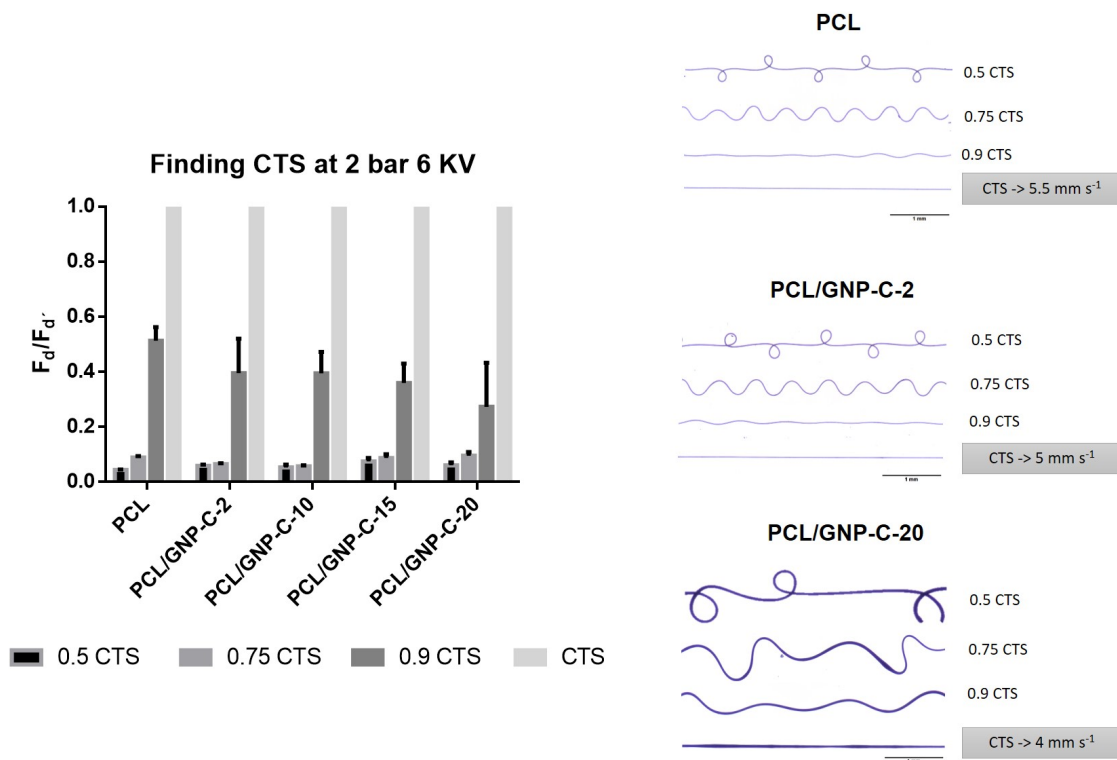


Figure 6.28: Critical translational speed (CTS) of PCL and PCL/GNP-C composites containing different filler contents. Graphical data represents the experimental ratio between the real fibre diameter (F_D) and the relative peak to peak fibre diameter (F'_D), while visual data represents the coiled, sinusoidal and straight shapes for 0.5 CTS, 0.75 CTS, 0.9 CTS and CTS for PCL, PCL/GNP-C-2 and PCL/GNP-C-20. Scale bars represent 1 mm.

Quantitative (F_D/F'_D) and qualitative (fibre morphology) data about CTS finding process for PCL and PCL/GNP-C composites containing different filler contents collected at increasing C_S are presented in Table B.5 and in Figure 6.28. PCL presented a F_D/F'_D ratio for 0.5 CTS, 0.75 CTS and 0.9 CTS of 0.04 ± 0.01 , 0.09 ± 0.01 and 0.51 ± 0.05 . In comparison, PCL/GNP-C-2 presented 0.06 ± 0.01 , 0.07 ± 0.01 and 0.40 ± 0.12 . All the other PCL/GNP-C composites displayed similar values to PCL and PCL/GNP-C-2. Although each material was printed at a combination of 2 bar and 6 KV, the used printing temperatures were different, as described in methods subsection 5.3.2. Thus, each material was obtained with a different CTS. For instance, PCL exhibited a CTS of 5.5 mm s^{-1} , while PCL/GNP-C-2 presented a CTS of 5 mm s^{-1} . In comparison, PCL/GNP-C-20 was obtained with a CTS of 4 mm s^{-1} .

Morphologically, 0.5 CTS presented a coiled shape, 0.75 CTS and 0.9 CTS displayed a sinusoidal one, while CTS presented a straight pattern. Repeatability of the process, mainly for PCL and PCL/GNP-C-2 composites, is demonstrated in Figure B.19. In comparison, PCL/GNP-C-20 presented more randomly distributed fibres, since the frequency of each coiling or sinusoidal cycle was not constant.

The second step evaluated the influence of feeding pressure (P), applied voltage (V) and collector speed (C_S) on F_D . A summary of the results is shown in Figure 6.29.

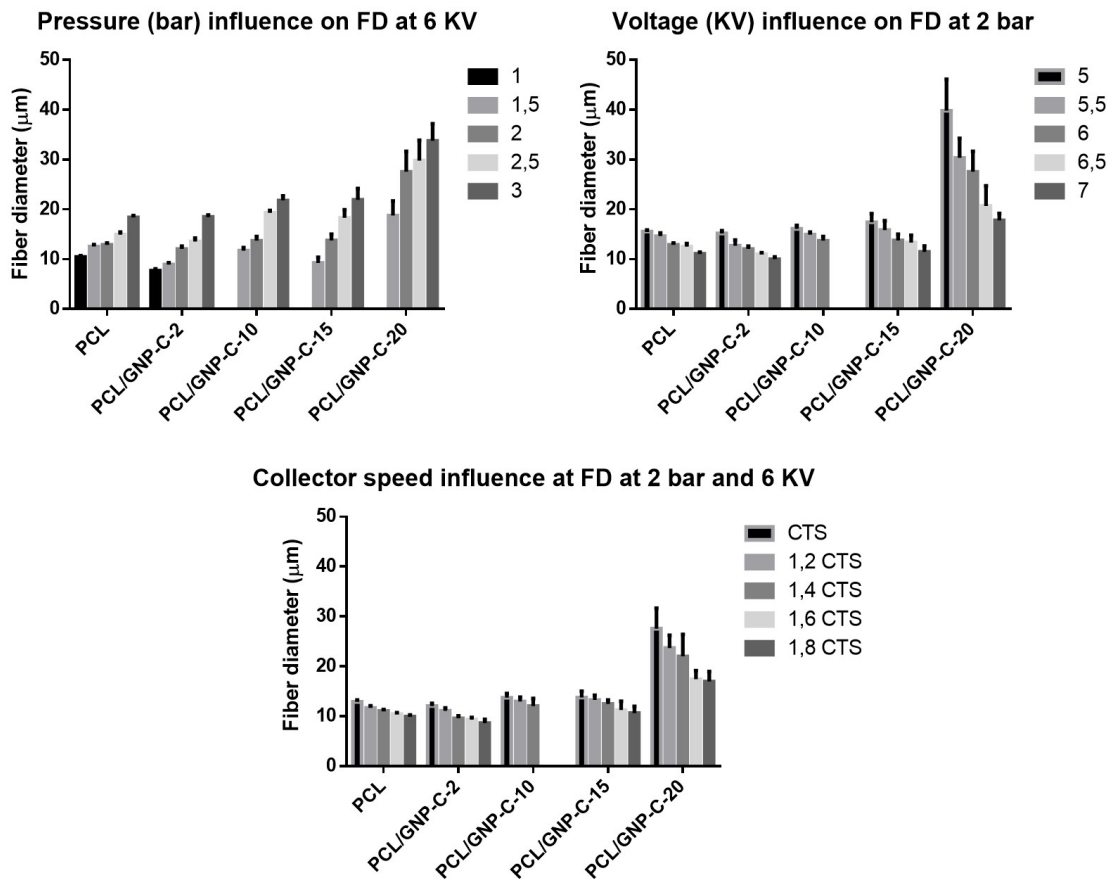


Figure 6.29: Influence of feeding pressure (P), applied voltage (V) and collector speed (C_S) on fibre diameter (F_D) for PCL and PCL/GNP-C composites containing different filler contents.

Concerning the influence of P (Table B.6), PCL presented a F_D of 10.47 ± 0.26 , 12.57 ± 0.36 μm for 1 and 1.5 bar, respectively. By increasing the P to 2, 2.5 and 3 bar, PCL F_D changed to 12.88 ± 0.40 , 14.92 ± 0.51 and 18.41 ± 0.38 μm , respectively. Thus, the higher the P, the higher the F_D . For PCL/GNP composites, similar values were observed. PCL/GNP-C-2 presented a minimum and maximum F_D of 7.72 ± 0.36 and 18.53 ± 0.31 μm , while PCL/GNP-C-10 presented 11.73 ± 0.62 and 21.82 ± 0.91 μm . In comparison, by loading PCL with 20 wt.% of @GNP, its minimum and maximum F_D drastically increased to 18.76 ± 2.94 and 33.77 ± 3.40 μm , respectively. It is worth mentioning that every experiment was performed at 6 kV.

Regarding the influence of voltage (Table B.7), PCL presented a F_D for 5 and 5.5 kV of 15.58 ± 0.25 and 14.64 ± 0.63 μm . By increasing the V to 6, 6.5 and 7 kV, PCL F_D changed to 12.88 ± 0.39 , 12.53 ± 0.62 and 11.09 ± 0.32 μm . Thus, the higher the applied voltage, the lower the F_D . The same tendency was verified for the PCL/GNP composites. For instance, PCL/GNP-C-2 presented a maximum and a minimum F_D of 15.20 ± 0.50 and 10.02 ± 0.46 μm , while PCL/GNP-C-10

presented 16.08 ± 0.69 and 13.72 ± 0.84 μm . In comparison, by loading PCL with 20 wt.% of @GNP, its maximum and minimum F_D drastically increased to 39.86 ± 6.31 and 17.83 ± 1.35 μm , respectively. It is worth mentioning that every experiment was performed at a 2 bar. So far, except for PCL/GNP-C-20, all materials can be printed with F_D between 10 and 20 μm .

Concerning the influence of C_S (Table B.8), PCL presented a F_D for CTS and 1.2 CTS of 12.88 ± 0.39 , 11.68 ± 0.41 μm . By increasing the C_S to 1.4 CTS, 1.6 CTS and 1.8 CTS, PCL F_D changed to 11.05 ± 0.30 , 10.44 ± 0.28 and 9.93 ± 0.35 μm . Thus, the higher the C_S , the lower the F_D . For PCL/GNP composites, analogous values were observed. It is worth mentioning that PCL/GNP-C-20, at $C_S = 1.6$ and 1.8 CTS can already be printed with F_D lower than 20 μm .

The C_S variation induced changes not only on F_D (Figure 6.29) but also on extrusion jet appearance (Figure 6.30).

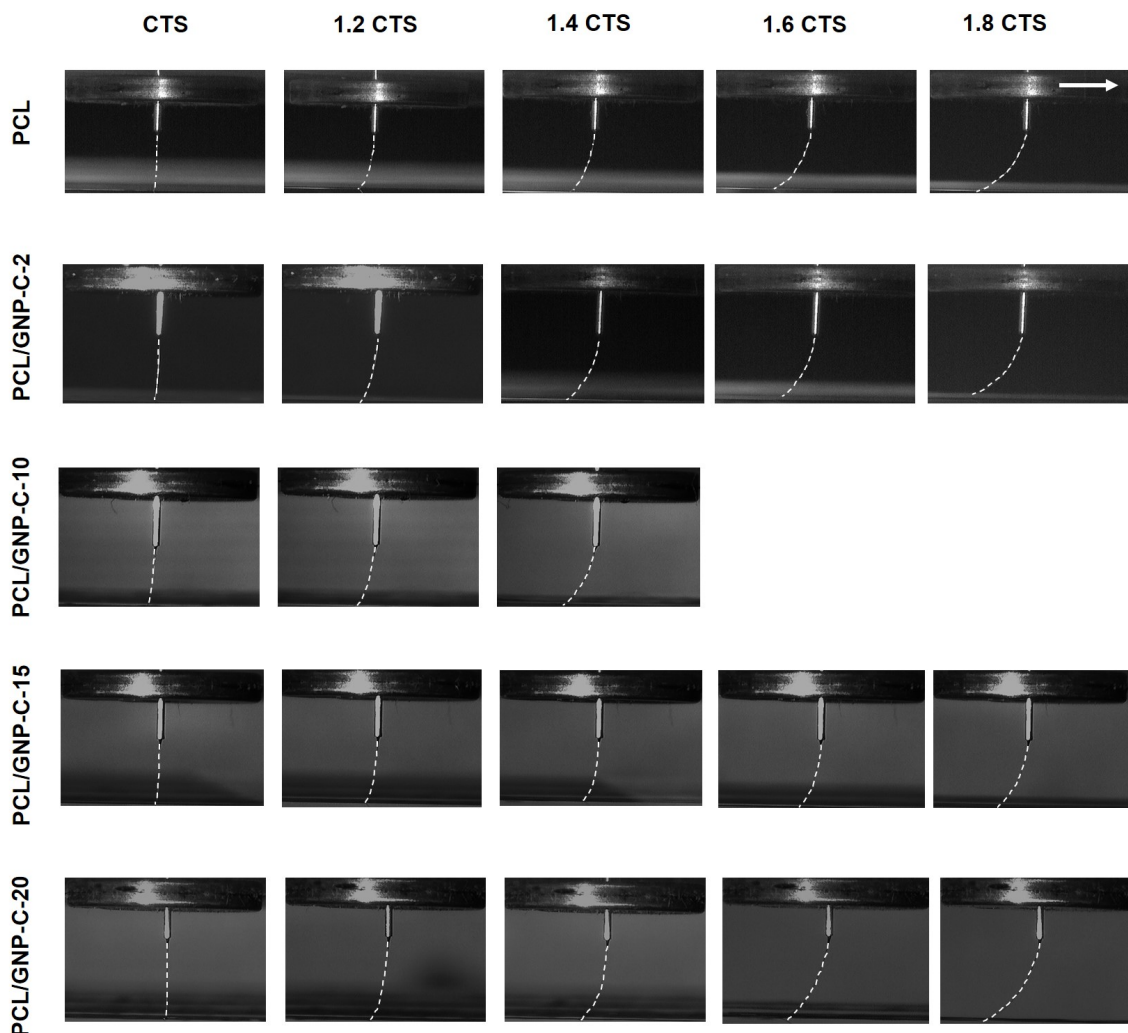


Figure 6.30: PCL and PCL/GNP-C composites containing different filler contents extrusion jet for 2 bar and 6 KV at several C_S , namely CTS, 1.2 CTS, 1.4 CTS, 1.6 CTS and 1.8 CTS. The white arrow indicates the movement direction.

Independently of the material, CTS images presented a straight extrusion jet, as expected since CTS is defined as the C_S that matches the speed of the electrified jet [134]. By increasing the C_S , the match is undone, and the jet starts to show jet-lag, *i.e.*, as the C_S starts to be much higher than the material extrusion speed, the jet-lag appears. Overall, the higher the C_S , the higher the jet-lag.

6.7 Preliminary study on scaffolds printability

Herein, it is demonstrated the non-optimized printing of PCL and PCL/GNP-C hexagonal microstructured scaffolds containing different filler contents (Figure 6.31).

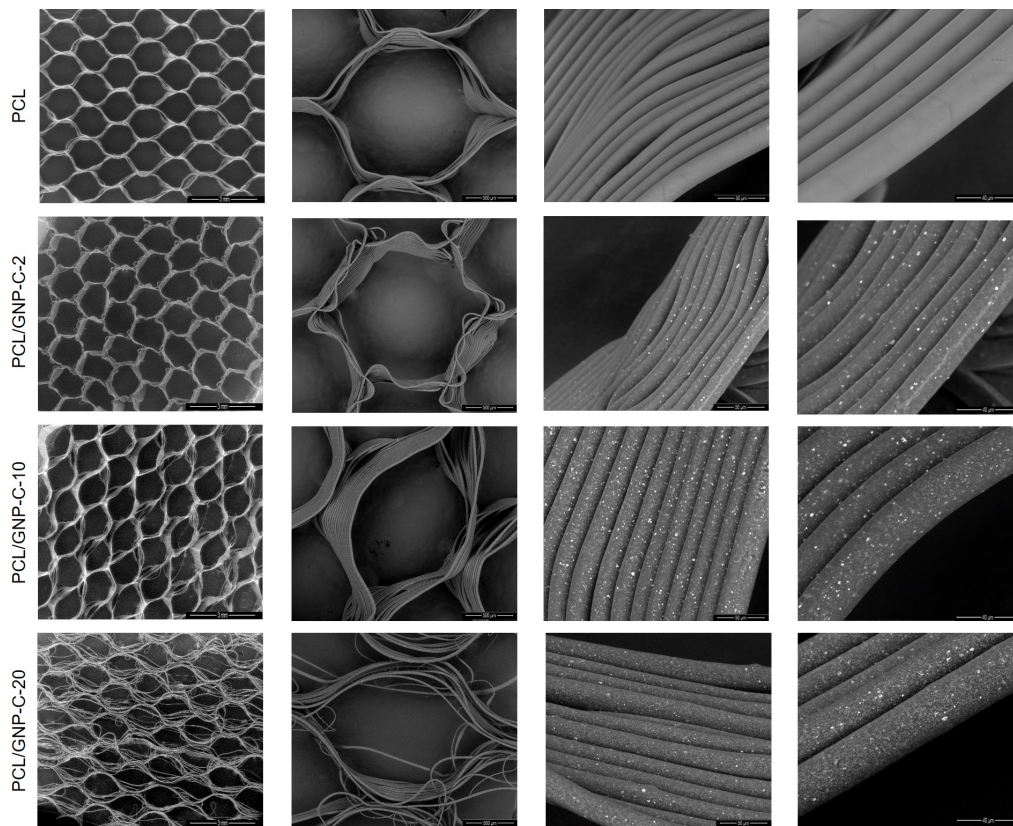


Figure 6.31: SEM images of PCL and PCL/GNP-C hexagonal microstructured scaffolds containing different filler contents, composed of multiple stacked microfibrils. From left to right, scale bars represent 3 mm, 500 μm , 50 μm and 40 μm .

Ideally, upon single F_d and morphology assessment, PCL and PCL/GNP scaffolds with linear (square) and non-linear (hexagon and re-entrant) patterns would be printed. However, during the present work, a complete study on such printing process was not possible. Therefore, this section appears as a preliminary study to show that the printing of PCL and PCL/GNP composites containing different filler contents is possible and that by loading PCL with @GNP-C, its printability is hampered.

Chapter 7

Discussion

The primary goal of the present work was to develop polycaprolactone/graphene-based materials (PCL/GBM) scaffolds via melt electrowriting (MEW) for tissue engineering (TE). For this purpose, specific objectives were defined: 1. to prepare magnetic GBM (@GBM) powders, namely graphene nanoplatelets (GNP) of grades M and C, via *in situ* precipitation; 2. to produce PCL/GNP composites filaments for both GNP grade materials by melt-blending; 3. to assess the morphological, chemical, thermal, rheological, crystallographic and magnetic properties of GNP powders and PCL/GNP composites; 4. to optimize PCL/GNP composites printability, and 5. to develop and characterize PCL/GNP scaffolds with linear and non-linear architectures.

Oxidized GNP (GNP-ox) is commonly obtained from pristine GNP by exfoliation methods, such as the modified Hummers method used here and in our group previous works [158]. The exfoliation process results in the introduction of several oxygen functionalities and consequent loss of structural, thermal, and electrical properties. To restore some of the properties of pristine GNP, over the years different reduction methods have been explored to produce reduced GNP (r-GNP), including chemical, thermal, and electrochemical reduction pathways [67].

Single-step *in situ* formation of magnetic nanoparticles on reduced graphene sheets has been previously described by Xue *et al.* [182] using a solution of iron chloride ($\text{FeCl}_2 \cdot 4 \text{H}_2\text{O}$) and oxidized graphene sheets (pH = 9, T = 180 °C, t = 10 hours). Overall, it was reported the efficient oxidation of Fe^{2+} into Fe_3O_4 nanoparticles and its deposition onto thermally reduced graphene sheets. Following this protocol, in this research, a solution of $\text{FeCl}_2 \cdot 4 \text{H}_2\text{O}$ and GNP-ox was used to produce magnetic and partially reduced GNP (@GNP), for both GNP grade materials.

Upon @GNP production, GNP powders morphology, particle size and stability was assessed. Transmission electron microscopy (TEM) revealed the oxidation of the powders through the loss of GNP planar form and sharp edges. Instead, both GNP-M-ox and GNP-C-ox presented wrinkled appearance and folded edges. This distortion is most probably due to the attachment of oxygen-containing functional groups to the basal plane of GNP sheets during oxidation. Additionally, it may occur due to platelets short dimensions allowing the oxygen-containing functional groups at the edges to form hydrogen bonds. Such a change in morphology has been reported by others [64, 158]. Iron nanoparticles incorporation and distribution across GNP surface was

confirmed by TEM and scanning electron microscopy (SEM). Both imaging techniques revealed that iron nanoparticles are better distributed and more exposed at the surface of @GNP-C. This is possibly explained by GNP-M higher number of graphene single layers and higher lateral dimensions, which seemed to affect iron nanoparticles morphology and drive them preferentially between graphene layers instead of being exposed at the surface, as in @GNP-C.

The particle size distribution in volume and number revealed that GNP-M grade materials presented a similar average particle size. For GNP-C grade materials, a similar trend was observed. In detail, GNP-M, GNP-M-ox and @GNP-M were obtained with an average particle size around 5 and 2 μm in volume and number, respectively. In comparison, GNP-C, GNP-C-ox and @GNP-C presented an average particle size < 2 and < 1 μm , in volume and number, respectively. The difference between the particle size distribution in volume and number is mainly due to the existence of agglomerates, which will take a relatively high volume of the sample. Concerning the iron nanoparticles, while Xue *et al.* [182] obtained spherical particles with sizes between 4 to 10 nm, in this work, the particles were obtained with an average size around 45 nm. The used proportion of GNP-ox/ $\text{FeCl}_2 \cdot 4\text{H}_2\text{O}$ (1:20) may explain such difference, since Xue *et al.* only used 1:10.

The reduction of oxygen-containing functional groups at the surface of oxidized GBM usually leads to the formation of unstable colloidal dispersions in aqueous solutions. Thus, limiting their potential for biomedical applications and requiring further chemical functionalization toward improving water solubility [67]. Nevertheless, in this work, both GNP-M and GNP-C grade materials exhibited comparable colloidal stability in aqueous dispersions, according to zeta (ζ)-potential measurements. The lower values were obtained to @GNP-M and @GNP-C, which presented a surface charge around -20 mV.

Upon GNP powders morphology, particle size and stability assessment, @GNP were incorporated in PCL by melt-blending at 90 °C (minimum printing temperature) under a rotor speed of 250 rpm for 3 minutes. Such mixing conditions have been reported by Potschke *et al.* [80] as the ideal ones to obtain PCL/multiwalled carbon nanotubes (PCL/MWCNT) composites nearly free of agglomerates.

To further determine @GNP particles or particle agglomerates average size as well as @GNP distribution in the polymeric matrix, PCL/GNP filaments cross-sections were performed and assessed via SEM. It is worth mentioning that cross-sections were made by cutting with a sharp blade which slightly compressed the filaments and affected @GNP orientation according to the cutting direction. Another procedure to obtain cross-sections is by using liquid nitrogen. Nevertheless, as the filament fracture occurs, the filler is released from the polymeric matrix, therefore making its use unfeasible.

Overall, in PCL/GNP-M filaments, @GNP-M presented an average size of 2.24 μm . In comparison, in PCL/GNP-C filaments, @GNP-C displayed an average size of 1.34 μm . These data is in agreement with @GNP-M and @GNP-C average size determined from TEM and DLS (Figure 6.5), since, according to these techniques, the average size of @GNP-M and @GNP-C was around 2 μm and 1 μm , respectively. Therefore, @GNP-M was more easily identifiable than @GNP-C in the polymeric matrix, due to presenting higher lateral dimensions and subsequently higher degree

of agglomeration.

Altogether, @GNP seemed well dispersed through the polymeric matrix. Nevertheless, more work would be necessary to confirm this. It is worth mentioning that the dispersion of @GNP in the polymeric matrix for both filaments and scaffolds was unsuccessfully assessed using TEM. Three approaches were performed. In each approach, PCL/GNP filaments and scaffolds were impregnated and embedded in Epon resin. In the first approach, samples were incubated at 65 °C for two days to promote resin polymerization, while in the second the incubation was performed at 37 °C for three days. In comparison, in the third approach, samples were incubated at room temperature for seven days. However, in any approach, due to the low hardness of the materials, the resin was not successfully impregnated. Therefore, PCL dissolved, and samples structure was lost.

Upon PCL/GNP filaments production and morphological evaluation, materials chemical, thermal, rheological, crystallographic and magnetic properties were assessed.

The introduction of oxygen functionalities on GNP-M-ox and GNP-C-ox, as well as its partial reduction into @GNP-M and @GNP-C, were confirmed by Fourier transform infrared spectroscopy (FTIR) and Energy dispersive x-ray spectroscopy (EDS). In comparison with GNP-ox, @GNP exhibited lower oxygen content given that oxygen-containing functionalities, such as carboxyl groups, were partially removed during the partial reduction and magnetization single-step process. It is worth mentioning that although not revealed in GNP-ox FTIR spectra, an additional band in the wavenumber range of 3000 and 3600 cm^{-1} , corresponding to O-H stretching vibrations, most probably related to adsorbed water molecules and hydroxyl groups, was expected as reported by Costa-Almeida *et al.* [183] and Al-Gaashani *et al.* [184] for graphene oxide (GO) instead of GNP-ox.

FTIR spectroscopy revealed two absorption bands at 535 cm^{-1} and 615 cm^{-1} for both @GNP-M and @GNP-C. However, the bands were not referred in the results chapter due to uncertainty about their functional group association. Nevertheless, Bertolucci *et al.* [185] and Mohammed *et al.* [186] hypothesized the band around 535 cm^{-1} corresponds to magnetite while the one around 615 cm^{-1} corresponds to maghemite. Therefore, suggesting that the magnetic powders could consist of a mixture between magnetite and maghemite. X-ray photoelectron spectroscopy (XPS) high-resolution spectra complements this data since @GNP-M and @GNP-C presented a Fe (II) 2p at.% of 57.8 and 54.1; and a Fe (III) 2p at.% of 42.2 and 45.9, respectively.

According to FTIR and XPS data, PCL and PCL/GNP filaments presented similar results. In opposition, EDS data revealed an increase in both O and Fe at.% with increasing @GNP loadings. FTIR and XPS techniques, having an analysis depth around a few nm, were performed to evaluate PCL and PCL/GNP composites surface. In comparison, EDS technique, presenting an analysis depth around a few μm , was performed to evaluate the samples as a whole. Therefore, the absence of surface changes from PCL to PCL/GNP filaments was expected since @GNP is not exposed at the surface of PCL/GNP composites but homogeneously distributed within its polymeric matrix (Figure 6.8). Considering such similarity between PCL and PCL/GNP filaments, overall, no significant changes were obtained in water contact angle experiments.

To further determine materials crystallization (T_C) and melting (T_m) temperatures, as well as degree of crystallization (χ_c), differential scanning calorimetry (DSC) analysis were performed.

As described above, by loading @GNP into PCL, PCL T_C increased around 94 %, indicating that PCL crystallization takes place earlier. Overall, @GNP is behaving as a crystallization nucleus as proposed by Castilla-Cortázar *et al.* [167] for PCL/GO, and similarly observed by Manafi *et al.* [168] for PLA/GNP composites. In comparison, PCL T_m remained unaffected for both filaments and scaffolds. Herein, we demonstrated that samples χ_c was not significantly influenced by the presence of @GNP since the obtained values varied between 39.1 and 49.7 % for both PCL/GNP filaments and scaffolds. In comparison, PCL presented a χ_c around 43 %. Several studies have shown different trends for PCL χ_c variation with the incorporation of GBM. For instance, Castilla-Cortázar *et al.* [167] revealed that by loading PCL with 0.5 wt.% of GO, its (χ_c) increased by 1.1 %. In another work, Duan *et al.* [187] outlined that by loading PCL with 1.0 wt.% of GO, its (χ_c) increased by 26 %.

Thermal stability of GNP powders were assessed through thermogravimetric analysis (TGA). GNP powders exhibited three main weight loss steps at temperatures above 100 °C, namely between 100-225, 225-600 and 600-1000 °C. The first weight loss concerned the loss of labile oxygen functionalities such as carboxyl groups. In contrast, the second weight loss regarded the partial combustion of carbon skeleton and more stable oxygen functionalities such as carbonyl groups. The third weight loss referred to continuous combustion of carbon skeleton.

GNP-M and GNP-C presented a total weight loss of 27.1 and 32.2 %, respectively, being that most of it was observed in the third step (17.9 and 24.3 %, respectively). In comparison, GNP-M-ox and GNP-C-ox lose a total of 68.9 and 71.2 %, respectively, being that most of it was observed in the first (34.7 and 32.8 %, respectively) and second (15.5 and 16.6 %, respectively) steps, thus demonstrating successful oxidation of GNP-M and GNP-C. Costa-Almeida *et al.* [183] outlined a similar result for GO. In detail, two main weight loss steps at temperatures above 100 °C were observed, namely between 145-225 and 225-630 °C, being the weight loss of 43.5 and 15.1 %, respectively.

In comparison, @GNP-M and @GNP-C presented a total weight loss of 10.2 and 8.9 %, respectively, being that most of it was observed in the third step (5.8 and 2.6 %, respectively), thus demonstrating successful partial reduction of GNP-M-ox and GNP-C-ox. Chang *et al.* [188] reported a similar result for rGO, which presented a total weight loss around 20 % being that most of it was observed above 500 °C. Notwithstanding, @GNP is not only partially reduced but also magnetic. Therefore, the 10 % weight loss difference between our work and Chang's is probably explained due to the presence of iron nanoparticles, which seemed to act as a thermal stabilizer since @GNP grade materials nearly did not degrade. Such behaviour has been reported by others. Fan *et al.* [171] outlined that by adding Fe_3O_4 to 2D-carbon flakes (2D-CF) in a proportion of 1:10 (2D-CF: Fe_3O_4), 2D-CF total weight loss decreased around 15 %. In another work, Xiu *et al.* [172] developed multiwalled carbon nanotubes (MWCNT) decorated with iron nanoparticles synthesized by co-precipitation by the use of $\text{FeCl}_2 \cdot 4 \text{H}_2\text{O}$ and $\text{FeCl}_3 \cdot 6 \text{H}_2\text{O}$ in a molar ration of 1:2, being MWCNT total weight loss decreased around 16.7 % with iron nanoparticles incorporation.

To further determine materials initial decomposition (5% weight loss, $T_{5\%}$) and maximum degradation rate temperatures (T_d), as well as the actual amount of @GNP in PCL/GNP composites, TGA analyses were performed for PCL/GNP filaments and scaffolds.

Regarding the filaments, by loading @GNP into PCL, PCL $T_{5\%}$ increased around 14-21 % for all samples. In comparison, PCL T_d increased around 10 % for PCL/GNP-M, and 4 % for PCL/GNP-C composites. Similar values were observed to PCL/GNP scaffolds for both GNP grade materials. Thus, suggesting that @GNP is behaving as a thermal stabilizer since PCL 5% weight loss and maximum degradation rate took place at higher temperatures. Such behaviour has been reported by others. Liang *et al.* [173] outlined that by adding 0.5 wt.% of GNP into polypropylene, its $T_{5\%}$ increased around 5 %, which was mainly attributed to the mass transport barrier effect of GNP two-dimensional layered structure. Nevertheless, the authors pointed out two additional factors to explain the filler behaviour, namely the dispersion status of GNP in the matrix as well as its lateral dimensions. For instance, when the dispersion of GNP is uniform, the formed path is tortuous, and the thermal properties are increased. In comparison, when GNP is heterogeneously dispersed in the matrix, the formed path is simple, and the thermal properties are weakened. On the other hand, the higher the samples lateral dimensions, the higher the tortuosity of the path, the higher the decompositions temperatures, the higher the thermal stability.

The actual amount of @GNP in PCL/GNP composites is the weight measured after PCL full decomposition, which took place around 545 °C (Table 6.4). By taking into account all samples, PCL/GNP composites were obtained with 75 % of the expected @GNP incorporated quantities. Such a result represents the average of the relative deviations between the amount of obtained and expected @GNP.

To further simulate the thermal behaviour of PCL and PCL/GNP composites during melt electrowriting (MEW), isothermal curves, under nitrogen atmosphere, were performed at 90 and 130 °C for 8 hours. At 90 °C, PCL presented a total weight loss of 6.85 %. In comparison, at 130 °C, the total weight loss was 8.57 %. Considering the thermal stability demonstrated by the polymer at these temperatures (Figure 6.18), as well as the temperature values itself (around 100 °C), the small weight loss is probably explained due to loss of water molecules. For PCL/GNP composites, similar values were observed. Overall, it can be concluded that after 8 hours, at 90 or 130 °C, the samples did not thermally degrade.

To infer about PCL and PCL/GNP filaments viscous behaviour during MEW printing, their rheological properties were assessed. Overall, PCL presented typical loss factor (loss (G'') / storage (G') moduli) values of a viscoelastic liquid [174, 175], which is in agreement with PCL being considered the gold standard polymer for 3D printing. At 90 °C, PCL/GNP-M-2, PCL/GNP-C-2 and PCL/GNP-C-10 presented similar values to PCL. In opposition, by loading PCL with 10 wt.% of @GNP-M and 15-20 wt.% of @GNP-C, PCL loss factor decreased around 50 to 70 %, thus indicating a possible hampering to the printing of these materials. At 130 °C, PCL/GNP-M-2, PCL/GNP-C-2, PCL/GNP-M-10 and PCL/GNP-C-10 presented similar values to PCL, thus overcoming the possible printability problem on PCL/GNP-M-10. Nevertheless, by loading 15 and 20 wt.% of @GNP-C, PCL loss factor still significantly decreased (\approx 88 %). Although this experi-

ment cannot guarantee the accurate or non-accurate printing of PCL/GNP composites, it gives an idea about the possible hampering to its printability.

The crystallographic patterns and magnetic behaviour of GNP powders, PCL/GNP filaments and scaffolds for both GNP-M and GNP-C grade materials, were assessed through X-ray diffraction (XRD) and Superconducting quantum interference device (SQUID) magnetometry.

The introduction of oxygen functionalities on the surface of GNP-M-ox and GNP-C-ox was confirmed by the presence of a peak around $2\theta = 10^\circ$, which corresponds to GO (001) typical reflection plane [176].

To the best of our knowledge, the intrinsic magnetism of graphene-based materials (GBM) has remained divergent and controversial due to the absence of reliable experimental results. Herein we demonstrated the presence of diamagnetic and ferromagnetic contributions in GNP-M, GNP-C and GNP-C-ox. In comparison, GNP-M-ox displayed paramagnetic and ferromagnetic contributions. Several studies have shown comparable results. For instance, Shukla *et al.* [189] reported the presence of ferromagnetism and diamagnetism in GO. On the other hand, Lang *et al.* [190] outlined an oxidation degree independent paramagnetic behaviour in GO.

The partial reduction of GNP-ox into @GNP was observed since the peak around $2\theta = 10^\circ$ did not appear in @GNP-M and @GNP-C. Overall, the miller indices indicated the characteristic reflection peaks related to the crystallographic structure of cubic spinel structures presenting an Fd_3m symmetry, which is characteristic of iron oxides materials, namely magnetite (Fe_3O_4) and maghemite (Fe_2O_3) structures. Such a set of reflection peaks has been reported by others [191, 192]. Nonetheless, an additional diffraction peak around $2\theta = 26.6^\circ$, corresponding to the reflection of Fe_2O_3 (211) was detected in @GNP-C [177].

@GNP-M ($a = 8.382 \text{ \AA}$) and @GNP-C ($a = 8.364 \text{ \AA}$) presented intermediate lattice parameters between Fe_3O_4 ($a = 8.396 \text{ \AA}$, JCPDS no. 19-0629) and Fe_2O_3 ($a = 8.346 \text{ \AA}$, JCPDS no. 39-1346). Thus confirming not only that the powders consist of a mixture between Fe_3O_4 and Fe_2O_3 , but also that @GNP-C present more Fe_2O_3 phase than @GNP-M. It is worth mentioning that Fe_3O_4 has a higher magnetic moment than Fe_2O_3 , so it was expected that @GNP-M presented a higher magnetic saturation (M_s) than @GNP-C. Notwithstanding, @GNP-M presented $M_s = 74 \text{ emu g}^{-1}$, while @GNP-C presented $M_s = 79 \text{ emu g}^{-1}$. As previously stated, @GNP-C presenting the higher M_s is probably explained not by @GNP-C being the material that presented the highest Fe_3O_4 phase, but rather, by being the material that presented the highest amount of Fe-O nanoparticles. To further support this conclusion, according to EDS data (Table 6.1, @GNP-M and @GNP-C presented an at.% of 34.39 and 36.99, while according to XPS data (Table 6.1, @GNP-M and @GNP-C presented a Fe 2p at.% of 4.37 and 22.74.

According to the temperature-dependent zero-field-cooled/field-cooled (ZFC/FC) experiment, @GNP-C revealed a ferromagnetic behaviour throughout the temperature range of 5 K to 370 K. Additionally, @GNP-C M_s increased with the decrease of temperature. It is worth mentioning that during the MEW process, the materials are submitted to temperatures from 90 to 120 °C as described in subsection 5.3.2, so it should be enhanced that the M_s variation with the temperature, is reversible, as reported by Abenojar *et al.* [193].

PCL orthorhombic crystalline form was confirmed by the presence of two diffraction peaks around $2\theta = 21.88^\circ$ and 24.21° corresponding to (110) and (200) lattice planes [180]. Thus, corroborating PCL degree of crystallization obtained through DSC, which was around 40 % (Table 6.2). Normalized diffractograms of PCL/GNP filaments revealed the presence of both Fe-O and PCL. A noticeable decrease in the intensity of the peaks of Fe-O material compared to the PCL peaks was observed, for both PCL/GNP-M and PCL/GNP-C composites. Having @GNP-M and @GNP-C as references, PCL/GNP filaments presented M_S values about 70 % of the expected ones. This result is in agreement with TGA since the actual amount of incorporated @GNP in the PCL/GNP composites was around 75 %. A similar trend was observed for PCL/GNP scaffolds. Thus, indicating that MEW process does not affect the magnetization state of the composites. In summary, the materials presented a typical behaviour of soft magnets.

So far, these results, namely @GNP-C presenting lower average size, and higher M_S than @GNP-M, enabled the selection of PCL/GNP-C instead of PCL/GNP-M composites for further printing evaluation via MEW.

It is worth mentioning that printing temperatures were set at 90°C for PCL and PCL/GNP-C-2, at 105°C for PCL/GNP-C-10 and PCL/GNP-C-15 and 120°C for PCL/GNP-C-20, and kept constant through the printing process, being its selection process related to previous rheological evaluation. For instance, according to those experiments (Figures 6.20 and 6.21, Table B.3), PCL/GNP-C-2 presented a similar behaviour to PCL at 90°C and subsequently was printed at the same temperature.

As previously referred, thermal analysis, under nitrogen atmosphere, revealed no significant weight loss for PCL and PCL/GNP composites after 8 hours at 90°C and 130°C . Nevertheless, as materials are printed under air atmosphere, to fully simulate the thermal behaviour of PCL and PCL/GNP composites during the printing process, this experiment could have been performed in an air atmosphere rather than a nitrogen one. For instance, Zue *et al.* [194] outlined the production of GO and assessed its thermal stability in air and nitrogen atmospheres. Overall, the authors reported that under air atmosphere, GO fully degraded, while under nitrogen atmosphere, GO presented a total weight loss of 60 %. Although Zue's work was not performed to evaluate materials long term stability, it showed that materials degradation was more evident under air atmosphere rather than nitrogen.

In this research, it was outlined that the higher the applied temperature, the lower the M_S . Therefore, there could be a magnetic concern on submitting the materials to long time printings at temperatures between 90°C and 120°C . Nevertheless, through the zero-field-cooled/field-cooled (ZFC/FC) measurement of @GNP-C, it is shown the M_S reversibility throughout the temperature range of 5 K to 370 K.

Herein, it was demonstrated PCL and PCL/GNP composites printability over a broad range of printing conditions with fibres diameters (F_D) around $20\ \mu\text{m}$, except for PCL/GNP-C-20, which was slightly higher (F_D around $30\ \mu\text{m}$). Regarding the literature, similar F_D for PCL fibres have been reported by others. For instance, Zaiss *et al.* [195] reported PCL scaffolds fabrication for bone TE with F_D around $15\ \mu\text{m}$, being the printing conditions: $T = 80^\circ\text{C}$, $P = 2\ \text{bar}$, $V = 20\ \text{KV}$.

In another work, Castilho *et al.* [135] outlined the fabrication of PCL hexagonal microstructured scaffolds with F_D around 20 μm , being the printing conditions: $T = 90\text{ }^\circ\text{C}$, $P = 1\text{ bar}$, $V = 3.5\text{ KV}$. Nevertheless, since to the best of our knowledge, no work has been published on PCL/GBM composites development via MEW [196], no comparison can be made about the non-influence of GBM incorporation on F_D . Additionally, although as a preliminary study, it was demonstrated the non-optimized printing of PCL and PCL/GNP-C hexagonal microstructured scaffolds, appearing that the higher the @GNP wt.%, the higher the degree of printing hampering.

In summary, these results demonstrated, for the first time, the compatibility of PCL/GNP composites with advanced fabrication technologies such as MEW through the printing of complex 3D microarchitectures.

Chapter 8

Conclusions and Future work

8.1 Conclusions

The present work focused on developing PCL/GBM scaffolds via MEW for TE. For this purpose, specific objectives were defined: 1. to prepare magnetic GBM (@GBM) powders, namely graphene nanoplatelets (GNP) of grades M and C, via *in situ* precipitation; 2. to produce PCL/GNP composites filaments for both GNP grades by melt-blending; 3. to assess the morphological, chemical, thermal, rheological, crystallographic and magnetic properties of GNP powders and PCL/GNP composites; 4. to optimize PCL/GNP composites printability, and 5. to develop and characterize PCL/GNP scaffolds with linear and non-linear architectures. Herein, the impact of chemical modifications on GNP properties, as well as the combination of PCL with different GNP fillers and wt.% were extensively characterized using multiple complementary techniques.

To achieve the proposed goals, oxidized GNP (GNP-ox) was obtained from pristine GNP by the modified Hummers method. This chemical modification step resulted in the introduction of several oxygen functionalities on GNP basal plane and edges, as demonstrated by a 6- to 7-fold decrease of C/O ratio in GNP-M-ox and GNP-C-ox, respectively. Hence, GNP-ox presented a wrinkled appearance and folded edges instead of the typical planar form and sharp edges of GNP. Afterwards, @GNP were obtained from GNP-ox via *in situ* precipitation for both GNP grade materials. Overall, iron nanoparticles were better distributed and more exposed at the surface of @GNP-C.

GNP-M, GNP-M-ox and @GNP-M were obtained with an average size of $\approx 2 \mu\text{m}$. In comparison, GNP-C, GNP-C-ox and @GNP-C presented an average size of $\approx 1 \mu\text{m}$. Iron nanoparticles displayed an average size of 45 nm. These results demonstrated that chemical modification (either oxidation or magnetization) did not influence particle dimensions. Zeta potential measurements revealed the colloidal stability of GNP, GNP-ox and @GNP for both GNP grade materials when using water as a solvent, being the obtained values $< -20 \text{ mV}$.

Afterwards, PCL/GNP composites filaments were obtained by melt-blending and its cross-sections observed via scanning electron microscopy (SEM). Overall, @GNP was well dispersed throughout the polymeric matrix. @GNP-M and @GNP-C particles or particle agglomerates were

identified with an average size of 2.24 and 1.34 μm , respectively. As @GNP were not exposed at the surface of PCL/GNP composites, but homogeneously distributed within its polymeric matrix, surface analysis techniques such as Fourier transform infrared spectroscopy, and X-ray photoelectron spectroscopy revealed no differences between PCL and PCL/GNP composites. In contrast, energy-dispersive X-ray spectroscopy, which is an in-depth analysis technique, revealed an increase in Fe at.% with increasing @GNP loadings. These results support the need of using multiple complementary techniques when assessing the properties of polymeric composites, such as PCL/GNP, which is often limited and simplistic in the literature.

The obtained PCL/GNP composites exhibited a 94 % increase in crystallization temperature, reaching 38.7 $^{\circ}\text{C}$, indicating that @GNP is behaving as a crystallization nucleus. In comparison, its melting temperature (≈ 55 $^{\circ}\text{C}$) and degree of crystallization (≈ 43 %) remained unaffected. Regarding PCL/GNP composites maximum degradation rate temperature (T_d), PCL T_d increased around 10 and 4 % with the incorporation of @GNP-M and @GNP-C, respectively. Therefore, indicating that @GNP is behaving as a thermal stabilizer. Concerning PCL/GNP composites loss factor, PCL presented typical values of a viscoelastic liquid. Nevertheless, with 15 and 20 wt.% loading of @GNP, PCL loss factor decreased around 50 - 80 %, therefore indicating a possible hampering to the printing of these materials.

Regarding samples crystallographic patterns assessment, miller indices of @GNP-M and @GNP-C indicated the characteristic reflection peaks of iron oxides materials, namely magnetite (Fe_3O_4) and maghemite (Fe_2O_3) structures. @GNP-M and @GNP-C presented intermediate lattice parameters between Fe_3O_4 and Fe_2O_3 , thus confirming that the powders consisted of a mixture between both structures. Normalized diffractograms of PCL/GNP composites revealed the presence of both Fe-O and PCL, being that the higher the @GNP wt.%, the higher the intensity of the peaks of Fe-O material compared to PCL.

Concerning magnetic behaviour evaluation, @GNP-C (79 emu g^{-1}) presented a higher magnetic saturation (M_S) than @GNP-M (74 emu g^{-1}). @GNP-C revealed ferromagnetic behaviour throughout the temperature range of 5 to 370 K. Additionally, the higher temperature, the lower the samples magnetic moment. Having @GNP-M and @GNP-C as references, PCL/GNP composites presented M_S values around 70 % of the expected ones. Overall, materials presented a soft magnet typical behaviour.

These results, namely @GNP-C presenting lower average size, and higher M_S than @GNP-M, enabled the selection of PCL/GNP-C instead of PCL/GNP-M composites for further printing studies. Therefore, PCL/GNP-C composites printability was investigated using MEW technique. Several key parameters were optimized, such as feeding pressure, applied voltage and collector speed.

Overall, fibres were obtained with a diameter of 20 μm for a broad range of printing conditions. By tuning distinct printing parameters, fibre diameter could be finely controlled, independently of chemical modification of GNP fillers. Notwithstanding, given PCL/GNP-C-20 higher viscosity, its printability was only accurate under highly specific printing conditions. Finally, we were able

to demonstrate a preliminary study on the printing of hexagonal microstructured scaffolds in non-optimized conditions for both PCL and PCL/GNP composites.

In summary, these results demonstrated, for the first time, that PCL/GNP composite filaments can be used as building units in combination with advanced fabrication technologies. The feasibility of printing graphene-PCL composites obtained from GNP with different grades and chemical modifications was proved by printing complex 3D microarchitectures using MEW. The obtained 3D structures can be further optimized and explored for applications in tissue engineering and regenerative medicine.

8.2 Ongoing and Future work

Following the promising results obtained for PCL/GNP composites printability, the study of PCL/GNP scaffolds stackability (1, 5, 15, 25 and 50 layers) with two pore sizes (0.3 and 0.6 mm) in linear (square) and non-linear (hexagon and re-entrant) patterns have already been initiated at University Medical Centre of Utrecht, in Professor Miguel Castilho's Lab. So far, printings on PCL and PCL/GNP-C-2 with 1, 5 and 15 layers for both pore sizes and shapes have been performed. Nevertheless, the work is still being optimized and is not included in this thesis.

Another initial key topic of this research was the achievement of four-dimensional (4D) printing due to the transference of @GNP magnetic properties to the composite scaffolds. During this research, materials magnetic properties were assessed and successfully evaluated. So far, PCL/GNP scaffolds are clearly attracted and deformed by the existence of a magnetic field. Nevertheless, the scaffolds are not able to fully achieve its original shape after magnetic field removal. Therefore, the work is still being optimized and is not included in this thesis.

Other future work includes the achievement of the primary long-term goal of the thesis, *i.e.*, the concept of TE, namely tissue regeneration (TR). So far, few experiments were performed with immortalized myoblast cells (C2C12), mainly with PCL scaffolds, to evaluate its attachment, proliferation and differentiation. Notwithstanding, procedure optimization is still necessary to assess and evaluate PCL/GNP composites performance.

Regarding future outcomes of the present work, a review article on "Stimuli-responsive polymeric carbon nanocomposites soft networks" is currently being written. Additionally, a scientific paper submission for Proceedings of the National Academy of Sciences of the United States of America (PNAS) Journal is being prepared by the whole team.

Funding acknowledgements

This work was financed by FEDER funds through the COMPETE 2020 - Operacional Programme for Competitiveness and Internationalisation (POCI), Portugal 2020, and by national funds (PID-DAC) through FCT/MCTES in the framework of the project POCI-01-0145-FEDER-031143, and Base Funding - UIDB/00511/2020 of the Laboratory for Process Engineering, Environment, Biotechnology and Energy – LEPABE.

Moreover, Miguel Castilho acknowledges funding from the Horizon 2020 research and innovation program under the Grant Agreement No. 874827 (Brav3) and from the Gravitation Program "Materials Driven Regeneration", funded by the Netherlands Organization for Scientific Research (024.003.013).

To conclude, the authors would like to thank to Ana Rita Malheiro and Rui Fernandes from the Histology and Electron Microscopy Service (HEMS) of i3S, Porto, for the assistance with TEM studies; to Daniela Silva from Centro de Materiais da Universidade do Porto (CEMUP) for her support with SEM analyses and XPS spectra.

Bibliography

- [1] T. G. Weiser, S. E. Regenbogen, K. D. Thompson, A. B. Haynes, S. R. Lipsitz, W. R. Berry, and A. A. Gawande, “An estimation of the global volume of surgery: a modelling strategy based on available data,” *The Lancet*, vol. 372, no. 9633, pp. 139–144, 2008.
- [2] A. Gleadall, D. Visscher, J. Yang, D. Thomas, and J. Segal, “Review of additive manufactured tissue engineering scaffolds: relationship between geometry and performance,” *Burns & trauma*, vol. 6, no. 1, p. 19, 2018.
- [3] J. M. Karp, P. D. Dalton, and M. S. Shoichet, “Scaffolds for tissue engineering,” *MRS bulletin*, vol. 28, no. 4, pp. 301–306, 2003.
- [4] F. J. O’Brien, “Biomaterials & scaffolds for tissue engineering,” *Materials today*, vol. 14, no. 3, pp. 88–95, 2011.
- [5] R. G. Bai, K. Muthoosamy, S. Manickam, and A. Hilal-Alnaqbi, “Graphene-based 3d scaffolds in tissue engineering: fabrication, applications, and future scope in liver tissue engineering,” *International journal of nanomedicine*, vol. 14, p. 5753, 2019.
- [6] Y. S. Kim, M. M. Smoak, A. J. Melchiorri, and A. G. Mikos, “An overview of the tissue engineering market in the united states from 2011 to 2018,” *Tissue Engineering Part A*, vol. 25, no. 1-2, pp. 1–8, 2019.
- [7] T. Boráň, M. Menezes-Ferreira, I. Reischl, P. Celis, N. Ferry, B. Gaensbacher, H. Krafft, M. Lipucci di Paola, D. Sladowski, and P. Salmikangas, “Clinical development and commercialization of advanced therapy medicinal products in the european union: how are the product pipeline and regulatory framework evolving?,” *Human Gene Therapy Clinical Development*, vol. 28, no. 3, pp. 126–135, 2017.
- [8] R. D. Abbott and D. L. Kaplan, “Engineering biomaterials for enhanced tissue regeneration,” *Current Stem Cell Reports*, vol. 2, pp. 140–146, Jun 2016.
- [9] C. P. Bergmann and A. Stumpf, *Biomaterials*, pp. 9–13. Berlin, Heidelberg: Springer Berlin Heidelberg, 2013.
- [10] F. G. Lyons, A. A. Al-Munajjed, S. M. Kieran, M. E. Toner, C. M. Murphy, G. P. Duffy, and F. J. O’Brien, “The healing of bony defects by cell-free collagen-based scaffolds compared

- to stem cell-seeded tissue engineered constructs,” *Biomaterials*, vol. 31, no. 35, pp. 9232 – 9243, 2010.
- [11] N. A. Pattanashetti, G. B. Heggannavar, and M. Y. Kariduraganavar, “Smart biopolymers and their biomedical applications,” *Procedia Manufacturing*, vol. 12, pp. 263 – 279, 2017. International Conference on Sustainable and Intelligent Manufacturing, RESIM 2016, 14-17 December 2016, Leiria, Portugal.
- [12] T. Adachi, Y. Osako, M. Tanaka, M. Hojo, and S. J. Hollister, “Framework for optimal design of porous scaffold microstructure by computational simulation of bone regeneration,” *Biomaterials*, vol. 27, no. 21, pp. 3964–3972, 2006.
- [13] Y. Chen, S. Zhou, and Q. Li, “Microstructure design of biodegradable scaffold and its effect on tissue regeneration,” *Biomaterials*, vol. 32, no. 22, pp. 5003–5014, 2011.
- [14] A. S. Mao and D. J. Mooney, “Regenerative medicine: current therapies and future directions,” *Proceedings of the National Academy of Sciences*, vol. 112, no. 47, pp. 14452–14459, 2015.
- [15] A. Atala, “Engineering organs,” *Current opinion in biotechnology*, vol. 20, no. 5, pp. 575–592, 2009.
- [16] J. B. Kim, R. Stein, and M. J. O’hare, “Three-dimensional in vitro tissue culture models of breast cancer—a review,” *Breast cancer research and treatment*, vol. 85, no. 3, pp. 281–291, 2004.
- [17] T. Sun, S. Jackson, J. W. Haycock, and S. MacNeil, “Culture of skin cells in 3d rather than 2d improves their ability to survive exposure to cytotoxic agents,” *Journal of biotechnology*, vol. 122, no. 3, pp. 372–381, 2006.
- [18] N. Binulal, M. Deepthy, N. Selvamurugan, K. Shalumon, S. Suja, U. Mony, R. Jayakumar, and S. Nair, “Role of nanofibrous poly (caprolactone) scaffolds in human mesenchymal stem cell attachment and spreading for in vitro bone tissue engineering—response to osteogenic regulators,” *Tissue Engineering Part A*, vol. 16, no. 2, pp. 393–404, 2010.
- [19] V. Martinelli, S. Bosi, B. Peña, G. Baj, C. S. Long, O. Sbaizero, M. Giacca, M. Prato, and L. Mestroni, “3d carbon-nanotube-based composites for cardiac tissue engineering,” *ACS Applied Bio Materials*, vol. 1, no. 5, pp. 1530–1537, 2018.
- [20] K. Minami, Y. Kasuya, T. Yamazaki, Q. Ji, W. Nakanishi, J. P. Hill, H. Sakai, and K. Ariga, “Highly ordered 1d fullerene crystals for concurrent control of macroscopic cellular orientation and differentiation toward large-scale tissue engineering,” *Advanced Materials*, vol. 27, no. 27, pp. 4020–4026, 2015.

- [21] Q. Cheng, K. Rutledge, and E. Jabbarzadeh, "Carbon nanotube–poly (lactide-co-glycolide) composite scaffolds for bone tissue engineering applications," *Annals of biomedical engineering*, vol. 41, no. 5, pp. 904–916, 2013.
- [22] H. S. Jung, Y.-j. Choi, J. Jeong, Y. Lee, B. Hwang, J. Jang, J.-H. Shim, Y. S. Kim, H. S. Choi, S. H. Oh, *et al.*, "Nanoscale graphene coating on commercially pure titanium for accelerated bone regeneration," *RSC Advances*, vol. 6, no. 32, pp. 26719–26724, 2016.
- [23] V. Mokkalapati, N. P. Tasli, Z. Khan, A. Tufani, S. Pandit, H. Budak, and F. Sahin, "Nab integrated graphene oxide membranes for enhanced cell viability and stem cell properties of human adipose stem cells," *RSC Advances*, vol. 6, no. 61, pp. 56159–56165, 2016.
- [24] A. Paul, A. Hasan, H. A. Kindi, A. K. Gaharwar, V. T. Rao, M. Nikkhah, S. R. Shin, D. Krafft, M. R. Dokmeci, D. Shum-Tim, *et al.*, "Injectable graphene oxide/hydrogel-based angiogenic gene delivery system for vasculogenesis and cardiac repair," *ACS nano*, vol. 8, no. 8, pp. 8050–8062, 2014.
- [25] D.-D. Kirn, M. M. Takeno, B. D. Ratner, and T. A. Horbett, "Glow discharge plasma deposition (gdpd) technique for the local controlled delivery of hirudin from biomaterials," *Pharmaceutical research*, vol. 15, no. 5, pp. 783–786, 1998.
- [26] C. E. Holy, S. M. Dang, J. E. Davies, and M. S. Shoichet, "In vitro degradation of a novel poly (lactide-co-glycolide) 75/25 foam," *Biomaterials*, vol. 20, no. 13, pp. 1177–1185, 1999.
- [27] D. Hutmacher, M. Hoque, and Y. Wong, "Design, fabrication and physical characterization of scaffolds made from biodegradable synthetic polymers in combination with rp systems based on melt extrusion," in *Virtual prototyping & bio manufacturing in medical applications*, pp. 261–291, Springer, 2008.
- [28] P. Dalton, T. Woodfield, and D. Hutmacher, "Snapshot: Polymer scaffolds for tissue engineering.," *Biomaterials*, vol. 30, no. 4, p. 701, 2009.
- [29] C. E. Holy, C. Cheng, J. E. Davies, and M. S. Shoichet, "Optimizing the sterilization of plga scaffolds for use in tissue engineering," *Biomaterials*, vol. 22, no. 1, pp. 25–31, 2000.
- [30] N. Bhardwaj and S. C. Kundu, "Electrospinning: a fascinating fiber fabrication technique," *Biotechnology advances*, vol. 28, no. 3, pp. 325–347, 2010.
- [31] D. W. Hutmacher, "Scaffold-based tissue engineering—design and fabrication of matrices using solid freeform fabrication techniques," *Advanced Manufacturing Technology for Medical Applications*, p. 162, 2005.
- [32] D. W. Hutmacher, M. Sittinger, and M. V. Risbud, "Scaffold-based tissue engineering: rationale for computer-aided design and solid free-form fabrication systems," *TRENDS in Biotechnology*, vol. 22, no. 7, pp. 354–362, 2004.

- [33] P. D. Dalton, C. Vaquette, B. L. Farrugia, T. R. Dargaville, T. D. Brown, and D. W. Hutmacher, "Electrospinning and additive manufacturing: converging technologies," *Biomaterials Science*, vol. 1, no. 2, pp. 171–185, 2013.
- [34] P. D. Dalton, D. Grafahrend, K. Klinkhammer, D. Klee, and M. Möller, "Electrospinning of polymer melts: Phenomenological observations," *Polymer*, vol. 48, no. 23, pp. 6823–6833, 2007.
- [35] D. W. Hutmacher and P. D. Dalton, "Melt electrospinning," *Chemistry—An Asian Journal*, vol. 6, no. 1, pp. 44–56, 2011.
- [36] S. Goenka, V. Sant, and S. Sant, "Graphene-based nanomaterials for drug delivery and tissue engineering," *Journal of Controlled Release*, vol. 173, pp. 75–88, 2014.
- [37] Y. Yang, A. M. Asiri, Z. Tang, D. Du, and Y. Lin, "Graphene based materials for biomedical applications," *Materials today*, vol. 16, no. 10, pp. 365–373, 2013.
- [38] O. Akhavan, "Graphene scaffolds in progressive nanotechnology/stem cell-based tissue engineering of the nervous system," *Journal of Materials Chemistry B*, vol. 4, no. 19, pp. 3169–3190, 2016.
- [39] S. R. Shin, Y.-C. Li, H. L. Jang, P. Khoshakhlagh, M. Akbari, A. Nasajpour, Y. S. Zhang, A. Tamayol, and A. Khademhosseini, "Graphene-based materials for tissue engineering," *Advanced drug delivery reviews*, vol. 105, pp. 255–274, 2016.
- [40] A. M. Jastrzębska, P. Kurtycz, and A. R. Olszyna, "Recent advances in graphene family materials toxicity investigations," *Journal of Nanoparticle Research*, vol. 14, no. 12, p. 1320, 2012.
- [41] D. G. Tamay, T. D. Usal, A. S. Alagoz, D. Yucel, N. Hasirci, and V. Hasirci, "3d and 4d printing of polymers for tissue engineering applications," *Frontiers in bioengineering and biotechnology*, vol. 7, 2019.
- [42] D. N. Bikiaris, G. Z. Papageorgiou, D. S. Achilias, E. Pavlidou, and A. Stergiou, "Miscibility and enzymatic degradation studies of poly(-caprolactone)/poly(propylene succinate) blends," *European Polymer Journal*, vol. 43, no. 6, pp. 2491 – 2503, 2007.
- [43] F. J. V. Natta, J. W. Hill, and W. H. Carothers, "Studies of polymerization and ring formation. xxiii. 1-caprolactone and its polymers," *Journal of the American Chemical Society*, vol. 56, no. 2, p. 455–457, 1934.
- [44] B. Azimi, P. Nourpanah, M. Rabiee, and S. Arbab, "Poly (-caprolactone) fiber: An overview," *Journal of engineered fibers and fabrics*, vol. 9, pp. 74–90, 09 2014.
- [45] M. A. Woodruff and D. W. Hutmacher, "The return of a forgotten polymer—polycaprolactone in the 21st century," *Progress in Polymer Science*, vol. 35, no. 10, pp. 1217 – 1256, 2010.

- [46] C. Sciences, "Polymers for Bone Tissue Repair," no. December, 2006.
- [47] K.-Y. Chang and Y.-D. Lee, "Ring-opening polymerization of epsilon-caprolactone initiated by the antitumor agent doxorubicin," *Acta biomaterialia*, vol. 5, p. 1075–1081, May 2009.
- [48] M. Okada, "Chemical syntheses of biodegradable polymers," *Progress in Polymer Science (Oxford)*, vol. 27, no. 1, pp. 87–133, 2002.
- [49] D. Mondal, M. Griffith, and S. S. Venkatraman, "Polycaprolactone-based biomaterials for tissue engineering and drug delivery: Current scenario and challenges," *International Journal of Polymeric Materials and Polymeric Biomaterials*, vol. 65, no. 5, pp. 255–265, 2016.
- [50] N. Siddiqui, S. Asawa, B. Birru, R. Baadhe, and S. Rao, "PCL-Based Composite Scaffold Matrices for Tissue Engineering Applications PCL - Based Composite Scaffold Matrices for Tissue Engineering Applications," *Molecular Biotechnology*, no. May, 2018.
- [51] C. X. Lam, S. H. Teoh, and D. W. Hutmacher, "Comparison of the degradation of polycaprolactone and polycaprolactone-(tricalcium phosphate) scaffolds in alkaline medium," *Polymer International*, vol. 56, no. 6, pp. 718–728, 2007.
- [52] P. Joshi and G. Madras, "Degradation of polycaprolactone in supercritical fluids," *Polymer Degradation and Stability*, vol. 93, no. 10, pp. 1901 – 1908, 2008.
- [53] V. Sinha, K. Bansal, R. Kaushik, R. Kumria, and A. Trehan, "Poly--caprolactone microspheres and nanospheres: an overview," *International Journal of Pharmaceutics*, vol. 278, no. 1, pp. 1 – 23, 2004.
- [54] M. Labet and W. Thielemans, "Synthesis of polycaprolactone: a review," *Chem. Soc. Rev.*, vol. 38, pp. 3484–3504, 2009.
- [55] M. Lotfi, M. Nejib, and M. Naceur, "Cell adhesion to biomaterials: concept of biocompatibility," *Advances in Biomaterials Science and Biomedical Applications*, vol. 8, pp. 208–240, 2013.
- [56] O. S. Manoukian, N. Sardashti, T. Stedman, K. Gailiunas, A. Ojha, A. Penalosa, C. Mancuso, M. Hobert, and S. G. Kumbar, "Biomaterials for tissue engineering and regenerative medicine," in *Encyclopedia of Biomedical Engineering* (R. Narayan, ed.), pp. 462 – 482, Oxford: Elsevier, 2019.
- [57] S. A. Sell, M. J. McClure, K. Garg, P. S. Wolfe, and G. L. Bowlin, "Electrospinning of collagen/biopolymers for regenerative medicine and cardiovascular tissue engineering," *Advanced drug delivery reviews*, vol. 61, no. 12, pp. 1007–1019, 2009.
- [58] S. Samavedi, C. O. Horton, S. A. Guelcher, A. S. Goldstein, and A. R. Whittington, "Fabrication of a model continuously graded co-electrospun mesh for regeneration of the ligament–bone interface," *Acta biomaterialia*, vol. 7, no. 12, pp. 4131–4138, 2011.

- [59] D. A. Taylor and A. G. Zenovich, "Cardiovascular cell therapy and endogenous repair," *Diabetes, Obesity and Metabolism*, vol. 10, no. s4, pp. 5–15, 2008.
- [60] D. Kai, M. P. Prabhakaran, G. Jin, and S. Ramakrishna, "Polypyrrole-contained electrospun conductive nanofibrous membranes for cardiac tissue engineering," *Journal of Biomedical Materials Research Part A*, vol. 99A, no. 3, pp. 376–385, 2011.
- [61] J. S. Choi, S. J. Lee, G. J. Christ, A. Atala, and J. J. Yoo, "The influence of electrospun aligned poly(epsilon-caprolactone)/collagen nanofiber meshes on the formation of self-aligned skeletal muscle myotubes," *Biomaterials*, vol. 29, p. 2899—2906, July 2008.
- [62] M. S. Kim, I. Jun, Y. M. Shin, W. Jang, S. I. Kim, and H. Shin, "The development of genipin-crosslinked poly(caprolactone) (pcl)/gelatin nanofibers for tissue engineering applications," *Macromolecular Bioscience*, vol. 10, no. 1, pp. 91–100, 2010.
- [63] A. K. Geim, "Graphene: status and prospects," *science*, vol. 324, no. 5934, pp. 1530–1534, 2009.
- [64] V. Singh, D. Joung, L. Zhai, S. Das, S. I. Khondaker, and S. Seal, "Graphene based materials: Past, present and future," *Progress in Materials Science*, vol. 56, no. 8, pp. 1178–1271, 2011.
- [65] A. Lukowiak, A. Kedziora, and W. Strek, "Antimicrobial graphene family materials: Progress, advances, hopes and fears," *Advances in Colloid and Interface Science*, vol. 236, pp. 101 – 112, 2016.
- [66] M. Pumera, "Electrochemistry of graphene: new horizons for sensing and energy storage," *The Chemical Record*, vol. 9, no. 4, pp. 211–223, 2009.
- [67] P. C. Henriques, I. Borges, A. M. Pinto, F. D. Magalhães, and I. C. Gonçalves, "Fabrication and antimicrobial performance of surfaces integrating graphene-based materials," *Carbon*, vol. 132, pp. 709 – 732, 2018.
- [68] D. R. Dreyer, R. S. Ruoff, and C. W. Bielawski, "From conception to realization: An historical account of graphene and some perspectives for its future," *Angewandte Chemie International Edition*, vol. 49, no. 49, pp. 9336–9344, 2010.
- [69] K. S. Novoselov, A. K. Geim, S. V. Morozov, D. Jiang, Y. Zhang, S. V. Dubonos, I. V. Grigorieva, and A. A. Firsov, "Electric field effect in atomically thin carbon films," *Science*, vol. 306, no. 5696, pp. 666–669, 2004.
- [70] R. S. Edwards and K. S. Coleman, "Graphene synthesis: relationship to applications," *Nanoscale*, vol. 5, pp. 38–51, 2013.
- [71] C. K. Chua and M. Pumera, "Chemical reduction of graphene oxide: a synthetic chemistry viewpoint," *Chem. Soc. Rev.*, vol. 43, pp. 291–312, 2014.

- [72] W. Chen, L. Yan, and P. R. Bangal, "Preparation of graphene by the rapid and mild thermal reduction of graphene oxide induced by microwaves," *Carbon*, vol. 48, no. 4, pp. 1146 – 1152, 2010.
- [73] H. Kim, A. A. Abdala, and C. W. Macosko, "Graphene/polymer nanocomposites," *Macromolecules*, vol. 43, no. 16, pp. 6515–6530, 2010.
- [74] J. R. Potts, D. R. Dreyer, C. W. Bielawski, and R. S. Ruoff, "Graphene-based polymer nanocomposites," *Polymer*, vol. 52, no. 1, pp. 5–25, 2011.
- [75] S. Sayyar, E. Murray, B. C. Thompson, S. Gambhir, D. L. Officer, and G. G. Wallace, "Covalently linked biocompatible graphene/polycaprolactone composites for tissue engineering," *Carbon*, vol. 52, pp. 296–304, 2013.
- [76] M. Wang, X.-Y. Deng, A.-K. Du, T.-H. Zhao, and J.-B. Zeng, "Poly (sodium 4-styrenesulfonate) modified graphene for reinforced biodegradable poly (ϵ -caprolactone) nanocomposites," *RSC Advances*, vol. 5, no. 89, pp. 73146–73154, 2015.
- [77] T. Yu, G. S. Wang, L. Liu, P. Wang, Z. Y. Wei, and M. Qi, "Synthesis of pcl/graphene oxide composites by in situ polymerization," in *Advanced Materials Research*, vol. 518, pp. 837–840, Trans Tech Publ, 2012.
- [78] G.-s. Wang, Z.-y. Wei, L. Sang, G.-y. Chen, W.-x. Zhang, X.-f. Dong, and M. Qi, "Morphology, crystallization and mechanical properties of poly (ϵ -caprolactone)/graphene oxide nanocomposites," *Chinese Journal of Polymer Science*, vol. 31, no. 8, pp. 1148–1160, 2013.
- [79] S. J. Chin, S. Vempati, P. Dawson, M. Knite, A. Linarts, K. Ozols, and T. McNally, "Electrical conduction and rheological behaviour of composites of poly (ϵ -caprolactone) and mwcnts," *Polymer*, vol. 58, pp. 209–221, 2015.
- [80] P. Pötschke, T. Villmow, and B. Krause, "Melt mixed pcl/mwcnt composites prepared at different rotation speeds: Characterization of rheological, thermal, and electrical properties, molecular weight, mwcnt macrodispersion, and mwcnt length distribution," *Polymer*, vol. 54, no. 12, pp. 3071–3078, 2013.
- [81] B. Fadeel, C. Bussy, S. Merino, E. Vázquez, E. Flahaut, F. Mouchet, L. Evariste, L. Gauthier, A. J. Koivisto, U. Vogel, C. Martín, L. G. Delogu, T. Buerki-Thurnherr, P. Wick, D. Beloin-Saint-Pierre, R. Hischer, M. Pelin, F. Candotto Carniel, M. Tretiach, F. Cesca, F. Benfenati, D. Scaini, L. Ballerini, K. Kostarelos, M. Prato, and A. Bianco, "Safety assessment of graphene-based materials: Focus on human health and the environment," *ACS Nano*, vol. 12, no. 11, pp. 10582–10620, 2018. PMID: 30387986.
- [82] Z. Peng, X. Liu, W. Zhang, Z. Zeng, Z. Liu, C. Zhang, Y. Liu, B. Shao, Q. Liang, W. Tang, and X. Yuan, "Advances in the application, toxicity and degradation of carbon nanomaterials in environment: A review," *Environment International*, vol. 134, p. 105298, 2020.

- [83] J. Russier, L. Oudjedi, M. Pignonier, C. Bussy, M. Prato, K. Kostarelos, B. Lounis, A. Bianco, and L. Cognet, "Direct visualization of carbon nanotube degradation in primary cells by photothermal imaging," *Nanoscale*, vol. 9, pp. 4642–4645, 2017.
- [84] G. P. Kotchey, B. L. Allen, H. Vedala, N. Yanamala, A. A. Kapralov, Y. Y. Tyurina, J. Klein-Seetharaman, V. E. Kagan, and A. Star, "The enzymatic oxidation of graphene oxide," *ACS Nano*, vol. 5, no. 3, pp. 2098–2108, 2011. PMID: 21344859.
- [85] C. Martín Jiménez, K. Kostarelos, M. Prato, and A. Bianco, "Biocompatibility and biodegradability of 2d materials: Graphene and beyond," *Chemical Communications*, vol. 55, 04 2019.
- [86] R. Kurapati, J. Russier, M. A. Squillaci, E. Treossi, C. Ménard-Moyon, A. E. Del Rio-Castillo, E. Vazquez, P. Samorì, V. Palermo, and A. Bianco, "Dispersibility-dependent biodegradation of graphene oxide by myeloperoxidase," *Small*, vol. 11, no. 32, pp. 3985–3994, 2015.
- [87] S. P. Mukherjee, A. R. Gliga, B. Lazzaretto, B. Brandner, M. Fielden, C. Vogt, L. Newman, A. F. Rodrigues, W. Shao, P. M. Fournier, M. S. Toprak, A. Star, K. Kostarelos, K. Bhattacharya, and B. Fadeel, "Graphene oxide is degraded by neutrophils and the degradation products are non-genotoxic," *Nanoscale*, vol. 10, pp. 1180–1188, 2018.
- [88] C. Bussy, H. Ali-Boucetta, and K. Kostarelos, "Safety considerations for graphene: Lessons learnt from carbon nanotubes," *Accounts of Chemical Research*, vol. 46, pp. 692–701, Nov. 2012.
- [89] C. J. Bullock and C. Bussy, "Biocompatibility considerations in the design of graphene biomedical materials," *Advanced Materials Interfaces*, vol. 6, no. 11, p. 1900229, 2019.
- [90] K. Kostarelos, M. Vincent, C. Hebert, and J. A. Garrido, "Graphene in the design and engineering of next-generation neural interfaces," *Advanced Materials*, vol. 29, no. 42, p. 1700909, 2017.
- [91] Kenry, W. C. Lee, K. P. Loh, and C. T. Lim, "When stem cells meet graphene: Opportunities and challenges in regenerative medicine," *Biomaterials*, vol. 155, pp. 236 – 250, 2018.
- [92] W. Hu, C. Peng, W. Luo, M. Lv, X. Li, D. Li, Q. Huang, and C. Fan, "Graphene-based antibacterial paper," *ACS Nano*, vol. 4, no. 7, pp. 4317–4323, 2010. PMID: 20593851.
- [93] S. Ryon, S. #1, Y.-C. Li, H. Jang, P. Khoshakhlagh, M. Akbari, A. Nasajpour, Y. S. Zhang, A. Tamayol, and A. Khademhosseini, "Graphene-based materials for tissue engineering Graphical Abstract HHS Public Access," *Adv Drug Deliv Rev*, vol. 105, pp. 255–274, 2016.
- [94] D. McManus, S. Vranic, F. Withers, V. Sanchez-Romaguera, M. Macucci, H. Yang, R. Sorrentino, K. Parvez, S.-K. Son, G. Iannaccone, *et al.*, "Water-based and biocompatible 2d

- crystal inks for all-inkjet-printed heterostructures,” *Nature nanotechnology*, vol. 12, no. 4, p. 343, 2017.
- [95] A. F. Rodrigues, L. Newman, N. Lozano, S. P. Mukherjee, B. Fadeel, C. Bussy, and K. Kostarelos, “A blueprint for the synthesis and characterisation of thin graphene oxide with controlled lateral dimensions for biomedicine,” *2D Materials*, vol. 5, p. 035020, may 2018.
- [96] K. Ghosal and D. K. Sarkar, “Biomedical applications of graphene nanomaterials and beyond,” *ACS Biomaterials Science and Engineering*, vol. 4, pp. 2653–2703, 06 2018.
- [97] A. N. Banerjee, “Graphene and its derivatives as biomedical materials: future prospects and challenges,” *Interface Focus*, vol. 8, no. 3, p. 20170056, 2018.
- [98] J.-O. You, M. Rafat, G. J. C. Ye, and D. T. Auguste, “Nanoengineering the heart: Conductive scaffolds enhance connexin 43 expression,” *Nano Letters*, vol. 11, no. 9, pp. 3643–3648, 2011. PMID: 21800912.
- [99] J. Park, S. Park, S. Ryu, S. H. Bhang, J. Kim, J.-K. Yoon, Y. H. Park, S.-P. Cho, S. Lee, B. H. Hong, and B.-S. Kim, “Graphene-regulated cardiomyogenic differentiation process of mesenchymal stem cells by enhancing the expression of extracellular matrix proteins and cell signaling molecules,” *Advanced Healthcare Materials*, vol. 3, no. 2, pp. 176–181, 2014.
- [100] S. R. Shin, B. Aghaei-Ghareh-Bolagh, X. Gao, M. Nikkhah, S. M. Jung, A. Dolatshahi-Pirouz, S. B. Kim, S. M. Kim, M. R. Dokmeci, X. Tang, *et al.*, “Layer-by-layer assembly of 3d tissue constructs with functionalized graphene,” *Advanced functional materials*, vol. 24, no. 39, pp. 6136–6144, 2014.
- [101] G. Schulze-Tanzil, “Activation and dedifferentiation of chondrocytes: Implications in cartilage injury and repair,” *Annals of Anatomy - Anatomischer Anzeiger*, vol. 191, no. 4, pp. 325 – 338, 2009.
- [102] K. Ghosal and K. Sarkar, “Biomedical applications of graphene nanomaterials and beyond,” *ACS Biomaterials Science & Engineering*, vol. 4, no. 8, pp. 2653–2703, 2018.
- [103] J. Liao, Y. Qu, B. Chu, X. Zhang, and Z. Qian, “Biodegradable csma/peca/graphene porous hybrid scaffold for cartilage tissue engineering,” *Scientific reports*, vol. 5, p. 9879, 2015.
- [104] H. H. Yoon, S. H. Bhang, T. Kim, T. Yu, T. Hyeon, and B.-S. Kim, “Dual roles of graphene oxide in chondrogenic differentiation of adult stem cells: Cell-adhesion substrate and growth factor-delivery carrier,” *Advanced Functional Materials*, vol. 24, no. 41, pp. 6455–6464, 2014.

- [105] V. Palmieri, F. Sciandra, M. Bozzi, M. De Spirito, and M. Papi, “3d graphene scaffolds for skeletal muscle regeneration: Future perspectives,” *Frontiers in Bioengineering and Biotechnology*, vol. 8, p. 383, 2020.
- [106] B. Chaudhuri, D. Bhadra, B. Mondal, and K. Pramanik, “Biocompatibility of electrospun graphene oxide–poly(-caprolactone) fibrous scaffolds with human cord blood mesenchymal stem cells derived skeletal myoblast,” *Materials Letters*, vol. 126, pp. 109–112, July 2014.
- [107] B. Chaudhuri, B. Mondal, S. Kumar, and S. Sarkar, “Myoblast differentiation and protein expression in electrospun graphene oxide (GO)-poly (-caprolactone, PCL) composite meshes,” *Materials Letters*, vol. 182, pp. 194–197, Nov. 2016.
- [108] A. Patel, Y. Xue, S. Mukundan, L. C. Rohan, V. Sant, D. B. Stolz, and S. Sant, “Cell-instructive graphene-containing nanocomposites induce multinucleated myotube formation,” *Annals of Biomedical Engineering*, vol. 44, pp. 2036–2048, Mar. 2016.
- [109] J. Mesquita-Guimarães, B. Henriques, F. Silva, J. Souza, A. N. de Oliveira, D. Hotza, R. do Nascimento, and M. Fredel, “Nanostructured biocompatible ceramics and glass-ceramics,” in *Nanostructured Biomaterials for Cranio-Maxillofacial and Oral Applications*, pp. 97–118, Elsevier, 2018.
- [110] M. J. Pavlovich, J. Hunsberger, and A. Atala, “Biofabrication: a secret weapon to advance manufacturing, economies, and healthcare,” *Trends in biotechnology*, vol. 34, no. 9, pp. 679–680, 2016.
- [111] A. Ovsianikov and B. N. Chichkov, *Three-Dimensional Microfabrication by Two-Photon Polymerization Technique*, pp. 311–325. Totowa, NJ: Humana Press, 2012.
- [112] T. Woodfield, J. Malda, J. de Wijn, F. Péters, J. Riesle, and C. van Blitterswijk, “Design of porous scaffolds for cartilage tissue engineering using a three-dimensional fiber-deposition technique,” *Biomaterials*, vol. 25, no. 18, pp. 4149 – 4161, 2004.
- [113] C. Mota, D. Puppi, F. Chiellini, and E. Chiellini, “Additive manufacturing techniques for the production of tissue engineering constructs,” *Journal of Tissue Engineering and Regenerative Medicine*, vol. 9, no. 3, pp. 174–190, 2015.
- [114] G. Vozzi, A. Previti, D. De Rossi, and A. Ahluwalia, “Microsyringe-based deposition of two-dimensional and three-dimensional polymer scaffolds with a well-defined geometry for application to tissue engineering,” *Tissue Engineering*, vol. 8, no. 6, pp. 1089–1098, 2002. PMID: 12542954.
- [115] J. Y. Tan, C. K. Chua, and K. F. Leong, “Indirect fabrication of gelatin scaffolds using rapid prototyping technology,” *Virtual and Physical Prototyping*, vol. 5, no. 1, pp. 45–53, 2010.

- [116] R. Landers, U. Hübner, R. Schmelzeisen, and R. Mülhaupt, "Rapid prototyping of scaffolds derived from thermoreversible hydrogels and tailored for applications in tissue engineering," *Biomaterials*, vol. 23, no. 23, pp. 4437 – 4447, 2002.
- [117] C. B. Highley, C. B. Rodell, and J. A. Burdick, "Direct 3d printing of shear-thinning hydrogels into self-healing hydrogels," *Advanced Materials*, vol. 27, no. 34, pp. 5075–5079, 2015.
- [118] G. Skeldon, B. Lucendo-Villarin, and W. Shu, "Three-dimensional bioprinting of stem-cell derived tissues for human regenerative medicine," *Philosophical Transactions of the Royal Society B: Biological Sciences*, vol. 373, no. 1750, p. 20170224, 2018.
- [119] S. C. Ligon, R. Liska, J. Stampfl, M. Gurr, and R. Mülhaupt, "Polymers for 3d printing and customized additive manufacturing," *Chemical reviews*, vol. 117, p. 10212—10290, August 2017.
- [120] B. Pant, M. Park, and S.-J. Park, "Drug delivery applications of core-sheath nanofibers prepared by coaxial electrospinning: a review," *Pharmaceutics*, vol. 11, no. 7, p. 305, 2019.
- [121] T. D. Brown, P. D. Dalton, and D. W. Hutmacher, "Direct writing by way of melt electrospinning," *Advanced Materials*, vol. 23, no. 47, pp. 5651–5657, 2011.
- [122] G. Hochleitner, F. Chen, C. Blum, P. D. Dalton, B. Amsden, and J. Groll, "Melt electrowriting below the critical translation speed to fabricate crimped elastomer scaffolds with non-linear extension behaviour mimicking that of ligaments and tendons," *Acta Biomaterialia*, vol. 72, pp. 110 – 120, 2018.
- [123] D. H. Reneker and I. Chun, "Nanometre diameter fibres of polymer, produced by electrospinning," *Nanotechnology*, vol. 7, pp. 216–223, sep 1996.
- [124] T. M. Robinson, D. W. Hutmacher, and P. D. Dalton, "The next frontier in melt electrospinning: Taming the jet," *Advanced Functional Materials*, vol. 29, no. 44, p. 1904664, 2019.
- [125] G. Hochleitner, M. Kessler, M. Schmitz, A. R. Boccaccini, J. Teßmar, and J. Groll, "Melt electrospinning writing of defined scaffolds using polylactide-poly(ethylene glycol) blends with 45s5 bioactive glass particles," *Materials Letters*, vol. 205, pp. 257 – 260, 2017.
- [126] F. Tournomousis, H. Ding, D. M. Kalyon, and R. C. Chang, "Melt Electrospinning Writing Process Guided by a "Printability Number"," *Journal of Manufacturing Science and Engineering*, vol. 139, 05 2017. 081004.
- [127] A. Hrynevich, B. Ş. Elçi, J. N. Haigh, R. McMaster, A. Youssef, C. Blum, T. Blunk, G. Hochleitner, J. Groll, and P. D. Dalton, "Dimension-based design of melt electrowritten scaffolds," *Small*, vol. 14, no. 22, p. 1800232, 2018.

- [128] T. Tylek, C. Blum, A. Hrynevich, K. Schlegelmilch, T. Schilling, P. D. Dalton, and J. Groll, "Precisely defined fiber scaffolds with 40 m porosity induce elongation driven m2-like polarization of human macrophages," *Biofabrication*, vol. 12, p. 025007, Feb. 2020.
- [129] H. Ding, K. Cao, F. Zhang, W. Boettcher, and R. C. Chang, "A fundamental study of charge effects on melt electrowritten polymer fibers," *Materials Design*, vol. 178, p. 107857, 2019.
- [130] F. M. Wunner, M.-L. Wille, T. G. Noonan, O. Bas, P. D. Dalton, E. M. De-Juan-Pardo, and D. W. Huttmacher, "Melt electrospinning writing of highly ordered large volume scaffold architectures," *Advanced Materials*, vol. 30, no. 20, p. 1706570, 2018.
- [131] G. Hochleitner, T. Jüngst, T. D. Brown, K. Hahn, C. Moseke, F. Jakob, P. D. Dalton, and J. Groll, "Additive manufacturing of scaffolds with sub-micron filaments via melt electrospinning writing," *Biofabrication*, vol. 7, no. 3, 2015.
- [132] N. Schaefer, D. Janzen, E. Bakirci, A. Hrynevich, P. D. Dalton, and C. Villmann, "3D Electrophysiological Measurements on Cells Embedded within Fiber-Reinforced Matrigel," *Advanced Healthcare Materials*, vol. 8, no. 5, pp. 1–7, 2019.
- [133] N. T. Saidy, F. Wolf, O. Bas, H. Keijdener, D. W. Huttmacher, P. Mela, and E. M. De-Juan-Pardo, "Biologically Inspired Scaffolds for Heart Valve Tissue Engineering via Melt Electrowriting," *Small*, vol. 15, no. 24, pp. 1–15, 2019.
- [134] M. de Ruijter, A. Hrynevich, J. N. Haigh, G. Hochleitner, M. Castilho, J. Groll, J. Malda, and P. D. Dalton, "Out-of-Plane 3D-Printed Microfibers Improve the Shear Properties of Hydrogel Composites," *Small*, vol. 14, no. 8, pp. 1–6, 2018.
- [135] M. Castilho, A. V. Mil, M. Maher, C. H. G. Metz, G. Hochleitner, J. Groll, P. A. Doevendans, K. Ito, J. P. G. Sluijter, and J. Malda, "Melt Electrowriting Allows Tailored Microstructural and Mechanical Design of Scaffolds to Advance Functional Human Myocardial Tissue Formation," vol. 1803151, pp. 1–10, 2018.
- [136] E. McColl, J. Groll, T. Jungst, and P. D. Dalton, "Design and fabrication of melt electrowritten tubes using intuitive software," *Materials and Design*, vol. 155, pp. 46–58, 2018.
- [137] A. Youssef, A. Hrynevich, L. Fladeland, A. Balles, J. Groll, P. D. Dalton, and S. Zabler, "The Impact of Melt Electrowritten Scaffold Design on Porosity Determined by X-Ray Microtomography," *Tissue Engineering - Part C: Methods*, vol. 25, no. 6, pp. 367–378, 2019.
- [138] M. Castilho, D. Feyen, M. Flandes-Iparraguirre, G. Hochleitner, J. Groll, P. A. Doevendans, T. Vermonden, K. Ito, J. P. Sluijter, and J. Malda, "Melt electrospinning writing of polyhydroxymethylglycolide-co- ϵ -caprolactone-based scaffolds for cardiac tissue engineering," *Advanced healthcare materials*, vol. 6, no. 18, p. 1700311, 2017.

- [139] G. Hochleitner, E. Fürsattel, R. Giesa, J. Groll, H.-W. Schmidt, and P. D. Dalton, “Melt electrowriting of thermoplastic elastomers,” *Macromolecular Rapid Communications*, vol. 39, no. 10, p. 1800055, 2018.
- [140] J. Song, H. Gao, G. Zhu, X. Cao, X. Shi, and Y. Wang, “The preparation and characterization of polycaprolactone/graphene oxide biocomposite nanofiber scaffolds and their application for directing cell behaviors,” *Carbon*, vol. 95, no. C, pp. 1039–1050, 2015.
- [141] S. F. Melo, S. C. Neves, A. T. Pereira, F. D. Magalhães, and I. C. Gonçalves, “3d printing of polycaprolactone/graphene-based materials composite scaffolds,”
- [142] J. M. Unagolla and A. C. Jayasuriya, “Enhanced cell functions on graphene oxide incorporated 3d printed polycaprolactone scaffolds,” *Materials Science and Engineering: C*, vol. 102, pp. 1 – 11, 2019.
- [143] W. Wang, G. Caetano, W. S. Ambler, J. J. Blaker, M. A. Frade, P. Mandal, C. Diver, and P. Bártolo, “Enhancing the hydrophilicity and cell attachment of 3d printed pcl/graphene scaffolds for bone tissue engineering,” *Materials*, vol. 9, no. 12, p. 992, 2016.
- [144] G. F. Caetano, W. Wang, W. H. Chiang, G. Cooper, C. Diver, J. J. Blaker, M. A. Frade, and P. Bártolo, “3D-printed poly(-caprolactone)/graphene scaffolds activated with p1-latex protein for bone regeneration,” *3D Printing and Additive Manufacturing*, vol. 5, no. 2, pp. 127–137, 2018.
- [145] C. Wan and B. Chen, “Poly (ϵ -caprolactone)/graphene oxide biocomposites: mechanical properties and bioactivity,” *Biomedical Materials*, vol. 6, no. 5, p. 055010, 2011.
- [146] Q. Bao, H. Zhang, J. X. Yang, S. Wang, D. Y. Tang, R. Jose, S. Ramakrishna, C. T. Lim, and K. P. Loh, “Graphene-polymer nanofiber membrane for ultrafast photonics,” *Advanced Functional Materials*, vol. 20, no. 5, pp. 782–791, 2010.
- [147] B. Ardeshirzadeh, N. A. Anaraki, M. Irani, L. R. Rad, and S. Shamshiri, “Controlled release of doxorubicin from electrospun PEO/chitosan/graphene oxide nanocomposite nanofibrous scaffolds,” *Materials Science and Engineering C*, vol. 48, pp. 384–390, 2015.
- [148] C. Zhu, T. Y. J. Han, E. B. Duoss, A. M. Golobic, J. D. Kuntz, C. M. Spadaccini, and M. A. Worsley, “Highly compressible 3D periodic graphene aerogel microlattices,” *Nature Communications*, vol. 6, pp. 1–8, 2015.
- [149] J. Li, F. Ye, S. Vaziri, M. Muhammed, M. C. Lemme, and M. Östling, “Efficient inkjet printing of graphene,” *Advanced Materials*, vol. 25, no. 29, pp. 3985–3992, 2013.
- [150] X. An, H. Ma, B. Liu, and J. Wang, “Graphene oxide reinforced polylactic acid/polyurethane antibacterial composites,” *Journal of Nanomaterials*, vol. 2013, 2013.

- [151] C. Zhang, L. Wang, T. Zhai, X. Wang, Y. Dan, and L. S. Turng, "The surface grafting of graphene oxide with poly(ethylene glycol) as a reinforcement for poly(lactic acid) nanocomposite scaffolds for potential tissue engineering applications," *Journal of the Mechanical Behavior of Biomedical Materials*, vol. 53, pp. 403–413, 2016.
- [152] Y. Y. Qi, Z. X. Tai, D. F. Sun, J. T. Chen, H. B. Ma, X. B. Yan, B. Liu, and Q. J. Xue, "Fabrication and characterization of poly(vinyl alcohol)/graphene oxide nanofibrous biocomposite scaffolds," *Journal of Applied Polymer Science*, vol. 127, no. 3, pp. 1885–1894, 2013.
- [153] Y. C. Shin, J. H. Lee, L. Jin, M. J. Kim, Y. J. Kim, J. K. Hyun, T. G. Jung, S. W. Hong, and D. W. Han, "Stimulated myoblast differentiation on graphene oxide-impregnated PLGA-collagen hybrid fibre matrices matrices," *Journal of Nanobiotechnology*, vol. 13, no. 1, pp. 1–11, 2015.
- [154] D. C. Marcano, D. V. Kosynkin, J. M. Berlin, A. Sinitskii, Z. Sun, A. Slesarev, L. B. Alemany, W. Lu, and J. M. Tour, "Improved synthesis of graphene oxide," *ACS nano*, vol. 4, no. 8, pp. 4806–4814, 2010.
- [155] C. Gonçalves, A. M. Pinto, A. V. Machado, J. A. Moreira, I. C. Gonçalves, and F. de Magalhães, "Biocompatible reinforcement of poly(lactic acid) with graphene nanoplatelets," 2018.
- [156] A. M. Pinto, J. Cabral, D. A. P. Tanaka, A. M. Mendes, and F. D. Magalhaes, "Effect of incorporation of graphene oxide and graphene nanoplatelets on mechanical and gas permeability properties of poly (lactic acid) films," *Polymer International*, vol. 62, no. 1, pp. 33–40, 2013.
- [157] E. Kuzelova Kostakova, L. Meszaros, G. Maskova, L. Blazkova, T. Turcsan, and D. Lukas, "Crystallinity of electrospun and centrifugal spun polycaprolactone fibers: a comparative study," *Journal of Nanomaterials*, vol. 2017, 2017.
- [158] A. M. Pinto, C. Gonçalves, D. M. Sousa, A. R. Ferreira, J. A. Moreira, I. C. Gonçalves, and F. D. Magalhães, "Smaller particle size and higher oxidation improves biocompatibility of graphene-based materials," *Carbon*, vol. 99, pp. 318 – 329, 2016.
- [159] N. Chandrasekar, K. Kumar, K. S. BALASUBRAMNIAN, K. Karunamurthy, and R. VARADHARAJAN, "Facile synthesis of iron oxide, iron-cobalt and zero valent iron nanoparticles and evaluation of their anti microbial activity, free radicle scavenging activity and antioxidant assay.," *Digest Journal of Nanomaterials & Biostructures (DJNB)*, vol. 8, no. 2, 2013.
- [160] T. F. Emiru and D. W. Ayele, "Controlled synthesis, characterization and reduction of graphene oxide: A convenient method for large scale production," *Egyptian Journal of Basic and Applied Sciences*, vol. 4, no. 1, pp. 74–79, 2017.

- [161] T. Elzein, M. Nasser-Eddine, C. Delaite, S. Bistac, and P. Dumas, "Ftir study of polycaprolactone chain organization at interfaces," *Journal of colloid and interface science*, vol. 273, no. 2, pp. 381–387, 2004.
- [162] M. P. Prabhakaran, J. Venugopal, C. K. Chan, and S. Ramakrishna, "Surface modified electrospun nanofibrous scaffolds for nerve tissue engineering," *Nanotechnology*, vol. 19, no. 45, p. 455102, 2008.
- [163] M. P. Araújo, O. Soares, A. Fernandes, M. Pereira, and C. Freire, "Tuning the surface chemistry of graphene flakes: new strategies for selective oxidation," *RSC advances*, vol. 7, no. 23, pp. 14290–14301, 2017.
- [164] P. Louette, F. Bodino, and J.-J. Pireaux, "Poly (caprolactone)(pcl) xps reference core level and energy loss spectra," *Surface Science Spectra*, vol. 12, no. 1, pp. 27–31, 2005.
- [165] E. S. Permyakova, P. V. Kiryukhantsev-Korneev, K. Y. Gudz, A. S. Konopatsky, J. Polčák, I. Y. Zhitnyak, N. A. Gloushankova, D. Shtansky, and A. M. Manakhov, "Comparison of different approaches to surface functionalization of biodegradable polycaprolactone scaffolds," *Nanomaterials*, vol. 9, no. 12, p. 1769, 2019.
- [166] S. Kumar, D. Azam, S. Raj, E. Kolanthai, K. Vasu, A. Sood, and K. Chatterjee, "3d scaffold alters cellular response to graphene in a polymer composite for orthopedic applications," *Journal of Biomedical Materials Research Part B: Applied Biomaterials*, vol. 104, no. 4, pp. 732–749, 2016.
- [167] I. Castilla-Cortázar, A. Vidaurre, B. Marí, and A. J. Campillo-Fernández, "Morphology, crystallinity, and molecular weight of poly (ϵ -caprolactone)/graphene oxide hybrids," *Polymers*, vol. 11, no. 7, p. 1099, 2019.
- [168] P. Manafi, I. Ghasemi, M. Karrabi, H. Azizi, and P. Ehsaninamin, "Effect of graphene nanoplatelets on crystallization kinetics of poly (lactic acid)," *Soft Materials*, vol. 12, no. 4, pp. 433–444, 2014.
- [169] M. Wojtoniszak, X. Chen, R. J. Kalenczuk, A. Wajda, J. Łapczuk, M. Kurzewski, M. Drozdziak, P. K. Chu, and E. Borowiak-Palen, "Synthesis, dispersion, and cytocompatibility of graphene oxide and reduced graphene oxide," *Colloids and Surfaces B: Biointerfaces*, vol. 89, pp. 79–85, 2012.
- [170] A. Ebrahiminezhad, A. Zare-Hoseinabadi, A. Berenjian, and Y. Ghasemi, "Green synthesis and characterization of zero-valent iron nanoparticles using stinging nettle (*urtica dioica*) leaf extract," *Green Processing and Synthesis*, vol. 6, no. 5, pp. 469–475, 2017.
- [171] X. Juan FAN and X. LI, "Preparation and magnetic property of multiwalled carbon nanotubes decorated by fe₃o₄ nanoparticles," *New Carbon Materials*, vol. 27, no. 2, pp. 111 – 116, 2012.

- [172] S. Venkateswarlu, D. Lee, and M. Yoon, "Bioinspired 2d-carbon flakes and fe₃o₄ nanoparticles composite for arsenite removal," *ACS Applied Materials & Interfaces*, vol. 8, no. 36, pp. 23876–23885, 2016. PMID: 27463424.
- [173] J. Liang, J. Wang, G. C. Tsui, and C. Tang, "Thermal properties and thermal stability of polypropylene composites filled with graphene nanoplatelets," *Journal of Thermoplastic Composite Materials*, vol. 31, no. 2, pp. 246–264, 2018.
- [174] A. Shahin-Shamsabadi, A. Hashemi, M. Tahriri, F. Bastami, M. Salehi, and F. M. Abbas, "Mechanical, material, and biological study of a pcl/bioactive glass bone scaffold: Importance of viscoelasticity," *Materials Science and Engineering: C*, vol. 90, pp. 280–288, 2018.
- [175] E. Blázquez-Blázquez, E. Pérez, V. Lorenzo, and M. L. Cerrada, "Crystalline characteristics and their influence in the mechanical performance in poly (ϵ -caprolactone)/high density polyethylene blends," *Polymers*, vol. 11, no. 11, p. 1874, 2019.
- [176] "Characterization techniques for graphene-based materials in catalysis."
- [177] A. Ruíz-Baltazar, R. Esparza, G. Rosas, and R. Pérez, "Effect of the surfactant on the growth and oxidation of iron nanoparticles," *Journal of nanomaterials*, vol. 2015, 2015.
- [178] S. Kostyuchenko, G. Ziborov, M. Dmitrieva, and A. Dmitriev, "Magnetic properties of magnetite nanowire arrays," in *Journal of Physics: Conference Series*, vol. 1199, p. 012026, IOP Publishing, 2019.
- [179] R. Grau-Crespo, A. Y. Al-Baitai, I. Saadoun, and N. H. De Leeuw, "Vacancy ordering and electronic structure of γ -fe₂o₃ (maghemite): a theoretical investigation," *Journal of Physics: Condensed Matter*, vol. 22, no. 25, p. 255401, 2010.
- [180] C. Baptista, A. Azagury, H. Shin, C. M. Baker, E. Ly, R. Lee, and E. Mathiowitz, "The effect of temperature and pressure on polycaprolactone morphology," *Polymer*, vol. 191, p. 122227, 2020.
- [181] M. Ahmadzadeh, C. Romero, and J. McCloy, "Magnetic analysis of commercial hematite, magnetite, and their mixtures," *Aip Advances*, vol. 8, no. 5, p. 056807, 2018.
- [182] Y. Xue, H. Chen, D. Yu, S. Wang, M. Yardeni, Q. Dai, M. Guo, Y. Liu, F. Lu, J. Qu, *et al.*, "Oxidizing metal ions with graphene oxide: the in situ formation of magnetic nanoparticles on self-reduced graphene sheets for multifunctional applications," *Chemical Communications*, vol. 47, no. 42, pp. 11689–11691, 2011.
- [183] R. Costa-Almeida, D. Bogas, J. R. Fernandes, L. Timochenco, F. A. Silva, J. Meneses, I. C. Gonçalves, F. D. Magalhães, and A. M. Pinto, "Near-infrared radiation-based mild photo-hyperthermia therapy of non-melanoma skin cancer with pegylated reduced nanographene oxide," *Polymers*, vol. 12, no. 8, p. 1840, 2020.

- [184] R. Al-Gaashani, A. Najjar, Y. Zakaria, S. Mansour, and M. Atieh, "Xps and structural studies of high quality graphene oxide and reduced graphene oxide prepared by different chemical oxidation methods," *Ceramics International*, vol. 45, no. 11, pp. 14439–14448, 2019.
- [185] E. Bertolucci, A. Galletti, C. Antonetti, M. Marracci, B. Tellini, F. Piccinelli, and C. Visone, "Chemical and magnetic properties characterization of magnetic nanoparticles," *Conference Record - IEEE Instrumentation and Measurement Technology Conference*, vol. 2015, pp. 1492–1496, 07 2015.
- [186] S. M. H. Mohammed, "Characterization of magnetite and hematite using infrared spectroscopy," vol. 2, no. 1, 2018.
- [187] T. Duan, Y. Lv, H. Xu, J. Jin, and Z. Wang, "Structural effects of residual groups of graphene oxide on poly(-caprolactone)/graphene oxide nanocomposite," *Crystals*, vol. 8, p. 270, Jun 2018.
- [188] B. Chang, H. Ming, A. Noor, A. Marlinda, N. Yusoff, M. Muhamad, I. Harrison, H. Lim, and C.-h. Chia, "Facile hydrothermal preparation of titanium dioxide decorated reduced graphene oxide nanocomposite," *International journal of nanomedicine*, vol. 7, pp. 3379–87, 07 2012.
- [189] V. Shukla, "Observation of critical magnetic behavior in 2d carbon based composites," *Nanoscale Advances*, vol. 2, no. 3, pp. 962–990, 2020.
- [190] T. Tang, F. Liu, Y. Liu, X. Li, Q. Xu, Q. Feng, N. Tang, and Y. Du, "Identifying the magnetic properties of graphene oxide," *Applied Physics Letters*, vol. 104, p. 123104, Mar. 2014.
- [191] H. Rashid, M. A. Mansoor, B. Haider, R. Nasir, S. B. A. Hamid, and A. Abdulrahman, "Synthesis and characterization of magnetite nano particles with high selectivity using in-situ precipitation method," *Separation Science and Technology*, vol. 55, pp. 1207–1215, Mar. 2019.
- [192] S. P. Schwaminger, C. Syhr, and S. Berensmeier, "Controlled synthesis of magnetic iron oxide nanoparticles: Magnetite or maghemite?," *Crystals*, vol. 10, p. 214, Mar. 2020.
- [193] E. C. Abenojar, S. Wickramasinghe, J. Bas-Concepcion, and A. C. S. Samia, "Structural effects on the magnetic hyperthermia properties of iron oxide nanoparticles," *Progress in Natural Science: Materials International*, vol. 26, pp. 440–448, Oct. 2016.
- [194] Y. Wang, Q. He, H. Qu, X. Zhang, J. Guo, J. Zhu, G. Zhao, H. A. Colorado, J. Yu, L. Sun, S. Bhana, M. A. Khan, X. Huang, D. P. Young, H. Wang, X. Wang, S. Wei, and Z. Guo, "Magnetic graphene oxide nanocomposites: nanoparticles growth mechanism and property analysis," *J. Mater. Chem. C*, vol. 2, pp. 9478–9488, Sept. 2014.

- [195] S. Zaiss, T. Brown, J. Reichert, and A. Berner, "Poly(-caprolactone) scaffolds fabricated by melt electrospinning for bone tissue engineering," *Materials*, vol. 9, p. 232, Mar. 2016.
- [196] J. C. Kade and P. D. Dalton, "Polymers for melt electrowriting," *Advanced Healthcare Materials*, p. 2001232, Sept. 2020.
- [197] L. Moroni, T. Boland, J. A. Burdick, C. D. Maria, B. Derby, G. Forgacs, J. Groll, Q. Li, J. Malda, V. A. Mironov, C. Mota, M. Nakamura, W. Shu, S. Takeuchi, T. B. Woodfield, T. Xu, J. J. Yoo, and G. Vozzi, "Biofabrication : a guide to technology and terminology," *Trends in Biotechnology*, pp. 1–19, November 2017.
- [198] S. Thampi, V. Muthuvijayan, and R. Parameswaran, "Mechanical characterization of high-performance graphene oxide incorporated aligned fibroporous poly(carbonate urethane) membrane for potential biomedical applications," *Journal of Applied Polymer Science*, vol. 132, no. 16, pp. 1–8, 2015.
- [199] L. Jin, D. Yue, Z.-W. Xu, G. Liang, Y. Zhang, J.-F. Zhang, X. Zhang, and Z. Wang, "Fabrication, mechanical properties, and biocompatibility of reduced graphene oxide-reinforced nanofiber mats," *RSC Adv.*, vol. 4, pp. 35035–35041, 2014.
- [200] H. S. Park, B. G. Choi, W. H. Hong, and S. Y. Jang, "Controlled assembly of graphene oxide nanosheets within one-dimensional polymer nanostructure," *Journal of Colloid and Interface Science*, vol. 406, pp. 24–29, 2013.
- [201] D. Zhang, B. Chi, B. Li, Z. Gao, Y. Du, J. Guo, and J. Wei, "Fabrication of highly conductive graphene flexible circuits by 3D printing," *Synthetic Metals*, vol. 217, pp. 79–86, 2016.
- [202] A. E. Jakus, E. B. Secor, A. L. Rutz, S. W. Jordan, M. C. Hersam, and R. N. Shah, "Three-dimensional printing of high-content graphene scaffolds for electronic and biomedical applications," *ACS Nano*, vol. 9, no. 4, pp. 4636–4648, 2015.
- [203] A. Kumar and C. K. Dixit, "Methods for characterization of nanoparticles," in *Advances in Nanomedicine for the Delivery of Therapeutic Nucleic Acids*, pp. 43–58, Elsevier, 2017.

Appendix A

Supplementary material for Chapter 4

In this Appendix, representative schemas about several additive manufacturing (AM) technologies are shown in [Figure A.1](#). Additionally, a list of other polymers/graphene-based materials (GBM) composites processed by those methods is presented in [Table A.1](#).

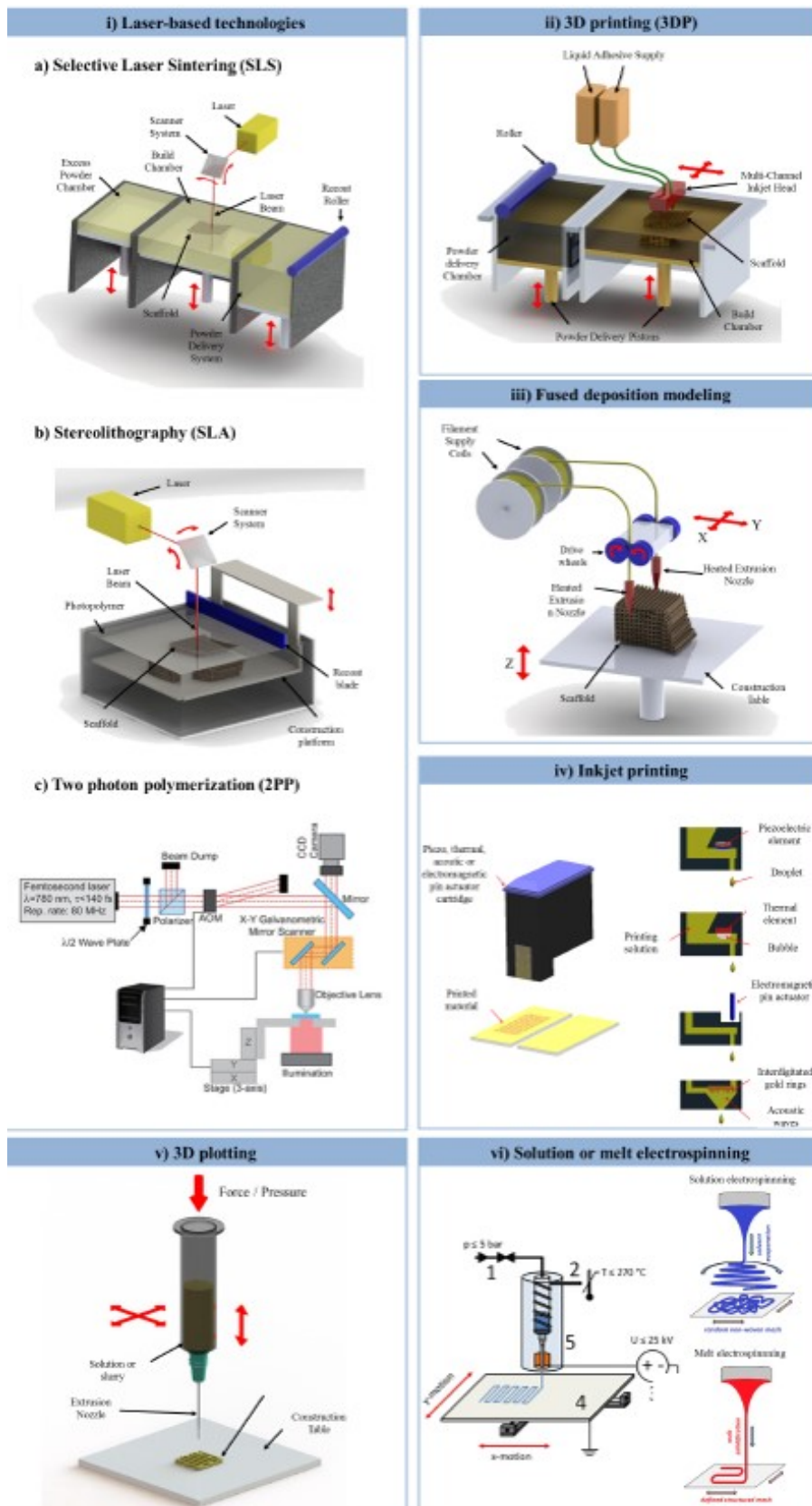


Figure A.1: Summary of AM techniques. Reprinted from [197] Copyright © 2017 Elsevier Ltd.

Table A.1: List of studies on AM of polymer/GBM 3D printed scaffolds, and its main goals.

Material	Technique	Aim	Ref
PVAc/GO	electrospinning	Develop fibre lasers with ultrashort and fast pulses (Photonics research field).	[146]
PEO/CS/GO	electrospinning	Perform a controlled release of Doxorubicin for lung cancer treatment.	[147]
GO inks	direct ink writing	Design and manufacture compressive G micro lattices for novel aerogels.	[148]
G films	Inkjet	Improve GBM ink formulations stability.	[149]
PLA/PU/GO	electrospinning	Investigate antibacterial properties and biocompatibility.	[150]
PLA/GO	electrospinning	Evaluate biological, mechanical, morphological and thermal properties.	[151]
PVA/GO	electrospinning	Scaffolds macro and microstructure investigation.	[152]
PLGA/Col/GO	electrospinning	Promote differentiation of myoblast for skeletal muscle regeneration.	[153]
PCU/rGO	electrospinning	Evaluate cytocompatibility and hemolytic capacity.	[198]
PAN/rGO	electrospinning	Control and stimulate the culture of ADSCs.	[199]
PVA/rGO	electrospinning	Improve GO dispersion within the polymeric matrix.	[200]
PLA/rGO	FDM	Develop flexible and highly conductive electric circuits.	[201]
PLGA/G	Inkjet	Evaluate the adhesion, proliferation, and differentiation capacity in hMSC through the use of neurogenic electrical stimulus.	[202]

Appendix B

Supplementary material for Chapter 6

In this Appendix, supplementary Figures and Table for graphene-based materials (GBM) morphological properties (Figures B.1 and B.6), particle size (Figures B.2, B.3 and B.4), and stability (Table B.1 and Figure B.5) are presented.

Regarding chemical characterization, PCL, PCL/GNP-M and PCL/GNP-C filaments Fourier transform infrared (FTIR) spectra are presented in Figure B.7, while its x-ray photoelectron spectroscopy (XPS) C 1s, O 1s and Fe 2p surveys and high-resolution spectras are presented in Figures B.8, B.9, B.10, B.11, B.12, B.13 and B.14. Additionally, Figure B.15 reveals PCL and PCL/GNP composites water contact angles with statistical analysis.

PCL, PCL/GNP-M and PCL/GNP-C filaments and scaffolds weigh loss derivate (dTG) curves, under nitrogen atmosphere, are presented in Figure B.16. On the other hand, Table B.2 contains its crystallization temperatures (T_{c1} and T_{c2}), melting temperatures (T_{m1} and T_{m2}), crystallization enthalpy (ΔH_{c1} , ΔH_{c2}), melting enthalpy (ΔH_{m1} , ΔH_{m2}) and degree of crystallization (χ_{c1} and χ_{c2}).

Loss factor (loss (G'') / storage (G') moduli) of PCL, PCL/GNP-M and PCL/GNP-C filaments at 90 °C, 130 °C and 180 °C are presented in Table B.3.

PCL/GNP-M and PCL/GNP-C filaments saturation (M_s) and remanent magnetization (M_r) are presented in Table B.4, while its dependence on the concentration of @GNP-M and @GNP-C is presented in Figure B.17. On the other hand, crystallographic patterns and magnetic-hysteresis (M-H) curves of PCL/GNP-M and PCL/GNP-C scaffolds are displayed in Figure B.18.

Fibre morphology of PCL and PCL/GNP-C filaments at different collector speeds (C_S) are presented in Figure B.19. On the other hand, Table B.5 contains information its critical translations speed (CTS), namely the ratio between the real fibre diameter (F_D) and the relative peak to peak fibre diameter (F'_D). Influence of feeding pressure (P), applied voltage (V) and C_S on F_D for PCL and PCL/GNP-C composites is presented in Tables B.6, B.7 and B.8.

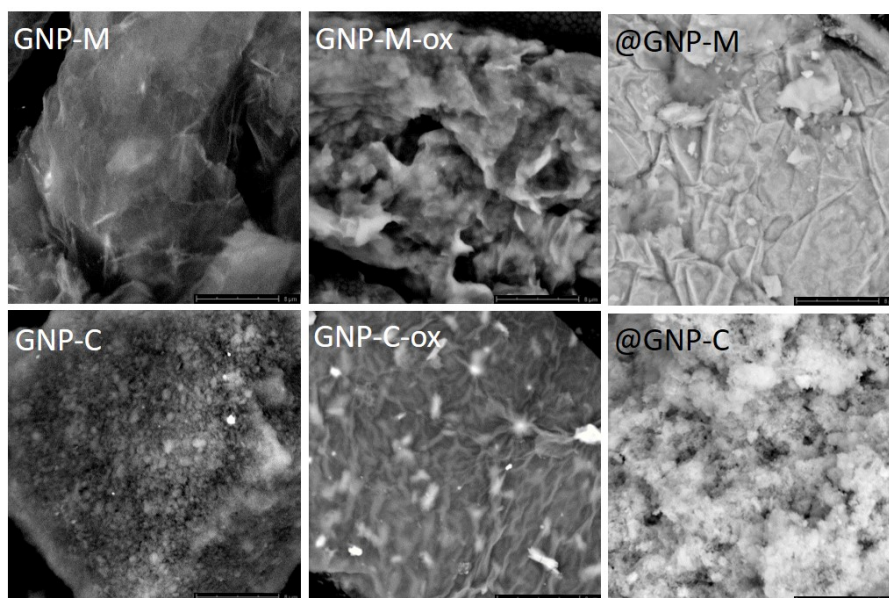
GBM morphological properties, particle size, and stability

Figure B.1: Scanning electron microscopy (SEM) images of GNP-M, GNP-M-ox, @GNP-M, GNP-C, GNP-C-ox and @GNP-C powders. Scale bars represent 8 μm.

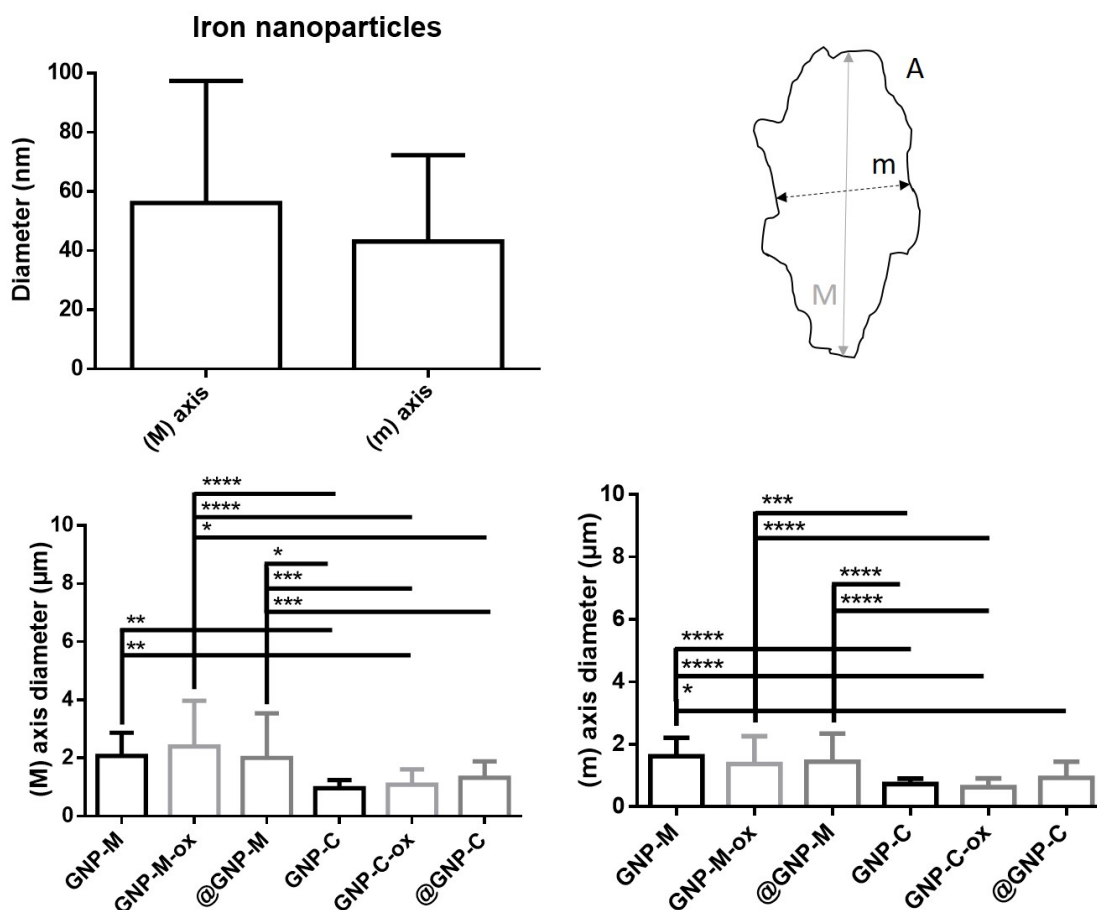


Figure B.2: Average particle size of iron nanoparticles and both grades of GNP from TEM images. Measurements were performed by using ImageJ software and are relative to the sample's major (M) and minor (m) axis. A) represents a graphene nanoplatelet as well as its (M) and (m) axis. Statistically significant differences are shown as * $p < 0.05$, ** $p < 0.01$, *** $p < 0.001$ and **** $p < 0.0001$.

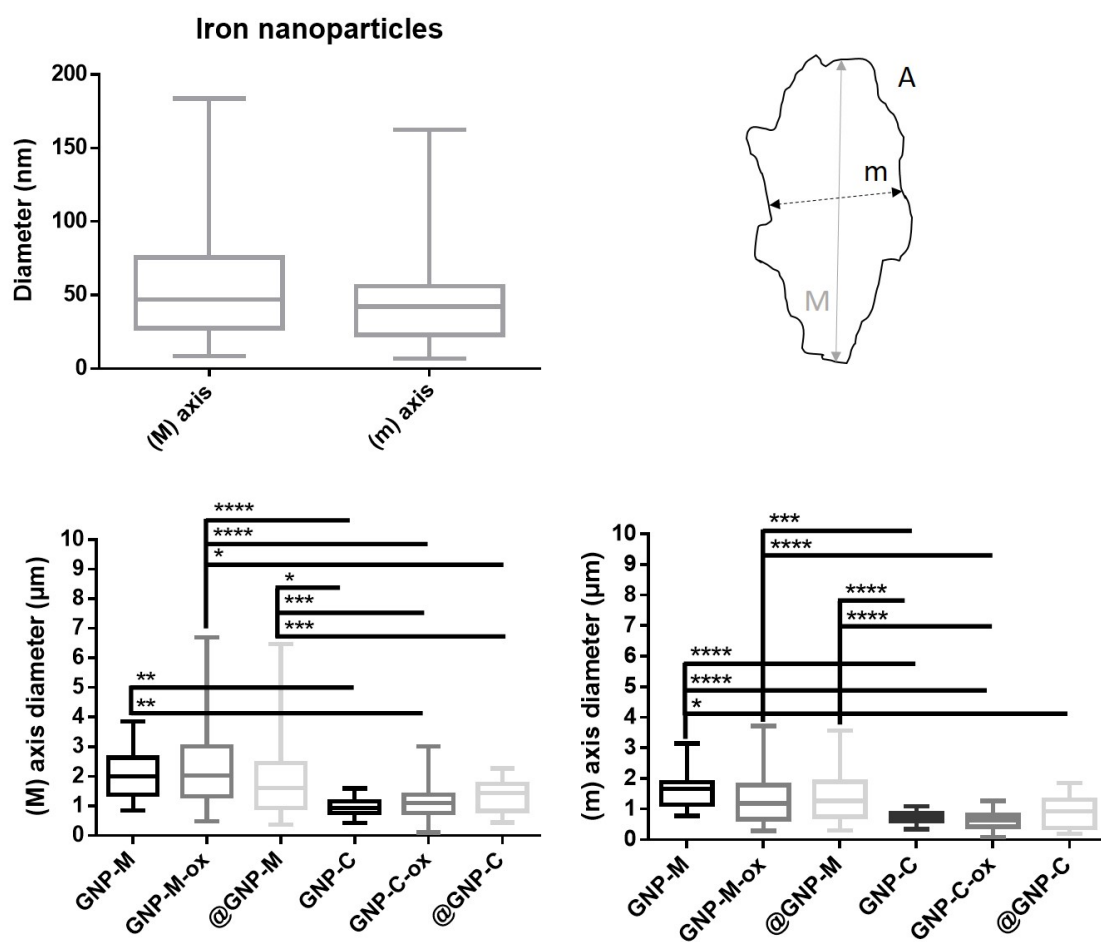


Figure B.3: Box-plot of particle size distribution in number of iron nanoparticles and both grades of GNP from TEM images. Measurements were performed by using ImageJ software and are relative to the sample's major (M) and minor (m) axis. A) represents a graphene nanoplatelet as well as its (M) and (m) axis. Statistically significant differences are shown as * $p < 0.05$, ** $p < 0.01$, *** $p < 0.001$ and **** $p < 0.0001$.

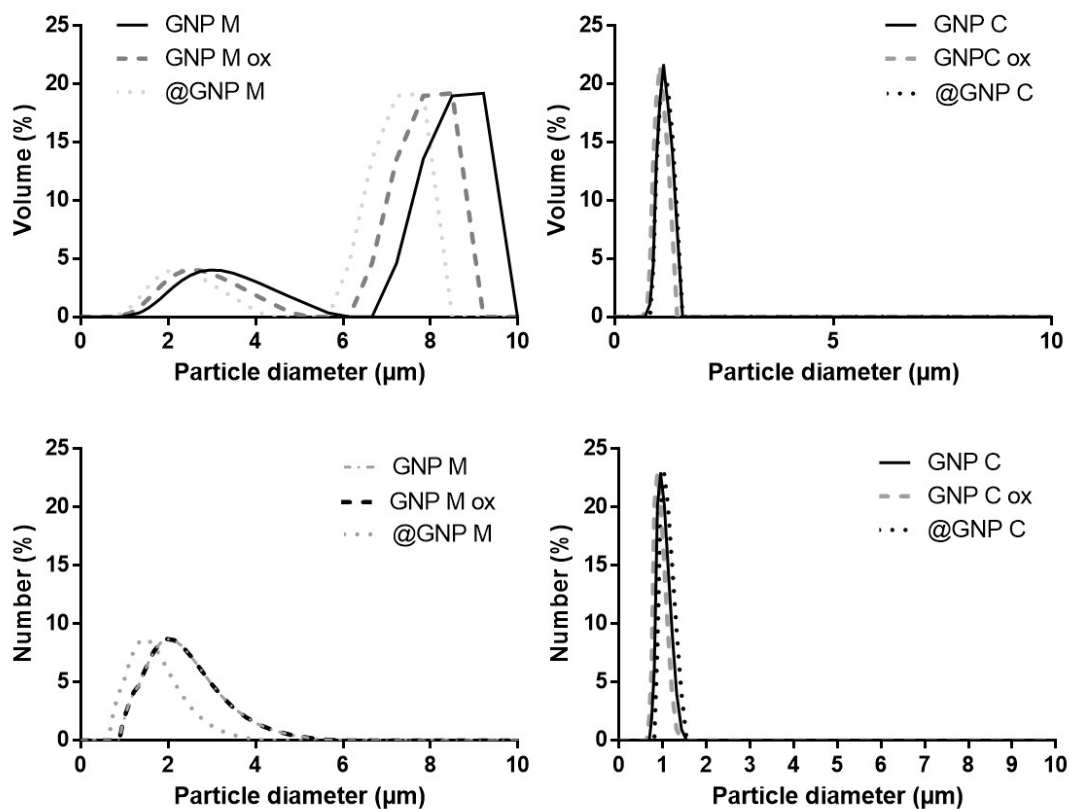


Figure B.4: Particle size distribution for both GNP-M and GNP-C grade materials in in volume (%) and number (%), determined by dynamic light scattering (DLS), using a Litesizer equipment.

Table B.1: Relationship between the zeta potential values (mV) and the solution stability behaviour. Adapted from [203].

Zeta potential (mV)	Stability behavior
0 to ± 5	Flocculation or coagulation
± 10 to ± 30	Incipient instability
± 30 to ± 40	Moderate stability
± 40 to ± 60	Good stability
$>\pm 60$	Excellent stability

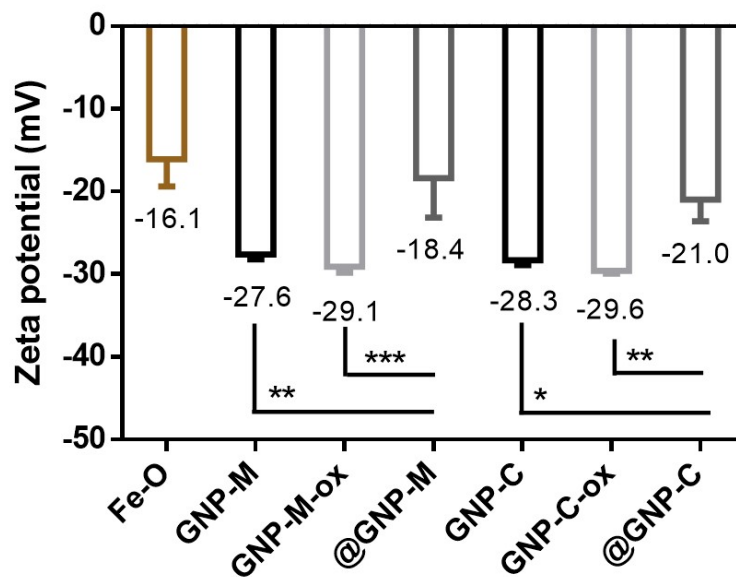


Figure B.5: Surface charge of iron nanoparticles (Fe-O), GNP-M, GNP-M-ox, @GNP-M, GNP-C, GNP-C-ox and @GNP-C aqueous dispersions at an initial concentration of $50 \mu\text{g mL}^{-1}$ and pH 7.4 ($n = 3$) determined with a Zetasizer equipment. Statistically significant differences are shown as * $p < 0.05$, ** $p < 0.01$, *** $p < 0.001$ and **** $p < 0.0001$.

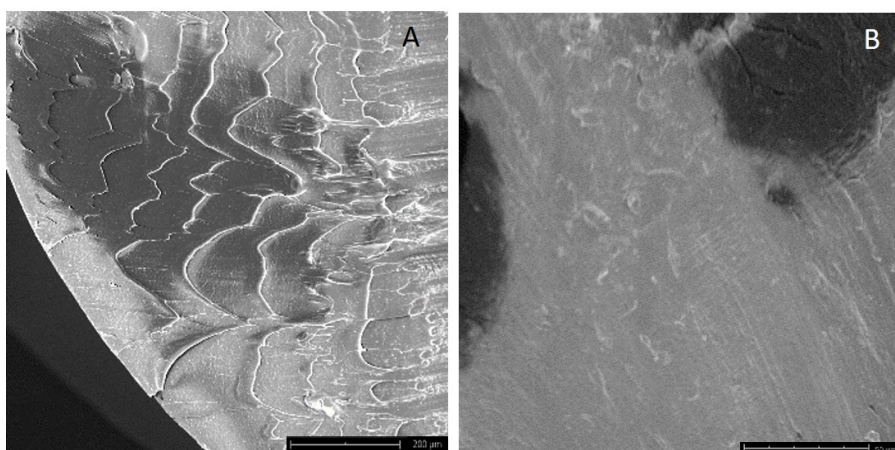


Figure B.6: SEM images of PCL/GNP-C-15 wt.% cross-section. Scale bars represent 500 and 50 μm for A) and B), respectively.

Chemical characterization

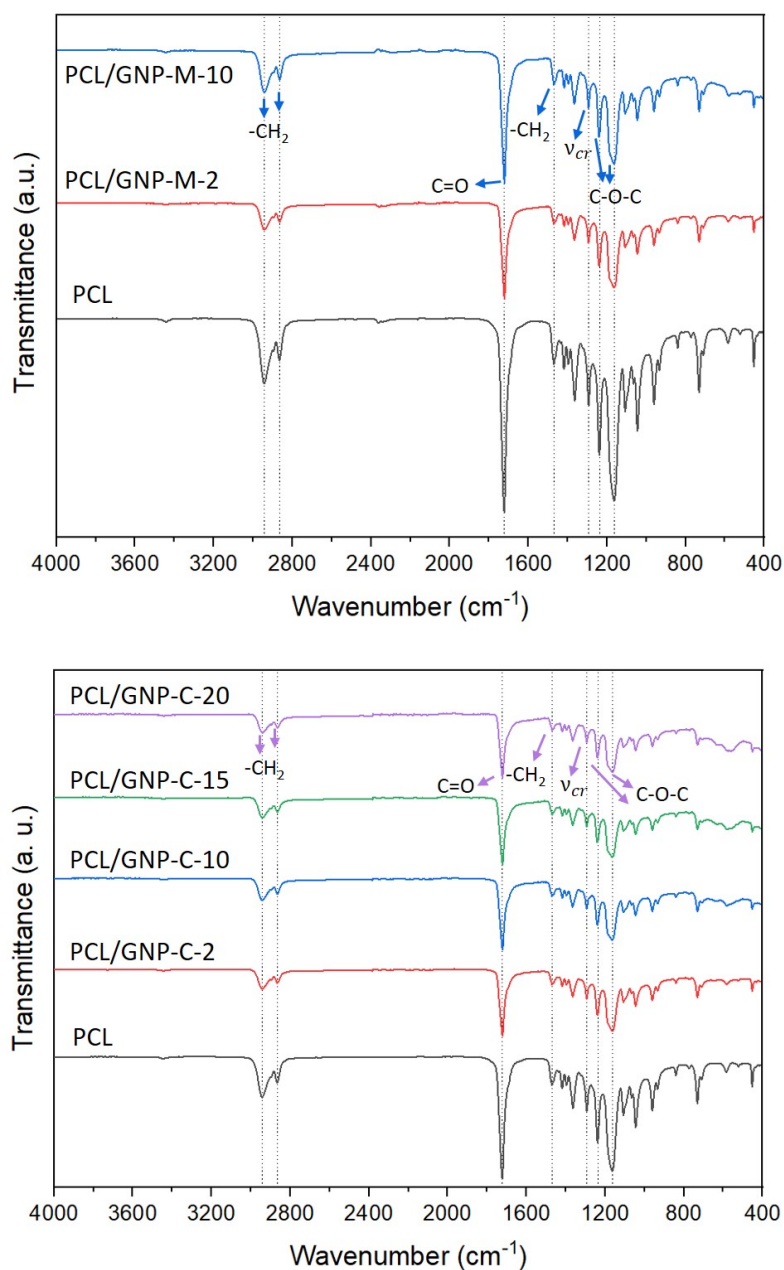


Figure B.7: FTIR spectra of PCL, PCL/GNP-M and PCL/GNP-C filaments. The arrows indicate the contribution of several surface functionalities, while the dotted lines points out similar peaks.

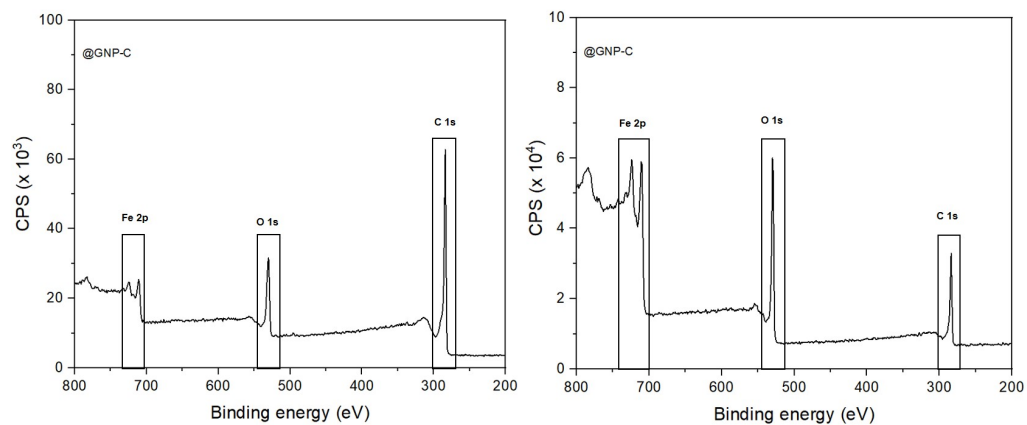


Figure B.8: XPS survey spectra @GNP-M and @GNP-C.

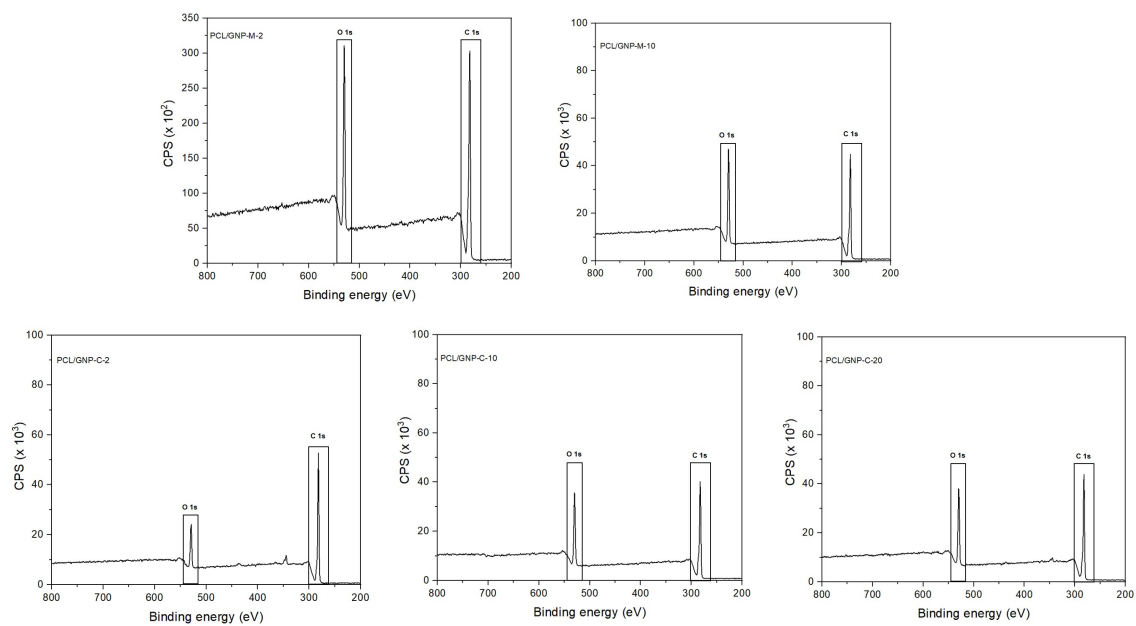


Figure B.9: XPS survey spectra for PCL/GNP-M and PCL/GNP-C filaments containing different filler contents.

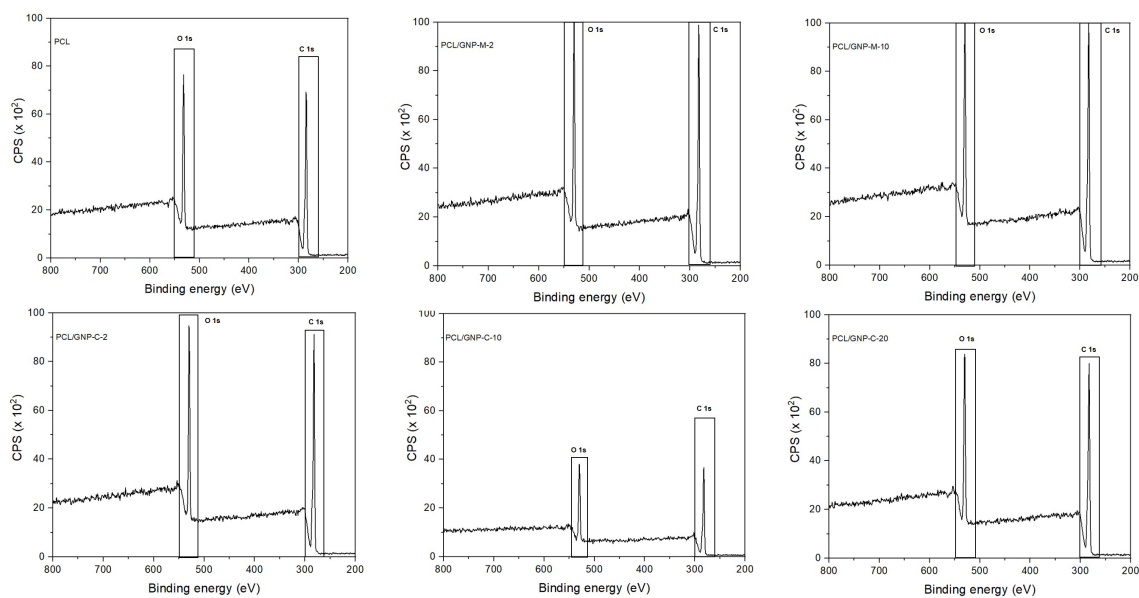
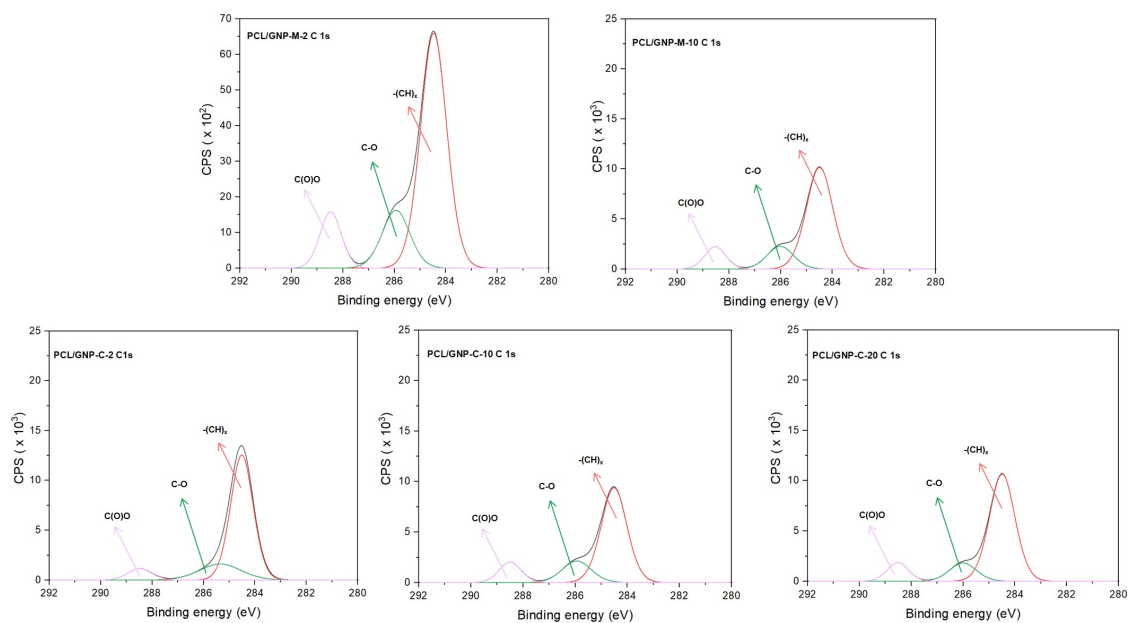


Figure B.10: XPS survey spectra for PCL, PCL/GNP-M and PCL/GNP-C scaffolds containing different filler contents.



Sample		Binding energy (eV)	C 1s (at. %)	Sample	Binding energy (eV)	C 1s (at. %)	
PCL/GNP-M-2	$-(CH)_x$	284.5	69.0	PCL/GNP-C-2	$-(CH)_x$	284.5	
	C-O	285.9	16.9		C-O	285.4	11.6
	C(O)O	288.5	14.1		C(O)O	288.5	9.0
PCL/GNP-M-10	$-(CH)_x$	284.5	69.1	PCL/GNP-C-10	$-(CH)_x$	284.5	
	C-O	286.0	16.3		C-O	286.0	14.6
	C(O)O	288.6	14.6		C(O)O	288.5	13.3
				PCL/GNP-C-20	$-(CH)_x$	284.5	
			C-O		286.0	14.7	
			C(O)O		288.5	12.4	

Figure B.11: XPS analysis of PCL/GNP-M and PCL/GNP-C filaments containing different filler contents. Deconvolution of high-resolution C 1s XPS spectra. Content of C 1s chemical groups resulting from spectra fitting.

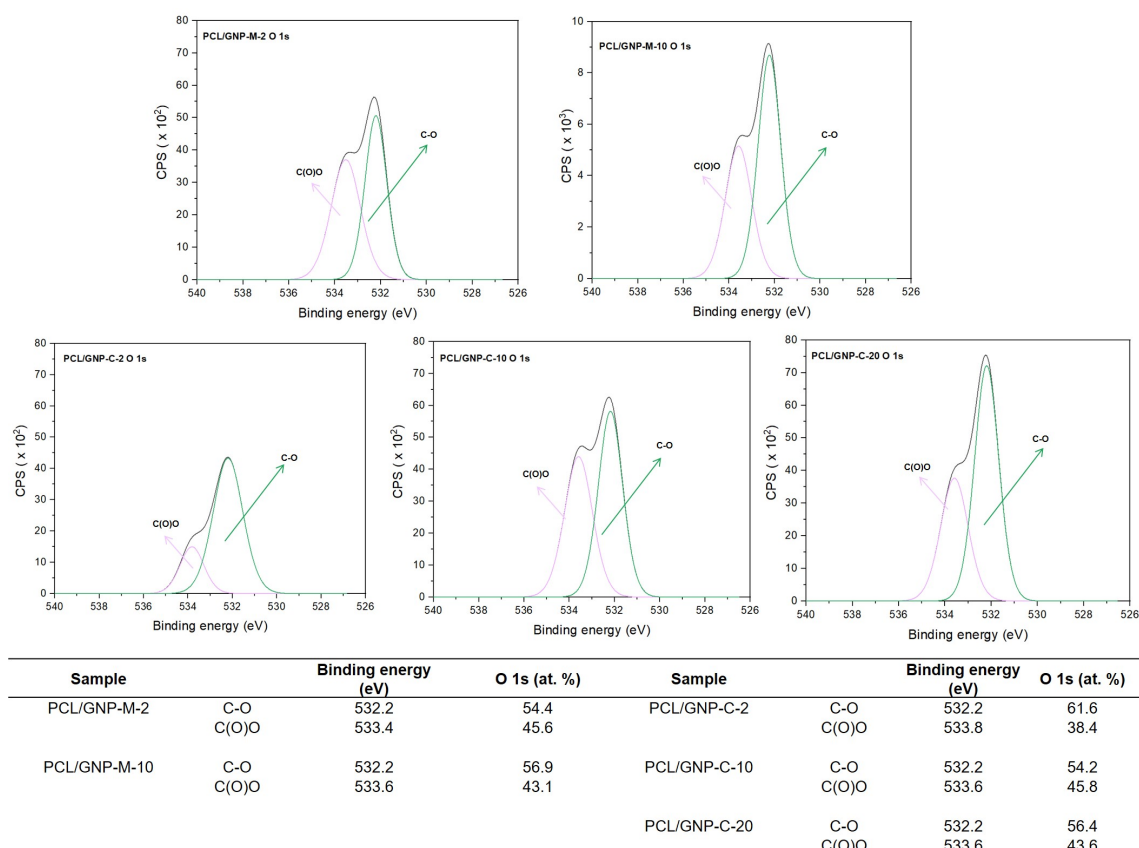


Figure B.12: XPS analysis of PCL/GNP-M and PCL/GNP-C filaments containing different filler contents. Deconvolution of high-resolution O 1s XPS spectra. Content of O 1s chemical groups resulting from spectra fitting.

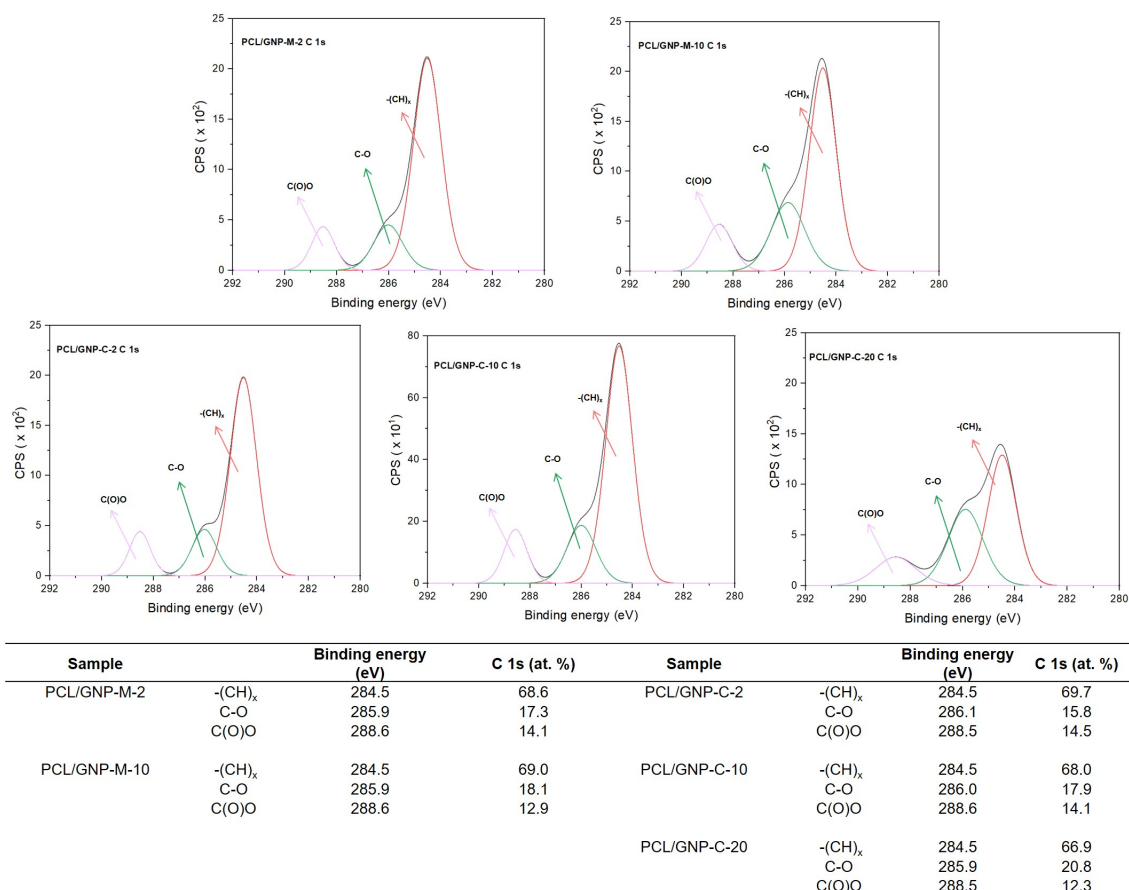


Figure B.13: XPS analysis of PCL/GNP-M and PCL/GNP-C scaffolds containing different filler contents. Deconvolution of high-resolution C 1s XPS spectra. Content of C 1s chemical groups resulting from spectra fitting.

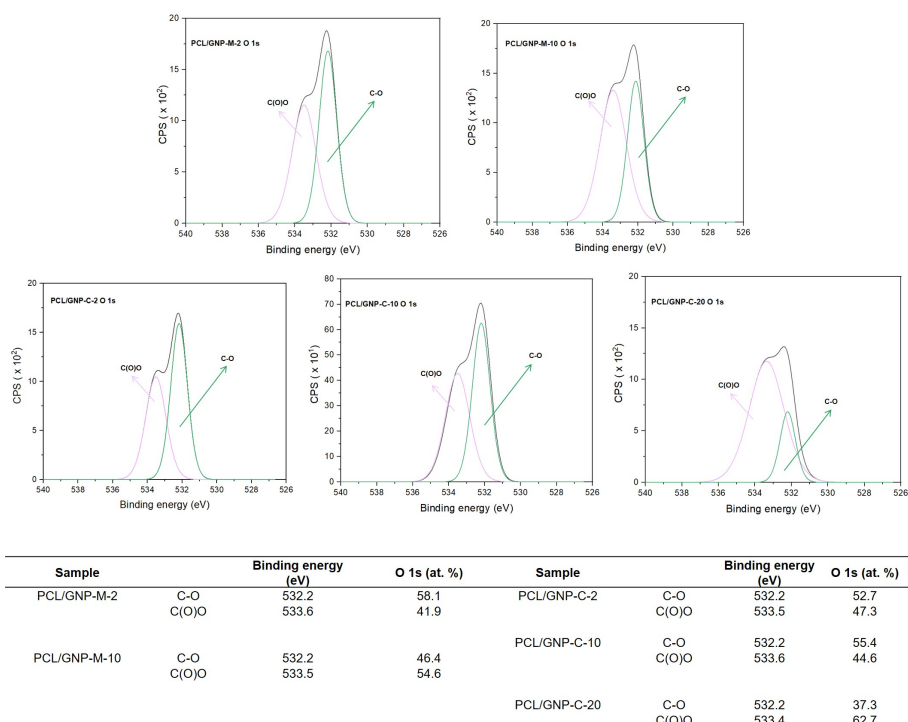


Figure B.14: XPS analysis of PCL/GNP-M and PCL/GNP-C scaffolds containing different filler contents. Deconvolution of high-resolution O 1s XPS spectra. Content of O 1s chemical groups resulting from spectra fitting.

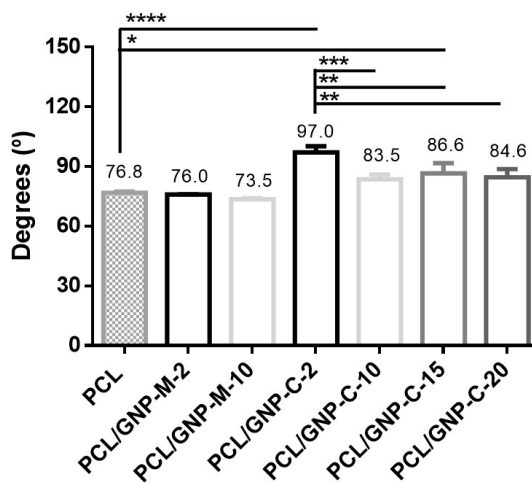


Figure B.15: Sessile drop water contact angle for PCL, PCL/GNP-M and PCL/GNP-C filaments containing different filler contents. Statistically significant differences are shown as * $p < 0.05$, ** $p < 0.01$, *** $p < 0.001$ and **** $p < 0.0001$.

Thermal analysis

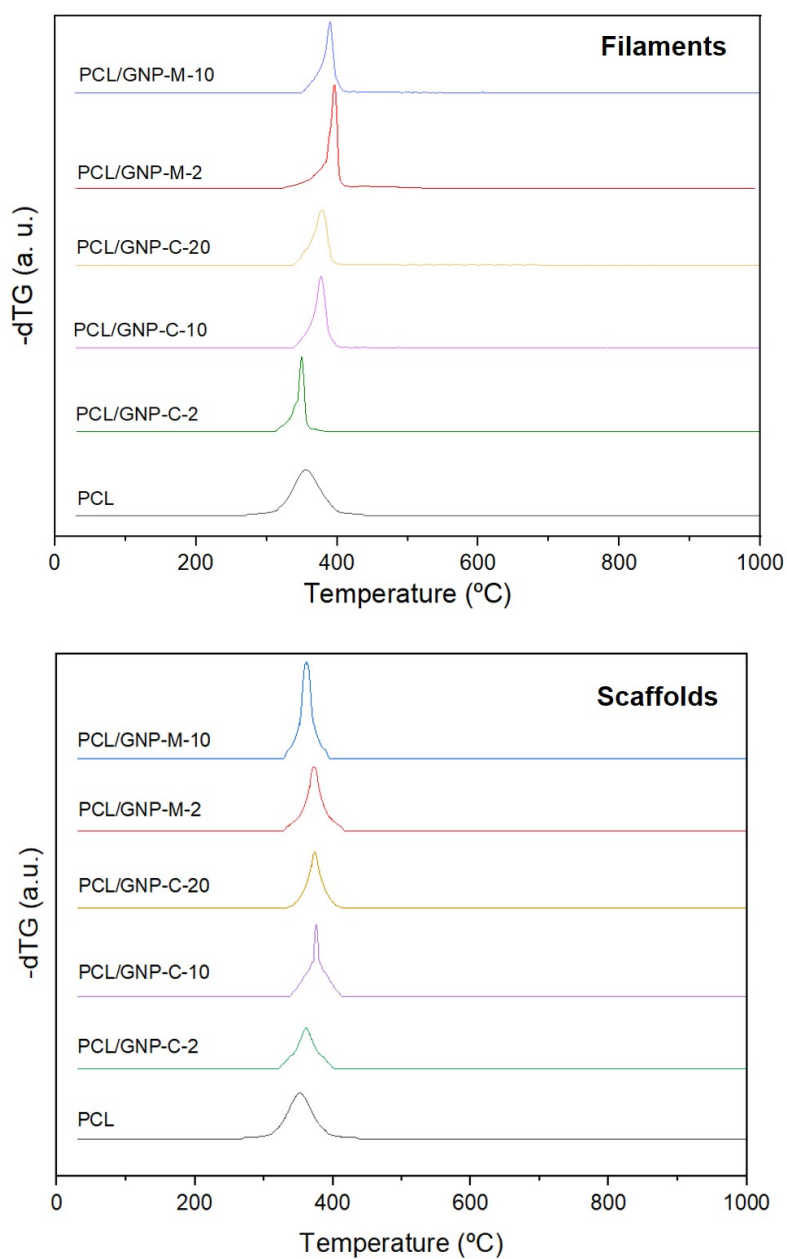


Figure B.16: -dTG curves for PCL, PCL/GNP-M and PCL/GNP-C filament and scaffolds containing different filler contents, under nitrogen atmosphere.

Table B.2: Crystallization temperatures (T_{c1} and T_{c2}), melting temperatures (T_{m1} and T_{m2}), crystallization enthalpy (ΔH_{c1} , ΔH_{c2}), melting enthalpy (ΔH_{m1} , ΔH_{m2}) and degree of crystallization (χ_{c1} and χ_{c2}) for PCL, PCL/GNP-M and PCL/GNP-C filaments and scaffolds containing different filler contents.

Type	Sample	T_{c1} (°C)	T_{c2} (°C)	T_{m1} (°C)	T_{m2} (°C)	ΔH_{c1} (J/g)	ΔH_{c2} (J/g)	ΔH_{m1} (J/g)	ΔH_{m2} (J/g)	χ_{c1} (%)	χ_{c2} (%)
Filaments	PCL	19.8	19.4	66.9	54.2	66.4	75.2	73.5	65.6	52.7	47.0
	PCL/GNP-M-2	36.2	36.3	65.5	55.5	70.8	70.0	64.6	66.5	47.3	48.7
	PCL/GNP-M-10	37.3	37.6	64.6	55.8	66.4	65.4	64.3	55.5	51.3	44.3
	PCL/GNP-C-2	36.2	36.3	61.6	55.7	69.8	70.1	62.3	66.0	45.6	48.2
	PCL/GNP-C-10	37.5	37.7	60.9	55.3	66.7	66.5	60.0	60.9	47.8	48.5
	PCL/GNP-C-15	38.6	38.6	60.8	55.5	58.7	58.4	50.7	53.4	42.8	45.1
	PCL/GNP-C-20	38.7	38.7	56.7	55.4	61.4	57.2	54.8	55.5	49.1	49.7
Scaffolds	PCL	19.8	19.4	66.9	54.2	63.6	63.4	63.6	55.1	45.6	39.5
	PCL/GNP-M-2	35.5	35.6	58.6	54.6	60.2	59.8	73.2	65.4	53.6	47.8
	PCL/GNP-M-10	37.4	37.3	58.7	55.2	55.0	54.4	60.6	66.6	48.3	48.7
	PCL/GNP-C-2	35.1	35.1	55.2	55.2	65.9	65.6	57.8	53.4	42.3	39.1
	PCL/GNP-C-10	37.1	37.0	56.3	55.7	48.5	48.3	65.4	57.4	52.1	42.1
	PCL/GNP-C-20	38.3	38.3	58.5	55.1	52.5	52.4	63.7	58.2	57.1	42.6

Rheological properties

Table B.3: Loss factor (G''/G') values for PCL, PCL/GNP-M and PCL/GNP-C filaments containing different filler contents at 90 °C, 130 °C and 180 °C.

Sample	Loss factor at					
	90 °C		130 °C		180 °C	
	mean	std	mean	std	mean	std
PCL	7.6	0.6	18.0	1.6	47.9	4.3
PCL/GNP-M-2	6.6	0.1	18.0	1.6	-	-
PCL/GNP-M-10	3.5	0.1	9.1	1.0	-	-
PCL/GNP-C-2	7.0	0.2	18.4	1.4	-	-
PCL/GNP-C-10	6.4	0.4	9.0	0.6	-	-
PCL/GNP-C-15	4.0	0.5	2.8	0.6	-	-
PCL/GNP-C-20	2.2	0.3	1.6	0.4	-	-

Crystallographic and magnetic characterization

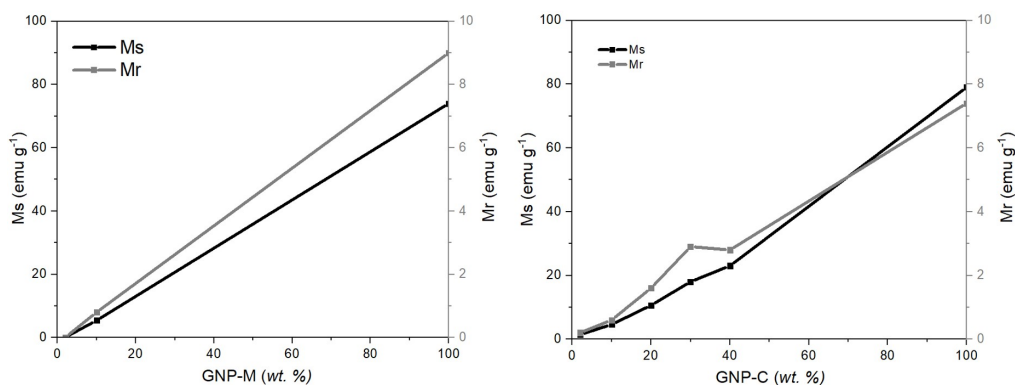


Figure B.17: Dependence of the saturation and remanent magnetization (M_s and M_r , respectively) on the concentration of A) @GNP-M and B) @GNP-C.

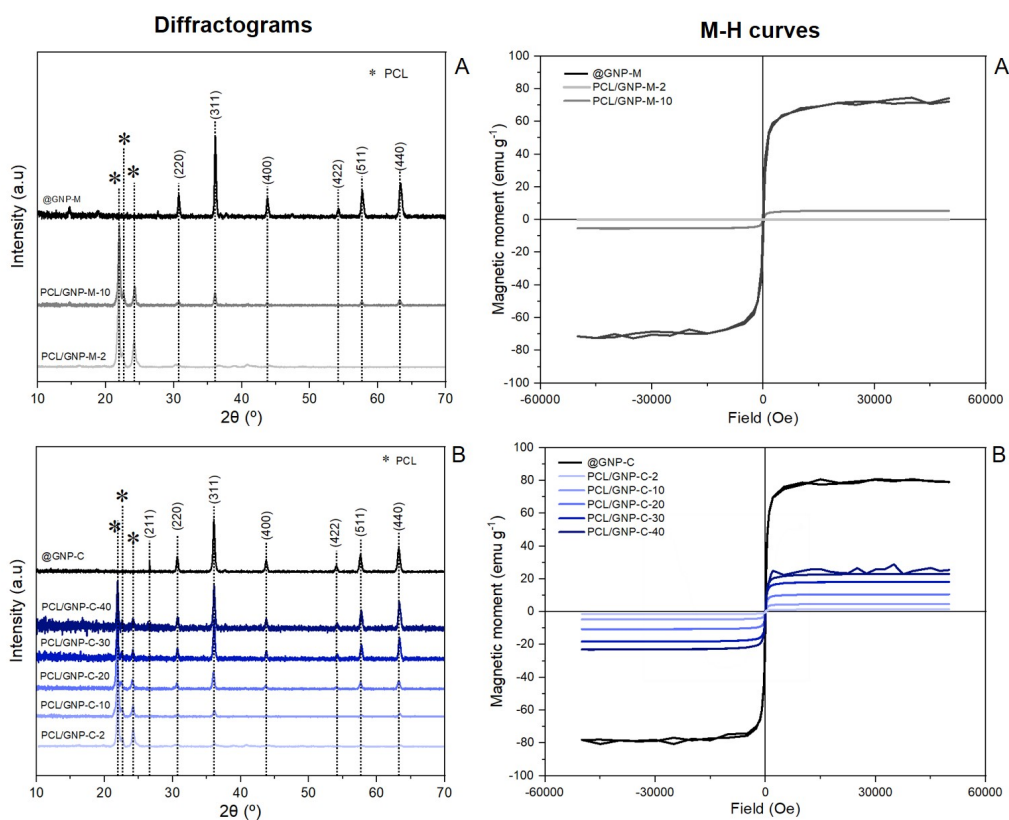


Figure B.18: Crystallographic patterns and M-H curves of A) PCL/GNP-M and B) PCL/GNP-C scaffolds containing different filler contents through XRD and SQUID, respectively, at room temperature.

Table B.4: Saturation magnetization (M_s), coercivity (H_c) and remanent magnetization M_r values of GNP, GNP-ox and @GNP powders, as well as PCL/GNP filaments and scaffolds containing different filler contents.

Sample	M_s (emu g ⁻¹)			M_r (emu g ⁻¹)	H_c (Oe)
	Expected (E)	Obtained (O)	O/E ratio (%)		
GNP-M	-	-	-	2.0E-03	35.0
GNP-C	-	-	-	9.0E-03	99.0
GNP-M-ox	-	-	-	3.0E-04	460.0
GNP-C-ox	-	-	-	8.0E-04	164.0
@GNP-M	-	74	-	9.0	97.0
@GNP-C	-	79	-	7.4	51.5
PCL/GNP-M-2	1.5	0.05	0.03	2.0E-03	68.0
PCL/GNP-M-10	7.4	5.4	72.9	0.8	94.0
PCL/GNP-C-2	1.6	1.4	87.5	0.2	52.0
PCL/GNP-C-10	7.9	4.6	58.2	0.6	54.0
PCL/GNP-C-20	15.8	10.6	67.1	1.6	64.5
PCL/GNP-C-30	23.7	18	75.9	2.9	62.0
PCL/GNP-C-40	31.6	23	72.8	2.8	61.5
PCL/GNP-M-2	1.5	-	-	2.0E-03	150.0
PCL/GNP-M-10	7.4	5.4	72.9	0.8	96.0
PCL/GNP-C-2	1.6	1.2	75.0	0.2	80.0
PCL/GNP-C-10	7.9	4.6	58.2	0.6	63.0
PCL/GNP-C-20	15.8	10.9	69.0	1.3	62.0

Fibre diameter and morphology

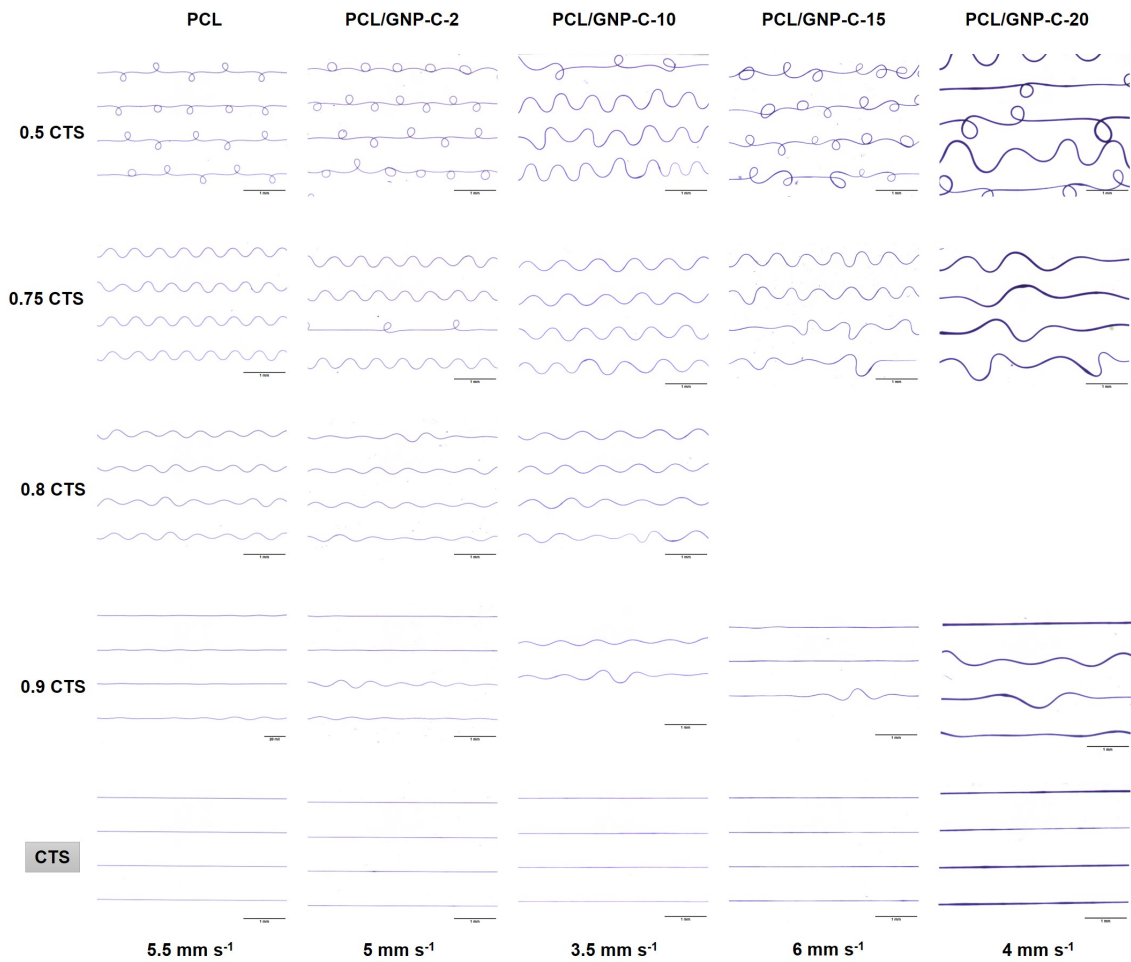


Figure B.19: Fibre morphology of PCL and PCL/GNP-C grade materials at 0.5 CTS, 0.75 CTS, 0.9 CTS and CTS. Scale bars represent 1 mm.

Table B.5: Critical translational speed (CTS) for PCL and PCL/GNP-C composites containing different filler contents. Ratio between the real fibre diameter (F_D) and the relative peak to peak fibre diameter (F'_D), for several collection speeds (C_S). C_S is expressed as $f \times \text{CTS}$.

Sample	f	CTS (mm/s)	F_D/F'_D		Sample	CTS (mm/s)	f	F_D/F'_D	
			mean	std				mean	std
PCL	0.5	5.5	0.04	0.01	PCL/ GNP-C-15	6	0.5	0.07	0.01
	0.75		0.09	0.01			0.75	0.09	0.01
	0.9		0.51	0.05			0.9	0.36	0.07
	1		1.00	0.00			1	1.00	0.00
PCL/ GNP-C-2	0.5	5	0.06	0.01	PCL/ GNP-C-20	4	0.5	0.06	0.01
	0.75		0.07	0.01			0.75	0.10	0.01
	0.9		0.40	0.12			0.9	0.27	0.16
	1		1.00	0.00			1	1.00	0.00
PCL/ GNP-C-10	0.5	3.5	0.05	0.01			0.5		
	0.75		0.06	0.01			0.75		
	0.9		0.40	0.08			0.9		
	1		1.00	0.00			1		

Table B.6: Influence of feeding pressure (P) on fibre diameter (F_D) for PCL and PCL/GNP-C composites containing different filler contents.

Sample	Pressure (bar)	F_D (μm)		Sample	Pressure	F_D (μm)	
		mean	std			mean	std
PCL	1	10.47	0.25	PCL/GNP-C-15	1		
	1.5	12.57	0.35		1.5	9.27	1.11
	2	12.88	0.39		2	13.76	1.27
	2.5	14.92	0.51		2.5	18.31	1.62
	3	18.40	0.37		3	21.95	2.23
PCL/GNP-C-2	1	7.72	0.36	PCL/GNP-C-20	1		
	1.5	8.92	0.40		1.5	18.76	2.94
	2	12.05	0.54		2	27.55	4.10
	2.5	13.58	0.64		2.5	29.84	4.02
	3	18.53	0.30		3	33.76	3.40
PCL/GNP-C-10	1						
	1.5	11.73	0.62				
	2	13.72	0.84				
	2.5	19.33	0.43				
	3	21.82	0.91				

Table B.7: Influence of applied voltage (V) on fibre diameter (F_D) for PCL and PCL/GNP-C composites containing different filler contents.

Sample	Voltage (KV)	F_D (μm)		Sample	Voltage (KV)	F_D (μm)	
		mean	std			mean	std
PCL	5	15.58	0.25	PCL	5	17.43	1.71
	5.5	14.64	0.63		5.5	15.85	1.88
	6	12.88	0.39		6	13.76	1.27
	6.5	12.53	0.62		6.5	13.35	1.47
	7	11.09	0.32		7	11.46	1.17
PCL/GNP-C-2	5	15.20	0.50	PCL/GNP-C-2	5	39.80	6.31
	5.5	12.72	1.12		5.5	30.34	3.92
	6	12.05	0.54		6	27.55	4.10
	6.5	10.97	0.34		6.5	20.69	4.03
	7	10.02	0.46		7	17.83	1.35
PCL/GNP-C-10	5	16.08	0.69				
	5.5	14.93	0.50				
	6	13.72	0.84				
	6.5						
	7						

Table B.8: Influence of collector speed (C_S) on fibre diameter (F_D) for PCL and PCL/GNP-C composites containing different filler contents. C_S is expressed as $f \times \text{CTS}$.

Sample	f	CTS (mm/s)	F_D (μm)		Sample	CTS (mm/s)	F_D (μm)		
			mean	std			mean	std	
PCL	1	5.5	12.88	0.39	PCL/GNP-C-15	1	6	13.76	1.27
	1.2		11.68	0.41		1.2		13.28	0.95
	1.4		11.05	0.39		1.4		12.47	0.79
	1.6		10.44	0.28		1.6		11.25	1.76
	1.8		9.93	0.35		1.8		10.65	1.32
PCL/GNP-C-2	1	5	12.05	0.54	PCL/GNP-C-20	1	4	27.55	4.10
	1.2		11.09	0.57		1.2		23.67	2.53
	1.4		9.61	0.47		1.4		22.01	4.38
	1.6		9.33	0.43		1.6		17.43	1.72
	1.8		8.63	0.77		1.8		16.95	2.03
PCL/GNP-C-10	1	3.5	13.72	0.84					
	1.2		13.66	1.03					
	1.4		12.97	0.82					
	1.6		12.08	1.49					

Appendix C

List of publications

1. R. Costa-Almeida, D. Bogas, J. R. Fernandes, L. Timochenco, F. A. Silva, J. Meneses, I. C. Gonçalves, F. D. Magalhães, and A. M. Pinto, “Near-infrared radiation-based mild photothermia therapy of non-melanoma skin cancer with pegylated reduced nanographene oxide.” *Polymers*, vol. 12, no. 8, p. 1840, 2020.

Appendix D

List of presentations

1. J. Meneses, C. Couto, R. Costa-Almeida, D. Bogas, L. Timochenco, J. R. Fernandes, M.C.L. Martins, I. C. Gonçalves, F. D. Magalhães, and A. M. Pinto, "Graphene-based materials for drug delivery and photothermal cancer therapy", IJUP, 2020.
2. A. Pinto, J. Meneses, L. Timochenco, F. Silva, R. Costa-Almeida, F. D. Magalhães, "From nanographene production scale-up to its biomedical applications", NanoPT, 2020.
3. R. Costa-Almeida, D. Bogas, L. Timochenco, F. Silva, J. R. Fernandes, J. Meneses, M. C. L. Martins, I. C. Gonçalves, F. D. Magalhães, A. Pinto, "Photothermal cancer therapy with graphene-based materials and their drug conjugates", GIF, 2020.